THE EFFECTS OF TIDAL INTERACTIONS ON THE PROPERTIES AND EVOLUTION OF HOT-JUPITER PLANETARY SYSTEMS

David John Alexander Brown

A Thesis Submitted for the Degree of PhD
at the
University of St Andrews

2013

The effects of tidal interactions on the properties and evolution of hot-Jupiter planetary systems.

by

David John Alexander Brown

Submitted for the degree of Doctor of Philosophy in Astrophysics

21st October 2013

University of St Andrews

600 YEARS

Declaration

I, David J. A. Brown, hereby certify that this thesis, which is approximately 60,000 words in length, has been written by me, that it is the record of work carried out by me and that it has not been submitted in any previous application for a higher degree.

Date Signature of candidate

I was admitted as a research student in September 2009 and as a candidate for the degree of PhD in September 2009; the higher study for which this is a record was carried out in the University of St Andrews between 2009 and 2013.

Date Signature of candidate

I hereby certify that the candidate has fulfilled the conditions of the Resolution and Regulations appropriate for the degree of PhD in the University of St Andrews and that the candidate is qualified to submit this thesis in application for that degree.

Date Signature of supervisor

Collaboration statement

Three of the Chapters in this thesis make use of previously published work. Chapter 4 is based on Brown et al. (2011), MNRAS, 415, 605-618. Chapters 5 and 6 are based on Brown et al. (2012), MNRAS, 423, 1503-1520 and Brown et al. (2012), ApJ, 760, 139. In all cases the majority of the analysis was carried out by the author. The contribution of the co-authors was as follows.

The work in Brown et al. (2011), MNRAS, 415, 605-618 was based on an idea developed as an undergraduate masters research project by Cassie Hall (supervised by Andrew Collier Cameron), and on a previous analysis of tidal inspiral in the WASP-19 system by Leslie Hebb. The author's analysis developed the methods used by these contributors to carry out a more rigourous analysis. Barry Smalley carried out spectral line analysis to provide lithium abundances that the author used to produce stellar age estimates.

The analysis in Brown et al. (2012), MNRAS, 423, 1503-1520 and Brown et al. (2012), ApJ, 760, 139 was carried out using computer code originally created by Andrew Collier Cameron, modified by several of the co-authors, and customised by the author. Michael Gillon and Monika Lendl obtained photometric data of the targets specifically for these papers. Spectroscopic transit observations were organised and carried out by Amaury Triaud, Rodrigo Diaz, Andrew Collier Cameron, David Anderson, and the author. Barry Smalley and Amanda Doyle carried out spectral line analysis to provide initial $v \sin I$ estimates for the targets. The remaining co-authors are other members of the SuperWASP consortium who had previously worked on the systems being investigated, or who had made use of the methods presented by the author.

Copyright Agreement

In submitting this thesis to the University of St Andrews we understand that we are giving permission for it to be made available for use in accordance with the regulations of the University Library for the time being in force, subject to any copyright vested in the work not being affected thereby. We also understand that the title and the abstract will be published, and that a copy of the work may be made and supplied to any bona fide library or research worker, that my thesis will be electronically accessible for personal or research use unless exempt by award of an embargo as requested below, and that the library has the right to migrate my thesis into new electronic forms as required to ensure continued access to the thesis. We have obtained any third-party copyright permissions that may be required in order to allow such access and migration, or have requested the appropriate embargo below.

The following is an agreed request by candidate and supervisor regarding the electronic publication of this thesis: Access to Printed copy and electronic publication of thesis through the University of St Andrews.

Date Signature of candidate

Date Signature of supervisor

Abstract

Thanks to a range of discovery methods that are sensitive to different regions of parameter space, we now know of over 900 planets in over 700 planetary systems. This large population has allowed exoplanetary scientists to move away from a focus on simple discovery, and towards efforts to study the bigger pictures of planetary system formation and evolution.

The interactions between planets and their host stars have proven to be varied in both mechanisms and scope. In particular, tidal interactions seem to affect both the physical and dynamical properties of planetary systems, but characterising the broader implications of this has proven challenging. In this thesis I present work that investigates different aspects of tidal interactions, in order to uncover the scope of their influence of planetary system evolution.

I compare two different age calculation methods using a large sample of exoplanet and brown dwarf host stars, and find a tendency for stellar model fitting to supply older age estimates than gyrochronology, the evaluation of a star's age through its rotation (Barnes, 2007). Investigating possible sources of this discrepancy suggests that angular momentum exchange through the action of tidal forces might be the cause.

I then select two systems from my sample, and investigate the effect of tidal interactions on their planetary orbits and stellar spin using a forward integration scheme. By fitting the resulting evolutionary tracks to the observed eccentricity, semi-major axis and stellar rotation rate, and to the stellar age derived from isochronal fitting, I am able to place constraints on tidal dissipation in these systems. I find that the majority of evolutionary histories consistent with my results imply that the stars have been spun up through tidal interactions as the planets spiral towards their Roche limits.

I also consider the influence of tidal interactions on the alignment between planetary orbits and stellar spin, presenting new measurements of the projected spin-orbit alignment angle, λ, for six hot Jupiters. I consider my results in the context of the full ensemble of measurements, and find that they support a previously identified trend in alignment angle with tidal timescale, implying that tidal realignment might be responsible for patterns observed in the λ distribution.

Acknowledgements

A great many people deserve to be thanked for helping me through this PhD. I have to start with my long-suffering girlfriend, Ellen Adams, for her unfailing support throughout this PhD. Without her advice, guidance, and shoulder to cry on I would have found the whole thing even more difficult than it was.

Thanks also to my family: Mum, Dad, and my brother James. They were always there when I needed to vent my frustration at someone, and kept me sane with regular visits. They have always believed in me, and are the reason for me even being in this situation in the first place.

Then I must thank my friends. First, John Parkin, my housemate for the last three years. He heroically coped with my foibles, absenteeism, and mess whilst working towards his own PhD. He makes a much better scientist than I ever will. Second, the whole of the University of St Andrews Lifesaving Club, but particularly Hannah Anderson-Knight, Christopher Harper, Ella Hunt, Robyn Ireland, Christina Samson, Sarah Shapiro, and Teddy Woodhouse. Thanks go to them for being some of the best friends I've ever had, for sticking by me through good and bad, and for supporting my crazy schemes. I don't think they realise what a significant impact they've had on my life.

Next, thanks to the astronomy group at St Andrews. Grant Miller, for sharing an office with me for almost three years and surviving; Noé Kains, for making me feel welcome when I arrived; Lee Kelvin, whose laugh I will never forget; Joe Llama and Jack O'Malley-James for the hare-brained ideas, Raphaelle Haywood for her unfailingly enthusiastic approach to life, and Claire Davies for giving me someone to chat sports with. Not to mention John MacLachlan, William Lucas, Jeremy Barber, Rim Fares, Craig Stark, Neil Parley, Carsten Weidner, and everyone else in the department.

Finally, I must also thank Prof. Andrew Cameron for his supervision. He gave me both the flexibility and freedom to pursue my own interests, both inside and outside of science, which kept me in touch with reality. He also encouraged me to become involved with the Planetarium outreach show; I never imagined that it would become such a big part of my life.

Advances are made by answering questions.
Discoveries are made by questioning answers.

Bernhard Haisch

For my Grandparents

Contents

List of Figures

List of Tables

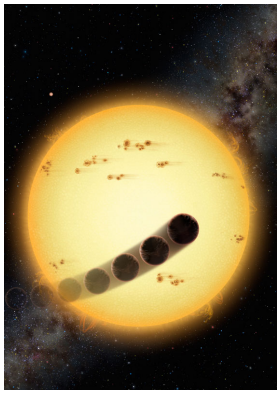

1

Introduction

The thirteen years since the turn of the century have been an exciting period for astronomy and astrophysics. The last year alone has seen the discovery of a new class of supernova (Foley et al., 2013), hints at the nature of dark matter (Aguilar et al., 2013; CDMS Collaboration et al., 2013), and a refined estimate of the age of the Universe (Planck Collaboration et al., 2013). That is only the tip of the iceberg though; since the beginning of the millennium astronomers have a found evidence that Mars used to have substantial quantities of water on its surface (Weitz & Parker, 2000; Fassett & Head, 2008; Rennó et al., 2009), confirmed that our Galaxy is a barred spiral (Churchwell et al., 2009), found evidence of water ice on the Moon (Pieters et al., 2009), observed a gas cloud spiralling into a black hole (Gillessen et al., 2012), and taken the first images of an extra-solar planet (Chauvin et al., 2004). There have been so many amazing discoveries that it is difficult to keep up with them. We have indeed, to misquote an old proverb, been living in interesting times.

From my own perspective the most exciting development has been the continued, rapid

rise of extra-solar planetary science to a position of prominence amongst astronomical research. In the course of my PhD I have seen the tendrils of exoplanet[1] research gradually infiltrate other areas of astrophysics, so that more and more of astronomy seems to relate back to these mysterious bodies. I have also witnessed public perception and excitement about planets outside the Solar system grow with each new discovery as we uncover the full diversity of other worlds.

1.1 A brief history of exoplanets

The idea that there might be planetary sized bodies outside of the Solar system has a long history. The first real indication that they might exist was the discovery of circumstellar discs (e.g. Smith & Terrile, 1984). After all, if there were discs of material around stars, then surely that material could form planets and other bodies? But it took a lot longer until proof was found that there really were other planets out there. That proof arrived from Wolszczan & Frail (1992), who carefully measured variations in the pulse timing of the binary pulsar PSR1257+12 and concluded that the observed variation was due to the presence of at least two planet sized companions.

Following Wolszczan & Frail's announcement, it was three years before the first planet around a main sequence star was discovered. When *51 Pegasi b* was announced (Mayor & Queloz, 1995) it was very different to what had been expected: a Jovian-type gas giant orbiting with semi-major axis smaller than that of Mercury. With the Solar system being the only known example up to that point, it was naturally assumed that other planetary systems would follow a similar pattern, with small rocky planets closer in and large, gaseous or icy planets further out. *51 Pegasi b* was therefore a surprise.

Astronomers were forced to reassess their assumptions and models of the formation and configuration of planetary systems. Targeted searches for Jupiter-like planets, using specifically designed instruments, had been running for several years, and astronomers scrambled to reanalyse the data from these programs. Other potential planetary signals were found and, with the benefit of hindsight, some previously posited close-in brown dwarf companions were considered in a new light. One example of such a process is the HD114762 system (Latham et al., 1989), in which the radial velocity signal of a substellar companion was originally

[1]Throughout this thesis I shall use extra-solar planet and exoplanet interchangeably.

thought to be a brown dwarf. It is now counted amongst the known extra-solar planets.

In the years since then the number of known planets has increased, with the rate of discovery accelerating towards the present day. The current tally of known extra-solar planets stands at 927, in 715 systems [2]. The majority of these have been detected through radial velocity monitoring or photometric transit observations, but contributions to this tally have also been made by micro-lensing, direct imaging, and timing measurements.

There are actually approximately twenty different signatures by which the presence of an extra-solar planet may be inferred (Perryman, 2000). Current instrumentation lacks the precision required to detect a significant fraction of these, but cutting-edge technology is bringing more of them within our reach. The method with which I am most familiar is detection through observations of photometric transits, the discovery rate from which initially lagged behind that from radial velocity surveys. But the launch, and outstanding success, of the Kepler space mission (Borucki et al., 2008) has led to greater parity between the two.

In the last few years the focus of exoplanet research has moved away from discovery towards attempts look at elements of the bigger picture: characterisation of the systems, analysis of the global properties of the full population, and simulations of possible routes for the formation and evolution of planetary systems. That's not to say that discovery projects are completely obsolete, as there will always be a drive for a larger data set (i.e. more planetary systems). Rather that large-scale search projects require greater justification as far as their science goals and required sample size are concerned. As such they are now more specialised, and aimed at pushing into specific regimes that have yet to be fully explored. There are ongoing and planned programs using the photometric transit (e.g. Borucki et al., 2008; Wheatley et al., 2013) and radial velocity (e.g. Ge et al., 2008) methods, not to mention gravitational micro-lensing (e.g. Dominik et al., 2008; Kains et al., 2013) and transit timing (Mazeh et al., 2013). Each is able to make a unique contribution to our exoplanet census thanks to the disparate sensitivity regimes of the different methods.

1.2 Planetary transits

The transit of a planet across the face of its host star causes a distinctive reduction in the flux emitted by the star for the duration of the transit. This repeats every time the planet returns

[2] as listed on `www.exoplanet.eu` as of 2013 August 7th

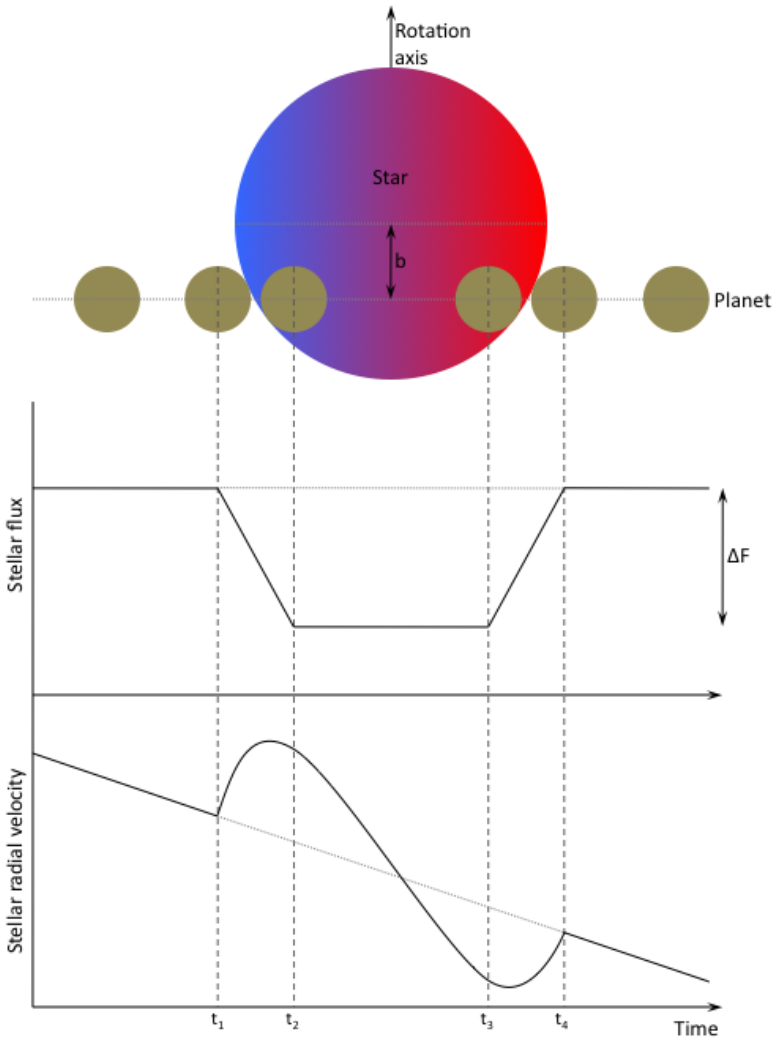

Figure 1.1: *An illustration of the detectable changes that are caused by the transit of a star by an extra-solar planet. The points t_1, t_2, t_3, and t_4 are known as the contact points, and mark the points at which the star enters/leaves the stellar disc, and the start/end of the period during which the planet is completely in front of the stellar disc. The impact parameter, b, is the shortest distance between the centre of the star and the transit chord. The change in stellar flux is defined as ΔF, and causes a detectable photometric signature.*
A spectroscopic signature is also produced, and is visible in the stellar radial velocity curve. This arises owing to the occultation by the planet of the blue-shifted and red-shifted stellar limbs, which affects the radial velocity measurement.

to the same point in its orbit, and thus the orbital period can be determined if multiple transits are detected. Knowledge of the period then enables the orbital separation of the planet from its host star to be determined using Kepler's third law.

The depth of a transit is defined as the difference between the average-in and -out of transit fluxes, divided by the average out-of-transit flux. This provides the ratio of the planetary

and stellar radii, and varies with impact parameter (and observational wavelength) owing to limb darkening. Accurately accounting for the effect of limb darkening on the transit lightcurve remains a significant problem; no single model has proven most successful at characterising limb-darkening, as the coefficients that are used depend on the wavelength being used (the effect becomes stronger as the wavelength decreases), and require data with a high signal-to-noise ratio (SNR) if they are to accurately replicate the observed variation in transit depth. Nevertheless, there are some models which are widely used throughout the literature (e.g. Claret, 2000, 2003, 2004a).

Until relatively recently transit searches were exclusively carried out from the ground by wide-angle survey telescopes such as SuperWASP (Pollacco et al., 2006) and HATnet (Bakos et al., 2002). However the vagaries of observing from the ground implicitly limit the SNR and precision that are achievable by such instruments. In 2006 the COROT (COnvection, ROtation and planetary Transits) satellite (Bordé et al., 2003) was launched, followed in 2009 by NASA's Kepler mission (Borucki et al., 2008), which was designed specifically to search for transiting terrestrial planets.

1.2.1 The WASP project

The Wide Angle Search for Planets (WASP) project is, to date, the most successful ground-based transiting planet survey. It has discovered more than 100 planets; the majority of these are similar in mass and radius to Jupiter, but the survey has also found several Saturn and Neptune size objects, as well as one or two brown dwarfs.

WASP uses two survey telescopes to carry out its initial scan for potential transit signatures: SuperWASP, on the Canary Islands, and WASP-S, in South Africa. Each consists of eight off-the-shelf camera lenses, and measures the flux from thousands of stars every night. These data are processed by an automatic search algorithm which identifies the most probable orbital and physical solution for the system based on the available data (Collier Cameron et al., 2006, 2007).

This initial phase is an important one, and provides the first validation step for potential transiting planets. Four parameters are directly measurable from transit lightcurves: the change in flux (ΔF); the total duration ($t_4 - t_1$); the width of the 'flat' section of the transit ($t_3 - t_2$), and the orbital period (P). From these it is possible to derive ratios of the planetary

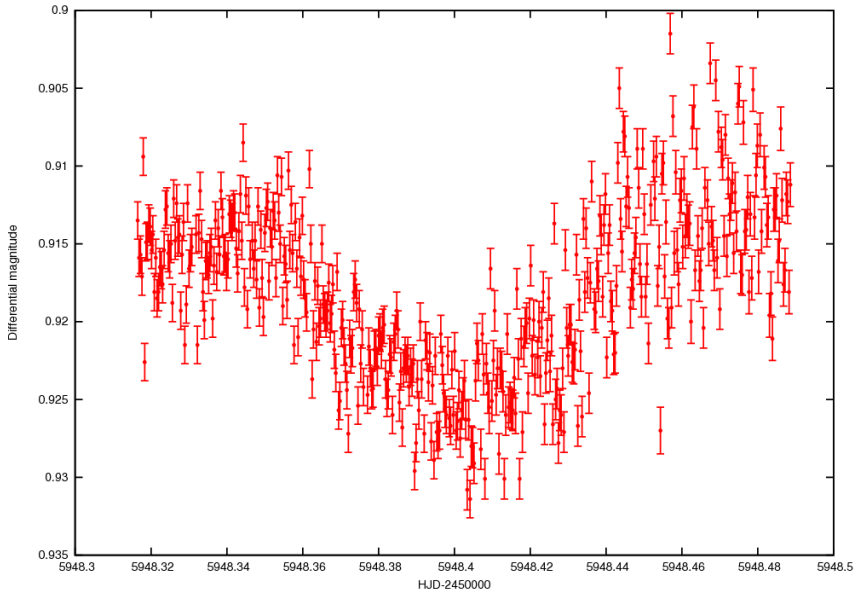

Figure 1.2: *Photometric transit observations for the exoplanet WASP-93, obtained by the author using the James Gregory Telescope at the University of St Andrews Observatory.*

and stellar radii (R_p/R_s), and of the stellar radius and orbital semi-major axis (R_s/a), as well as the impact parameter b. By using Kepler's 3rd law it is then possible to determine the stellar density (ρ_s) and, if the stellar mass is known, the stellar radius (R_s). For WASP candidates an estimate of the stellar mass is made using the (J-K) colour of the target as listed in the 2MASS database (Skrutskie et al., 2006). Planetary and orbital parameters then follow, and enable a decision to be made regarding the plausibility of the transit being planetary in origin.

1.2.2 Candidate confirmation

To confirm that the signals detected by transit searches are truly planetary in origin, follow-up observations are usually made. Precise photometric observations (see Figure 1.2) can be used to pin down the stellar and planetary radii, as well as the ephemeris of the orbit, whilst radial velocimetry is used in conjunction with this to obtain the mass of the planet. This follow-up work is an essential part of the discovery process, as there are a variety of false positive signals which can impersonate the effect of a planetary transit; eclipsing binary stars, background blends, and hierarchical triple systems are just some of the examples of such mimic sources (Collier Cameron et al., 2007). Some can often be easily ruled out through either the shape of the transits, the depth of the transits, or a combination of both, and there have been attempts to create diagnostics which can help to distinguish true planetary events from binary star transits (e.g. Tingley & Sackett, 2005).

Not all planet discoveries are able to be followed up. (Micro-lensing events, for example, are non-repeatable, but a great deal of care is taken to ensure that the detections are robust.) This is particularly a problem for Kepler as it pushes towards smaller and smaller planets. Kepler discoveries are too small, or require too much telescope time, for traditional follow-up to be viable. Thus the long list of Kepler 'candidates' as compared to their list of 'planets'; many of the former are very strong candidate planets, but cannot be confirmed at this time using the instruments that are available. The Kepler science team have managed to create some very interesting, innovative methods for discovery confirmation (for example the BLENDER routine, Torres et al. 2011), but for some of their candidates even these are unable to completely rule out all false-positive scenarios.

SuperWASP follow-up

During my PhD I have been heavily involved in the follow-up program of the WASP project, and have carried out both spectroscopic and photometric observations of extra-solar planet candidates.

The main contribution that I made to the follow-up program was through photometric candidate confirmation using the James Gregory Telescope at the University of St Andrews observatory. Figure 1.2 shows an example of photometric transit observations that I made as part of this program. Over the course of more than 70 nights I observed more than 45 candidate transiting systems; to date 5 have been confirmed as planetary in nature, while several others remain strong candidates but require spectroscopic follow-up observations to fully cement their planetary status.

I also made contributions to the radial-velocity program through observing runs at the Observatoire de Haute-Provence (OHP) and at ESO's La Silla site. My nine night run at the OHP made use of the SOPHIE spectrograph, and directly led to confirmation of at least one WASP planet. My two runs at La Silla were for ten nights and eight nights, using the HARPS instrument.

1.3 What can transits tell us?

As well as the basic information already discussed, a transiting planet can provide a wealth of detail about the stellar system that it is part of. The combination of photometric detection and

radial velocity follow-up is a powerful one that can reveal a whole host of useful information.

1.3.1 Physical properties

One of the most important properties of a transiting system is the limited range of possible system geometries that is imposed - since transits are visible the inclination of the system must be well constrained. It is this which allows us, in combination with the aforementioned follow-up observations, to place excellent limits on a planet's mass and radius. This in turn provides us with the information needed to determine planets' bulk compositions. A remarkable range of exoplanetary structures have been deduced, from gas giants similar to Jupiter or Saturn, to planets with greatly extended atmospheres, massive cores, or a significant proportion of their mass in the form of ices. The existence of 'ocean planets', which would have the majority of their bulk composed of water, has also been postulated (Léger et al., 2004), and some may have been discovered (Kaltenegger et al., 2013). Thanks to the contribution of the Kepler satellite, we have even found planets with masses down to a few times that of the Earth, including bodies which appear to be rocky in nature (e.g. Fressin et al., 2012; Barclay et al., 2013).

The planetary interior models used to determine these compositions are commonly derived from models of the Solar system planets, for which the composition is well known, with the details of each layer varying from planet to planet depending on their observed properties (Baraffe et al., 2010). The majority of the Jovian exoplanets appear to follow a similar structure: outer envelopes of hydrogen and helium, with some heavier metal enrichment, and a core of heavy elements such as carbon, nitrogen, and oxygen in their volatile, molecular forms. Some studies (e.g. Sudarsky et al., 2000) have also postulated the presence of silicate and iron cloud decks, and it is thought that phase transitions may exist within planetary interiors, particularly where hydrogen and helium are present (Chabrier, 2009), which can create challenges for theoretical models of planetary structure.

Eclipse events, both primary (transits) and secondary, can also provide information on the atmospheric composition and structure of the exoplanet involved. During a transit some of the light from the star passes through the atmosphere of the planet, and spectroscopic observations of this light can reveal some of the atmosphere's constituents. The height at which the atmosphere is opaque to tangential rays is wavelength dependent, which leads to similarly wavelength dependent changes in the ratio of the in- and out-of-transit spectra (Brown et al.,

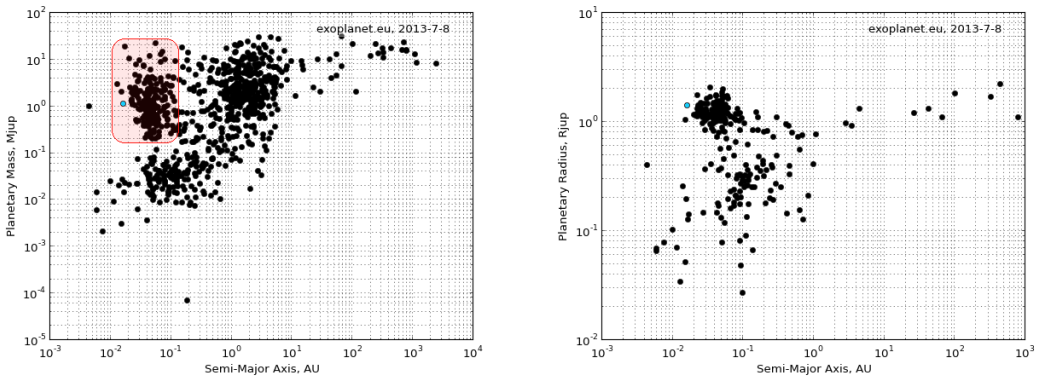

Figure 1.3: Left: *Planetary mass as a function of orbital semi-major axis.* ***Right:*** *Planetary radius as a function of orbital semi-major axis. In both plots the axes use logarithmic scales. Plots are taken from* `www.exoplanet.eu`
In both plots it is apparent that there are certain regions of parameter space which are more densely populated than others. Planets found inside the red region in the left-hand panel were generally discovered by wide, shallow, ground-based transit searches. The planet marked in blue is WASP-19, one of the systems which will be discussed in Chapter 4.
The advent of the Kepler space mission has pushed the limit of the distribution towards the lower left corner of both plots, whilst micro-lensing experiments probe the parameter space at the opposite corner of the figures.

2002). If the transit is observed to be deeper in a particularly bandpass, then that implies that the species which corresponds to that bandpass is present in the planet's atmosphere (Charbonneau et al., 2002). Observations at different wavelengths allow the presence, or otherwise, of different chemical species to be deduced. Once a set of measurements for a given planet has been built up they can be compared to model atmospheric spectra to gain further information about the planet. These measurements are very difficult to carry out, and can be subject to controversy (e.g. Swain et al., 2009; Gibson et al., 2011), but there is still great excitement about their potential (Barstow et al., 2013).

1.3.2 Orbital parameters

Geometrical and temporal arguments for the visibility of planetary transits imply a selection effect in favour of large planets at small orbital separations. As previously noted, the fact that transits are visible limits the range of orbital inclinations, with the limiting value being dependent on a/R_s. There is also a generally accepted minimum number of transit detections required before a signal is considered a candidate; the closer the planet is to the star, the more rapidly these repetitions can be seen. Finally, the larger the planet relative to its host star, the greater the change in flux/transit depth, and the lower the SNR for which the signal will be detectable.

It is therefore not surprising that a large number of such planets have been found by transit search programs. Many of them have masses and radii similar to Jupiter, but orbit their host stars with semi-major axes less than or equal to that of Mercury (see the area marked in red in Figure 1.3). Known as 'hot Jupiters', they have been discovered down to very small semi-major axes (e.g. Hellier et al., 2009; Hebb et al., 2010; Sasselov, 2003). A large fraction of the known hot Jupiters have been found by wide, shallow, ground-based transit searches, of which they constitute the main harvest. Whilst such surveys were dominant, it was hot Jupiters which were the most common form of known planet. But they are poorly represented in the Kepler sample, indicating that they are actually rather rare.

Current theories of planet formation are unable to produce hot Jupiters in situ, as the protoplanetary disc close-in to the star would be too hot for sufficiently massive cores to form, preventing the planet from accumulating sufficient gas (Melo et al., 2006). The commonly held view is therefore that hot Jupiters formed further out from the star before moving inwards under the influence of some migration mechanism. There are several competing hypotheses for what this mechanism might be, but conclusive evidence for one or more of them being dominant has yet to emerge.

In the near future it may be possible to distinguish between them using the spectroscopic transit signature (see Figure 1.1). This phenomenon provides information on the alignment of the planetary orbit to the rotation of the host star, and will be discussed further in Chapters 5 and 6. When the angle between the orbital and rotation axes is measured, it is used to classify the system as 'aligned' or 'misaligned' according to some pre-existing criterion (e.g. Winn et al., 2010a).

Observations by the Kepler satellite have revealed a fascinating variety in the architecture of planetary systems. Examples with almost every conceivable combination of single and multiple planets, both gaseous and terrestrial, and with a wide range of orbital distances, eccentricities, and periods have been found. The possibilities seem to be endless.

1.4 Star-planet interactions

Some hot Jupiters exhibit evidence of interactions with their host stars. There are three main forms of such an interaction: magnetic; radiational, and gravitational. These can affect the fundamental parameters of the star and/or planet, and can even change the course of the

system's evolution.

Examination of the minimum orbital separation for hot Jupiters reveals that the inner limit of the distribution is at approximately twice the Roche limit, the orbital separation at which a planet fills its Roche lobe and is tidally disrupted (Ford & Rasio, 2006). This agrees with models of the distribution expected if the formation process leaves hot Jupiters on highly eccentric orbits that are later circularised (Ford & Rasio, 2006; Rice et al., 2008). It has also been suggested that the limit results from tidal forces, or from extreme irradiation-induced mass loss that causes planets to 'evaporate' before they reach the Roche limit (Ford & Rasio, 2006). It is likely that the true explanation is some combination of all of these explanations, and of others that have yet to be determined.

1.4.1 Magnetic fields: chromospheric spots

Very close in hot Jupiters might interact with a star through their respective magnetic fields. The stellar coronal field and the planet's magnetosphere can interact to produce bright chromospheric spots on the surface of the star. In the Solar system this has been observed in the Jupiter-Io system, but the situation in hot Jupiter systems is analogous, and it has been suggested that such spots might explain modulation in the chromospheric activity of some extra-solar planets.

The chromospheric spots have been claimed to rotate in phase with the orbit of the planet, rather than the rotation of the star, suggesting that they are induced by the planet rather than resulting from a process within the star itself (Shkolnik et al., 2003, 2005). However, the spots show an offset in phase compared to the longitude of the planet, with the magnitude of the offset varying from system to system (Shkolnik et al., 2008). Moreover the modulation phenomenon is not consistently observed, and in some cases the level of stellar activity was found to be higher outside of the observed events than during them.

Several models have been proposed for chromospheric signature generation, including Alfven waves and magnetic reconnection. Currently the latter seem to be provide the best explanation, through energy dissipation in loops connecting the magnetic fields of the two bodies (Lanza, *priv. comm.*). The available data are limited and few in number though, and whilst it is clear that something is occurring, the root cause remains uncertain.

One alternative might be intermittent, excess absorption of the chromospheric activity

indicators. A small number of very-hot Jupiter hosts have been found to be under-active compared to other stars of similar spectral type, and it has been posited that a tail of material, produced through atmospheric blow-off, might be the cause. (Fossati et al., 2013)

1.4.2 Radiation: atmospheric blow-off

One of the most obvious ways in which stars and planets can interact is through the star's radiation. The stellar wind radiates outwards from the star, and can interact with the planet's magnetosphere. Examples of this interaction are abundant in our own Solar system (e.g. the Aurora Borealis), but the more extreme conditions that are found in many exoplanet systems produce correspondingly more impressive results.

The mass and radius of a hot Jupiter can be strongly affected by the properties of its host's stellar wind, with the X-ray emission derived wind in particular having a large impact through irradiation of the planet. The incident X-ray flux slowly strips the atmosphere away from the planet by exciting molecules such that their velocities are greater than the planet's escape velocity. In principle this is easily detectable, as the stripping of the atmosphere will produce an observably extended radius, which in turn results in a deeper transit. This can easily be misconstrued as simply a bigger planet, with a correspondingly lower density, but in the case of atmospheric stripping the depth of the transit will be wavelength dependent.

Such an effect has been observed for the exoplanet HD209458 (Vidal-Madjar et al., 2003), which has been confirmed to be undergoing atmospheric loss owing to stellar irradiation (Ehrenreich et al., 2008, and references therein). It has been suggested that the planet WASP-12 b might be undergoing similar irradiation-induced mass loss (Fossati et al., 2013), but alternative suggestions for the unusual transit profile have also been put forward (Vidotto et al., 2010).

Other examples of atmospheric blow-off can be found in the literature.

1.4.3 Gravitation: tides

Some hot Jupiters are close enough to their host stars to be undergoing tidal interactions, in a fashion analogous to the Earth-Moon system. There is a long history (Darwin, 1880) of research into tides within the Solar system, as well as in binary stars. This has been extended to hot Jupiter systems in recent years, with some interesting results. I will discuss this further

in Chapter 3, and my own work on this area is the subject of Chapter 4.

1.5 Conclusion

As I alluded to at the start of the Chapter, it is an interesting and exciting time to be working in the field of exoplanetary science. New discoveries are being made, new avenues of research opened up, and new ideas put forward and tested every day. So much is in flux as our knowledge of planets outside of the Solar system continues to evolve. We are gradually learning that dynamical processes can shape planetary systems in chaotic and unpredictable ways, leading to a bewildering variety of outcomes, some of which are catastrophic. By studying the evolutionary paths to the various planetary end products, we can also learn about the importance of catastrophic dynamical events such as the Late Heavy Bombardment in the history of our own Solar system, and in the assembly of the one habitable planet that we know of.

In this thesis I will investigate one of the most consequential of these processes: the tidal interactions between a planet and its host star. Using hot Jupiter systems, I will show that their influence on the geography and history of planetary systems is marked. Figure 1.3 offers clues that tides are gradually eroding the inner boundary of the planet distribution, but how severe is this erosion? When does it happen? How long does it take? To answer these questions, we must first study the host stars to establish ages for systems which offer an insight into tidal processes. Only once these have been determined can we ascertain the role of tides in the evolution of many of the physical and orbital parameters of extra-solar planetary systems.

Nota Bene

Throughout this thesis I have used the UTC time standard and Barycentric Julian Dates. My results and analyses make use of the equatorial Solar and Jovian radii and masses, taken from Allen's Astrophysical Quantities. When discussing inclinations relative to the line of sight, I use i to refer to the inclination of the planetary orbit, and I to refer to the inclination of the stellar rotation axis.

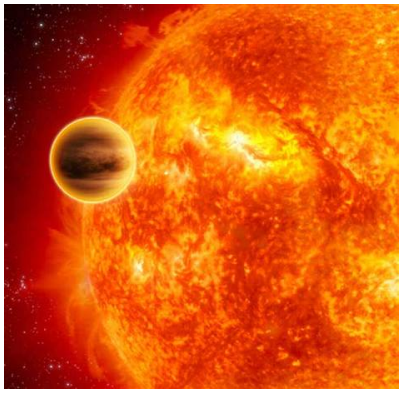

2

Age determination for exoplanet host stars

Facets of the stellar model fitting work presented in this Chapter have appeared in a range of WASP discovery publications. All work discussed is my own.

Stellar ages are generally poorly understood, and poorly characterised. The root of the problem is that stellar age determination is a notoriously difficult exercise, owing to our incomplete knowledge regarding the intricacies of stellar structure. Yet they are becoming increasingly important as a stepping stone to a better understanding of planetary systems. As the focus of the exoplanet community shifts from discovery to characterisation, the evolution of exoplanet systems has become a hot topic. In order to fully comprehend the timescales involved in such processes as planetary formation and destruction, orbital migration and circularisation, and intra-system dynamical interactions, it is vital that we are able to accurately assess the ages of exoplanet host stars.

A wide range of methods exist for the evaluation of stellar age. At first glance they seem to use a disparate array of phenomena: X-ray activity; Hα emission; Ca II H and K emission;

asteroseismology; lithium abundance; stellar rotation period, and Galactic space velocity are just some of the examples. Yet on closer inspection the physical situation underlying this assortment of techniques is both more simple and more complex than it might appear on the surface, and many of the plethora of metrics and parameters can be traced back to the same physical underpinnings: stellar rotation, and convective zone depth. Does this lead to broad agreement between the different methods, or do they produce a broad span of estimates? Are some of the methods more suitable, or reliable, in a given context than others? Is that even a valid question to ask?

In this Chapter I will address these questions for two age estimation methods, stellar model fitting and gyrochronology. I will apply these methods to a large sample of planetary systems, and look at the overall properties of the set of results that I obtain. My sample consists of 137 planetary and brown dwarf systems. The majority (97) of these are the host stars for the complete set of sub-stellar companions discovered by the WASP project as of 2013 March 1st, including many which have yet to be published but for which I was able to obtain data through my collaborators. The remainder are systems with measured spin-orbit alignment, as listed in the Holt-Rossiter-McLaughlin database of René Heller [1] as of 2013 January 10th.

2.1 The importance of spectral type

The temperature of a star determines its spectrum, from which both its broad-band colours and spectral type can be found, thus determining many of its physical properties. Mass, radius, and temperature, not to mention the very structure of the star, are governed by the spectral type. The last of these has particularly far-reaching consequences. Is the star fully convective, or does it have a radiative core? How large and massive is the surface convective zone compared to the global mass and radius of the star? These points plays a role in many observable quantities, including tidal strength (Zahn, 1977), the properties of the stellar magnetic field and wind, stellar activity (Noyes et al., 1984a), and the mixing processes that govern stellar abundances.

The effects of spectral type on the physical properties of a star can be characterised through the use of theoretical models of stellar evolution. In fact the global properties of a star are entirely determined by its mass, age, rotation, and chemical composition (Vogt,

[1] `www.aip.de/People/RHeller`

1926; Russell, 1927). Many different sets of models are available for determining these properties, but they are all predicated on the same basic idea. A choice of input physics is made, and a set of initial parameters chosen. These parameters are then evolved according to the chosen physical principles, and the evolution of the stellar parameters recorded at each time step. This is repeated for a large number of initial parameter sets to build up a grid results such that the parameters of a star of a particular spectral type at a particular age can be found.

Although different sets of stellar models may appear to be very different, Southworth (2009) noted that they are often based on the same, or similar, physical underpinnings as each other, differing only in their implementation of said physics.

2.1.1 Stellar model fitting

Stellar model fitting (also known as isochrone fitting) as a means of stellar age estimation is fairly ubiquitous. This method's widespread use probably originates from its adaptability, and from the relative simplicity of its implementation. At its core the method simply compares measured stellar parameters to theoretical models appropriate for the metallicity, $[M/H]$, of the star being examined. The underlying physics, however, can be complex, as these models require detailed knowledge (or assumptions) of stellar structure. For some other methods, such as asteroseismology, this is not the case.

When used for this purpose, the model data are usually presented as isochrones, lines of constant age with varying spectral type, rather than as lines of constant mass with varying age (mass tracks). $[Fe/H]$ is widely used, including for the work presented herein, as an easily available proxy for overall metallicity, assuming that all other elemental abundances follow Solar ratios; this is not strictly correct, and there is evidence (e.g Edvardsson et al., 1993) that the Solar $[Mg/Fe]$, $[O/Fe]$, and $[Al/Fe]$ differ from mean field star values. However the creation of stellar models requires that assumptions be made regarding Solar abundances, for which the commonly assumed values have changed over time, and are in fact still debated (Asplund et al., 2006; Lodders, 2010; Basu & Antia, 2013). I use a value of $Z_{\odot} = 0.0189$. There is also a well-established trend between iron abundance and overall metallicity in both field stars and exoplanet hosts (e.g Bodaghee et al., 2003; Gilli et al., 2006), although recent studies show that the latter are overabundant in metals (Neves et al., 2009; Adibekyan et al., 2012).

Traditionally, the effective temperature, $T_{\rm eff}$ was measured from high resolution spectra and, in conjunction with the absolute stellar magnitude $M_{\rm v}$, interpolated through the theoretical data to obtain estimates of the stellar radius, stellar mass, and stellar age for the star (e.g. Edvardsson et al., 1993; Lachaume et al., 1999). For cases in which the distance to the object is poorly known, some studies replaced $M_{\rm v}$ with the stellar surface gravity, $\log(g_s)$ (e.g. Konacki et al., 2005; Bouchy et al., 2005). This can often be difficult to determine precisely however, even with very high quality spectra, but transiting planets offer an alternative choice of parameter space. The geometry of a transit means that the stellar density can be constrained to high precision using high signal-to-noise transit photometry (Seager & Mallén-Ornelas, 2003). Modern attempts at isochronal analysis in exoplanetary studies therefore tend to use the parameter space of $[T_{\rm eff}, (\rho_s/\rho_\odot)^{-1/3}]$ (Sozzetti et al., 2007).

Limitations

As previously mentioned, one of advantages of the stellar model fitting procedure is its simplicity. Very little data is required, and it is easily extendable through variation in the choice of stellar models used. The method is also applicable to a broad range of spectral types, in principal. But in reality, there are regions of parameter space in which it is difficult to obtain useful results.

In particular, it can be hard to find the ages of stars with spectral type later than mid-late G. These stars have nuclear burning timescales that are longer than the age of the Galactic disc. Such stars evolve very slowly, and have effective temperatures such that they fall into regions of parameter space in which theoretical isochrones are closely spaced (see Figure 2.1). This makes determining accurate and precise ages very difficult, even if the physical parameters of the star are well constrained, as even small error bars in $T_{\rm eff}$ and $\rho^{-1/3}$ can cover a wide range of ages. As far as exoplanet hosts are concerned, Triaud (2011) suggested that stars with $M_s < 1.2\,M_\odot$ were particularly problematic. The complex shapes of isochrones, particularly near the main-sequence (MS) turn-off, can also present issues, and interpolating through them is not always a valid approach owing to their non-uniform spacing (Soderblom, 2010). In addition, the less pronounced radius increase (and therefore density decrease) during the MS lifetime, $\tau_{\rm MS}$, of low mass stars compared to their more massive relations has an impact on age estimates.

One also has to be aware of the limits on the area of parameter space that the chosen

stellar models cover, and of the format of those models. The minimum and maximum stellar mass are rarely problematic given the propensity for the host stars of transiting exoplanets to be of F or G spectral type and therefore broadly similar to the Sun (Bentley e.g. 2010, for WASP targets; Batalha et al. e.g. 2010, for Kepler targets). However the lower and upper limits on the stellar *age* are much more likely to come into play, and in some sets of stellar models the maximum isochrone age is greater than the currently accepted age of the Universe! In addition, most stellar model formulations struggle with very young systems, as close to the zero-age MS the isochrones compact, leading to similar problems as experienced with K- and M-dwarfs.

The choice of stellar model being used can have a large impact on the derived properties of planetary systems, particularly through the introduction of systematic errors (Southworth, 2009). This suggests that multiple sets of stellar models should be used if at all possible, in preference to relying on a single formulation.

2.2 Stellar rotation as a fundamental parameter

Stellar rotation plays a central role in governing many of emergent properties of the stars that we observe. Several of the metrics that are used for determining stellar age can be traced back to stellar rotation, and in some sense are merely acting as its proxies.

Research linking stellar rotation to activity, for example, has a long history. Vaughan et al. (1981) noted that many 'cool' stars appeared to exhibit quasi-periodic variation in their chromospheric activity level, as measured using emission in the Ca II H and K spectral lines. This was followed up by Noyes et al. (1984a,b), who found that the period of the activity cycle could be linked to the rotation period through the convective turnover time. They also found that, for slowly rotating stars, there was an additional dependence on stellar structure as parametrized by spectral type. These results are not surprising, as stellar activity is known to be correlated with the surface magnetic field, which is influenced by rotation (via convection within the star as a result of the stellar dynamo) and spectral type. The Noyes et al. equation,

$$P_{\rm cyc} \propto P_{\rm rot}^{(1.25\pm0.5)} \tag{2.1}$$

linking the cycle period of chromospheric activity, $P_{\rm cyc}$, and rotation period, $P_{\rm rot}$, is merely the fundamental expression of these interdependencies.

In light of this relationship, stellar activity is often used as a proxy for stellar age (e.g. Soderblom et al., 1991; Donahue, 1993; Mamajek & Hillenbrand, 2008), although many formulations provide implausible ages for both very active and very inactive stars (Mamajek & Hillenbrand, 2008). In this way it is possible to indirectly use stellar rotation as a proxy for age. But it is also possible to use the rotation of a star to directly infer its age.

Although it had been suggested by several authors that stellar rotation could change over time (Parker, 1958; Schatzman, 1962; Kraft, 1967), the link between rotation and age was first characterised by Skumanich (1972) in the well-known Skumanich law,

$$P_{\rm rot} \propto t^{\zeta}, \tag{2.2}$$

which relates stellar rotation period to time. Since that landmark paper a substantial body of work has built up that looks at the relationship between stellar rotation and age (see Barnes & Kim (2010) for an excellent summary of the history of stellar rotation studies), and the Skumanich law continues to provide a solid foundation for such work.

2.2.1 The Skumanich exponent, ζ

Skumanich (1972) suggested a value for the Skumanich exponent of $\zeta = 0.5$, but more recent work has shown that no single value of the exponent is able to correctly reproduce the observed rotational period distributions for all stellar populations. For example, the period distributions of stars in open clusters are not adequately described using $\zeta = 0.5$, and a discontinuity in the relationship between $P_{\rm rot}$ and spectral type has been observed in the Hyades, Praesepe, and M37 clusters. In the Hyades this break appears at spectral types K8-M2 (Scholz & Eislöffel, 2007), in Praesepe it seems to occur at around M1 spectral type (Covey et al., 2011), or $0.3 - 0.65\,M_{\odot}$ (Delorme et al., 2011a; Scholz et al., 2011), and in M37 it is found at around $0.8\,M_{\odot}$ (Hartman et al., 2009). It seems likely that these breaks arise as a result of the aforementioned difference in structure between very low mass stars and earlier spectral types, although the loss of the radiative core happens at lower stellar mass than the break in rotational period.

It is possible to determine a value for ζ using stellar cluster data. By plotting stellar (B-V) colour as a function of rotation period, $P_{\rm rot}$, and fitting a curve to the data, the period-colour relation for a given cluster can be determined (Stepien, 1988). This has been done for both the

Hyades (Radick et al., 1987) and Pleiades (Hartman et al., 2010) clusters, and in combination with their respective ages this allows a value of ζ to be calculated. This period-colour-age relation can then be calibrated using data from other stellar clusters. The Coma-Berenices cluster, for example, has also been studied (Collier Cameron et al., 2009), and an almost linear relationship, similar to that for F, G, and K stars in the Hyades, found between (J-K) colour and $P_{\rm rot}$. Using the Hyades to calibrate their observations, Collier Cameron et al. found only a small deviation from the standard Skumanich exponent, obtaining $\zeta = 0.56$. This value has since been used by Delorme et al. (2011b) to analyse Praesepe in a similar manner. These, and similar studies for other clusters such as NGC2301 (Sukhbold & Howell, 2009), M34 (James et al., 2010), NGC6811 (Meibom et al., 2011), and M35 (Meibom et al., 2009), show that although stars of any given spectral type can be born with disparate rotation rates, the $P_{\rm rot}$ distribution becomes narrower over time. This occurs owing to the fact that magnetic braking affects rapidly rotating stars more strongly than slower rotators, so that the rate of spin down increases with increasing initial rotation rate.

There is also evidence that the Skumanich exponent is not constant across the full colour range. A value of $\zeta = 0.35$ has been suggested for stars with $0.5 \lesssim (J-K) \lesssim 0.8$ in Praesepe (Agüeros et al., 2011), whilst a different study found that an exponential braking law,

$$P_{\rm rot} \propto e^{t/\tau}, \tag{2.3}$$

with a mass-dependent τ reproduces the data for very low mass stars (Scholz et al., 2011).

Whatever the exponent, or indeed the precise equation, the principle behind the Skumanich law remains the same. The rotation of a star slows down as it ages. This fundamental stellar property arises owing to the action of magnetic braking on isolated stars (Weber & Davis, 1967)

2.2.2 Magnetic braking

Magnetic braking is most potent for stars with very strong magnetic fields, but it can be seen to be acting on any star with a convective zone. This segment of the stellar structure is essential for the generation, via the dynamo effect, of a star's surface magnetic field (Reiners et al., 2009), which couples to the rotation of the star. This generates a magnetic flux that in turn couples to the stellar wind.

Assuming a Weber-Davis model (Weber & Davis, 1967) for the stellar wind, then near the stellar surface the magnetic field lines are radial. The stellar wind must follow these field lines, and so the magnetic field exerts a torque on the wind. As the wind moves outward the magnetic field (and therefore the applied torque) weakens, and the particles that make up the stellar wind are free to travel along straight lines (when viewed in the initial frame of reference). The wind particles effectively drag the stellar magnetic field lines with them, forcing them into a spiral shape when viewed from above the rotation pole of the star. In the co-rotating frame of reference it is motion of the stellar wind that is radial close to the star; due to the reduced torque this particle outflow then curves backwards as the distance from the stellar surface increases, conserving angular momentum and slowing the rotation of the star (Reiners et al., 2009). Over the star's main-sequence lifetime this causes the rotation period to gradually increase, such that a precise measurement of the period can, given knowledge of ζ, lead to an estimate of the stellar age through equation (2.2).

The strength of the magnetic braking torque is strongly dependent on the strength of the stellar magnetic field, which is determined by the interior structure of the star (Scholz & Eislöffel, 2007). The size of the convective zone compared to the radiative core fundamentally affects the dynamo action that generates the magnetic field; whilst fully convective stars are capable of generating strong magnetic fields, the form of those fields is fundamentally different to that found in stars with both convective and radiative components (Scholz & Eislöffel, 2007). It is also possible for the stellar dynamo to saturate at high rotation rates, restricting the strength of the stellar magnetic field and therefore stetting an upper limit on the rate of magnetic braking (Collier Cameron & Jianke, 1994). It is thought that for Sun like stars, this saturation occurs at approximately ten times the solar rotation rate (Soderblom, 1998).

2.2.3 Gyrochronology

The strong link between stellar rotation and time that is encapsulated in equation (2.2) allows rotation period to be used as a proxy for stellar age. Gyrochronology, a method for determining a cool star's age through measurement of its rotation period and colour, was suggested by Barnes (2003) and developed in Barnes (2007). It arose from observations showing that by the age of the Hyades, the rotation of stars in stellar clusters tends to converge onto a single period-colour-age relation. As a model independent method it can provide a useful alternative to isochronal fitting, or to other age estimation procedures that require measurement of the

distance to the star in question.

Calibrating with transiting planets

As well as being useful for stellar model fitting, planetary systems are also useful calibrators for gyrochronology. The radial velocity follow-up which is carried out as part of the confirmation process for most transiting planets (see Chapter 1, section 1.2.2) provides measurement of the projected rotation velocity, $v \sin I$, of the star. This is often constrained to high precision, particularly for more rapidly rotating stars where the ambiguity of rotation as compared to macroturbulence effects is reduced, and can therefore be used to provide reasonably well-constrained rotation periods.

It is also sometimes possible to determine the rotation period from high-precision photometric follow-up. For active stars, the presence of star spots in the transit chord leads to visible anomalies in the transit lightcurve. If the same starspot is present during consecutive transits, then its movement through the transit can provide measurement of the rotation period of the star (Silva-Valio, 2008; Dittmann et al., 2009; Sanchis-Ojeda et al., 2011). If the host star is particularly active then rotational modulation can be seen in the out-of-transit lightcurve (Alonso et al., 2008), and can be modelled to provide a measure of the rotation period. If sufficiently precise photometry is available, for example from the Kepler satellite, then this is nearly always possible unless the active-region lifetime is much shorter than the stelar rotation period (or the stars are particularly inactive).

These direct measurements are obviously preferable to an indirect calculation based on $v \sin I$ and R_s.

Strengths and weaknesses

Barnes (2007) showed that this method provides age estimates that are more self-consistent than those from either stellar model fitting or activity-age relations, and it has been demonstrated that, if rotation periods have been measured and the equations correctly calibrated, gyrochronology can provide ages with an accuracy of 10 percent for F, G, K, and M spectral types (Collier Cameron et al., 2009; Mamajek & Hillenbrand, 2008; Delorme et al., 2011a). These are significant caveats though, and in my sample there are few systems with measured

rotation period. For the other systems, the rotation period is inferred using

$$P_{\rm rot} = \frac{2\pi R_s}{v \sin I} \sin i. \tag{2.4}$$

This is not an ideal situation; measurement errors on R_s and $v \sin I$ can very quickly propagate into large errors in the rotation period, whilst $v \sin I$ can be difficult to measure for slowly rotating stars. Furthermore, the sine function itself causes problems when determining the inclination i, with $\sin i = 0.99 \pm 0.01$ allowing $79° < i < 90°$ (Soderblom, 1985). Finally, Vican (2012) found that, for a sample of stars observed by the DEBRIS survey, gyrochronology ages calculated using directly measured $P_{\rm rot}$ and inferred $P_{\rm rot}$ differed by an average factor of 1.6 (see their figure 2). However, Soderblom (2010) claim that the use of $v \sin I$ is reasonable if stellar rotation is the dominant contribution to line broadening.

The use of derived rotation periods is thus far from perfect, but is necessary if a suitable sample size is to be reached. Using directly measured rotation periods is not a perfect solution either though, as differential rotation on the stellar surface can produce discrepancies between the measured value and the true equatorial rotation period (Soderblom, 2010).

One major problem with gyrochronology is that it is only applicable if the natural rotational evolution of the star is allowed to progress without any outside influence. There are several factors which can prevent this from happening. The most relevant in the context of this thesis are the torques that act on both the star and its close-in exoplanets as a result of tidal interactions (see Chapter 4). If the mass ratio and orbital semi-major axis are sufficiently small, then these torques may be strong enough to overwhelm the natural spin-down, at least for short periods of time, and either cause it to accelerate or slow down. If this, or some other outside influence is present and not acknowledged, then the calibration of the gyrochronology equations can be incorrect.

Another detail to consider is the presence of the magnetic braking boundary at mid-to-late F spectral type. A previously observed discontinuity in the relationship between mass and rotation rate was confirmed by Kraft (1967). Stars later than this break appear to have less angular momentum for their mass than stars earlier than the break. Several hypotheses for the presence of this jump in rotation rate were put forward, including the observation that it coincided roughly with the appearance of the surface convective envelope, which had been suggested by Schatzman (1962) to be necessary for the magnetic braking phenomenon

previously discussed. The exact position of the break was solidified when (Wolff et al., 1986) showed that stars with earlier spectral type than F8 show little-to-no relation between $P_{\rm rot}$ and stellar age. This is significantly earlier than the breaks in rotation period at M spectral types seen in young stellar clusters (and mentioned previously).

The applicability of gyrochronology to stars above this break is therefore non-existent, a fact which is sidestepped in Barnes (2007) by limiting the method to "solar-type (FGKM) stars". In fact stars earlier than F8 are usually disregarded when modelling the spin-down rate of low mass stars (Stepien, 1988), and any study using gyrochronology should be wary of utilising it more broadly than this. It is worth noting though that the early spectral types at which gyrochronology breaks down are those for which stellar model fitting can provide strong age constraints, such that the two methods are nicely complementary.

2.3 Implementation

Given some of the problems discussed in sections 2.1.1 and 2.2.3, I made the decision to limit the parameter space in which I was working. I restricted myself to working only with those systems which fell between spectral types F7 and G9 (inclusive). This was carried out using the effective temperatures given in table B1 of Gray (2008), leading to limits of $6226\,\mathrm{K} \leq T_{\rm eff} \leq 5273\,\mathrm{K}$. This accounted for both the magnetic braking boundary problem and the K-dwarf $\tau_{\rm MS}$ issue, whilst retaining the sweet spot for ground-based transit surveys. Applying these limits reduced my sample from its original size of 137 systems to only 73 systems.

2.3.1 Stellar model ages

There are generally two ways in which stellar models are presented: either evolutionary tracks with fixed mass and varying time, or isochrones of a fixed age with varying mass, although the latter are derived from the former. Evolutionary tracks are calculated covering a range of stellar masses, using variable time steps. The isochrones are then interpolated through the evolutionary tracks. Since the primary characteristic that I am trying to determine is stellar age, I choose to work with isochrones where they are available.

Based on the homogeneous analysis of Southworth (2009, 2010), who considers several different stellar model formulations and compares their effectiveness, accuracy, and precision,

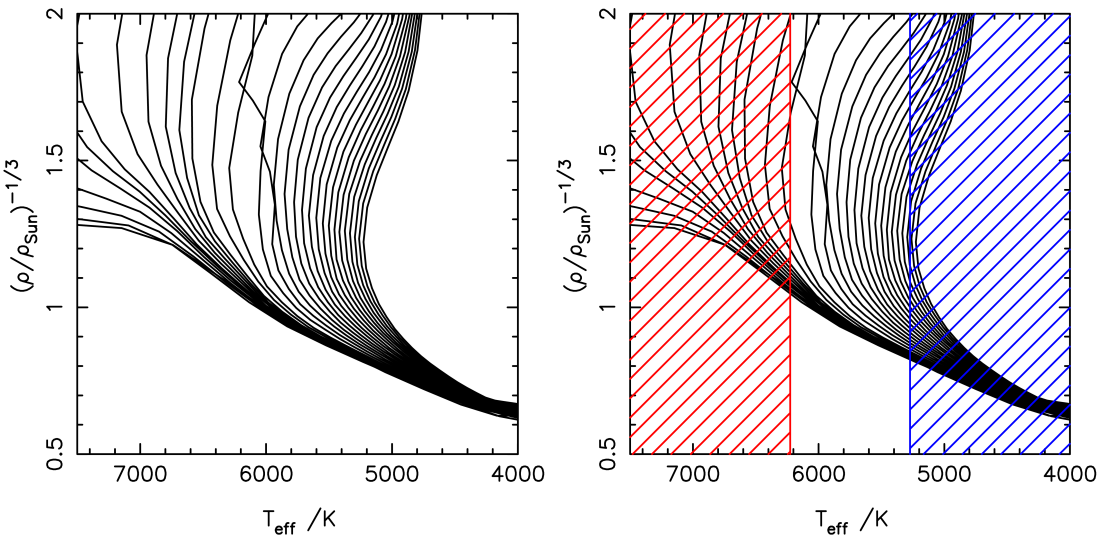

Figure 2.1: *An illustration of the effect of my limited $T_{\rm eff}$ parameter space on the Yonsei-Yale stellar models.* ***Left:*** *The full set of stellar models, for ages from 0.1 Gyr to 20 Gyr.* ***Right:*** *The parameter space available after accounting for some of the factors discussed in sections 2.1.1 and 2.2.3. The region marked in red (bounded at $T_{\rm eff} = 6226\,K$) shows the region disallowed by consideration of the magnetic braking boundary, whilst the area in blue (bounded at $T_{\rm eff} = 5273\,K$) indicates those systems with predicted main-sequence lifetimes longer than the age of the Galactic disc.*

I have chosen to use five sets of stellar models in my analysis. These are the Padova isochrones (Girardi et al., 2010; Marigo et al., 2008), the Yonsei-Yale (YY) isochrones (Demarque et al., 2004), the Teramo isochrones and evolutionary tracks (Pietrinferni et al., 2004), the Victoria-Regina (VRSS) isochrones and evolutionary tracks (VandenBerg et al., 2006), and isochrones from the Dartmouth Stellar Evolution database (DSEP; Dotter et al. 2008). Figure 2.2 illustrates the subtle differences between the appearance of the different models.

The main difficulty of stellar model fitting is that it is an attempt to fit a single point to a three-dimensional ($[Fe/H]$, $T_{\rm eff}$, $(\rho_s/\rho_\odot)^{-1/3}$) parameter space in order to derive associated parameters (age and stellar mass, $M_s/M_\odot$). The problem can trivially be reduced to a two-dimensional one by considering only a single metallicity value at a time, which I achieve by neglecting the uncertainty in $[Fe/H]$, but this does little to reduce the difficulty of the task.

There are many possible fitting procedures. The simplest is to merely take the closest isochrone as the age of the system, but this often provides only crude estimates and has an accuracy that is constrained by the ages for which isochrones have been provided. A more involved approach would be to find the two closest isochrones and interpolate between them. Other approaches include the Bayesian approach of Pont & Eyer (2004).

I have chosen to describe the $[T_{\rm eff}, (\rho_s/\rho_\odot)^{-1/3}]$ surface to which the stellar data is being

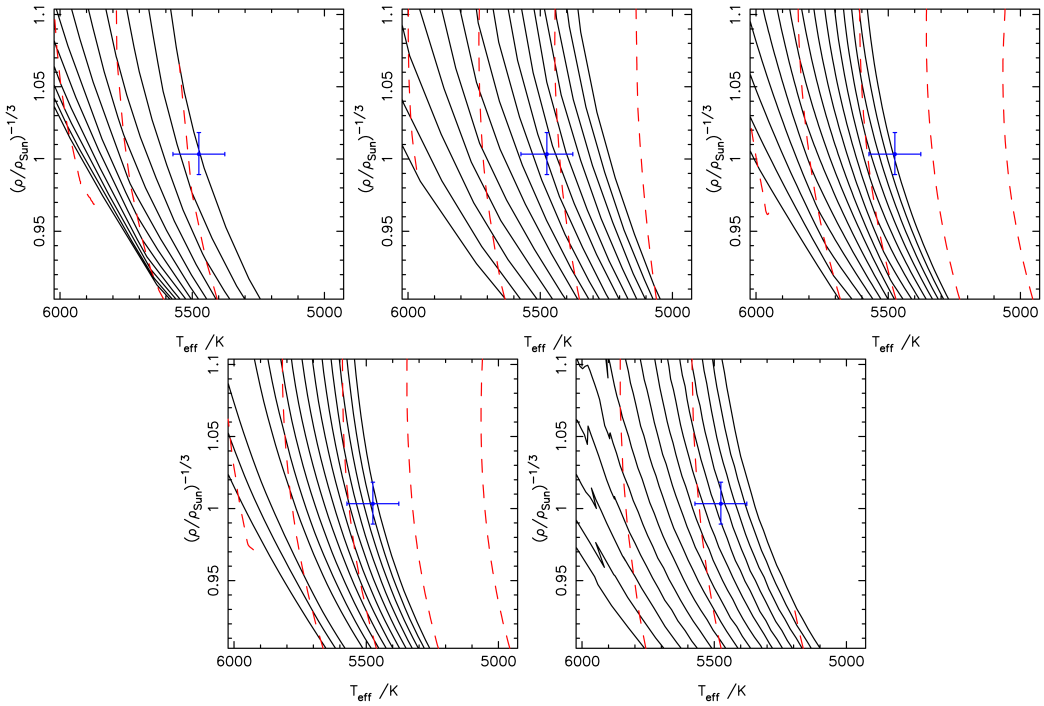

Figure 2.2: *Isochronal fits to four different sets of stellar models for the hot Jupiter host star WASP-19. The solid black lines are isochrones of constant age, whilst the dashed red lines are evolutionary tracks of constant mass. Stellar data and associated errors are shown in blue.* ***Top left:*** *Padova stellar models of (left to right)* 1.0, 1.3, 1.6, 2.0, 2.5, 3.2, 4.0, 5.0, 6.3, 7.9, 10.0, *and* 12.6 *Gyr, with interpolated evolutionary tracks of (right to left)* 0.9, 1.0, *and* $1.1\,M_{\odot}$ ***Top right:*** *Yonsei-Yale stellar models of* $1-15$ *Gyr in* 1 *Gyr increments, with interpolated evolutionary tracks of* 0.8, 0.9, 1.0, *and* $1.1\,M_{\odot}$. ***Middle left:*** *Teramo stellar models o f*$1-15$ *Gyr in* 1 *Gyr increments (omitting* 4 *Gyr) and evolutionary tracks of* $0.7-1.1\,M_{\odot}$ *in* $0.1\,M_{\odot}$ *increments.* ***Middle right:*** *VRSS stellar models of* $1-15$ *Gyr, in* 1 *Gyr increments, and evolutionary tracks of* $0.7-1.1\,M_{\odot}$ *in* $0.1\,M_{\odot}$ *increments.* ***Bottom:*** *DSEP stellar models of* $1-15$ *Gyr, in* 1 *Gyr increments, and evolutionary tracks of* 0.8, 0.9, *and* $1.0\,M_{\odot}$.
These figures illustrate the differences between the five stellar model formulations, particularly the differing age ranges that they cover, and their varied appearances in the $T_{\rm eff}-\rho^{-1/3}$ *parameter space used to carry out the fits.*

fit, and then to use this description to define a small plane over which I can interpolate the stellar data. For this purpose I use a Delaunay triangulation, computed for a sub-region of the full stellar model parameter space that is centred on the measured stellar parameters. Computing the triangulation for the complete set of isochrones or evolutionary tracks is time-intensive, and restricting the routine to this sub-region decreases runtime significantly.

Delaunay triangulation

Delaunay triangulation is a particular method for creating a triangular mesh for a set of data points. It is built upon work by Delaunay (1934), but has since been heavily developed (e.g. Pál & Bakos, 2006; Lin & Manocha, 1996). I have used the implementation of J. Bernal (see Bernal 1988, 1991, for example).

There are several specific properties of a Delaunay triangulation that distinguish it from other triangulation methods (see Figure 2.3). First, it maximises the minimum angle within the triangulation, avoiding distorted, 'skinny' triangles. Second, no data other than the vertices of a given triangle may lie within its circumcircle. Third, for any pair of triangles, the sum of the angles opposite their common side must be less than 180°. This last property is particularly useful, as it allows the use of a technique known as "edge swapping". If a pair of triangles does not meet the third criterion, then swapping the common side such that it bisects those angles creates a Delaunay pair (Figure 2.4). In my implementation, which incrementally expands the triangulation by adding a single triangle at a time, this process is used to optimise the initially computed triangulation.

Calculating age

Once the triangulation is complete the task of interpolating for the measured stellar data is simplified. I use one of the triangulation routines to identify the component of the triangulation that encloses the measured parameters that I am trying to fit to the model data. I then linearly interpolate through the selected triangle, using a method described in (Press et al., 2007), to identify the age that would be associated with a model data at the same location as the measured parameters.

The 'centroid' of a triangle lies at the intersection of the lines joining the triangles vertices to the midpoints of their opposing sides (see Figure 2.5) By definition it is the point where the areas $\mathscr{A}(\mathbf{abM})$, $\mathscr{A}(\mathbf{bcM})$, and $\mathscr{A}(\mathbf{caM})$ are equal, and it's coordinates are given by

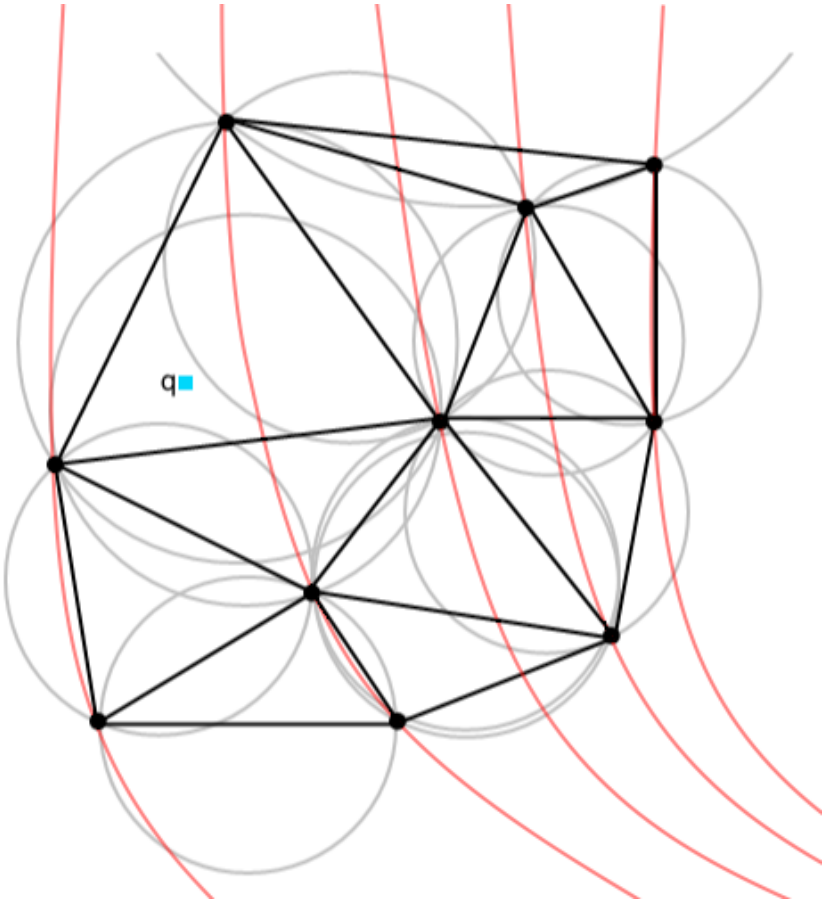

Figure 2.3: *A schematic example of Delaunay triangulation as applied to stellar isochrones. The black circles represent the model data that make up the isochrones (red lines), whilst the blue square, point* **q**, *represents the measured stellar data. The triangulation is computed such that the minimum angle across all of the triangles produced is as large as possible. The grey arcs show the circumcircles of the triangles; each circumcircle contains only the data that form the vertices of the corresponding triangle.*
Once this triangulation is complete, the triangle containing point **q** *is identified. The vertices of this triangle are then used to interpolate the measured stellar data (see Figure 2.5).*

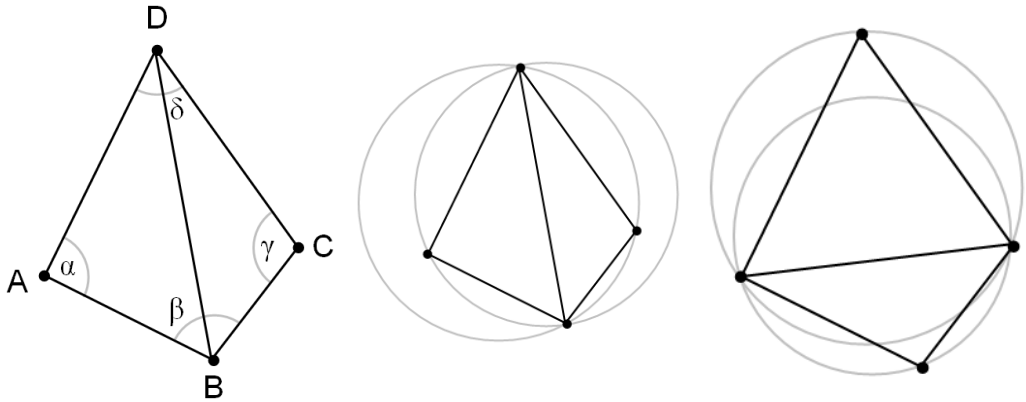

Figure 2.4: *An example of the edge swapping procedure used to check for Delaunay compliance, and to optimise the final triangulation.* ***Left:*** *The sum of angles α and γ is greater than* 180°*. This pair of triangles is therefore not a Delaunay pair.* ***Middle:*** *The circumcircles of the two triangles intersect with the fourth vertex in the pair, also rendering the triangulation non-Delaunay.* ***Right:*** *Swapping the line D-B to the line A-C makes this pair of triangles Delaunay compliant. The opposing angles now add up to less than* 180°*, and the two circumcircles contain only the vertices of their respective triangles.*
As each datum is added to the triangulation, the new triangles that are created are checked for Delaunay compliance, and modified if necessary using this procedure. Once the triangulation is complete, edge swapping is used to optimise the solution.

$$M_{i=0,1} = \frac{1}{3}(a_i + b_i + c_i). \tag{2.5}$$

By extension, any point in the plane defined by the triangles vertices can be defined as a linear combination of the three vertices, with coefficients that sum to unity:

$$\mathbf{q} = \alpha\mathbf{a} + \beta\mathbf{b} + \gamma\mathbf{c} \tag{2.6}$$

For any given point, the coefficients (weights) can be determined using the areas of the plane and of the three component triangles:

$$\alpha = \mathscr{A}(\mathbf{bcq})/\mathscr{A}(\mathbf{abc}) \tag{2.7}$$

$$\beta = \mathscr{A}(\mathbf{caq})/\mathscr{A}(\mathbf{abc}) \tag{2.8}$$

$$\gamma = \mathscr{A}(\mathbf{abq})/\mathscr{A}(\mathbf{abc}) \tag{2.9}$$

Since the $[T_{\rm eff}, (\rho_s/\rho_\odot)^{-1/3}]$ coordinates for the vertices of the triangle enclosing the measured parameters are known, it is trivial to calculate these weights. The ages known to correspond to the same vertices can then be used alongside the weights to calculate the age corresponding to the measured parameters using equation (2.6). This method provides a unique

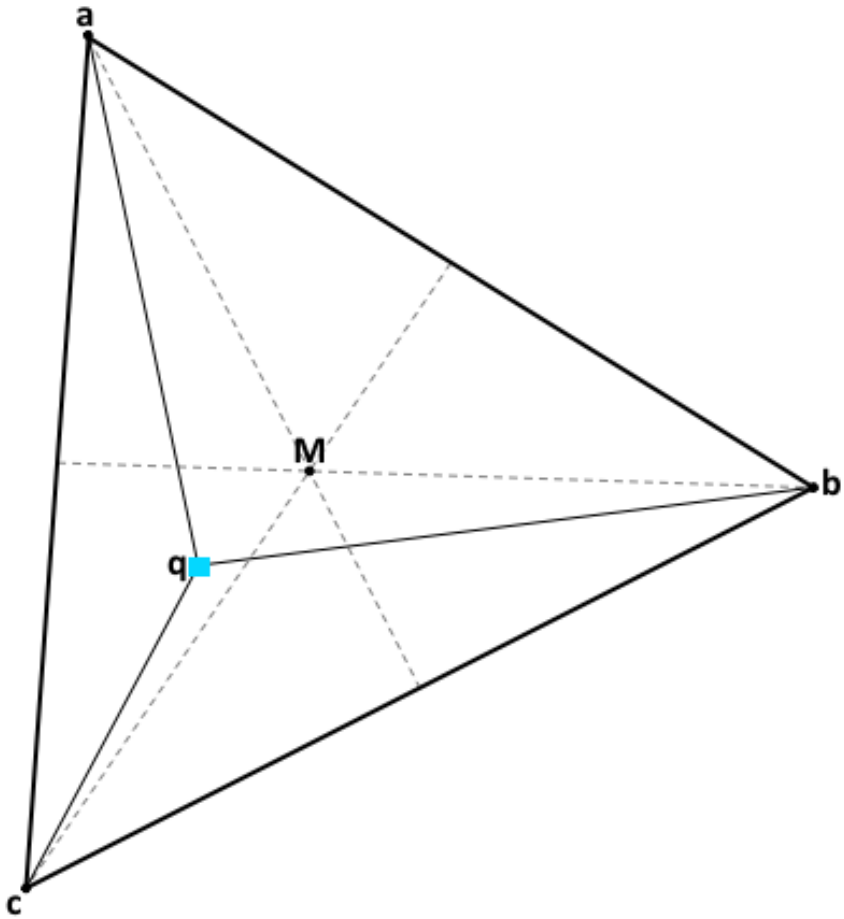

Figure 2.5: *An illustration of the coordinates used for my age interpolation routine.* **a**, **b**, *and* **c**, *the black circles, are the vertices of the triangle that has been selected from Figure 2.3 as containing the measured stellar parameters, which are found at point* **q**, *the blue square.* **M** *is the 'centroid' of the selected triangle. Each vertex is given a weight according to the ratio of the areas of the component triangles (***abq**, **bcq**, *and* **caq***) to the area of the enclosing triangle (***abc***). These weights are then used to interpolate the age at* **q** *according to equation (2.6).*

solution, as the three vertices of the triangle define a unique plane in three dimensions (Press et al., 2007).

The specific property of the Delaunay triangulation to maximise the minimum angle of all triangles is particularly important in this context, as the stellar model data are not distributed uniformly in $[T_{\rm eff}, (\rho_s/\rho_\odot)^{-1/3}]$ parameter space. Making the triangles as equi-angular as possible helps with the interpolation process, as it decreases the chance that two vertices will share an age.

Uncertainties in the calculated age are determined by following the same interpolation procedure using data corresponding to eight points around the error ellipse. These are the extremes of the error bars on $T_{\rm eff}$ and $(\rho_s/\rho_\odot)^{-1/3}$, and the points at 45° between the error

bars. The shape of the isochrones and evolutionary tracks is such that simply using the error bars can underestimate the uncertainty in the age; using the intermediate points helps to alleviate this. Using additional points around the error ellipse would obviously increase the accuracy of the uncertainties, but would also decrease the efficiency of the fitting routine.

After determining the age of the system, an estimate for the stellar mass and its associated uncertainties is produced in the same fashion. If separate evolutionary tracks are available then the triangulation and search procedure is repeated using these, otherwise data from the isochrones is interpolated. Note that this is carried out in a 2-dimensional plane in $[T_{\rm eff}, (\rho_s/\rho_\odot)^{-1/3}]$ parameter space *for a specified [Fe/H]*; the uncertainty in the metallicity is not accounted for in this analysis.

2.3.2 Gyrochronology calculations

I have used three different formulations of the $P_{\rm rot}$-colour-age relation to calculate ages for the systems listed in Table A.1. The first is from Barnes (2007), but uses updated coefficients from Meibom et al. (2009) and James et al. (2010) that were derived from studies of the M35 and M34 clusters respectively.

$$\log(t/Gyr) = \frac{1}{0.5344}\left[\log(P) - \log(0.770) - 0.553\log(B-V-0.472)\right] \tag{2.10}$$

The second formulation was derived from the period-colour relation for the Coma-Berenices cluster by Collier Cameron et al. (2009):

$$t = 591\left[\frac{P}{9.30 + 10.39(J-K-0.504)}\right]^{\frac{1}{0.56}} \text{Myr} \tag{2.11}$$

The third and final formulation is similar to equation 2.11, but was derived by Delorme et al. (2011b) using a study of the Hyades cluster:

$$t = 625\left[\frac{P}{10.603 + 12.314(J-K-0.570)}\right]^{\frac{1}{0.56}} \text{Myr} \tag{2.12}$$

To calculate the ages I used data from the papers listed as references in Table A.2. Broadband colour indices for the WASP systems were derived using data from NOMAD (Zacharias et al., 2004) and 2MASS (Skrutskie et al., 2006) for the (B-V) and (J-K) colours respectively,

whilst those for the other systems were taken from the SIMBAD online data repository[2].

For systems with available stellar rotation period measurements, I created a Gaussian distribution with mean and variance set to the listed value and 1σ error respectively. The distribution was sampled 10,000 times, and for each sample I calculated age estimates using equations (2.10), (2.11), and (2.12). The age estimates in Table A.2 were then calculated by sorting the results, calculating the median, and finding the values which encompassed the central 68.3 percent of the dataset.

For the majority of the planetary systems in my sample there exists no direct measurement of the stellar rotation period. For these cases I sampled Gaussian distributions for the projected stellar rotation, $v \sin I$, the orbital inclination, i, and the stellar radius, R_s, 10,000 times in the same manner as described previously. For each set of sampled data I calculated the rotation period using equation (2.4), assuming that the systems are aligned along the line of sight such that $i = I$, and then used the gyrochronology equations to calculate age estimates. The values for $P_{\rm rot}$ and age listed in Table A.2 are all the medians of their respective sampled datasets, with 1σ error bars as before.

2.4 Results and discussion

I calculated stellar ages for all of the systems in my sample using all five of the stellar model sets, and all three gyrochronology formulations. The results that I obtained can be found in Appendix A.

In the discussion that follows I will concentrate on the results for the Yonsei-Yale stellar models, and for my second gyrochronology formulation (Equation 2.11). Similar analysis for the other combinations can be found in Appendix B. All comparisons between different methods utilise only those systems with valid results for both methods. The maximum permitted age for any star was set to the current best estimate of the age of the Universe (Planck Collaboration et al., 2013, and other papers in the series); systems with calculated ages greater than this were disregarded. This is perhaps a somewhat unrealistic upper bound; the age of the Galactic disc might be more suitable, and is thought to be somewhat younger than the Universe, but using that introduces its own set of problems. Do the thick and thin discs have the same age, and if not, which should be used? Or should the sample be split up by popula-

[2] `http://simbad.u-strasbg.fr/simbad/`

tion, and if so how would that be done (disc component membership is a difficult attribute to characterise)? For simplicity, I have stuck to the age of the Universe.

2.4.1 Comparing the methods

My initial point of comparison between the two methods was a simple scatter plot. The dashed line in Figure 2.6 denotes $y = x$, and in the case where the two methods provided similar answers, I would expect a tightly correlated sequence centred on the line (within errors). However there are a preponderance of points lying towards the isochronal side of the line, suggesting that stellar model fitting tends to return ages that are older than those preferred by gyrochronological methods.

Another interesting facet of Figure 2.6 is the distribution of the points along both axes. More than half of the systems lie within a region defined by $\mathrm{age}_{\mathrm{gyro}} < 4\,\mathrm{Gyr}$ and $\mathrm{age}_{\mathrm{iso}} < 6\,\mathrm{Gyr}$. This is not entirely surprising given the region of parameter space to which I have restricted the study. Rough estimates of τ_{MS} for stars at the limit of my parameter space are $\tau_{\mathrm{MS}} = 3.5\,\mathrm{Gyr}$ for an F7 star and $\tau_{\mathrm{MS}} = 11.4\,\mathrm{Gyr}$ for a G9 star (using masses from table B1 of Gray 2008). A drop-off after roughly 4 Gyr is consistent with this, as systems at the hotter end of the parameter range start to evolve off the MS, and are therefore no longer targeted by transit search programs.

In terms of the different methods, 75 percent of the gyrochronology estimates are less than 4 Gyr, with the youngest and oldest systems being 0.14 and 9.68 Gyr old respectively. For the stellar model fitting estimates, 68 percent are younger than 6 Gyr, with the estimates ranging from 1.45 to 13.4 Gyr. It therefore seems that gyrochronology tends to return stellar age estimates which occupy a slightly more narrow range, and which are more biased towards younger ages than the results from stellar model fitting.

The distributions for the different methods highlight the difference between the stellar model fitting and gyrochronology methods. Binning the data in 1 Gyr increments produced the distributions shown in Figure 2.7. Both show a similar overall structure, with a peak at the lower end of their age range followed by a tail towards older systems, but the peaks and median values of the two distributions differ by around 2 Gyr, with the gyrochronology distribution clearly peaking at a younger age. A 2D Kolmogorov-Smirnov (KS) test on the two datasets indicates that there is a less than 1 percent probability of the two having a common

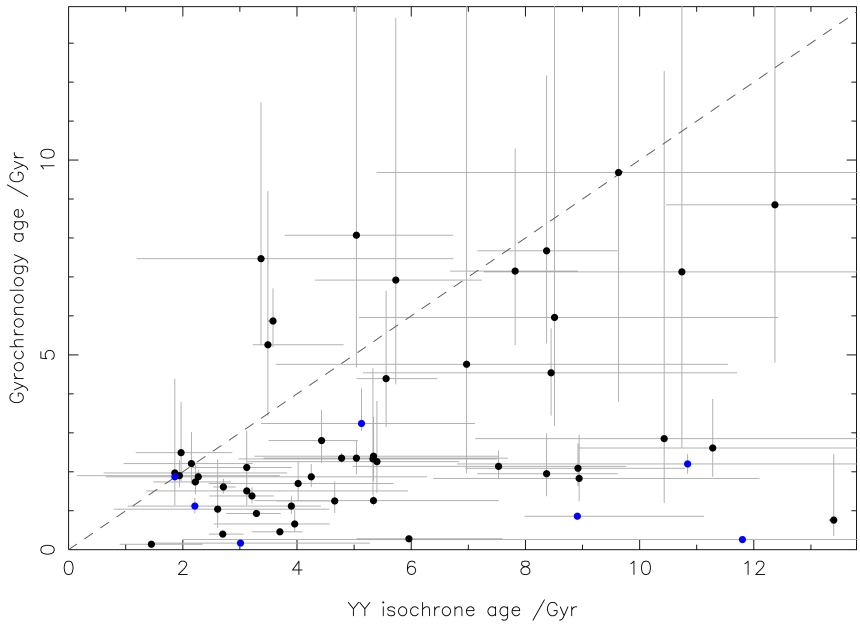

Figure 2.6: *Gyrochronology age, calculated using equation (2.11), as a function of stellar model fitting age, found using the Yonsei-Yale isochrones. The dashed line denotes $y = x$; systems clustered around this line show similar age values for different methods of calculation. The maximum age on both axes is set to the age of the Universe. Direct measurements of the stellar rotation period were available for systems marked in blue. For systems marked in black, $P_{\rm rot}$ was inferred from $v \sin I$ and R_s. It appears that gyrochronology tends to return younger system ages than stellar model fitting.*

parent distribution.

One drawback of the KS test is that it fails to account for the uncertainties in my age estimations. I therefore evaluated the χ^2 goodness-of-fit of my data to the line $\text{age}_{\text{Gyro}} = \text{age}_{\text{Iso}}$,

$$\chi^2 = \Sigma \frac{(\text{age}_{\text{Gyro}} - \text{age}_{\text{Iso}})^2}{\sigma^2_{\text{Gyro}} + \sigma^2_{\text{Iso}}}, \tag{2.13}$$

where σ_{Gyro} and σ_{Iso} are the average uncertainties in each value of the gyrochronological and isochrone fitting ages respectively. I found that $\chi^2 = 698.2$, with a reduced value of $\chi^2_{\text{red}} = 9.8$, suggesting that my ages are a poor fit for the null hypothesis that the two methods return the same age values. The P-value for this result is $P(\chi^2) \sim 0$, a strong indication of significance.

2.4.2 Δage analysis

To further investigate this bias, I calculated the differences between the two ages for each of the systems in my sample. I then binned the results in 0.1 Gyr increments and produced a cumulative probability distribution, Figure 2.8. If the two methods were producing broadly similar results, then I would expect that the distribution would pass through the intersection

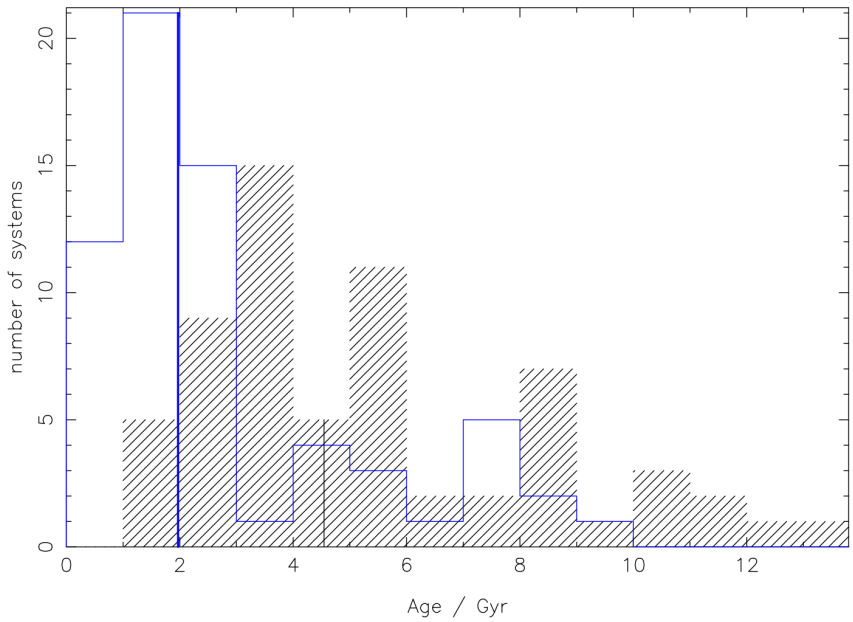

Figure 2.7: *Age distributions for the results that I obtained from stellar model fitting using the Yonsei-Yale isochrones, and from gyrochronology using equation (2.11). The gyrochronology (blue, open) distribution seems to peak at a younger age than the distribution for stellar model fitting (black, hashed). Thick, vertical lines denote the medians of the distributions, and show the same offset.*

of the lines Δage $= 0$ and probability $= 0.5$. Given the preliminary results from the previous section this is unlikely to be the case, but the deviation from this 'ideal case' will be interesting to characterise.

Figure 2.8 shows an apparent offset towards positive Δage, in line with the conclusion from the previous section that stellar model fitting is returning ages which are slightly older than those from gyrochronology. The distribution passes through probability $= 0.5$ at 2.3 Gyr, which roughly corresponds to the offset between medians seen in Figure 2.7. The average upper and lower error bars on Δage are 4.2 and 2.1 Gyr respectively, so this is a 1.1σ effect. For comparison, all the other possible combinations of stellar models and gyrochronology equations also show positive offsets of between 2.2 and 4.1 Gyr, giving significance of between 1.2σ and 2.7σ for the effect.

It seems that there might be a disagreement between the ages that are produced by gyrochronology and stellar model fitting. Does this correlate with a physical parameter in the systems that I am studying? Is it that stellar model fitting is overestimating ages, or that gyrochronology is underestimating ages (or a combination of the two)?

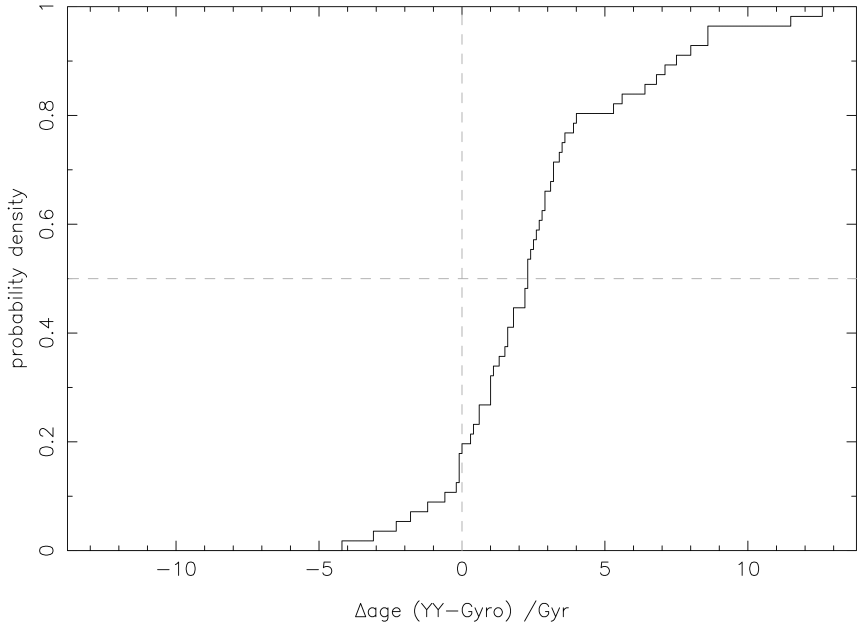

Figure 2.8: *A cumulative probability distribution for the difference between the age results obtained by stellar model fitting using the Yonsei-Yale isochonres, and by gyrochronology using equation (2.11). The dotted lines denote* $\Delta\text{age} = 0$ *and* $\text{probability} = 0.5$. *If the two methods produced similar stellar age distributions, the plot would pass through the intersection of these lines. The x -axis range is* $\pm$ *the age of the Universe. There is an apparent offset towards positive* Δage*, again suggesting that stellar model fitting is returning ages which are older than those from gyrochronology.*

2.4.3 The influence of tidal interactions

One possibility might be that the spin rate of the star is being modified somehow. As noted in Section 2.2.3, gyrochronology is only applicable if no external factors act to modify the natural stellar spin-down, but if hot Jupiter host stars are rotating more rapidly than expected then their age would be underestimated.

Angular momentum exchange between the star and the planet's orbit provides one route by which such a scenario might play out. The chief method of angular momentum exchange within planetary systems is through tidal interaction, which has well-documented consequences for stellar spin. This process will be investigated further in Chapter 4; in the context of this Chapter, I am interested in the possibility of a link between the strength of the tidal interactions and the magnitude of the difference between my age estimates.

To investigate this possibility I calculated the theoretical tidal timescale for each of my systems using equations from Albrecht et al. (2012b). They present two different approaches for estimating the tidal evolution timescales for hot Jupiter systems, and calculate said timescale for a large sample of planets for which the Rossiter-McLaughlin effect has been measured. In

their paper they present two approaches. In the first they consider a bimodal sample of planet hosting stars: those with convective envelopes, and those with radiative envelopes. In the second approach they consider the mass of the convective envelope, which they link to stellar effective temperature. Unfortunately this second approach relies on an unspecified proportionality constant, and the relation between $T_{\rm eff}$ and $M_{\rm CZ}$ that they derived is also unknown. I therefore consider their first approach, which is encapsulated in the equations

$$\frac{1}{\tau_{\rm CE}} = \frac{1}{10 \cdot 10^9} q^2 \left(\frac{a/R_s}{40}\right)^{-6} \tag{2.14}$$

and

$$\frac{1}{\tau_{\rm RA}} = \frac{1}{0.25 \cdot 5 \cdot 10^9} q^2 \left(1+q\right)^{5/6} \left(\frac{a/R_s}{6}\right)^{-17/2}, \tag{2.15}$$

where $q = M_p/M_s$ is the ratio of the planetary and stellar masses, a is the planet's orbital semi-major axis, and R_s is the stellar radius. Both equations return a timescale in years. $\tau_{\rm CE}$ is the tidal timescale for alignment through dissipation in convective envelopes, whilst $\tau_{\rm RA}$ is the equivalent dissipation in radiative envelopes. The choice of which to apply to any given system is determined by its effective temperature. For systems with $T_{\rm eff} < 6250\,{\rm K}$ I use equation (2.14), whilst for the remaining systems I use equation (2.15).

In Figure 2.9 I plot Δage as a function of tidal timescale. If angular momentum exchange is the cause of the discrepancy between the two age estimation methods, then I would expect the difference to be greatest for systems with the shortest tidal timescales (i.e. the strongest tides). Unfortunately the evidence is inconclusive. For the main body of the sample, there might be a slight tendency for Δage to increase as $\tau_{\rm tidal}$ decreases, but the size of the uncertainties on the former mean that any conclusion is tentative at best. The slight trend is also countered somewhat by a single system for which both quantities are large, although Δage for the system is only an upper limit.

Considering only the stars in my sample with directly measured rotation period (the blue data in Figure 2.9) reveals a stronger trend, but a sample size of only seven systems means that this must also, for the moment, remain a tentative conclusion.

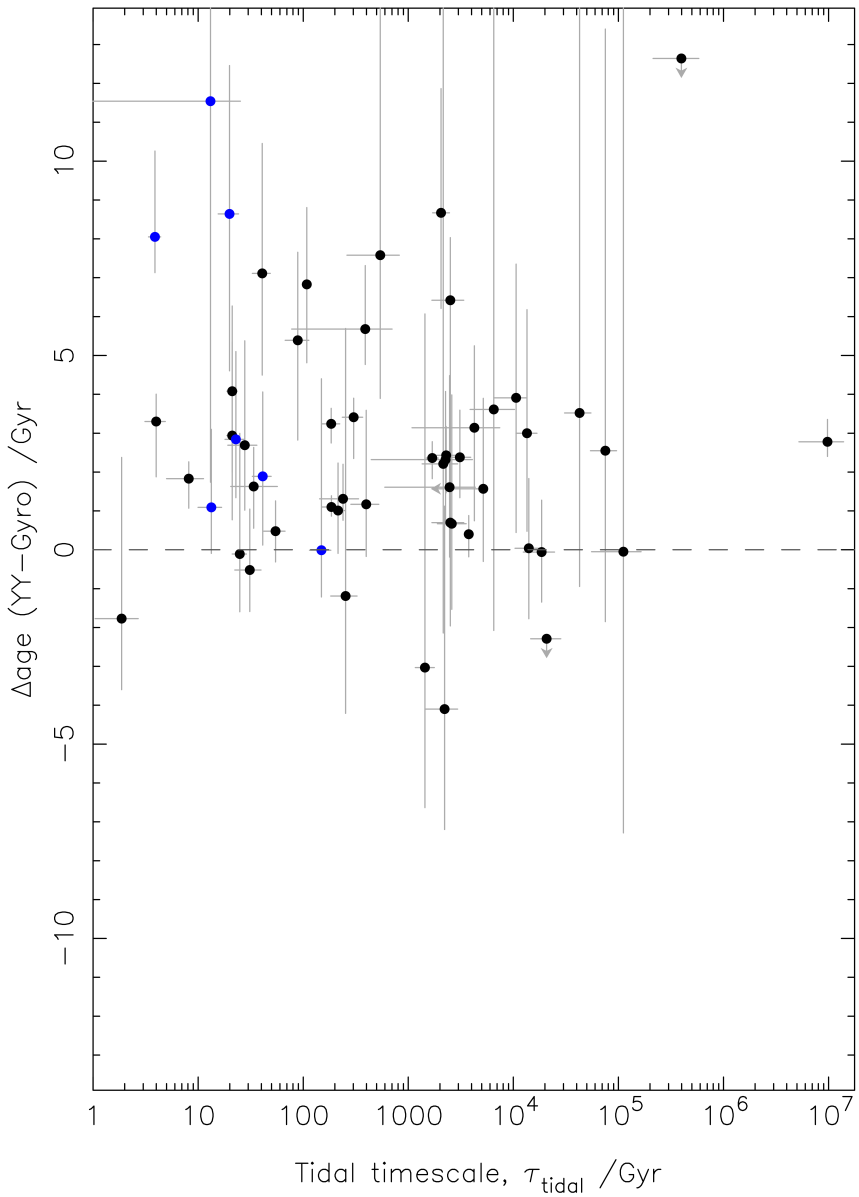

Figure 2.9: *Δage as a function of $\tau_{\rm tidal}$, the tidal realignment timescale. The shorter the timescale, the stronger the tidal interactions within the system, and the greater the angular momentum exchange. There appears to be a slight trend for Δage to increase with decreasing $\tau_{\rm tidal}$, but the evidence is inconclusive. Legend as for Figure 2.6.*

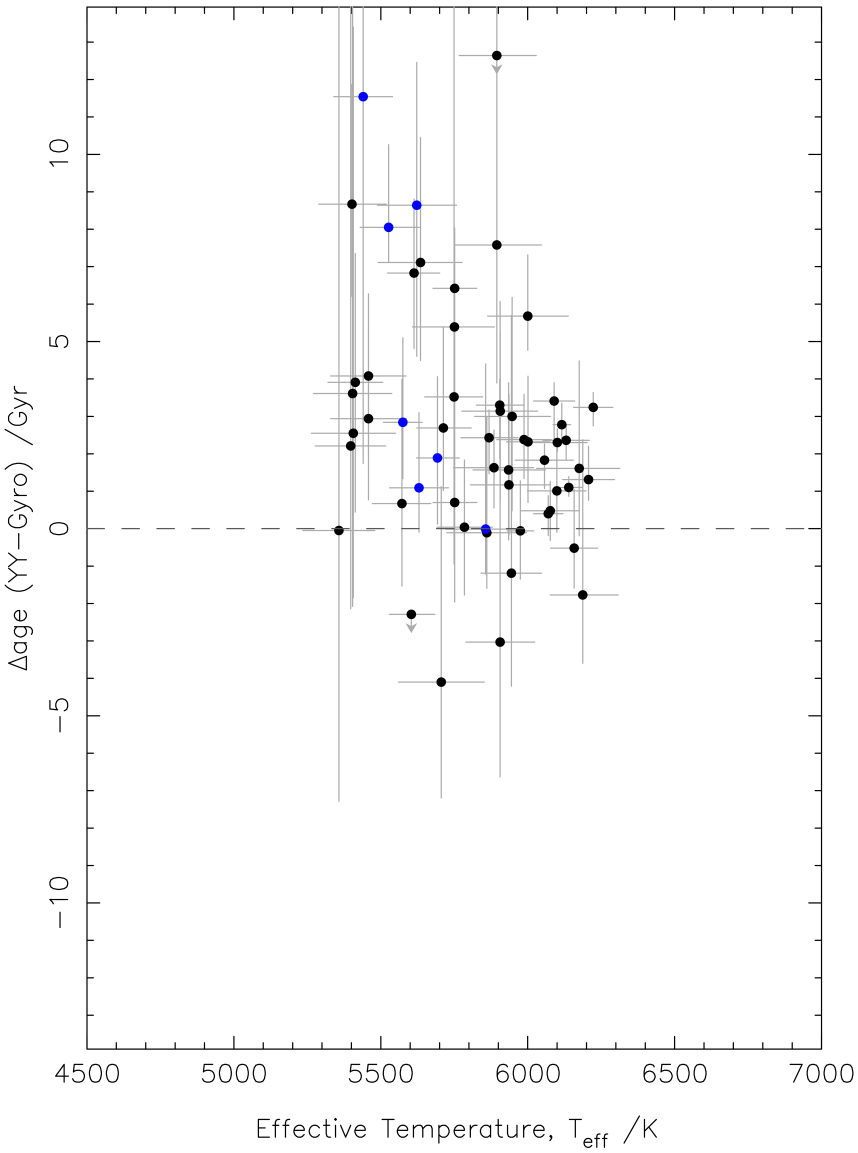

Figure 2.10: *Δ*age *as a function of $T_{\rm eff}$, the stellar effective temperature. There is a clear trend for* Δage *to increase with decreasing $T_{\rm eff}$, towards later spectral types. Legend as for Figure 2.6.*

2.4.4 A link with spectral type?

Another possible reason for the discrepancy between the two different methods might be some bias with spectral type, which could affect either the isochrone or gyrochronology results. To see whether any such trend is exhibited in my sample, I plotted Δage as a function of effective temperature. Figure 2.10 shows a possible trend for the difference in age to increase as $T_{\rm eff}$ decreases.

From Figure 2.11 it seems that there might be some difference in the dependence on $T_{\rm eff}$ between the two methods. The gyrochronology results are distributed evenly across the tem-

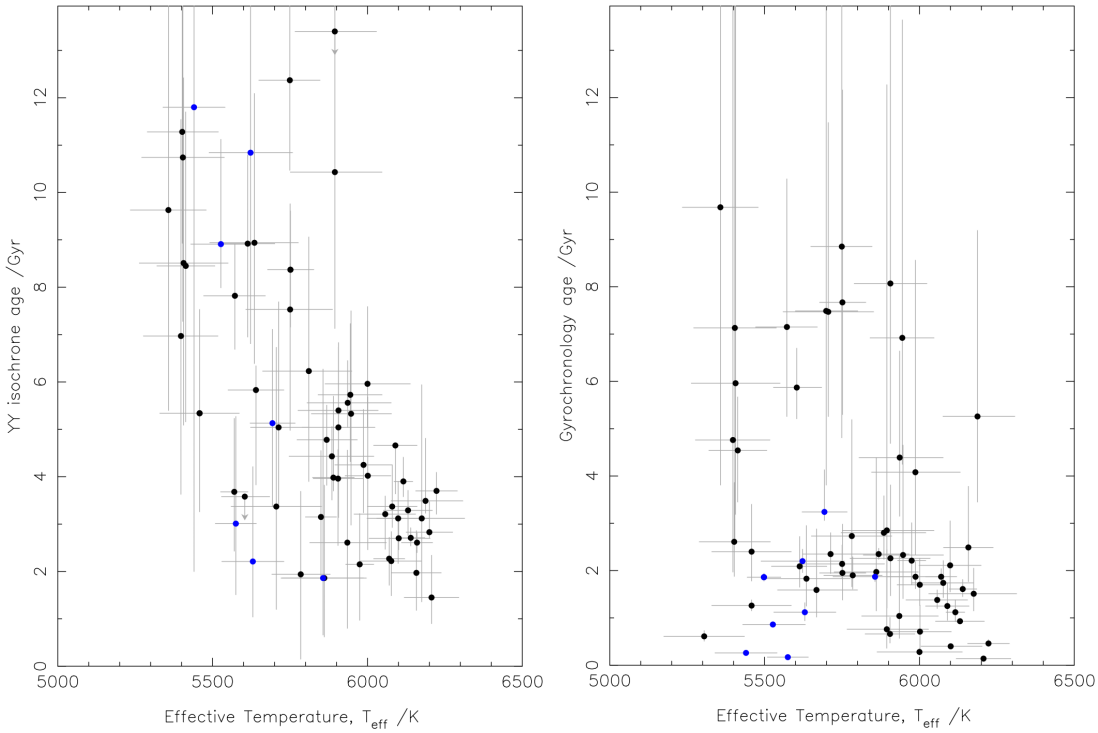

Figure 2.11: *Age as a function of stellar effective temperature.* ***Left:*** *Ages calculated through stellar model fitting using the Yonsei-Yale isochrones.* ***Right:*** *Ages calculated through gyrochronology using (2.11). Legend as for Figure 2.6. Whilst the ages from stellar model fitting show the same trend with $T_{\rm eff}$ as Δage, the ages from gyrochronology show no such trend.*

perature range that I am considering, with a roughly equal number of both old and young systems at all temperatures, although the uncertainty on the age estimates increases dramatically for age $\gtrsim 4$ Gyr. In contrast, the isochrone results seem to show a trend with $T_{\rm eff}$, with the oldest stars also being the coolest; this is a selection effect, as old, hot stars will have evolved off the main sequence. There is also a strong trend in the uncertainties on the isochrone results, with the younger, hotter stars exhibiting more precise ages. The trend in Δage with temperature therefore seems to result entirely from the isochronal results.

This dependence of the stellar model fitting uncertainties on stellar effective temperature concurs with a study by Pont & Eyer (2004), who noted that the size of the observational uncertainties relative to the separation of the isochrones was an important parameter for stellar model fitting, and one which was most favourable for young, hot, early-type systems.

My sample has revealed some interesting potential differences between the ages obtained using the stellar model fitting and gyrochronology methods. Whilst the range of ages covered by the two methods is broadly similar, the way that those ranges are occupied is somewhat different. It therefore seems as though the questions that I asked at the start of this Chapter

are indeed valid. Whilst gyrochronology might provide more precise age values, their accuracy could be suspect for systems that are experiencing strong tidal interactions, leading to discrepancies between the results from the two methods. This discrepancy appears to be around 2 Gyrs on average, and might suggest that the stellar rotational clock of exoplanet hosts is reset at approximately this age. If hot Jupiters form through Kozai migration followed by tidal migration and circularisation (see Chapters 5 and 6), the discrepancy in age estimates could provide useful information on the delay between the formation of the system and the appearance of the hot Jupiter.

2.5 Systems with measured spin-orbit angles

An area of planet research where tides are widely thought to play a role is the angle of alignment between the stellar spin axis and the planet's orbital axis. Examining a sample of planetary systems for which this angle has been measured might therefore be able to shed more light on whether tidal interactions influence the estimation of stellar age.

The topic of spin-orbit angles will be the subject of Chapters 5 and 6 of this thesis, so I will not dwell on the background here. Suffice it to say that for planetary systems we have measured a variety of angles between the rotation axis of the host star and the orbital axis of the planet. The most common method for measuring this angle, known as λ, is the Rossiter-McLaughlin effect (Holt, 1893; Schlesinger, 1910, 1916; Rossiter, 1924; McLaughlin, 1924), but the complementary method of Doppler tomography (Collier Cameron et al., 2010a) is also gaining traction.

Once the angle has been measured, the system is classified as 'aligned' or 'misaligned' according to some criterion. For this Chapter I will be using that of Winn et al. (2010a), who define a system as 'misaligned' if $\lambda \geq 10^\circ$ to $> 3\sigma$. It is thought that tidal interactions are involved in determining whether a system is 'aligned' or 'misaligned', with tidal realignment thought to produce the evolution of orbits from one group to the other.

Planets with measured spin-orbit angles are particularly useful for calibrating gyrochronology. The Rossiter-McLaughlin effect provides stronger constraints on $v \sin I$ than a standard radial velocity curve, thanks to the unique shape of the spectroscopic transit signature. This leads to more precise derived rotation periods, which in turn provide more precise gyrochronology ages. Doppler tomography is an even more valuable method, however, as it is

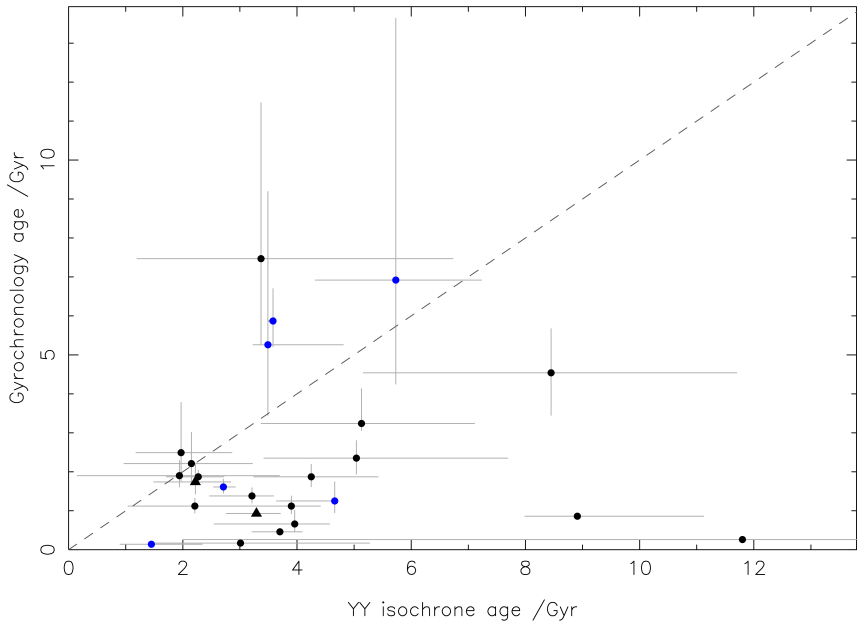

Figure 2.12: *As Figure 2.6 for the sub-sample of systems with measured spin-orbit alignment angle, λ. The dashed line denotes $y = x$, and the maximum age on both axes is set to the age of the Universe. Black data denote systems which are judged to be 'aligned' according to the criterion of Winn et al. (2010a), whilst blue data mark 'misaligned' systems. Filled triangles mark systems for which λ was measured through Doppler tomography. Even for this reduced sample, there is a clear tendency for stellar model fitting ages to be older than those from gyrochronology.*

able to disentangle the true stellar rotation from the spectroscopic effects of turbulence in the stellar photosphere.

From the sample that I have previously analysed, I selected all the systems for which I was able to find measurements of λ in the literature. To do this I used the Holt-Rossiter-McLaughlin database of René Heller[3], as of 2013 January 10th. This selection procedure left 35 systems in my alignment sample.

Examination of Figure 2.12 reveals much the same picture as Figure 2.6. 76 percent of the systems lie on the stellar model fitting side of the $x = y$ delineation, and 72 percent of the systems lie within the box bounded by $\mathrm{age}_{\mathrm{gyro}} < 4\,\mathrm{Gyr}$ and $\mathrm{age}_{\mathrm{iso}} < 6\,\mathrm{Gyr}$. For the full set of systems with measured alignment angles it therefore seems as though the pattern is similar to that found previously. This is supported by the age distributions (Figure 2.13), with the peak in the gyrochronology distribution appearing 2 Gyr younger than the peak in the stellar model fitting distribution; a KS test reveals that the probability of a common parent distribution is less than 1 percent.

As with the full sample of results, I calculated the χ^2 goodness-of-fit for this sample to

[3] `www.aip.de/People/RHeller`

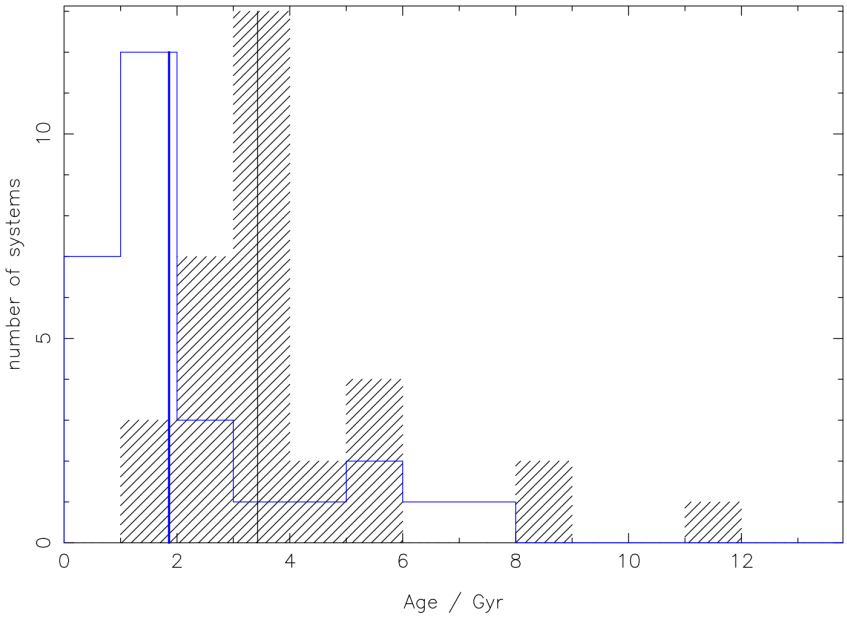

Figure 2.13: *As Figure 2.7 for the sub-sample of planets with measured spin-orbit alignment angles. Legend as for Figure 2.7. The gyrochronology distribution clearly peaks at a younger age than the stellar model fitting distribution, and the median values are similarly offset.*

the line $\text{age}_{\text{Gyro}} = \text{age}_{\text{Iso}}$ using equation (2.13). I found $\chi^2 = 287.5$, $\chi^2_{\text{reduced}} = 8.7$, and $P(\chi^2) \sim 0$, indicating that, to high significance, the data in this sample are again a poor fit to the hypothesis that the different methods return the same ages.

Splitting the sample into 'aligned' (black data) and 'misaligned' (blue data) groups uncovers some interesting differences though. The 'aligned' systems appear to show a bias towards older stellar model fitting ages, with 84 percent of such systems lying to the right of the the line denoting equal estimates. But the 'misaligned' systems are split evenly between those for which stellar model fitting returned an older estimate, and those for which the reverse is true, although the sample size is very small.

The cumulative probability distributions for these different groups again reinforce the conclusions from the scatter plot. Figure 2.14 displays distributions for all of the systems with measured λ (grey distribution), and for the 'aligned' (black distribution) and 'misaligned' (blue distribution) sub-samples. As expected given the preceding discussion, the distribution for the 'misaligned' sub-sample passes through $\Delta\text{age} = 0.0$, indicating that the results from the two methods agree reasonably well. The other distributions still show offsets to positive Δage of 1.8 Gyr for the full alignment sample and 2.3 Gyr for the 'aligned' sub-sample. A 2D KS test on the 'aligned' and 'misaligned' distributions returns a probability of $\sim$ 20 percent that they are drawn from the same parent distribution.

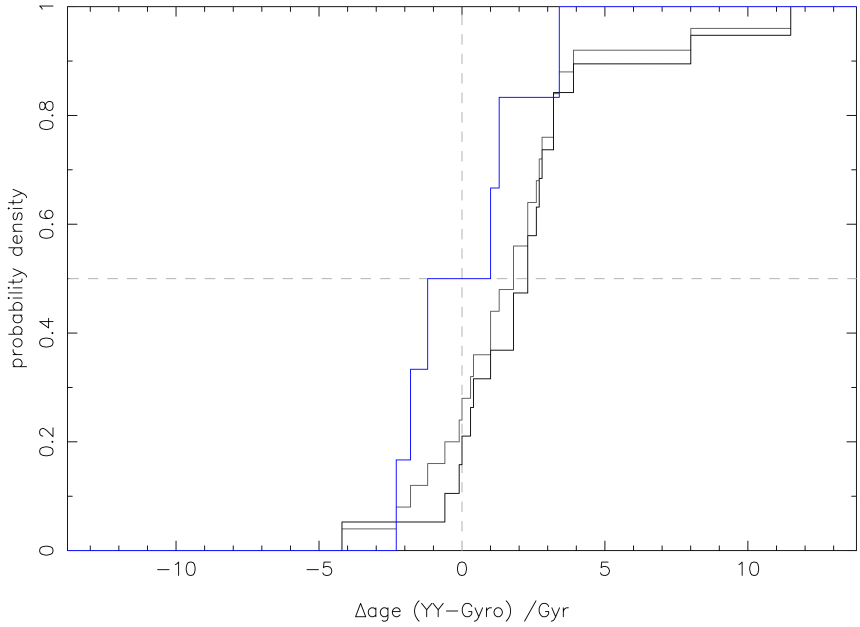

Figure 2.14: *As Figure 2.8 for the sub-sample of planets with measured spin-orbit alignment angles. The dotted lines denote* $\Delta\text{age} = 0$ *and* $\text{probability} = 0.5$. *The x -axis range is* $\pm$ *the age of the Universe. The grey distribution was calculated for all of the systems in this sub-sample. The black distribution and blue distribution were calculated for 'aligned' and 'misaligned' systems only. There is a clear offset towards positive* Δage *for the both the full distribution and the 'aligned' distribution, but the 'misaligned' distribution passes through* $\Delta\text{age} = 0$.

For the systems in the 'aligned' sampled, it is likely that the inclination of the stellar rotation axis to the line of sight, I, is close to 90° (see the work of Schlaufman 2010). However there is no such guarantee for the 'misaligned' systems, and in fact I may be significantly lower than this value. This would affect the relationship between the measured $v \sin I$ and the true rotation velocity such that the former would be much smaller than the latter, with the true rotation period therefore being shorter than the value estimated using $v \sin I$. Since my gyrochronology estimates are based on the derived rotation period in most cases, they will therefore be overestimated compared to the actual gyrochronology age; this could be sufficient to bring them in line with the stellar model fitting estimates. Checking the results of Schlaufman (2010) shows that all six of the 'misaligned' systems are, to varying degrees, rotating more slowly than expected given their age, indicating misalignment of I and lending support to this idea.

Looking at Δage as a function of τ_{tide} (Figure 2.15), we see a similar pattern. The small number of 'misaligned' systems (blue data) show no discernible trend with tidal timescale, but the 'aligned' sample (black data) have two data which suggest that there might be a correlation, with the biggest difference in age found in the systems with the strongest tides. A note of caution must be sounded , however, as the two data which indicate the possibility

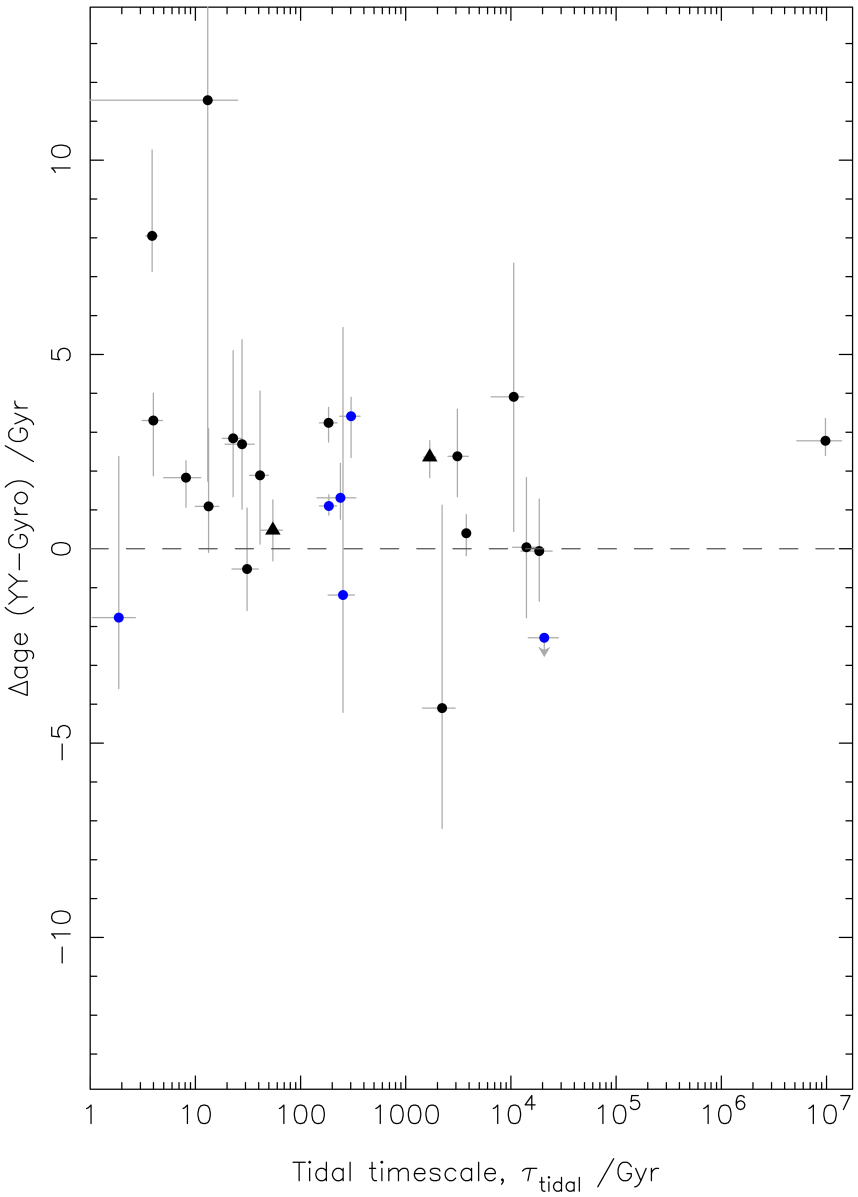

Figure 2.15: *As Figure 2.9 for the sub-sample of planets with measured spin-orbit alignment angles. Legend is as for Figure 2.12.*
The 'misaligned' systems show no trend, but the 'aligned' systems hint at a trend for Δage *to increase with decreasing* $\tau_{\rm tidal}$. *This is based on two data points only though, one of which has substantial* 1σ *uncertainties on the former quantity.*

of a trend are the same as for Figure 2.9.

2.5.1 Discussion

Saffe et al. (2005) conducted a similarly motivated study of exoplanet host star ages. They focused on estimating age through the use of the chromospheric activity indicator, $R'_{\rm HK}$, but also compared their results to the age as calculated using stellar model fitting, lithium abundance, metallicity, and kinematics. Using a sample of over 100 systems, they found that isochrone

ages tended to be older than chromospheric ages, both for their exoplanet host sample and a sample of Solar neighbourhood stars, regardless of which calibration was used for their chromospheric results. They caution though that the dispersions on the two distributions are such that the difference could be nullified.

This provides an interesting comparison to the work that I have presented in this Chapter. Chromospheric activity is known to be correlated with stellar rotation (e.g. Wilson, 1963; Skumanich, 1972), so I would expect a similar pattern to emerge when comparing chromospheric ages to isochrones as when looking at gyrochronology and isochrones. As such, the broad similarity between my conclusion and that of Saffe et al. (2005) is encouraging. However Saffe et al. provide no suggestion for the source of the discrepancy, merely pointing out that the characteristics of the various methods that they use inherently limit them to certain age ranges. One factor might be a known bias towards older ages from isochronal analysis, owing to the uneven spacing of data in stellar models near the zero-age MS (Soderblom, 2010).

A second potential explanation can be found in Alves et al. (2010). Their study of 147 stars with planets, with a comparison sample of 85 stars without detected planets, found that stars with planets tended to have greater angular momentum at a given mass than stars without planets. The difference was most pronounced in stars with $M_s > 1.25 M_\odot$, and the stars with the most massive planets were found to have the greatest angular momenta relative to the Sun. This would seem to support my tentative conclusion that angular momentum exchange as a result of tidal action is responsible for the discrepancy in age results. The increase in the angular momentum of a star with one or more planets would in turn decrease its rotation period compared to a star without planets, throwing off the gyrochronology calibration which is carried out using stellar cluster members which have no known companions. Further support comes from Lanza (2010), who suggests that gyrochronology may not always provide accurate age estimates for planetary systems as plotting $P_{rot} t^{-\zeta}$ as a function of $T_{\rm eff}$ for planet hosting stars gives a poor fit to the period-colour relation of Barnes (2007). This implies that exoplanet host stars are systematically faster rotators than stars with similar ages and properties that do not appear to have any associated planets, an implication which was also put forward by Lanza (2010) who found that the rotation periods of hot Jupiter hosts were, on average, a factor of 0.7 faster than non-planet hosting stars. Such a discrepancy would clearly lead to underestimation of the gyrochronology ages of stars with known planets.

However, another finding of Alves et al. (2010) was that stars with planets definitely follow the established relation between rotation and mass that was described by Kraft (1967). Rapid rotators are mostly those stars hotter than 5800 K, whilst slower rotators are cooler. Furthermore, they carried out KS tests on the $v \sin I$ distributions of their two samples, finding that the results were inconsistent with different origins. This would seem to contradict the conclusions that I have drawn.

2.6 Conclusion

In this Chapter I have examined two methods for estimating the ages of exoplanet host star: stellar model fitting, and gyrochronology. Using a sample of planet hosting stars, I have shown that there seems to be a discrepancy between the results that I obtain with the two methods, and that this discrepancy shows an apparent trend with stellar effective temperature. Furthermore, I have shown that there are hints of a correlation between the tidal realignment timescale for a system and the difference between the age estimates that are obtained. In addition, I examined the same trends in the context of a sample of systems with measured spin-orbit alignment angles, finding similar results for 'aligned' systems. 'Misaligned' systems were found to have similar age estimates from the two methods. However, the sample sizes that I have had access to are limited, particular when considering the sub-sample of systems with measured spin-orbit alignment. Whilst the conclusions that I have drawn are interesting, they must remain tentative and preliminary until the sample sizes can be increased.

In the coming Chapters, I will explore other aspects of exoplanetology on which tidal interactions may have an effect. I will also use the ages that I have calculated to inform the analysis that I carry out. As I stated in the introduction to this Chapter, these ages are vital for understanding the timescales of certain processes, some of which I will explore in the rest of this thesis.

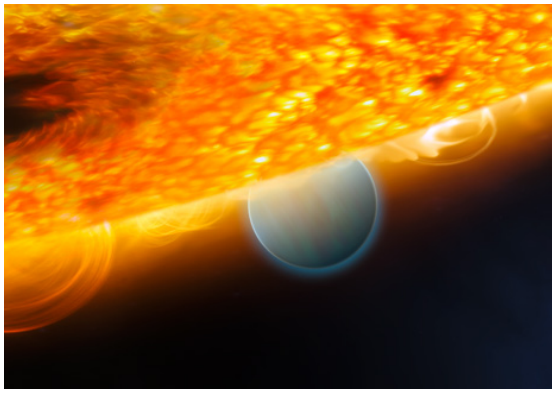

3

Tidal interactions: theoretical background

Tidal interactions between stars and planets were first studied in the context of the Solar system, both as they pertained to star-planet coupling (Goldreich & Soter, 1966), and as applied to planet-satellite systems (Darwin, 1880). Tides have also been extensively studied in the context of binary systems (e.g. Hut, 1980), but the extension of theory to cover planetary systems is comparatively recent, even by the standards of the exoplanets field. The Jovian masses and small orbital separations of hot Jupiter planets make them ideal candidates for studies of tidal theory.

Tidal interactions can lead to long-term changes in the orbital parameters of a hot Jupiter, specifically the eccentricity and the semi-major axis (e.g. Mardling & Lin 2002; Jackson et al. 2008b; Barker & Ogilvie 2009b; Jackson et al. 2009). One possible end result of this process is the spiral-in of the planet towards its host until it reaches the Roche limit, the orbital distance at which tidal forces on the orbiting body become strong enough to disrupt its structure (Eggleton, 1983). At this point the planet undergoes mass transfer through the L1 point (Gu

et al., 2003). Previous studies of such tidal evolution have generally focused on the effect of tidal interactions on these two orbital parameters whilst neglecting the evolution of other parameters that are involved, such as stellar spin. There are, of course, exceptions to this, such as the paper of Dobbs-Dixon et al. (2004).

In Chapter 2 I discussed the possibility that tidal interactions might distort gyrochronological ages of exoplanet host stars. In this Chapter, I will review the relevant theories of tidal interactions in the context of a planet-satellite pair, before extending my discussion to binary stars, and then hot Jupiter systems. I will finish by discussing some previous studies of tidal interactions in hot Jupiter systems.

3.1 A simple picture of tidal interactions

Consider a two-body system consisting of a planet and satellite in circular, equatorial orbits about their mutual centre-of-mass [1], and with the satellite orbiting asynchronously with the planet's rotation. The gravitational force exerted on the planet by the satellite is stronger on the side of the planet that is closer to the satellite, leading to an elongation of the planet's shape. If the planet was perfectly elastic then we would expect that elongation to be symmetric about the line joining the centres of mass of the two bodies, but this is rarely the case. Instead, internal friction within the planet introduces a 'lag' in the position of the tidal bulge compared to the position of the satellite (note that this 'lag' can actually have the tidal bulge leading the satellite).

Figure 3.1 shows the basic geometry of the system being considered. The offset of the bulge axis by angle ϵ means that the gravitational forces on tidal bulges A and B are applied along different lines. The different distances between the satellite and the two bulges mean that these forces also have different strengths. These effects combine to produce a net torque on the planet, which in turn leads to the exchange of angular momentum between the planet's rotation and the satellite's orbit.

The direction of this angular momentum exchange depends on the relationship between the rotation period of the planet, $P_{\mathrm{rot},1}$, and the orbital period of the satellite, $P_{\mathrm{orb},2}$. If $P_{\mathrm{rot},1} < P_{\mathrm{orb},2}$ then $\epsilon > 0$ (i.e. bulge A leads the satellite, as in Figure 3.1) and the net torque opposes the rotation of the planet, causing its period to increase and its angular momentum

[1] For the purpose of this discussion I shall neglect the rotation of the satellite, and assume that it is a rigid body.

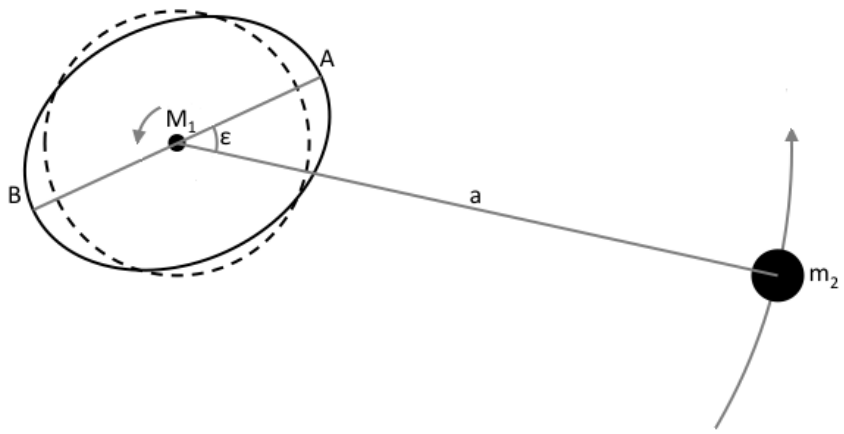

Figure 3.1: *An illustration of the basic geometry of the tidal force exerted on a planet by its satellite. The gravitational pull of the satellite on the planet causes its shape to elongate, but internal friction within the planet means that tidal bulge A is closer to the satellite than bulge B. This leads to a stronger gravitational force on one side of the planet than the other, producing a net torque on the planet which acts to modify the spin period of the planet and, through angular momentum transfer, the orbital period of the satellite. In the case illustrated here, the planet's spin period is shorter than the orbital period, so the tidal bulge is dragged ahead of the satellite's orbit by an angle ϵ. This is known as the lag angle, and is the angle between the line joining the centres of mass of the two bodies, and the long bulge axis of the planet. M_1 is the mass of the planet, m_2 is the mass of the satellite, and a is the orbital distance of the satellite. Adapted from Goldreich & Soter (1966). Figure not to scale.*

to decrease. The planet-satellite system can be considered as a closed system, as the influence of other bodies (e.g. the star around which the planet orbits) will often be negligible[2], and therefore the total angular momentum of the system must remain constant. The angular momentum of the satellite's orbit must therefore increase.

The gravitational force exerted by the planet on the satellite must also be considered. Again, the difference in distance between the satellite and the two tidal bulges leads to a net force, this time in the satellite's instantaneous direction of travel. This causes the satellite to move into a higher orbit, increasing its orbital separation. By Kepler's laws its orbital velocity must therefore decrease, and its orbital period increases. The increase in orbital separation outweighs the decrease in velocity such that orbital angular momentum increases, satisfying the law of conservation of angular momentum. This occurs for any prograde orbit that fulfils the relationship between the orbital and rotational periods, regardless of relative inclination between the equatorial and orbital planes.

The converse case of the satellite orbiting more quickly than the planet is rotating ($P_{\mathrm{rot},1} > P_{\mathrm{orb},2}$) is analogous but with the outcomes reversed. The net torque is in the direction of the planet's rotation, causing it to accelerate and increasing its angular momentum. The satellite

[2]This is obviously only true in the simple two-body case. In the Solar system, the tidal effect on the giant planets is more complex owing to the large number of satellites.

feels a net force opposing its orbit, decreasing its orbital distance and increasing its orbital velocity, with the orbital angular momentum of the satellite necessarily decreasing during this inward movement. In this case, unless a restoring force is applied then the satellite's orbit will decay until it is destroyed through tidal disruption (Counselman, 1973).

There is, of course, an intermediate case in which the orbit is said to be synchronised: $P_{\mathrm{rot},1} = P_{\mathrm{orb},2}$. For a given rotation period this occurs at a specific orbital radius (the corotation radius). It is possible for a system to evolve into this synchronised case, but it requires a careful balance between the decay (growth) of the orbit, and the spin-down (spin-up) of the star, with classical theories suggesting that this is impossible unless $e = 0$ (Ferraz-Mello et al., 2008).

Retrograde orbits present a slightly more complicated scenario, but will always lead to the satellite moving inwards (Barker & Ogilvie, 2009b). As before, a torque acts to slow the rotation of the planet, decreasing its angular momentum. But the retrograde orbit of the planet means that its angular momentum vector is in the opposite direction, so it too must therefore decrease in magnitude, and the satellite spirals inwards.

In the rest of this Chapter, I shall concentrate on the case of prograde orbital motion.

3.1.1 Energy dissipation

While the total angular momentum of the system is conserved during tidal interactions, the total *energy* of the system is not. The internal friction responsible for the lag angle ϵ also dissipates a significant quantity of energy within the planet's interior, diminishing the total energy of the system. This dissipation is often characterised through the so-called 'tidal quality factors', Q_1 and Q_2. These are more correctly termed the 'specific dissipation' functions, and define the level by which the tidal bulges distort the interacting bodies from perfect elasticity or fluidity (Goldreich & Soter, 1966). They are linked to the lag angle by

$$\frac{1}{Q} = \tan(2\epsilon) \approx 2\epsilon, \tag{3.1}$$

and represent the fact that the two bodies are undergoing forced oscillations, dissipating a small amount of energy over each oscillation period. The Q parameters are thus analogous to the quality factors in forced, damped harmonic oscillators (Murray & Dermott, 1999), although this is strictly only correct over a narrow frequency range and for low-order analyses

(Greenberg, 2009). The values of Q for a given system determine the timescales involved in the orbital decay/growth that arises as a consequence of the tidal interactions (Counselman, 1973)

Although I have presented tidal interactions as cause and effect, in reality they are a set of inter-linked and co-dependent processes, and the situation is far more complex than I have implied. The precise internal structure of the planet has a strong influence, as it dictates the tidal friction and energy dissipation qualities of the system (Goodman & Lackner, 2009). As such, there can be substantial differences between tidal interactions involving gas giants, and those involving terrestrial planets, and the values of Q can vary by orders of magnitude from system to system. For example, Goldreich & Soter (1966) found that the values in the Solar system separate into two broad groupings: values of $10 \lesssim Q_p \lesssim 500$ apply to the terrestrial planets and the satellites of the gas giants, whilst the gas giants themselves have $Q_p \gtrsim 5 \times 10^4$ ($6 \times 10^4 - 2 \times 10^6$ in the case of Jupiter; Yoder & Peale 1981).

It is common in the literature to see the 'reduced' tidal quality factors,

$$Q' = \frac{3Q}{2k_2}, \tag{3.2}$$

where k_2 is the 2nd order Love number of the body and measures the level of central condensation of an object (objects which have their mass concentrated at their centre have low k_2; Ragozzine & Wolf 2009). For a homogeneous, fluid body $k_2 = 3/2$ and Q' reduces to Q. Use of Q' is usually implemented owing to the prevalence of the Q/k_2 term in many tidal equation formulations, and is a simple procedure as it is easy to calculate k_2 for stars (Kopal, 1959) and gas giants (Sterne, 1939a,b), assuming that the interior structure is known.

3.2 Binary stars

The simple scenario that I have outlined so far is only an approximation to the true situation. I have neglected, for the most part, the effect of the tides raised on the secondary body by the primary body, and have assumed negligible rotation of the secondary. In reality these are both factors which must be considered, particularly when the two components are comparable in size, mass, and angular momentum, as is common in close binaries (Alexander, 1973).

The possible range of potential tidal factors, Q', is very different for binary stars than for

the planet-satellite systems previously discussed. By modelling inertial waves in the outer convective envelope and including turbulent viscosity as an energy dissipation source, Barker & Ogilvie (2009b) found a large range of $10^8 \lesssim Q'_s \lesssim 10^{12}$ for F-stars. It has been suggested that the lower bound on Q'_s might be as small as 10^6, but this would require extremely efficient dissipation in order to meet known constraints from binary circularisation (Ogilvie & Lin, 2007). Accounting for differential rotation does not significantly affect Q'_s, but introducing Coriolis forces can reduce its value by up to 4 orders of magnitude (Ogilvie & Lin, 2007).

Tidal interactions between the stars in a close binary pair can be very complex. Two main methods are generally used to model them. The first is the equilibrium tide, which approximates the star's shape under the assumption of equilibrium with a time-dependent potential (Eggleton et al., 1998). The second is known as the dynamical tide, which describes the elastic response of the star to the deformation of the stellar surface. This second component accounts for oscillations and resonances within the star that are set up by tidal forces (Zahn, 1989).

3.2.1 The dynamical tide

A major factor in binary star tides is the different composition of a star compared to planets and satellites. The fluidic nature of a star, as opposed to the essentially solid nature of terrestrial planets and satellites, means that it can oscillate. There are several normal modes which can be excited in a star; all are damped, with the higher order modes decaying more rapidly (Eggleton et al., 1998). They fall into two main categories: radial, and non-radial.

Radial pulsations are generated by sound waves resonating in the interior of the star, and are standing waves with a node at the centre of the star and an anti-node at its surface. The period of such waves is proportional to the square root of the star's mean density. (Carroll & Ostlie, 2006)

Non-radial pulsations are described by the real parts of the spherical harmonic functions, with the two indices governing the radial and longitudinal contributions. P-modes are sound waves, so called thanks to the restoring force provided by pressure, and are only fully-described by the specification of both the radial and angular nodes. F-modes are surface gravity waves, whilst g-modes result from internal gravity waves. These modes involve large-scale motion of stellar material, particularly within the star. This separates them from p-

modes, which are confined to the stellar surface (Carroll & Ostlie, 2006), and allows efficient tidal dissipation at high frequencies (Ogilvie & Lin, 2007).

3.3 Hot Jupiter systems

Hot Jupiter systems share similarities with both the planet-satellite example with which I opened this Chapter, and with the binary stars that I have just discussed. The primary similarity with the latter is the consideration of stellar structure, whilst the mass ratio between the two bodies has more in common with the interactions seen in the Solar system.

Observations of planetary systems indicate that values for Q' could be several orders of magnitude greater than those for planet-satellite pairs in the Solar system (Pont, 2009). Estimates from binary stars ($Q'_s \sim 10^6$ Barker & Ogilvie 2009b) are often used as an approximation in hot Jupiter systems, but it is becoming increasingly apparent that this is a poor fit. In fact, Solar-type host stars and binary stars appear to have radically different Q'_s, possibly due to differences in the primary tidal forcing frequency, which falls in the range of inertial waves for binaries, but outside the range for hot Jupiters (Ogilvie & Lin, 2007). Carone & Pätzold (2007) found $2 \times 10^7 < Q'_s < 1.5 \times 10^9$ for OGLE-56, whilst Lanza et al. (2011) claim $4 \times 10^6 < Q'_s < 2 \times 10^7$ (assuming that the system started on the main-sequence already close to synchronicity). Further analysis of planets with circular orbits will allow a firm upper limit to placed on the range of possible values, as the circularisation timescale for such systems is necessarily shorter than their age (Matsumura et al., 2008).

Q'_p and k_2 are generally poorly known for planetary systems owing to the uncertainty surrounding hot Jupiter structures, although it is possible to estimate values using geophysical and/or astrophysical models and seismic data. $Q'_{p,\mathrm{Jupiter}}$ is sometimes assumed to be applicable to hot Jupiters, but there is evidence that the value of Q'_p could vary by several orders of magnitude between systems. Matsumura et al. (2008) suggested that a range of $10^5 \lesssim Q'_p \lesssim 10^9$ would be sufficient to explain eccentric planet orbits, whilst Barker & Ogilvie (2009b) put forward a range of $6 \times 10^4 \lesssim Q'_p \lesssim 2 \times 10^6$ and Gu et al. (2003) obtained theoretical estimates of 10^8 for both Q'_s and Q'_p.

It has been suggested that tides might be responsible for the lack of close-in, massive planets (Pätzold & Rauer, 2002). Once a planet with mass greater than some critical mass is within the corotation radius of its host, then tidal friction will lead to rapid inward migration

to the Roche limit. Tidal disruption of such massive planets might therefore be the source of the observed 'pile-up' at $P_{\rm orb} \sim 3$ days that is observed in the hot Jupiter population (Butler et al., 2006). In addition, Rasio & Ford (1996) found a clear boundary in the mass-separation diagram for extra-solar planets at twice the Roche limit. The lack of hot Jupiters with orbits closer-in than this distance can be explained as a natural consequence of tidal circularisation and migration from highly-eccentric orbits: those planets with initial periastron distances inside their Roche limit are destroyed during the process, whilst the remainder evolve into circular orbits with separation greater than or equal to twice the Roche limit.

Gu et al. (2003) added support to this idea by noting that eccentricity damping during inward migration can easily provide sufficient energy to inflate a planet out to its Roche radius, making Roche lobe overflow a plausible mechanism for explaining the 'pile-up'. Further support came from Levrard et al. (2009), who noted that if the total angular momentum of a system is less than some critical value, then there are no tidal equilibrium states and the inspiral to disruption of the planet is inevitable, regardless of the specific tidal model used. The survival time for the planet seems to largely depend on the dissipation within the star (Matsumura et al., 2010), although Jackson et al. (2008b) noted that for large values of Q'_s (Q'_p), system evolution was independent of the tides raised on the star (planet).

Energy dissipation within the interacting bodies by tidal friction primarily occurs through conversion into heat. This has several interesting consequences for extra-solar planets. For example, tidal heating can affect the habitability of terrestrial planets through several effects such as increasing vulcanicity, and driving outgassing to replenish the planet's atmosphere (Jackson et al., 2008a). Tidal heating has also been suggested as a potential explanation for the subset of planets with apparently inflated radii (Gu et al., 2003; Ibgui & Burrows, 2009), although this is still debated (e.g. Leconte et al., 2010).

3.4 Modelling tidal interactions

There have been many approaches in the literature to modelling tidal interactions, but there is currently no consensus on which is best, as no model can perfectly describe the tidal evolution of a 2-body system.

All tidal models use the idea of a 'forcing frequency' at which the tidal potential drives distortion of material within the tidally interacting bodies. For circular orbits there is a single

frequency, but eccentric orbits introduce several additional components of the tidal potential, each of which acts at a different frequency. Inclined orbits similarly introduce additional forcing frequencies, and considering higher order terms in either e or i also introduces additional harmonic frequencies (Greenberg, 2009). The standard approach to calculating the tidal effect in these systems is to adopt a 'lag-and-add' approach. Every component of the tidal potential is considered to induce a separate response in the primary body, producing a separate distortion with its own ϵ, at a different, very specific frequency that is different for each component (Greenberg, 2009). The total response of the body is then assumed to be the sum of the responses from the individual components.

It is possible to implement this idea in many different ways. The two most common are the constant time lag model, and the constant phase lag model.

3.4.1 Constant time lag model

The constant time lag model of tidal interaction was first put forward by Darwin (1880), and extended by Alexander (1973) and Hut (1980, 1981), among others. In this formulation $\epsilon \propto \nu_{\text{force}}$, which is equivalent to assuming a constant time lag for all frequencies. τ_{lag} is an intrinsic property of the tidally-forced body and is independent of the orbital configuration.

The idea of a constant time lag follows directly from the equations of motion of a tidally-forced, viscous fluid body (the traditional equilibrium tide approach). Some assumptions must be made however. First, we must assume that tidal dissipation results from a viscous force proportional to the tidal flow velocity. Second, the equilibrium structure of the primary body must be spherically symmetric. Third, the tidal dissipation is weak and non-resonant (Socrates & Katz, 2012).

This model is widely used in the literature in a variety of guises and for a range of purposes (e.g. Heller et al., 2010) Studies making use of the Hut equations tend to truncate them to second order, but this is not valid for cases with $e \lesssim 0.2$, for which the complete equations must be used (Leconte et al., 2010).

3.4.2 Constant phase lag model

Described by Goldreich & Soter (1966) and subsequently developed by Jackson et al. (2008c), Ferraz-Mello et al. (2008), and Heller et al. (2010), the constant phase lag model characterises

the lag of the tidal bulge in terms of the angle ϵ. Under this model, ϵ is generally assumed to be the same for all tidal components, regardless of forcing frequency, which greatly simplifies the model and is generally equivalent to considering Q to be constant owing to equation (3.1). However, this approach is only truly applicable for systems with $e << 1$ and $\epsilon << 1$ (Leconte et al., 2010).

3.4.3 Alternative approaches

The two approaches that I have already described are the most common methods for modelling tidal interactions. There are, however, alternatives available in the literature. One such example is that of Dobbs-Dixon et al. (2004), who describe an approach which utilises constant Q' factors to model the evolution of the stellar spin, the planetary spin, the semi-major axis of the planet's orbit, and the eccentricity of the orbit. This model is derived directly from the early work by Eggleton et al. (1998).

It is possible that this approach might not be valid owing to the sensitive dependence of Q' on the detailed interior structure of the bodies involved (Ogilvie & Lin, 2004, 2007; Miller et al., 2009; Matsumura et al., 2010). It has also been suggested that parametrizing tidal evolution in this manner is not equivalent to the more traditional approaches that I have described above (Leconte et al., 2010), as no simple relation exists between Q' and Δt (Leconte et al., 2010).

Another alternative parametrization of tidal theory comes from Hansen (2010, 2012), who used an equilibrium tide framework in conjunction with the model of Eggleton et al. (1998) to develop an empirical model of tidal interactions, calibrated using the known distributions of star and planet properties in planetary systems. Through the use of tidal dissipation constants, σ, Hansen avoided the problems that arise from the frequency dependence of different tidal components.

3.5 Discussion

Several of the studies mentioned in this Chapter have integrated their tidal equations backwards in time to determine the evolutionary history of the systems being studied. This is a reasonable approach to take if one is to refrain from making assumptions regarding initial conditions, but is not always a suitable method. The capture of orbiting bodies into resonance

states is a hysteretic process, so integrating backwards should be avoided for systems which are observed to be in synchronous or resonant orbits (Mardling & Lin, 2002).

Another factor that some early studies of tidal interactions in hot Jupiter systems failed to account for was the natural spin evolution of the star, despite the well-known effect of magnetic braking on the rotation period of isolated stars (see Chapter 2). This might have been due to the Sun-like nature of many transiting planet hosts, for which mass loss through the stellar wind is negligible and can often be neglected (Pätzold et al., 2004). In addition, the strength of the magnetic braking contribution towards a system's evolution is reduced for systems with low mass ratio (e.g. binary stars or large planets around low mass stars) or in which the spin of the primary body is particularly slow (Matsumura et al., 2010). However, Barker & Ogilvie (2009a) found that the inclusion of stellar magnetic braking produced very different evolutionary histories for exoplanet systems, concluding that it was vital to consider the coupled evolution of orbit and stellar spin. They also noted that during stellar spin down the rate of angular momentum loss through magnetic braking outweighed the tidal transfer rate of angular momentum from planetary orbit to stellar spin. Other studies have looked at the large scale effect of the presence of exoplanets on stellar rotation (e.g. Pont, 2009; Alves et al., 2010; Lanza, 2010), and at the effect of tidal interactions specifically (e.g. Leconte et al., 2010)

An exciting possibility was suggested by Ragozzine & Wolf (2009), who commented that tidal bulges more than 2000 km high could produce additional dimming during a planetary transit of up to 2×10^{-4}. Although this signal is likely to be degenerate with the unknown limb-darkening coefficients, detecting this effect is possible with the precision achievable by the Kepler spacecraft. Welsh et al. (2010), for example, have detected ellipsoidal variations in the Kepler light curve of HAT-P-7. Another potentially observable consequence of tidal interactions is orbital precession (e.g. Miralda-Escudé, 2002; Jordán & Bakos, 2008), although it appears that even for very rapidly rotating systems this is, for the moment, unobservable (Iorio, 2011).

3.6 Conclusion

In this Chapter I have described the basic theoretical background of tidal interactions, and the differences between planet-satellite, binary star, and star-hot Jupiter systems. I have briefly

outlined the different approaches that can be taken to modelling said interactions, and have discussed some previous studies of tidal interactions in hot Jupiter systems.

Pont (2009) suggested that tidal effects were likely to have played a role in the fact that exoplanet host stars are observed to be rotating faster than expected. Assuming that this was the case, he posited that planets with $M_p \sim 2\,M_{\rm Jup}$ and $P_{\rm rot} \sim 3\,$days might exhibit strong enough coupling to spiral into the Roche limit within a stellar lifetime. In the next Chapter I discuss my investigation into this possibility, laying out my implementation of the Dobbs-Dixon et al. (2004) model, and showing its application to two transiting hot Jupiter systems.

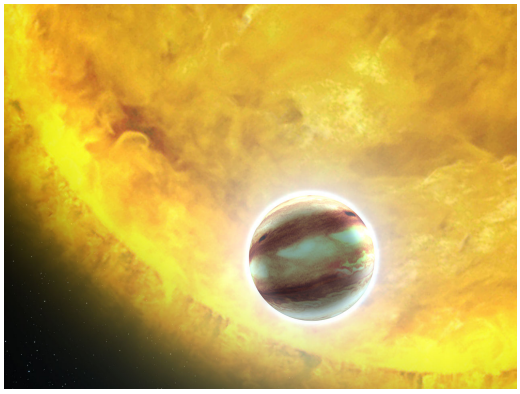

4

Tidal-interaction governed evolution in the WASP-18 and WASP-19 systems

This chapter uses material from Brown et al. (2011), MNRAS, 415, 605-618. This paper was my own work, but built upon an undergraduate masters project by Cassie Hall (supervised by Prof. Andrew Collier Cameron), and on a previous analysis of the WASP-19 system by Leslie Hebb.

In this chapter I will discuss the methods that I have developed for modelling the tidal interactions between hot Jupiter extra-solar planets and their host stars. To demonstrate their use, I apply said methods to the WASP-18 and WASP-19 systems, investigating the effects of tidal interactions on their orbital eccentricities, orbital semi-major axes, and planetary and stellar rotation rates. By fitting the resulting evolutionary tracks to the observed parameters of the systems, including the ages determined for the analysis in Chapter 2, I am able to place constraints on the stellar and planetary reduced tidal quality factors, Q'_s and Q'_p, on the stellar

ages, and on the remaining lifetimes of the two hot Jupiters. I further examine a range of evolutionary histories consistent with my results, and find that the majority imply that both stars have been spun up through tidal interactions as the planets spiral towards their Roche limits. I end with a closer look at WASP-19 A's age, concluding that the system is likely to be old, and that WASP-19 b might be in the final stages of the spiral-in process. I am unable, however, to rule out the possibility that it has a substantial remaining lifetime.

4.1 Tidal and wind evolution

Following Eggleton et al. (1998), Mardling & Lin (2002), and Dobbs-Dixon et al. (2004) tidal energy is dissipated within a star and planet whose spin axes are aligned with the orbital axis at rates defined by the tidal quality factors $Q'_s = 3Q_s/2k_s$ and $Q'_p = 3Q_p/2k_p$, where k_s and k_p are the tidal Love numbers of the two bodies. The eccentricity of the orbit evolves at a rate (Dobbs-Dixon et al., 2004)

$$\begin{aligned}\frac{\dot{e}}{e} &= \frac{81}{2}\frac{n}{Q'_p}\frac{M_s}{M_p}\left(\frac{R_p}{a}\right)^5\left[-f1(e)+\frac{11}{18}\frac{\Omega_p}{n}f_2(e)\right]+\\ &\quad+\frac{81}{2}\frac{n}{Q'_s}\frac{M_p}{M_s}\left(\frac{R_s}{a}\right)^5\left[-f1(e)+\frac{11}{18}\frac{\Omega_s}{n}f_2(e)\right]\end{aligned} \tag{4.1}$$

where

$$f_1(e) = \left(1+\frac{15}{4}e^2+\frac{15}{8}e^4+\frac{5}{64}e^6\right)/(1-e^2)^{13/2} \tag{4.2}$$

and

$$f_2(e) = \left(1+\frac{3}{2}e^2+\frac{1}{8}e^4\right)/(1-e^2)^5. \tag{4.3}$$

The star and planet have masses M_s and M_p, radii R_s and R_p, and rotation rates Ω_s and Ω_p respectively. The orbital frequency is defined by Kepler's 3rd law, $n^2 = G(M_s+M_p)/a^3$.

If the system is fully aligned, then the total angular momentum of the orbit and the axial rotation of the star and the planet, perpendicular to the orbit, is (Dobbs-Dixon et al., 2004)

$$L_{\text{tot}} = M_pM_s\sqrt{\frac{Ga(1-e^2)}{M_p+M_s}}+\alpha_sM_sR_s^2\Omega_s+\alpha_pM_pR_p^2\Omega_p. \tag{4.4}$$

The stellar and planetary moments of inertia are determined by their effective squared radii of gyration, α_s and α_p.

Angular momentum is carried away from the system via a magnetically-channelled, thermally-driven stellar wind, at a rate described by a standard Weber-Davis model,

$$\dot{L}_{\rm wind} = -I_s \kappa \Omega_s \mathrm{Min}(\Omega_s, \tilde{\Omega})^2, \tag{4.5}$$

where the stellar moment of inertia $I_s = \alpha_s M_s R_s^2$ (Weber & Davis, 1967). The physical scaling of the braking rate is determined by the constant of proportionality κ, and $\tilde{\Omega}$ is the 'saturation' rotation rate above which the stellar magnetic field strength is assumed to become independent of the stellar rotation rate.

I also used expressions from Dobbs-Dixon et al. (2004) to describe the tidal spin evolution of the planet under the effect of the tidal torque,

$$\dot{\Omega}_p = \frac{9}{2}\left(\frac{n^2}{\alpha_p Q'_p}\right)\left(\frac{M_s}{M_p}\right)\left(\frac{R_p}{a}\right)^3\left[f_3(e) - f_4(e)\frac{\Omega_p}{n}\right], \tag{4.6}$$

and the star under the influence of both tidal and wind torques:

$$\begin{aligned}\dot{\Omega}_s &= \frac{9}{2}\left(\frac{n^2}{\alpha_s Q'_s}\right)\left(\frac{M_p}{M_s}\right)^2\left(\frac{R_s}{a}\right)^3\left[f_3(e) - f_4(e)\frac{\Omega_s}{n}\right] \\ &\quad -\kappa\Omega_s \mathrm{Min}(\Omega_s, \tilde{\Omega})^2.\end{aligned} \tag{4.7}$$

The polynomials $f_3(e)$ and $f_4(e)$ have the form

$$f_3(e) = \left(1 + \frac{15}{2}e^2 + \frac{45}{8}e^4 + \frac{5}{16}e^6\right)/(1-e^2)^6 \tag{4.8}$$

and

$$f_4(e) = \left(1 + 3e^2 + \frac{3}{8}e^4\right)/(1-e^2)^{9/2}. \tag{4.9}$$

The total angular momentum of the system evolves as

$$\begin{aligned}\dot{L}_{\rm tot} &= M_p M_s \sqrt{\frac{G}{M_p + M_s}}\left[\frac{\dot{a}(1-e^2) - 2ae\dot{e}}{2\sqrt{a(1-e^2)}}\right] + \\ &\quad + \alpha_s M_s R_s^2 \dot{\Omega}_s + \alpha_p M_p R_p^2 \dot{\Omega}_p.\end{aligned} \tag{4.10}$$

By setting this angular momentum loss rate equal to equation (4.5), dividing by the orbital

angular momentum,

$$L_{\rm orb} = M_p M_s \sqrt{\frac{Ga(1-e^2)}{M_p + M_s}}, \tag{4.11}$$

and rearranging, an expression for the evolution of the orbital semi-major axis can be obtained:

$$\frac{\dot{a}}{a} = 2\left[\frac{\dot{e}}{e}\frac{e^2}{1-e^2} - \frac{I_s\dot{\Omega}_s}{L_{\rm orb}} - \frac{I_p\dot{\Omega}_p}{L_{\rm orb}} - \frac{I_s\kappa\Omega_s{\rm Min}(\Omega_s,\tilde{\Omega})^2}{L_{\rm orb}}\right]. \tag{4.12}$$

Integrating this equation under the assumption of a circular orbit ($e = 0$), neglecting dissipation in the planet, and assuming a slowly-rotating star ($\Omega_s/n << 1$), leads to an estimate of the time remaining to spiral-in for the orbiting planet,

$$t_{\rm remain} = \frac{2Q'_s}{117n}\frac{M_s}{M_p}\left(\frac{a}{R_s}\right)^5, \tag{4.13}$$

giving a result almost identical to the estimate of the same quantity derived from a slightly different formulation by Levrard et al. (2009). The quantity a/R_s is derived directly from the transit duration for a transiting planet, enabling $t_{\rm remain}$ to be estimated from directly-observed quantities for a given value of Q'_s.

Leconte et al. (2010) suggested that parametrizing the tidal evolution equations using stellar and planetary tidal quality factors which are constant in time could, if truncated to O(e^2), produce both qualitatively and quantitatively incorrect evolutionary histories for systems with $e > 0.2$. Despite using a constant tidal quality factor model the tidal equations that I used for this work are not truncated in this fashion, and thus do not suffer from the problems that Leconte et al. describe.

4.2 Computational method

An estimate of the value of the scaling constant for magnetic braking, κ, is required to implement equation (4.5). Following the standard Weber-Davis model, the rate of change of the rotation rate of an isolated star owing to magnetic braking can be described by

$$\dot{\Omega}_s = -\kappa\Omega_s^3. \tag{4.14}$$

Integrating this under the assumption that $\Omega_2 << \Omega_1$ and $t_2 >> t_1$ gives

$$\kappa = \frac{\Omega_2^{-2}}{2t_2}, \tag{4.15}$$

which leads to the standard power law for magnetic braking,

$$P \propto t^{\zeta}, \tag{4.16}$$

with $\zeta = 0.5$ (Skumanich, 1972). This neglect of the initial conditions is justified by the observed strong convergence of spin rates to a narrow period-colour relation in the Hyades (Radick et al., 1987), and in other clusters of similar ages. I set $\Omega_2 = \Omega_{s,\mathrm{Hyades}}$, calculated by scaling the P_{rot}-(J-K) colour relationship found for the Coma-Berenices cluster by Collier Cameron et al. (2009) and using J and K magnitudes taken from the SIMBAD on-line data archive, to obtain an estimate for κ at the age of the Hyades. This value is assumed to be constant throughout the evolution of the system. For simplicity, I assumed that in all cases the planet's rotation was initially tidally locked such that $\Omega_{p,0} = n$, but Ω_p was permitted to evolve independently thereafter.

Recent work on tidal interactions has found that the braking law exponent, ζ, diverges slightly from the ideal Skumanich value in some environments (see section 2.2.1, Chapter 2). If equation 4.14 is generalised to raise Ω to the power β, then

$$\kappa = \frac{\Omega^{-\frac{1}{\zeta}}}{t/\zeta}, \tag{4.17}$$

a universal expression for κ with $\beta = \frac{1}{\zeta} + 1$, is derived. I calibrated my implementation of the magnetic braking power law using the stars listed in table 4 of Collier Cameron et al. (2009), finding that an exponent of $\zeta = 0.495 \pm 0.002$ gave good agreement between the measured rotation periods and the evolved stellar rotation rates calculated using my method. I found that there was little to differentiate the evolutionary tracks produced using values of α within this range, and therefore adopted the central value of $\zeta = 0.495$.

Starting from a given set of initial conditions $(t_0, e_0, \Omega_{s,0}, \Omega_{p,0}, a_0)$, I carried out forward integration of the four equations (4.1), (4.6), (4.7), and (4.12) using a fourth-order Runge-Kutta scheme, adapted from algorithms in Press et al. (1992). The unit of time was 1 Gyr, and the integration was allowed to run for the approximate main-sequence lifetime, $t_{\mathrm{MS}} \simeq$

$7(M_s/M_\odot)^{-3}$ Gyr for a star of mass M_s, or until the planet reached the Roche limit, as defined by Eggleton (1983). To calculate the stellar radius of gyration the metallicity and mass of the star were used to select an appropriate table from Claret (2004b, 2005, 2006, 2007); at each timestep the code interpolates through this data using the current time to derive a value for α_s. This is not an entirely accurate method, as the series of papers by Claret provides only tables for discrete values of metallicity and stellar mass that in many cases do not coincide with the metallicity of the systems being studied. In these cases the table that most closely corresponds to the system parameters was used.

The observed values of e, Ω_s and a, and their uncertainties, were used to evaluate the goodness-of-fit statistic at each timestep according to

$$\chi^2(t) = \frac{(e_{\rm obs} - e(t))^2}{\sigma_e^2} + \frac{(\Omega_{\rm s,obs} - \Omega_{\rm s}(t))^2}{\sigma_{\Omega_s}^2} + \frac{(a_{\rm obs} - a(t))^2}{\sigma_a^2}. \tag{4.18}$$

A Bayesian prior on the stellar age t was added to this to obtain the statistic

$$C = \chi^2(t) + \frac{(t_{\rm obs} - t)^2}{\sigma_t^2}, \tag{4.19}$$

where $t_{\rm obs}$ and σ_t are the stellar age estimated from the star's density and effective temperature (Sozzetti et al., 2007) (see Chapter 2), and its associated uncertainty. The age of the system was taken to be the time of the step at which C was a minimum.

This forward integration method was built into two separate computational schemes: a grid search that carried out the integration for each node in a four-dimensional grid in a_0-e_0-log(Q'_s)-log(Q'_p) parameter space, and a Markov-chain Monte-Carlo (MCMC) optimisation scheme to determine the posterior probability distributions of log(Q'_s), log(Q'_p), e_0 and a_0, and to refine the estimates of the initial parameters returned by the grid search.

4.2.1 Grid Search method

A grid search is a very simple search algorithm that slowly and methodically covers the full extent of the parameter space that has been defined. It applies user-supplied evaluation routines to find the best solution to the problem.

Each free parameter is assigned a stepsize. This is used in conjunction with that parameter's permitted range to determine the number of grid points for that parameter. The

algorithm works its way through all possible combinations of these points. At each node the set of parameters corresponding to that node are evaluated, and the result stored for later comparison.

The two downsides of this algorithm are its slow speed, and its discrete nature. The more free parameters you have, the greater the number of nodes, and the slower the run time. Moreover the algorithm *only* evaluates at those nodes, so if the best solution lies between two or more nodes, then the grid search will return only an approximate solution. On the other hand, a grid search is both reliable and easy to build.

In my implementation the set of parameters at each node are used as the starting conditions for the integration scheme outlined above. Each node therefore acquires as an associated parameter the minimum value of C found for that integration. The best-fitting set of initial parameters, and thus the best-fitting evolutionary history, is taken to be that from the node with the absolute minimum value of the associated C statistic values.

4.2.2 Markov-chain Monte-Carlo simulation

Markov-Chain Monte-Carlos (MCMCs) are a set of Bayesian analysis methods which take advantage of the properties of Monte Carlo integration to accurately sample an unknown distribution by drawing a large number of samples from it. The strength of MCMC is that each step is predicated on the current state of the chain. Most commonly implemented in the form of a random walk algorithm, the basic MCMC method has several available variations in the way that the Markov chain is produced, and in which the sampling is carried out. For my work I use the Metropolis-Hastings method (Metropolis et al., 1953; Hastings, 1970).

The premise of Metropolis-Hastings is that the parameter steps are taken from a known, proposed distribution, and matched to the desired posterior distribution; a basic outline of the method is shown in Figure 4.1. The new parameter set, P_k, is generated from the previous set, P_{k-1}, and evaluated. In my case the proposed distribution for each parameter is taken to be Gaussian, and the evaluation is carried out using the forward integration model described in section 4.2. The C statistic value for the new parameter set is compared to that from the previous set using $\Delta C = C_k - C_{k-1}$; if the fit is better ($\Delta C < 0$) then the new set of parameters is accepted, and the chain moves to that point in parameter space. If the fit is worse, then the step is accepted with probability $e^{-\Delta C/2}$. If the step is rejected then the chain remains where

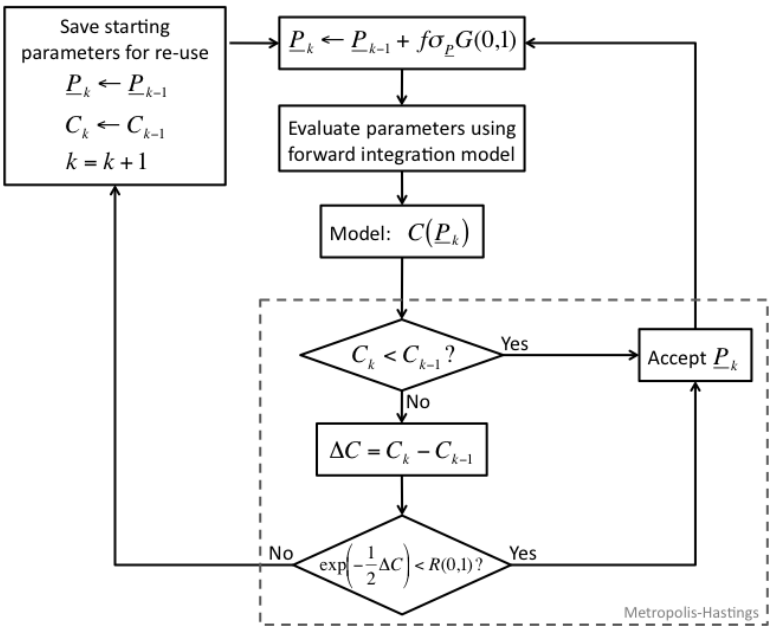

Figure 4.1: *A flowchart illustrating the basic working of the MCMC algorithm. When generating new parameters, the scale factor f is of order unity but tuned to provide an acceptance rate of roughly 25 percent. The secondary check for acceptance allows the Markov chain to climb out of local minima, preventing erroneous solutions and poor convergence.*

it was, and saves another copy of the last successfully accepted parameter set[1]. Another set of new parameters is then generated.

The purpose of the second acceptance checking phase is to try and prevent the chain from falling into local minima in the C-surface. If the steps that the algorithm is taking are too small then the algorithm could potentially become stuck in such a minimum for some time, leading to a 'poorly mixed' chain and slow convergence. The random number comparison allows the chain to climb back out of local minima before it gets stuck, although the success of this approach still relies on the size of the steps that the algorithm is taking. This in turn depends on the choice of proposed distribution, but can be modified through additional scaling. The ideal rate of acceptance is roughly 25 percent (Tegmark et al., 2004).

There are two phases to an MCMC algorithm: the 'burn-in' phase, and the 'production' phase. Since the posterior distribution is unknown, the chain must be started from an arbitrary combination of parameters; under my optimisation scheme, these coordinates are set to the centre of the parameter space unless this lies within $3\sigma_C$ of the coordinates of the best-fitting initial result from the grid search, in which case the origin coordinates are set to lie outwith the

[1]This becomes key when calculating uncertainties at the end of the MCMC run, as it affects the shape of the posterior distribution.

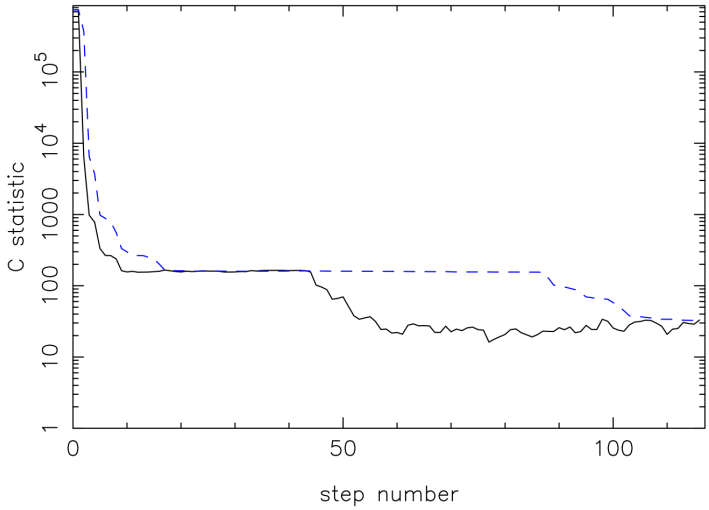

Figure 4.2: *An illustration of the burn-in procedure and evaluation for my MCMC algorithm. The progression of the C statistic for the current step is shown by the solid, black line. The dotted, blue line marks the progression of the median value of C. Note the importance of the* ≥ 100 *steps criterion in this situation, as without it 'burn-in' would have been judged to be complete at the earlier plateau in C. Data taken from my analysis of the WASP-18 system.*

$3\sigma_C$ contour in parameter space. The algorithm then randomly iterates around the available parameter space according to the Metropolis-Hastings decision maker until the chain has converged on the desired distribution. Once this has been achieved, the steps taken up to that point are discarded (they were not drawn from the posterior distribution), and the chain is said to have 'burnt-in'. The production phase then begins, and the desired number of samples are taken.

Determining when burn-in is complete is of the utmost importance. For my work, I use the method of Knutson et al. (2008), judging this phase to be complete when the minimum value of the test statistic from the current integration exceeds the median of all previous minimum C statistic values for the first time, with the proviso that 100 successful steps must have been completed (see Figure 4.2). This additional criterion is applied to ensure that the chain has truly converged on the posterior distribution. Following the completion of burn-in I then carry out an intermediate, 'rescaling' phase of 100 successful steps, using these to calculate new error bars for my parameters that are fed into the algorithm at the parameter generation phase.

My 'production' phase runs for 10000 successful steps, giving a total chain length of

roughly 40000 steps when accounting for the optimum acceptance rate. The best-fitting set of parameters are taken to be the median values of the respective posterior probability distributions, with 1σ errors derived from the values that delineate the central 68.3 percent of the distribution. I chose this approach over the absolute minimum, as the latter strongly depends on the precise sampling of the parameter space by any given Markov chain. This set of parameters are then integrated forward in time to provide the best-fitting evolutionary history for the system.

4.2.3 Defining my parameter space

I assumed that the orbit of the planet would monotonically shrink throughout the integration, thus placing a lower limit on the initial semi-major axis of $a_{0,\mathrm{min}} = a_{\mathrm{obs}}$. The upper limit on the same parameter was set at $a_{0,\mathrm{max}} = 0.1$ AU, a value which encompasses 80 percent of the current distribution for transiting planets which have known semi-major axes. The ranges of the tidal quality factors were set to $4.0 \leq \log(Q'_p) \leq 10.0$ and $5.0 \leq \log(Q'_s) \leq 10.0$ such that the commonly accepted ranges of values ($10^5 - 10^6$ for Q'_s, $10^7 - 10^8$ for Q'_p; Baraffe et al. 2010) were encompassed together with an additional section of parameter space.

The initial eccentricity distribution for the ensemble of exoplanets is the subject of much discussion. A value of $e_{0,\mathrm{max}} = 0.2$ encompasses 81 percent of the present distribution and limits my parameter space to the region of validity for the tidal equations defined by Leconte et al. (2010). However Kozai scattering (Kozai, 1962), can pump orbital eccentricity to large values, and it has been suggested that short period planets are captured at periastron from such highly eccentric orbits. If this is the case then a much higher upper limit on e_0 could be justified.

It is important to consider the initial times at which the integrations commence. Meibom & Mathieu (2005) carried out a survey of tidal circularisation in binary stars, and found that open clusters show a characteristic orbital period at which binaries with the most common initial eccentricity circularise (they define a circularised orbit as one with $e = 0.01$). This period was found to vary with the age of the cluster. However it is questionable whether exoplanets, owing to the much lower secondary mass, will tend to circularise at the same orbital period. In fact Hansen (2010) applied the formalism of Meibom & Mathieu (2005) to planetary systems, finding that circularisation periods were generally much shorter than for stellar binaries. I therefore set $e_{0,\mathrm{max}} = 0.8$, a value encompassing 99 percent of the current

distribution for transiting exoplanets, to allow for the possibility of eccentric orbits produced by Kozai oscillations.

Note that stellar and planetary obliquities greater than 0.0 are not considered by the integration methods that I used for this work owing to the algebraic formulation that underlies my computational methods. I therefore assumed that the orbital and spin angular momentum vectors were either aligned or anti-aligned.

4.3 The WASP-18 system

The hot Jupiter WASP-18 b orbits the star HD10069, an F6 star with an effective temperature $T_{\rm eff} = 6400 \pm 100\,$K and a V magnitude of 9.3, situated approximately 100 pc from the Earth. It was the first planet *confirmed* to have a period of less than a day, orbiting its host in just 0.94 days. A measurement of the Rossiter-McLaughlin effect by Triaud et al. (2010) showed that the system is well aligned, with an angle of $\lambda = 4.0 \pm 5.0\,^{\circ}$. On the other hand, Albrecht et al. (2012b) found $\lambda = 13 \pm 7\,^{\circ}$, indicating a slight misalignment. However any obliquity resulting from this is likely to be small, and so the assumption of spin-orbit alignment required for my analysis seems fairly well justified. In the absence of a measured rotation period for WASP-18, I assumed that the inclination of the stellar axis is 90° such that $\sin I = 1.0$ and $v_{\rm rot} = v \sin I$.

As shown in Appendix A, my isochrone fitting using the YY isochrones provides an age of $< 1.17\,$Gyr for this system. This can be further constrained using the observed lithium abundance to $\sim 0.6\,$Gyr, whilst Hellier et al. (2009) assigned the system an age of $0.5-1.5\,$Gyr. One of the secondary aims of considering the tidal interactions in this system was to attempt to improve upon these values.

An observed system age of $0.63 \pm 0.53\,$Gyr was used for the calculation of the C-statistic for this system, in line with previously discussed age estimates. WASP-18 b has a radius of the order of that of Jupiter, but is significantly more massive. Lacking a means of calculating α_p however, I set $\alpha_p = \alpha_{\rm Jup}$ as a reasonable estimate.

Since the observed system age is consistent with the age of the Hyades, I compared $P_{{\rm rot},s}$ from Table 4.1 to $P_{{\rm rot},s}(t = t_{\rm Hyades})$, as calculated for my derivation of κ for the system, finding the observed stellar rotation period to be shorter than the expected rotation period of 7.00 days at the age of the Hyades. I therefore set $t_0 = 150\,$Gyr$\approx t_{\rm M35}$, calculating $\Omega_{s,0}$ by

Table 4.1: *System parameters for WASP-18, primarily taken from Hellier et al. (2009). The rotation period is taken from Table A.2, and the age is taken as the VRSS result from Table A.1. The J-K colour was calculated using data taken from the SIMBAD on-line database, and λ was taken from Triaud et al. (2010).*

Parameter	Value	Units
M_s	1.25 ± 0.13	$M_\odot$
R_s	$1.216^{+0.067}_{-0.054}$	$R_\odot$
$J - K$	0.278 ± 0.032	
$T_{\rm eff}$	6400 ± 100	K
$v \sin I$	10.77 ± 0.04	$\mathrm{km\,s^{-1}}$
$P_{{\rm rot},s}$	$5.58^{+0.94}_{-0.72}$	days
System age	$0.66^{+1.02}_{-0.60}$	Gyr
M_p	10.30 ± 0.69	$M_{\rm Jup}$
R_p	$1.106^{+0.072}_{-0.054}$	$R_{\rm Jup}$
a	0.02026 ± 0.00068	AU
e	0.0092 ± 0.0028	
i	86.0 ± 2.5	$^\circ$
$P_{\rm orb}$	$0.94145299 \pm 0.00000087$	days
λ	$5.0^{+3.1}_{-2.8}$	$^\circ$

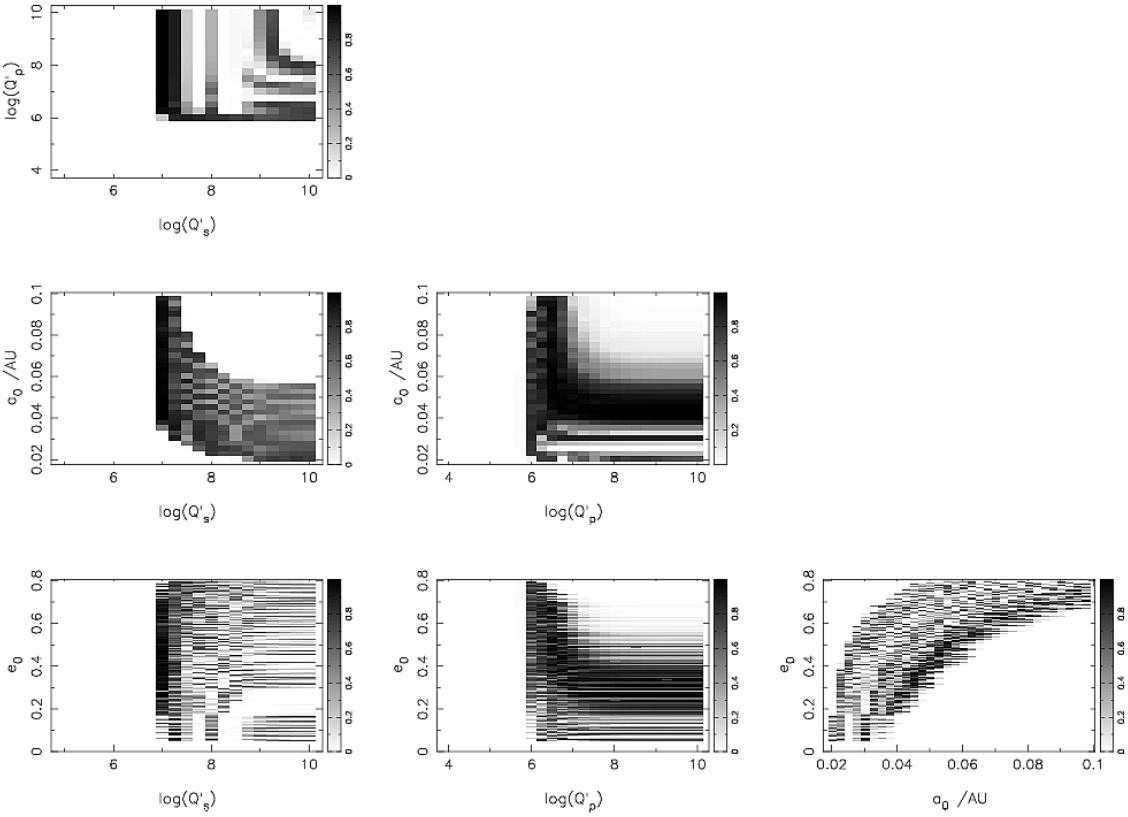

Figure 4.3: *Projection maps of the C-statistic probability density for WASP-18. The projections indicate distinct ranges of* $\log(Q'_s)$*,* $\log(Q'_p)$ *and* a_0 *that give high probability, corresponding to a low value of the C-statistic.* e_0 *provides a less clear cut high probability region, with several individual values giving good results. The best-fitting initial parameters were found to be* $a_0 = 0.0427\,AU$*,* $e_0 = 0.245$*,* $\log(Q'_s) = 7.00$ *and* $\log(Q'_p) = 7.50$*, giving a system age of* $0.654\,Gyr$*.*

scaling the period colour relation of Collier Cameron et al. (2009) to this age.

The C-statistic values returned by the grid search were converted into probability densities according to

$$P(C) = e^{-\frac{C^2}{2}}, \tag{4.20}$$

and plotted as a set of projection maps (Fig. 4.3). These indicate regions of high probability, and therefore low points in the C-statistic surface, for each pair of initial parameters, and appear to show that there are a range of values for each parameter that could produce plausible evolutionary histories with a good quality of fit. This is particularly noticeable in e_0 and $\log(Q'_p)$, indicating that these parameters have a lesser impact on the orbital and spin evolution of the system than a_0 and $\log(Q'_s)$. This is, to a certain extent, unsurprising; the current orbital eccentricity for WASP-18 b is more uncertain than the orbital separation, and so will have less influence on the value of the C-statistic. It is also interesting to note the generally sharp transitions in Fig. 4.3 between regions with $P(C) > 0.4$ and those with $P(C) \approx 0$. This

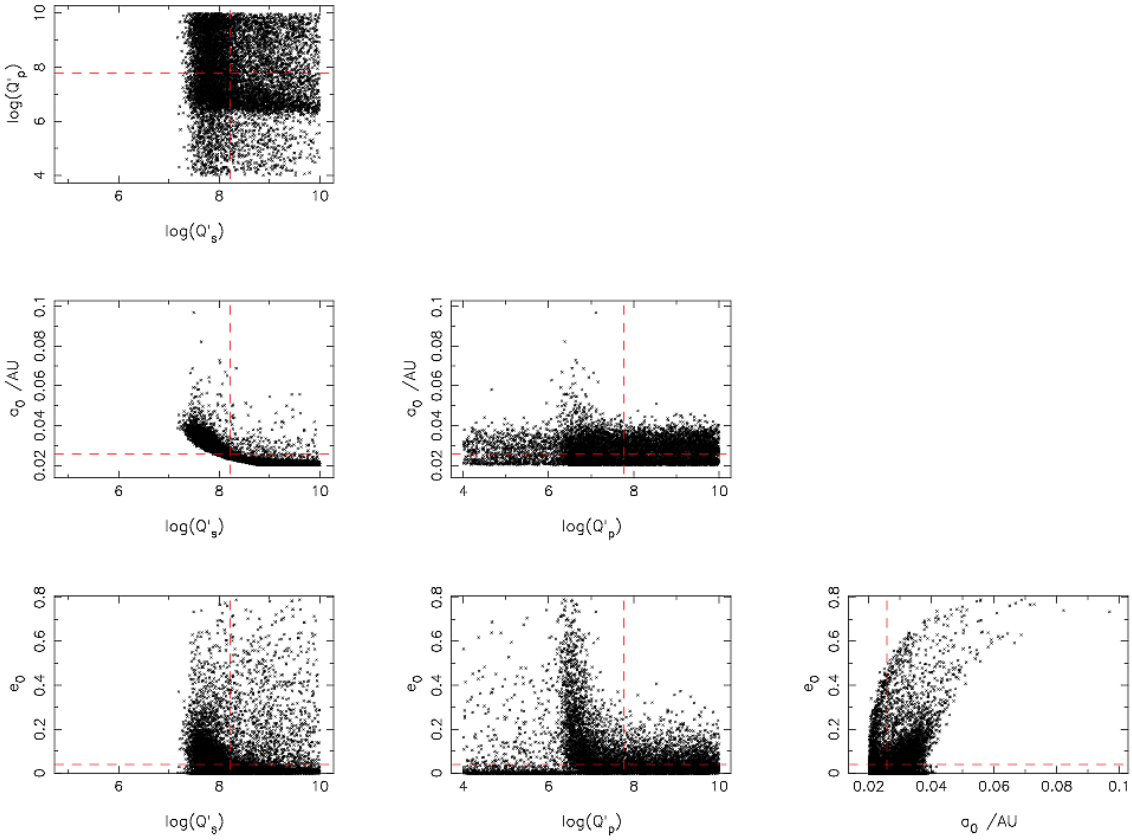

Figure 4.4: *The posterior probability distributions of each pair of jump parameters produced by the MCMC analysis of the WASP-18 system. Note the clear correlations between several of the integration parameter pairs; these arise from the dependence of tidal energy dissipation on the orbital eccentricity, and from the strong coupling that exists between the orbital eccentricity and the orbital separation. The location of the best-fitting parameters are denoted by the dashed lines.*

indicates that although the values of the initial parameters are somewhat uncertain, they are generally well constrained to a smaller region of parameter space than I have allowed for.

The best-fitting combination of initial parameters in these projection maps was found to be $a_0 = 0.0428$ AU, $e_0 = 0.245$, $\log(Q'_s) = 7.00$ and $\log(Q'_p) = 7.50$, indicating a system age of 0.654 Gyr in good agreement with the broad estimates derived from stellar model fitting in Chapter 2. However the gyrochronology estimate of $0.41^{+0.04}_{-0.03}$ Gyr that I calculated for Chapter 2 is inconsistent with the age returned by the Grid Search. From the evolutionary track I derived an extremely short remaining lifetime of 0.006 Gyr, implying that the planet is currently spiralling in towards its host and is on the verge of reaching the Roche limit. This seems incredibly short, and would mean that somehow WASP-18 b has been observed during a very short window of opportunity. This result is, however, at odds with the results that I obtained from my second integration method, the MCMC algorithm.

The posterior probability distributions produced by the MCMC integration scheme (Fig. 4.4)

indicate significant correlation between many of the pairs of initial orbital parameters, in particular a_0 and $\log(Q'_s)$ although it is also noticeable in several of the other distributions. Some correlation is to be expected; the orbital circularisation time-scale depends on energy dissipation within both the star and the planet (Miralda-Escudé, 2002), and so a correlation between the eccentricity and the quality factors that govern tidal energy dissipation is unsurprising. The correlation between a_0 and e_0 may arise as a result of the strong coupling between eccentricity and separation noted by Jackson et al. (2008b). The rapidity with which the orbital separation can decrease is intrinsically linked to the efficiency with which energy is dissipated within the system, a process that is governed by the tidal quality factors. Moreover, inspection of equation (4.12) indicates that $\dot{a} \propto Q^{-1}$, so the form of the correlation between a_0 and $\log(Q'_s)$ that is observed is also as expected. In fact it is surprising that little to no correlation is observed between a_0 and $\log(Q'_p)$

The best-fitting parameters found using the MCMC code are set out in Table 4.2, and imply a stellar age of $0.579^{+0.305}_{-0.250}$ Gyr, in agreement with all of the stellar model fitting age estimates previously derived for the system. Fig. 4.5 displays the evolution of the stellar rotation for the set of best-fitting parameters; it is important to recall that the age estimate is not evaluated solely on the basis of this parameter, and that the observed orbital eccentricity and semi-major axis play a part as well.

The value of $\log(Q'_s)$ returned by the MCMC-derived integration scheme does not agree with the best-fitting value obtained from the grid search of the defined parameter space. Nor do the values of a_0 and e_0. I attribute this to the adoption of the set of median parameters from the MCMC scheme to avoid chance encounters with local minima, as well as the discrete nature of the grid search. Comparison of the solution with the lowest value of the C test statistic shows a value of $\log(Q'_s)$ that fits more closely to the grid search result, albeit still in disagreement, although I note that the minimum test statistic value for the grid search is an order of magnitude lower than that for the MCMC exploration of the available parameter space. It is also worth noting that although Figs. 4.3 and 4.4 are broadly similar in form, they differ somewhat in detail. The same correlations between parameters are visible in both figures, but the cutoff in $\log(Q'_s)$ occurs at a slightly greater value in Fig.4.4 than Fig. 4.3. Additionally, the MCMC algorithm explores a narrower range of both a_0 and e_0 parameter space than the grid search, but does explore the lower end of $\log(Q'_p)$ space, a region which the grid search suggests gives poor results. Again, this is probably attributable to the differences

Table 4.2: *The initial orbital parameters and tidal quality factors of the best-fitting tidal evolution histories produced by the grid search and MCMC integration schemes for the WASP-18 system. The* 1σ *error bars for the MCMC derived values are estimated from the parameter values that encompass the central* 68.3 *percent of the final parameter distributions, and in some cases are inflated by the presence of short 'tails' in the distributions.*

Parameter	Units	Grid search	MCMC
a_0	AU	0.0427	$0.0258^{+0.0052}_{-0.0044}$
e_0		0.245	$0.0399^{+0.1023}_{-0.0351}$
$\log(Q'_s)$		7.00	$8.21^{+0.90}_{-0.52}$
$\log(Q'_p)$		7.50	$7.77^{+1.54}_{-1.25}$
age	Gyr	0.654	$0.579^{+0.305}_{-0.250}$
t_{remain}	Gyr	0.006	$0.076^{+0.790}_{-0.044}$

in the manner in which the two algorithms explore the delineated parameter space.

Using equation (4.13) with the data from Table 4.2 and the best-fitting value of $\log(Q'_s)$ from the MCMC scheme, I estimate that WASP-18 b will reach its Roche limit 0.086 Gyr from now. The evolutionary track produced using the MCMC results implies a remaining lifetime of < 0.818 Gyr for the planet, consistent with this value. These are, respectively, 2.40 and < 22.84 percent of the expected main-sequence lifetime of the host star, which I estimate to be 3.58 Gyr. These remaining lifetimes suggest that the WASP-18 planetary system might have a short life expectancy, as found by Hellier et al. (2009). Although potentially quite short, these values are far more reasonable than the value of 6 Myr derived from the grid search.

The evolution of the stellar rotation period (Fig. 4.5) for the set of initial parameters returned by the MCMC integration scheme indicates that the rotational evolution of the star under the influence of tides initially differs little from my simulation in which the rotation period is governed purely by a Skumanich-type magnetic braking law. However the evolution of the rotation period rapidly diverges from this ideal case, with the rate of spin-down slowing gradually as the star ages and the planet migrates towards its host under the influence of tidal interactions. The final spiral-in of the planetary companion causes a rapid and substantial spin-up of the star; during this process the stellar rotation period is reduced by almost a factor of two from its maximum 6.26 day period to 3.16 days at the Roche limit, suggesting significant spin up of the host star. Furthermore, Fig. 4.5 clearly shows that, for the age estimate returned by my MCMC integration scheme, the observed rotation period of the host star is

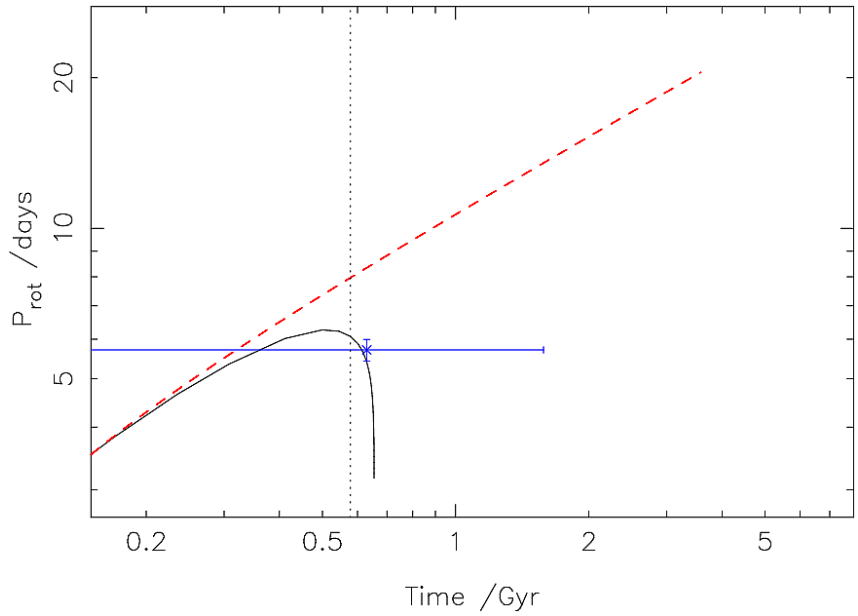

Figure 4.5: *The evolution of the rotation period of WASP-18 from the best-fitting initial conditions found by the MCMC exploration of the allowed parameter space (black, solid line), along with the evolution that would occur in the absence of tidal interactions (red, dashed line). For reference, the observed parameters are plotted with associated errors, and the best-fitting age given by the MCMC integration scheme is denoted (black, dotted line). The tide-governed evolution diverges from the ideal rotational evolution early on, with the effect of tidal interactions on the the rotation of the host star increasing with time until the rotation period dramatically decreases during the final spiral-in of the planetary body.*

inconsistent with the rotation period of 7.96 days that would be expected at the same age if tidal interactions played no part in the evolution of stellar rotation.

Although the best-fitting parameters that I have adopted imply that WASP-18 b is in the process of its final spiral in, the true picture is slightly more ambiguous, as evidenced by the large upper uncertainty on the remaining lifetime. Within the 1σ parameter ranges there exist combinations of the initial parameters that produce evolutionary tracks of a different form to that displayed in Fig. 4.5. These evolutionary tracks follow the stellar rotation curve produced by a purely magnetic braking scenario for a much longer period of time, and exhibit little spin up of the host star. Furthermore, in semi-major axis space they indicate that the planet stays at approximately the same semi-major axis for the duration of the star's main-sequence lifetime. In these cases the age of the system lies towards the lower end of the adopted range, owing to the necessity of conforming to the calculated stellar rotation period, and the planet has a long remaining lifetime. Note however that these solutions form only a minority of the evolutionary tracks consistent with the parameter ranges that I adopt from the MCMC results. More prevalent were tracks of the same form as that displayed in Fig. 4.5, but with the spin-up taking place much later such that the stellar rotation implies an age consistent with the

gyrochronological estimate and magnetic-braking only scenario.

I attempted to further constrain the range of possible tidal quality factors by visually fitting to the observed parameters and their associated 1σ uncertainties. Starting from the best-fitting initial orbital separation and eccentricity, I investigated the evolution of the system across the range of values for both $\log(Q'_s)$ and $\log(Q'_p)$. I found that changing the value of $\log(Q'_p)$ made no difference to the evolution of the orbital separation or rotation period, but had a strong effect on the eccentricity evolution of the planetary orbit. $\log(Q'_s)$, in contrast, strongly affected the evolution of all integration parameters. Moreover I found that changing the initial semi-major axis, within the adopted range, made a significant difference to the evolution of the stellar rotation period, whilst modifying e_0 merely affected the evolution of the orbital eccentricity. I therefore conclude that the two most important parameters with respect to the stellar rotation are Q'_s and a_0. Hansen (2012) agrees with this, noting that in the case of WASP-18 the stellar tides appear to be particularly important, and that they could in fact have reversed the direction of stellar spin!

I was unable to constrain the permissible ranges of the two tidal quality factors any further, owing to the range of values that a_0 was able take, but found that for the majority of the possible combinations the rotational evolution of WASP-18 A gradually diverges from that expected of a purely magnetic braking scenario, and that the star is eventually spun-up by a substantial amount during the final in-spiral of its planetary companion. Fig. 4.6 shows the rotational period evolution resulting from several values of $\log(Q'_s)$ within the permissible range, with $\log(Q'_p)$, a_0, and e_0 set to values adopted from the MCMC search.

4.4 The WASP-19 system

The transiting hot Jupiter WASP-19 b orbits a late G-dwarf star with an orbital period of 0.7888399 ± 0.0000008 days. The host star has been measured to have $T_{\rm eff} = 5500 \pm 100$ K, periodic sinusoidal flux variations that indicate a detectable level of intrinsic variability and activity, and a metallicity slightly greater than solar at $[\mathrm{M/H}] = 0.1 \pm 0.1$ dex (Hebb et al., 2010). Measurements of the Rossiter-McLaughlin angle for the system, which have yielded $\lambda = 4.6 \pm 5.2\,^\circ$ (Hellier et al., 2011) and $\lambda = 15 \pm 11\,^\circ$ (Albrecht et al., 2012b), indicate that the system is generally well-aligned.

The age of the system is still somewhat uncertain, with Hebb et al. (2010) only able to

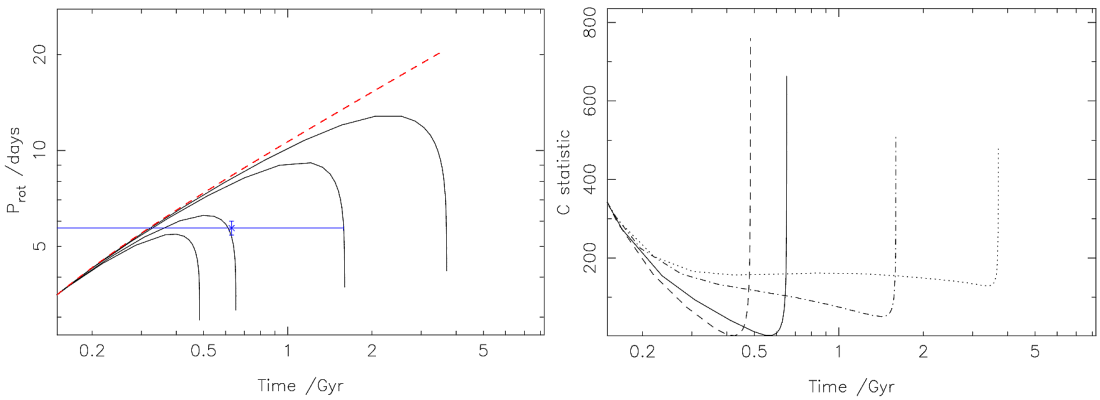

Figure 4.6: *Evolutionary tracks for WASP-18 produced using several different values of* $\log(Q'_s)$ *within the range consistent with the observed system parameters. The tracks were calculated using the values of* e_0, a_0 *and* $\log(Q'_p)$ *adopted from the MCMC solution and, from left to right (at the end of the track):* $\log(Q'_s) = 8.02$, $\log(Q'_s) = 8.21$, $\log(Q'_s) = 8.70$ *and* $\log(Q'_s) = 9.11$. ***Left:*** *The evolution of stellar rotation period with time for WASP-18. The dashed line shows the evolution expected from a Skumanich-type magnetic braking law. Changing the value of* Q'_p *has no effect on the evolution of the rotation period with time.* ***Right:*** *The evolution of the C test statistic with time for the tracks in the upper panel. The time at which C is a minimum is taken to be the age of the system given the set of initial parameters used for that evolutionary track.*

determine a constraint of > 1.0 Gyr. Several studies (e.g. Hansen (2010); Weidner & Horne (2010)), as well as the exoplanet encyclopedia[2], cite an age of 0.6 ± 0.5 Gyr for the star and attribute it to Hebb et al.. I believe that this originates from the abstract of Hebb et al. which quotes that age as one of two possibilities. However the text of that paper favours the older age constraint. For my analysis I used an age of $t_{age} = 5.5 \pm 4.5$ Gyr, consistent with the isochronal fit and lower bound on the age quoted by Hebb et al., as well as my own isochronal analysis of the system which suggests a much older age for the system (this estimate is consistent with the lower bound on my isochronal estimates; see Appendix A), and set $\alpha_p = \alpha_{\rm Jup} = 0.26401$. Comparing the stellar rotation period from Table 4.3 to the rotation period expected at the age of the Hyades, I found that $P_{{\rm rot},s} > P_{\rm rot,Hyades} = 8.60$ days and thus set $t_0 = t_{\rm Hyades}$ and $\Omega_{s,0} = \Omega_{s,\rm Hyades}$.

Fig. 4.7 shows the C-statistic probability density projection maps produced from the grid search results for the WASP-19 system. They indicate a fairly small region of high probability for $\log(Q'_s)$ and $\log(Q'_p)$, but appear to show that there are broader ranges of both e_0 and a_0 that give strong solutions. The absolute maximum probability, and thus the minimum value of the C statistic, was found to occur when the initial conditions were $a_0 = 0.0939$ AU, $e_0 = 0.735$, $\log(Q'_s) = 6.25$ and $\log(Q'_p) = 10.0$, giving a system age of 2.11 Gyr that is

[2]www.exoplanet.eu

Table 4.3: *System parameters and 1σ limits for WASP-19, taken from the free eccentricity fit of Anderson et al. (2013) with the exceptions of the J-K colour which is derived from data taken from SIMBAD, the age which is taken from Hebb et al. (2010), and the rotation period (Collier Cameron,* priv. comm.*).*

Parameter	Value	Units
M_s	0.969 ± 0.023	$M_\odot$
R_s	0.993 ± 0.018	$R_\odot$
$J - K$	0.43	
$T_{\rm eff}$	5475 ± 98	K
$v \sin I$	4.63 ± 0.27	$\mathrm{km\,s^{-1}}$
P_{rot}	10.5 ± 0.2	days
System age	$5.5^{+9.0}_{-4.5}$	Gyr
M_p	1.165 ± 0.023	$M_{\rm Jup}$
R_p	1.383 ± 0.031	$R_{\rm Jup}$
a	0.01653 ± 0.00013	AU
e	$0.0019^{+0.0055}_{-0.0015}$	
i	79.42 ± 0.39	
$P_{\rm orb}$	$0.78883951 \pm 0.00000032$	days

consistent with the existing literature constraint of > 1.0 Gyr from Hebb et al. (2010), but which is younger than the ages that I obtained using stellar model fitting. Using the period-colour relation of Collier Cameron et al. (2009) I calculated a gyrochronological system age of 0.86 ± 0.03 Gyr (see Table A.2), immediately suggesting that gyrochronological analysis is inappropriate for this system.

Comparing the sets of projection maps for the two systems, it is apparent that there are similarities in the forms of Figs. 4.3 and 4.7, particularly in the $a_0 - \log(Q'_s)$ and $e_0 - a_0$ maps. However the range of probability values covered by the greyscale is slightly narrower for WASP-19, where the maximum probability is approximately 0.8, compared to WASP-18, where the maximum probability is almost 1.0. From this I deduce that the best-fitting orbital solution for WASP-19 is less certain than my best-fitting grid search solution for WASP-18. This lower maximum probability, coupled with the form of the projection maps, also suggests that the range of tidal quality factors for which valid orbital solutions exist is greater for this system than it was for WASP-18.

The posterior probability distributions produced by the MCMC algorithm exhibit a strong correlation between a_0 and $\log(Q'_s)$, of a similar form to that observed for the WASP-18 system albeit extended to lower values of $\log(Q'_s)$. Also present is a correlation between e_0 and a_0

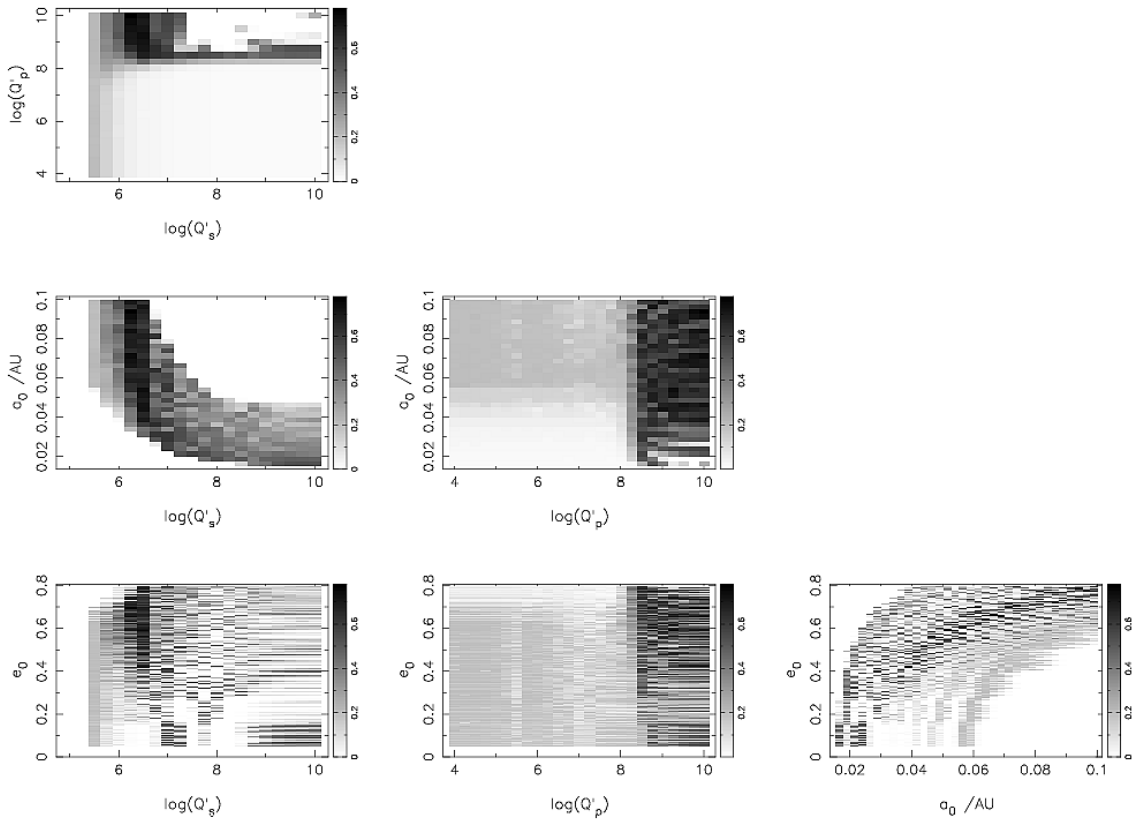

Figure 4.7: *C-statistic probability density projection maps for WASP-19. A small region of high probability is clearly visible in* $\log(Q'_s)$ *and* $\log(Q'_p)$ *parameter space, but in* a_0 *and* e_0 *the range of values that give high probability solutions are much broader. The point of maximum probability, indicating the minimum in the C-statistic surface, was found to occur at parameter space coordinates of* $a_0 = 0.0939\,AU$, $e_0 = 0.735$, $\log(Q'_s) = 6.25$ *and* $\log(Q'_p) = 10.0$, *giving a system age of* $2.11\,Gyr$.

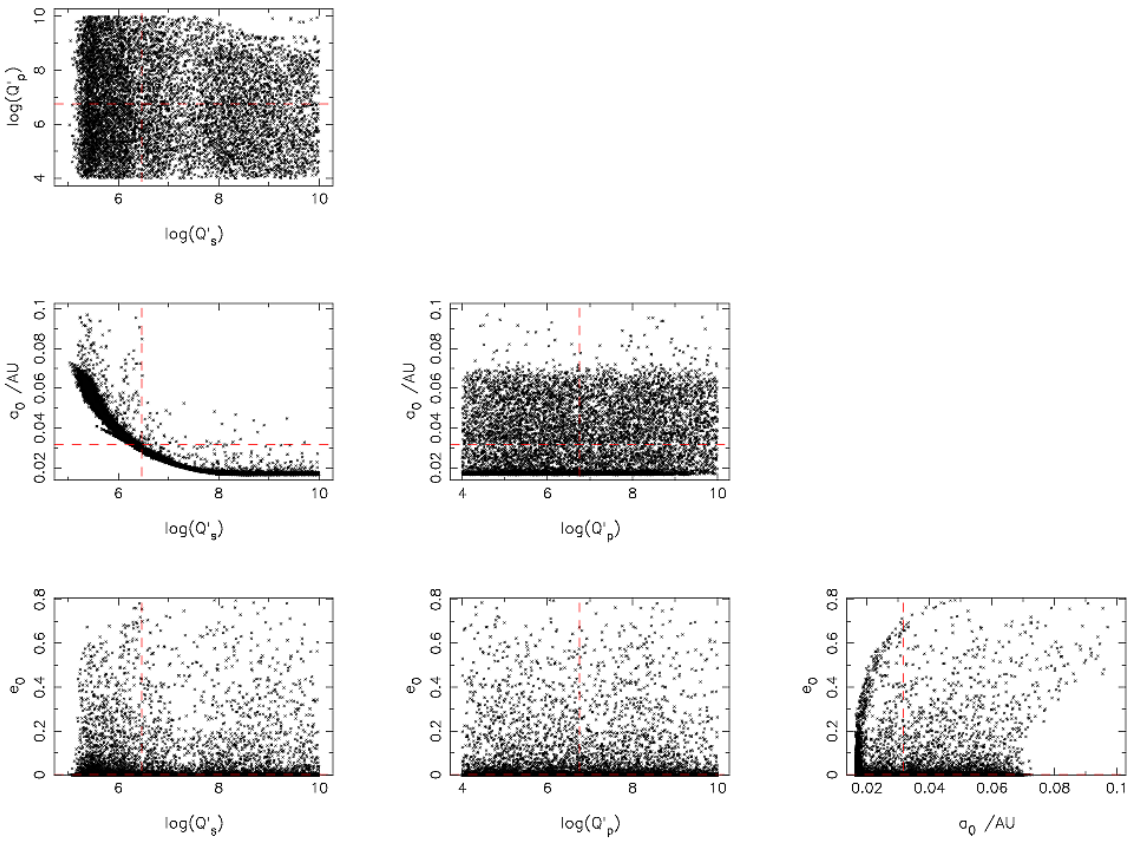

Figure 4.8: *The posterior probability distributions of each pair of integration parameters produced by the MCMC analysis of the WASP-19 system. The correlations between the parameters are substantially different than those for the WASP-18 system, with that between* $\log(Q'_s)$ *and* a_0 *being the only particularly noticeable correlation. The location of the best-fitting parameters are denoted by the dashed lines.*

that is somewhat similar to that apparent in Fig. 4.4, but the other correlations that were present in the distributions for WASP-18 are absent for WASP-19. The region of parameter space explored by the MCMC algorithm is also substantially greater for the WASP-19 system than it was for the WASP-18 system, although this is not unexpected after the comparative appearance of Figs. 4.3 and 4.7.

It is also interesting to note the relative lack of agreement between the results from the grid search and the MCMC search methods for this system; the only search parameter for which the two sets of results agree is $\log(Q'_s)$. This is also apparent from inspection of Figs 4.7 and 4.8, as the region of greatest probability in the former does not match the location of the adopted parameters in the latter. As for the WASP-18 system, I attribute this to the adoption of the set of median parameters from the MCMC scheme; comparison of the solution with the lowest value of the C test statistic shows that it more closely fits with the location of the high probability region in Fig. 4.7. Fortunately the stellar tidal quality factor, the most important parameter when considering the evolution of the stellar rotation, is relatively well constrained in my MCMC-derived solution.

The probability distribution for the initial orbital eccentricity of the WASP-19 system also shows weaker clustering than for the WASP-18 system, and the clustering that is present encompasses a much smaller range of eccentricity values above $e_0 = 0$. This may be symptomatic of the fact that the eccentricity of the system is not well known; previous analysis of the parameters of the system found little difference in the fit to the observed transit lightcurve between the cases in which the orbit was forced to be circular, and in which the eccentricity was allowed to float (Hebb et al., 2010). In the latter case, the best-fitting eccentricity value was only $0.02^{+0.02}_{-0.01}$, and it is this value that I used in my calculation of the C statistic.

The best-fitting parameters given by the MCMC integration scheme, set out in Table 4.4, imply a stellar age of $1.60^{+2.84}_{-0.79}$ Gyr, in broad agreement with the loose constraint of age $>$ 1.0 Gyr found by Hebb et al. (2010). The gyrochronological age that I calculated for the system also agrees with this age estimate but lies at the lower end of the range, suggesting that gyrochronology provides a possible, if unlikely estimate for the age of WASP-19 A. The data in Table 4.4 further imply a remaining lifetime for the planet of < 1.114 Gyr. One possibility allowed by this is that WASP-19 b is in the final, spiral-in stage of its orbital evolution, a conclusion seemingly supported by the stellar rotation period evolutionary track that results from

Table 4.4: *The initial orbital parameters and tidal quality factors of the best-fitting tidal evolution histories produced by the grid search and MCMC integration schemes for the WASP-19 system. The* 1σ *error bars for the MCMC derived values are estimated from the parameter values that encompass the central* 68.3 *percent of the final parameter distributions.*

Parameter	Grid search	MCMC	Updated	Units
a_0	0.0939	$0.0317^{+0.0228}_{-0.0146}$	$0.0317^{+0.0228}_{-0.0089}$	AU
e_0	0.735	$0.0017^{+0.0597}_{-0.0016}$		
$\log(Q'_s)$	6.25	$6.47^{+2.19}_{-0.95}$	$6.47^{+0.67}_{-0.95}$	
$\log(Q'_p)$	10.0	$6.75^{+1.86}_{-1.77}$		
age	2.11	$1.60^{+2.84}_{-0.79}$		Gyr
$t_{\rm remain}$	0.0038	$0.0067^{+1.1073}_{-0.0061}$		Gyr

integration of the best-fitting parameters (Fig. 4.9). As with the WASP-18 system I attempted to further constrain the range of possible tidal quality factors by visually fitting to the observed parameters; in this case I was able to reduce the upper limit on $\log(Q'_s)$ and raise the lower limit on a_0 (these are accounted for in Table 4.4). Updating the limits on these parameters had no effect on the 1σ limits of the age or remaining lifetime.

The observed spin rate of WASP-19 is inconsistent with evolution governed only by magnetic braking; Fig. 4.9 shows that, at the system age implied by my MCMC solution, the observed period of 10.5 ± 0.2 days is substantially less than the period of 15.9 days implied by the magnetic braking only model. It is possible that WASP-19 b is in the process of spiralling-in to the Roche limit, spinning up its host as it does so.

Fig. 4.10 shows the rotational period evolution resulting from $\log(Q'_s)$ values within the 1σ limits returned by the MCMC search scheme. These are consistent with the idea that WASP-19 b might be approaching its Roche limit; for the best-fitting tidal quality factors the end of the evolutionary track is at $P_{\rm rot} = 10.5$ days compared to the observed $P_{\rm rot} = 10.5 \pm 0.2$ day, placing the planet precisely on the Roche limit and suggesting that the WASP project has been fortunate to observe the planet at all.

Much as with the WASP-18 system though, this is not the entire picture presented by my results. I have only been able to obtain an upper limit on $t_{\rm remain}$, the value of which represents a significant 69.6 percent of the estimated age, and 13.7 percent of the MS lifetime of the host star. As well as the possibilities already discussed, there must therefore also exist solutions that more closely follow the stellar rotation evolution expected when only magnetic braking

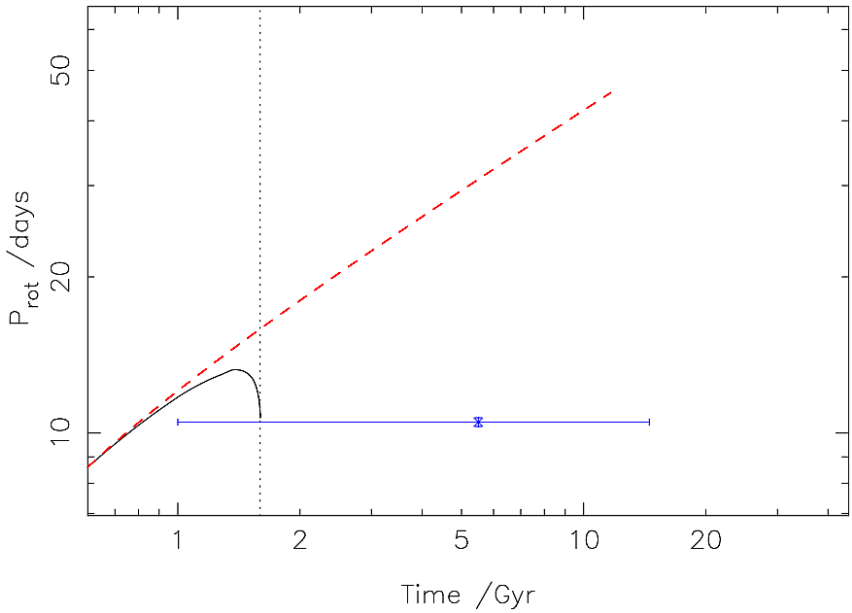

Figure 4.9: *The evolution of the rotation period of WASP-19 from the best-fitting initial conditions found by the MCMC exploration of the allowed parameter space (black, solid line), along with the evolution that would occur in the absence of tidal interactions (red, dashed line). The tide-governed evolution follows the gradual spin-down of the isolated evolution closely until spiral-in of the planet begins, at which point the stellar rotation period rapidly decreases. The observed rotation period is plotted with associated errors, and implies that WASP-19 b is in the final spiral-in stage of its orbital evolution. Furthermore it is irreconcilable with the expected spin down from magnetic braking alone, and can only be explained by invoking spin-up during tidal interactions.*

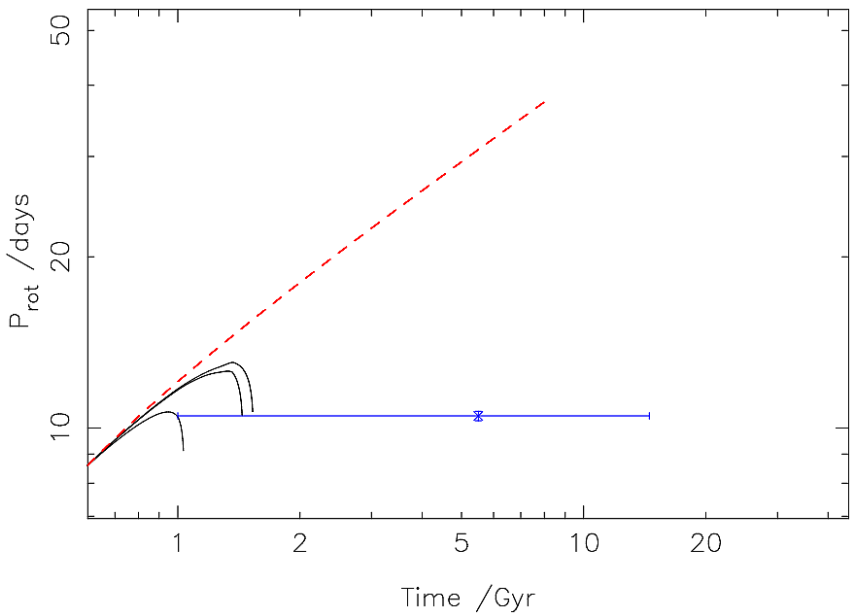

Figure 4.10: *The evolution of stellar rotation period with time for WASP-19 for a range of* $\log(Q'_s)$ *values. The dashed line shows the evolution expected from a Skumanich-type magnetic braking law, whilst the three solid lines are the evolution that results from the best-fitting* e_0, a_0 *and* $\log(Q'_p)$ *given by the MCMC algorithm, and, from left to right (at the observed system age),* $\log(Q'_s) = 6.14$, $\log(Q'_s) = 6.47$ *and* $\log(Q'_s) = 6.52$. *These tracks imply that WASP-19 b is very close to the Roche limit, and will reach it in less than 10 Myr.*

is acting on the star. To investigate this I characterised the orbital evolutionary tracks for each $\log(Q'_s) - a_0$ node from the grid search that was consistent with my results from the MCMC algorithm. Since my investigation into WASP-18 b's future evolution led me to the conclusion that e_0 and $\log(Q'_p)$ have little effect on the evolution of the stellar rotation, I set these parameters to the MCMC values from Table 4.4.

I found that for each value of a_0 there was only a very narrow range of $\log(Q'_s)$ values that gave solutions with an age ≥ 1.0 Gyr *and* a rotation period at that age consistent with the observed value. In fact only 13 percent of the nodes investigated gave such solutions. The majority of the nodes gave solutions that either did not reach an age of 1.0 Gyr, instead showing the distinctive spiral-in signature at younger ages, or that followed the magnetic braking-only track for much longer such that the spin-up induced by the final spiral-in was insufficient to reduce the stellar rotation period back to the observed value. Tracks that fell into this latter category often returned ages consistent with the gyrochronological calculation, although some did return older ages consistent with the 1.0 Gyr lower limit owing to the influence of the orbital eccentricity and semi-major axis.

This raises questions concerning WASP-19 A's true age. The evidence from isochrone fitting (see Appendix A) implies that the star is much, much older than 1 Gyr. This is supported by the investigation of Hebb et al. (2010) into the space velocity of the star, which found that 65 percent of simulated stars with similar stellar properties in a small volume around WASP-19 A were older than 1.0 Gyr. But the rotation period of WASP-19 A implies a younger age of 0.86 ± 0.03 Gyr through gyrochronology. The lithium abundance of $\log(A[Li]) < 1.0$ quoted by Hebb et al. is consistent with either estimate as it only constrains the age to greater than 0.6 Gyr. There therefore appear to be two main possibilities; either the star is old and has been spun up by the infall of the planet, or the star is younger, still following its natural spin down and more dense and/or hotter than expected for its age. Both of these are consistent with the results that I obtained from the two search methods, so which is the more plausible?

4.4.1 Is W19 young or old?

I decided to consider my results for WASP-19 in the context of a larger ensemble of planetary systems with similar stellar and planetary properties, assuming that the value of $\log(Q'_s) = 6.47$ adopted for WASP-19 is applicable to the other systems under consideration. I found that for 7 of the 9 planetary systems in the sample (see Table 4.5) the projected remaining

Table 4.5: *A comparison of the WASP-19 system to a sample of transiting hot Jupiter systems with $M_p > M_{\rm Jup}$ in close orbits around stars similar to, or cooler than, WASP-19 A. I calculate the remaining lifetime for each planet using equation 4.13, assuming that the stellar tidal quality factor of $\log(Q'_s) = 6.47$ adopted for WASP-19 A is applicable across the entire sample. Note that the remaining lifetime for WASP-19 b quoted here does not agree with the value derived from the evolutionary track displayed in Fig. 4.9.*

System	M_p /$M_{\rm Jup}$	R_p /$R_{\rm Jup}$	M_s /$M_\odot$	R_s /$R_\odot$	a /AU	P /days	$t_{\rm remain}$ /Gyr	Age /Gyr
WASP-19	1.14	1.28	0.95	0.93	0.0164	0.7888399	0.012	$1.60^{+2.84}_{-0.79}$
WASP-2	0.847	1.079	0.84	0.834	0.03138	2.1522254	1.708	$11.9^{+8.1}_{-4.3}$ [a]
WASP-4	1.12	1.416	0.93	1.365	0.023	1.3382282	0.017	$7.0^{+5.2}_{-4.5}$ [a]
WASP-5	1.63	1.171	1.00	1.15	0.02729	1.6284246	0.080	3.0 ± 1.4 [b]
WASP-10	3.06	1.08	0.71	0.783	0.0371	3.0927616	1.818	0.8 ± 0.2 [c]
CoRoT-1	1.03	1.49	0.95	1.11	0.0254	1.5089557	0.093	
CoRoT-2	3.31	1.465	0.97	0.902	0.0281	1.7429964	0.159	
OGLE-TR-113	1.24	1.11	0.78	0.77	0.0229	1.4324772	0.224	> 0.7 [d]
TrES-3	1.91	1.305	0.92	0.813	0.0226	1.30618608	0.111	$0.1^{+0.7}_{-0.0}$ [a]

(a)Southworth (2010) (b)Anderson et al. (2008) (c)Christian et al. (2009)
(d)Melo et al. (2006)

lifetime is < 1 Gyr. Furthermore I found that WASP-4 b has a remaining lifetime of 0.017 Gyr, and calculated that it lies at a distance of only 1.4 times the Roche limit from its host star; this places it in apparently similar circumstances to WASP-19 b. WASP-2 b and WASP-10 b have remaining lifetimes at least one order of magnitude greater than those of the rest of the sample, but they also have significantly longer orbital periods.

It is interesting to consider the range of the stellar tidal quality factor that produces certain threshold values of $t_{\rm remain}$. I found that if I excluded the longer period WASP-2 and WASP-10 systems, $\log(Q'_s) > 7.10$ leads to an estimated $t_{\rm remain} \geq 1.0$ Gyr for all planets in the sample, whilst a remaining lifetime greater than 0.1 Gyr requires $\log(Q'_s) > 6.12$. For WASPs -2 b and -10 b I found that the values required were 6.24 and 5.24, and 6.22 and 5.22 respectively.

The tidal evolution solution that I presented previously would seem to support the hypothesis that the star is old, with stellar spin up accounting for the rotation period. But the results in Table 4.5 would seem to add weight to the idea that the system is actually younger than expected. The likelihood of observing one system in such a condition is low, but to observe two such systems as Table 4.5 implies has been done with WASPs -4 and -19, seems incredulous.

Considering the remaining lifetimes in the context of the total planetary lifetime suggests a different scenario. Equation (4.13) can also be used to calculate the total planetary lifetime

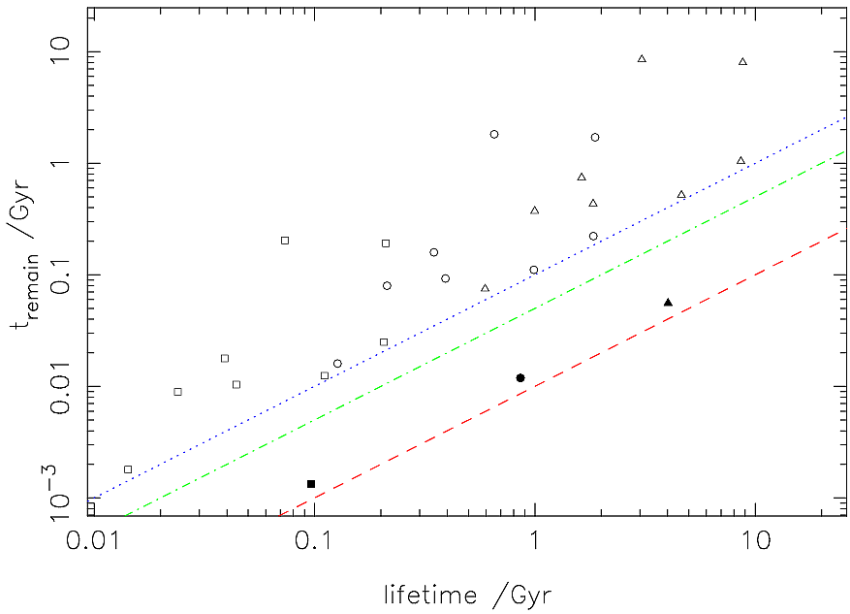

Figure 4.11: *Remaining lifetime as a function of total planetary lifetime for the sample of transiting planets in Table 4.5, as calculated using 4.13 assuming that the values of* $\log(Q'_s)$ *and* a_0 *adopted for the WASP-19 system from my MCMC results apply universally. Displayed are the results for* $\log(Q'_s) = 5.52$ *(squares),* $\log(Q'_s) = 6.47$ *(circles) and* $\log(Q'_s) = 7.14$ *(triangles). The data for WASP-19 b are denoted by filled symbols. The lines represent* $t_{\rm remain} = 1$ *percent (red, dash),* 5 *percent (green, dot-dash) and* 10 *percent (dark blue, dot) of the total planetary lifetime. WASP-19 b is clearly separate from the rest of the sample, indicating that it is in a unique situation.*

if the initial semi-major axis is known. I calculated the total planetary lifetimes assuming that the value adopted for WASP-19 b, $a_0 = 0.0317$ AU applied unilaterally across the sample of hot Jupiters, and in Fig. 4.11 remaining lifetime is plotted as a function of total lifetime. It is immediately apparent that WASP-19 b is a special case, being clearly separated from the rest of the sample. The remaining lifetime of WASP-19 b is only between 1 and 2 percent of the total lifetime, whilst for all of the other planets in the sample this figure is greater than 10 percent. The short remaining lifetime of WASP-4 b is thus somewhat misleading, as it represents a significant portion (≈ 12.6 percent) of the total lifetime of the planet.

There are several ways in which the remaining lifetimes calculated here can be analysed, one of which is to examine the probability that the system has actually been observed in its present configuration. I calculated this for the systems in Table 4.5, disregarding those with no literature age estimate. For WASP-19 I calculated the probability using both my own adopted age estimate of 5.5 ± 0.45 Gyr, and the younger age of 0.6 ± 0.5 that can be found in the literature. Fig. 4.12 displays the results for a range of $\log(Q'_s)$ values consistent with the 1σ limits derived from the MCMC posterior probability distributions. For the value of $\log(Q'_s)$ adopted from the MCMC solution I found that two systems, including WASP-19 at my older

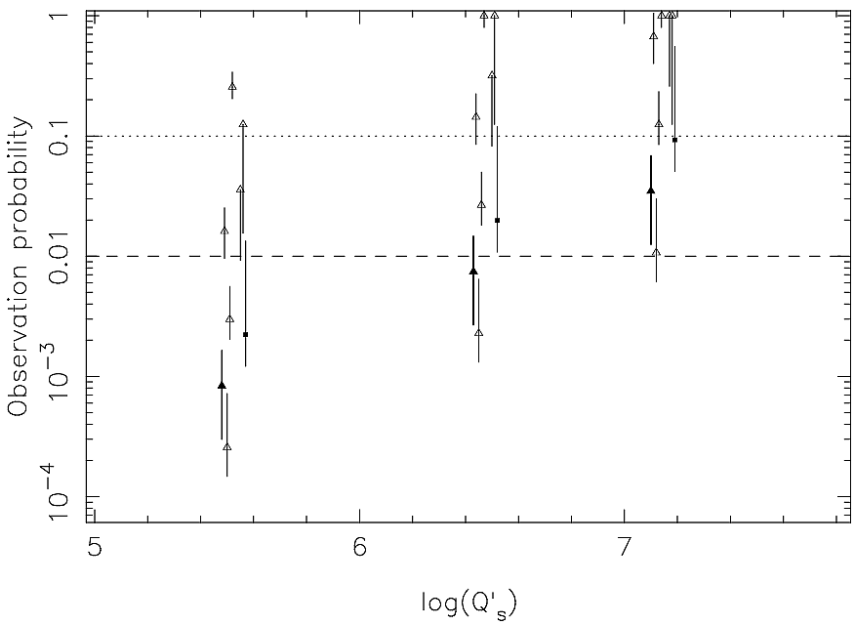

Figure 4.12: *The probability of observing the systems in Table 4.5 in their present configuration, as a function of* $\log(Q'_s)$ *within the range encompassed by the* 1σ *errors from the MCMC results. Systems without a stellar age in the literature were disregarded. The data are offset slightly from the true value of* $\log(Q'_s)$ *to aid clarity for the error bars. Systems for which* $P > 1$ *are plotted at* $P = 1$*. WASP-19 is denoted by filled symbols; triangles for the probability using the age estimate from the MCMC results, squares for the probability calculated using the estimate of* 0.6 ± 0.5 *Gyr prevalent in the literature. At* $\log(Q'_s) = 6.47$ *two systems, including WASP-19 with its older age, show a probability of observation that is less than 1 percent. Increasing the stellar tidal quality factor increases the probability that I have observed the systems in the state implied by their remaining lifetimes.*

age estimate, have a probability of observation of less than 1 percent. Using the younger age estimate for WASP-19 pushes the probability up to 2 percent, which is more plausible (see analysis in Hellier et al. 2011). Increasing the value of $\log(Q'_s)$ to my upper limit of 7.14 increases the probability of observing WASP-19 b to approximately 3.5 percent for the older age, and approximately 9 percent for the younger age. If the lower limit of $\log(Q'_s) = 5.52$ is considered then four systems, including both ages of WASP-19, have observation probabilities less than 1 percent. This is an entirely implausible situation.

However this analysis assumes that all of the planets in my chosen sample started at the same distance from their respective host stars, and that they experience tidal interactions of the same strength. It seems somewhat unlikely that this accurately represents reality, as the planetary systems in the sample show significant variation in their properties. Previous studies (Matsumura et al., 2010; Hansen, 2010) have found that different planetary systems are likely to experience different strengths of stellar and planetary tide, so describing these systems with a single value is almost certainly unphysical. This would, of course, mean that the observational probabilities for several of these hot Jupiters could be significantly greater.

To further muddy the waters, the isochronal fits presented in Table A.1 add further evidence for an old age for the star. Investigating the values of $T_{\rm eff}$ and ρ_s required for a stellar age of 0.6 ± 0.5 Gyr in the Padova and YY models, assuming the same metallicity. The results are given in Table 4.6; it proved very difficult to reach such a low age. The correction required to the effective temperature if the stellar density is correct is not improbable, but the converse is not necessarily true. Modifying the stellar density by the amount that my results indicate is required would mean a large change to either the stellar mass or radius, or both, either of which would have a dramatic effect on my estimates of the planetary parameters. This is notwithstanding the more likely case, which is that both the temperature and density are in need of an adjustment.

For completeness I attempted to force an age of 0.6 Gyr by adjusting the stellar metallicity, whilst leaving the effective temperature and stellar density at the values from Hebb et al. (2010). I found that the upper limit of $Z = 0.03$ imposed on the Padova isochrones prevented me from reaching such a low age, leaving a lowest estimate of $6.15^{+3.47}_{-1.75}$ Gyr which could be consistent with a star of the age of the Hyades. When fitting to the Yonsei-Yale isochrones I found that a value of $[Fe/H] = 0.70$ gave an age of $3.06^{+2.54}_{-1.40}$ Gyr, the lowest that I was able to achieve. Fitting to the 0.6 Gyr isochrone itself would require a much greater metallicity, but given that this value of the iron abundance is already 0.43 dex greater than the maximum elemental abundance found by Hebb et al. (2010) (specifically the upper 1σ limit on the Calcium abundance), it is clear that such a fit would be utterly inconsistent with the current spectral analysis.

It therefore seems that a combination of increased elemental iron abundance, greater stellar density and higher effective temperature *could* produce stellar model fits more consistent with the young stellar age suggested by gyrochronology. However even adjusting all three parameters in concert requires an increase in stellar density that is not supported by the currently fitted values, as well as much higher [Fe/H].

As noted previously, the constraint placed on the age of WASP-19 A by the lithium abundance has the potential to rule out the young stellar age, as the detection of a substantial lithium abundance in a stellar spectrum strongly implies a young age for the star. The original analysis in Hebb et al. (2010) utilised only 34 spectra from the CORALIE spectrograph (Queloz et al., 2000b), but thanks to an ongoing radial velocity observation program I now

Table 4.6: *The age estimates obtained through fitting the stellar parameters of WASP-19 A from Anderson et al. (2013) to stellar models. Adjusting the stellar density, effective temperature or iron abundance in isolation lowers the age that the model fit returns. Obtaining an age of* 0.6 *Gyr required the parameters to be increased beyond their* 1σ *limits when done in isolation. If adjusted as a set, the required age could be obtained with more plausible values.*

Model	$\rho_s/\rho_\odot$	$T_{\rm eff}$ /K	[Fe/H]	age /Gyr
Padova	0.990 ± 0.043	5475 ± 98	0.02	> 8.25
Padova	1.49 ± 0.05	5475 ± 98	0.02	< 3.45
Padova	0.990 ± 0.043	5950 ± 100	0.02	$0.67^{+1.64}_{-0.65}$
Padova	0.990 ± 0.043	5475 ± 98	0.2	$6.15^{+3.47}_{-1.75}$
Padova	1.28 ± 0.05	5575 ± 100	0.12	< 2.66
Yonsei-Yale	0.990 ± 0.043	5475 ± 98	0.02	$8.91^{+1.47}_{-0.92}$
Yonsei-Yale	1.60 ± 0.05	5475 ± 98	0.02	< 1.75
Yonsei-Yale	0.990 ± 0.043	6075 ± 98	0.02	< 1.48
Yonsei-Yale	0.990 ± 0.043	5475 ± 98	0.70	$3.06^{+2.54}_{-1.40}$
Yonsei-Yale	1.35 ± 0.05	5550 ± 100	0.15	< 1.48

have access to additional data on WASP-19 A. Since the publication of Hebb et al. (2010) a further 3 spectra have been taken using CORALIE, and 36 spectral measurements have been obtained using the HARPS high precision échelle spectrograph (Mayor et al., 2003). This latter set of individual spectra were co-added into a single spectrum with a higher signal-to-noise ratio, from which it was possible for Barry Smalley to improve the constraint on the lithium abundance. Hints of a lithium line were present but only at the level of the spectral noise, limiting the results to an upper limit of $\log(\epsilon_{Li}) < 0.5$. This allowed the placement of a lower limit on the age of WASP-19 A of 2.0 Gyr (Sestito & Randich, 2005), making an older age for the star more palatable.

The final piece of evidence to be considered is the proximity of WASP-19 b to the Roche limit. Using the observed system parameters and their associated uncertainties with the formulation of Eggleton (1983), I calculated that the Roche limit for WASP-19 b is at 0.0148 ± 0.0025 AU, in agreement with the observed orbital separation of $0.0164^{+0.005}_{-0.0006}$ AU. Hellier et al. (2011) place the planet slightly further from the star at 1.21 times the Roche tidal radius, but they use a different formulation for calculating the limit.

I conclude that the evidence is in favour of WASP-19 A being old. Whilst there is evidence for the star being young, it is more circumstantial than that which points to an older star. The upper limit on the lithium abundance and the results from stellar model fitting in particular

point towards an age in excess of 1.0 Gyr. If WASP-19 A is indeed old, then the exploration of tide-governed evolution presented herein suggests that WASP-19 b might be spiralling into the Roche limit, spinning up its host as it does so. During my exploration of possible evolutionary histories I found that those which returned a stellar age of > 1.0 Gyr tended to exhibit a very short remaining lifetime. There were, however, some histories that married an older age for the star to a long remaining lifetime for the planet, so I am unable to completely rule out that scenario.

4.5 Discussion

I have calculated an age for the WASP-18 system of $0.579^{+0.305}_{-0.250}$ Gyr, in agreement with the $0.630^{+0.950}_{-0.530}$ Gyr age found from stellar isochrones by Hellier et al. (2009). Using an MCMC algorithm I find tidal quality factors of $\log(Q'_s) = 8.21^{+0.90}_{-0.52}$ and $\log(Q'_p) = 7.77^{+1.54}_{-1.25}$. My results imply that WASP-18 b will reach the Roche limit in $0.076^{+0.790}_{-0.044}$ Gyr, and that in most cases it will cause its host to spin up as it does so. I am unable to place stronger constraints on the status of the system with respect to planetary infall owing to the range of evolutionary histories that I find to be compatible with its observed parameters, but a large number of the evolutionary tracks investigated imply that the planet is in the process of spiralling in to its host star. My results for the WASP-18 system seem roughly consistent with the work of Matsumura et al. (2010).

For the WASP-19 system I found tidal quality factors of $\log(Q'_s) = 6.47^{+0.67}_{-0.95}$ and $\log(Q'_p) = 6.75^{+1.86}_{-1.77}$. These values give a stellar age of $1.60^{+2.84}_{-0.79}$ Gyr, in agreement with the constraint of age ≥ 1.0 Gyr found by Hebb et al. (2010), and imply a remaining lifetime of $0.0067^{+1.1073}_{-0.0061}$ Gyr. I have investigated the possibility that WASP-19 A is younger than previously predicted, in line with the predictions of gyrochronology. After considering the evidence for both the old and young stellar age possibilities, I conclude that the older age is more probable based on a re-analysis of the spectral lithium abundance and updated stellar model fits. I therefore suggest that WASP-19 b could be in the final stages of its spiral-in stage, and on the verge of reaching the Roche limit. I found that this scenario was more prevalent amongst those evolutionary histories with a stellar age > 1.0 Gyr, but that there were some instances in which the older stellar age coincided with a substantial remaining planetary lifetime. I am therefore unable to rule out the possibility that it will be some time before the planet falls into the star.

Tidal interactions between these two hot Jupiters and their host stars will dramatically affect the evolution of the stellar rotation periods, counteracting and then reversing the spin-down that is expected from evolution according to a Skumanich-type magnetic braking law. The observed rotation periods are irreconcilable with such an evolution of the rotation period, and strongly suggest that falling in hot Jupiters cause their host stars to spin up during their inward, tidal interaction governed migration. It is worth noting that my results seem to point towards a more diverse range of stellar tidal dissipation strength than is commonly considered in the literature. The ranges of $\log(Q'_s)$ that I have attributed to the two systems investigated herein are slightly disparate, for which there may be several possible explanations. I turn to the work of Pinsonneault et al. (2001), which shows that the mass of the convective zone is a function of $T_{\rm eff}$, and therefore of spectral type. From their fig. 1, I note that the effective temperature of WASP-18 A lies close to the point at which the mass of the convective zone becomes negligible, implying a convective zone mass of $M_{\rm CZ} \approx 0.001\,{\rm M}_\odot$. WASP-19 A, with its much lower effective temperature, would have $M_{\rm CZ} \approx 0.030\,{\rm M}_\odot$. In my work I have assumed that the star rotates as a single body, but I have made no assumption about where the majority of tidal dissipation takes place. If this process occurs in the convective zone then the discrepancy in the masses, and therefore depths, of the convective zones of the two stars could provide an explanation for the disagreement as to the value of Q'_s, with a larger convective zone allowing for more efficient dissipation and hence a smaller quality factor.

This study also provides a further warning against using gyrochronology to estimate the ages of hot Jupiter host stars. Owing to the tidal spin-up of its host star by the in-falling planet, the age that I have found for the WASP-19 planetary system is greater than the age found using gyrochronology alone. The situation for the WASP-18 system is less clear cut, but there is no doubt that gyrochronology will not provide an accurate estimate of the system age at all points during its evolution. I therefore suggest that care should be taken when applying gyrochronology to hot Jupiter systems. The two systems studied herein are extreme examples of this class of planet, with extremely short orbital periods and very close orbits, but the incompatibility of gyrochronology with my results supports my findings from Chapter 2.

The substantially reduced rotation period that results from tidal spin-up may provide a means of detecting stars that have either been planet hosts in the past, or that have unseen planetary companions that are in the process of spiralling in to the Roche limit. Measurement of such an anomalous rotation period would provide a strong indication of the current or

previous existence of a hot Jupiter around that star. Searching for such systems could help to pinpoint targets for extra-solar planet searches, although Lanza (2010) found that the rotation period evolution of F- and G-type planet hosts does not differ substantially from similar stars without hot Jupiters. My results disagree with this conclusion, and it should be noted that the final spiral-in of the planet does not appear to have been considered by that study. An earlier study by Barnes (2001) similarly found that there was generally no difference in rotation between planet hosts and other solar-type stars, or even between planet hosts and the members of open clusters. However they did identify one system, τ Boo, with anomalously fast stellar rotation, suggesting that it might be due to tidal effects causing stellar spin-up.

4.6 Conclusion

In this Chapter I have carried out detailed modelling of the tidal interactions in two hot Jupiter systems: WASP-18 and WASP-19. By doing so I have been able to place limits on the the tidal dissipation strengths for both the planets and stars, and have characterised the evolutionary histories and futures of the two systems. In the next Chapter I will consider six more WASP hot Jupiter systems, and examine the alignment between the axes of their stellar spins and planetary orbits.

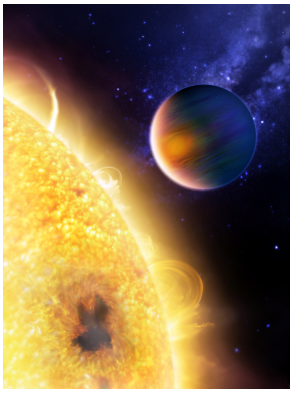

5

Spin-orbit alignment measurements for six WASP hot Jupiters

This chapter uses material from, and is based on, Brown et al. (2012), MNRAS, 423, 1503-1520 and Brown et al. (2012), ApJ, 760, 139

5.1 Introduction

The eight planets of the Solar system all orbit in roughly the same plane, the ecliptic. What is more, the ecliptic is fairly well aligned with the Solar equatorial plane, with the angle between them being a mere $7.155 \pm 0.002°$ (Beck & Giles, 2005). An alternative way of looking at the situation would be that the orbital axes for the Solar system planets are well aligned with the Sun's rotation axis. This commonly known as 'spin-orbit alignment'.

There is no guarantee, however, that this holds true for the orbits of extra-solar planets. It is known that binary stars can exhibit a range of angles between their mutual orbit and the

two spin axes (Hube & Couch, 1982; Company et al., 1988; Albrecht et al., 2007, 2009), but measuring the alignment angle, or 'obliquity', for an exoplanet is more difficult owing to the greater mass, radius, and luminosity ratios that are involved.

The first observation of the alignment angle for a transiting planet was made by Queloz et al. (2000a) for HD 209458 b. Since then the number of planetary systems with known spin-orbit alignment angles has steadily increased, with the majority having been measured through the Rossiter-McLaughlin effect.

5.1.1 Rossiter-McLaughlin effect

The most common method by which the alignment of an exoplanet's orbit is measured is the Rossiter-McLaughlin (RM) effect (Holt, 1893; Schlesinger, 1910, 1916; Rossiter, 1924; McLaughlin, 1924). This is a directly measurable effect, and is observable during planetary transits as a spectroscopic signature (see Figure 1.1).

Stellar rotation necessarily implies that the two limbs of the stellar disc have very different velocities along our line of sight. At one limb the stellar material has a velocity directly towards the observer along the line of sight (the approaching limb), whilst at the other the velocity is directly away (the receding limb). More generally, the two halves of the stellar disc can be considered as approaching and receding, with a dividing line along the stellar rotation axis at which the rotation velocity is entirely tangential to the line of sight.

During a transit, when the planet is in front of the approaching limb or hemisphere of the star it blocks some of the blue-shifted light from that region. This leads to a small net red-shift in the stellar spectrum. Similarly, when it is in front of the receding hemisphere, there is a small net blue-shift in the spectrum as some of the red-shifted light is eclipsed. The combination of these leads to a slight anomaly in the radial velocity (RV) sinusoid for the system, visible at the time of transit. The precise form of the RM anomaly depends on the impact parameter, b, the projected stellar rotation, $v \sin I$, and the projected alignment angle, λ (see Figure 5.1).

Despite the popularity of the RM effect, there are a growing number of systems for which λ has been measured using alternative means. In some cases this is out of necessity owing to limitations in the applicability of the RM effect, whilst in others it arises from a desire to expand the repertoire of analysis methods. Examples of the alternatives currently avail-

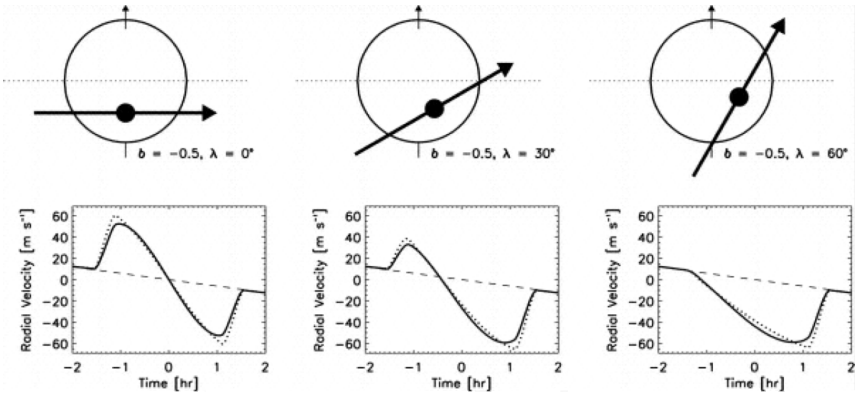

Figure 5.1: *An example of how changing the parameters and geometry of a planetary system can affect the form of the Rossiter-McLaughlin anomaly. In the first figure the transit is well-aligned, and the transit path has equal length across both hemispheres of the star. This leads to a symmetric anomaly. Increasing the tilt of the orbit relative to the rotation axis of the star changes the relative length of the transit chord for each hemisphere, leading to asymmetric signals. The dotted lines indicate the cases with no limb darkening. (figure 2 from Gaudi & Winn 2007)*

able include analysis of the effect of star spots on the photometric transit observations (e.g. Sanchis-Ojeda et al., 2011; Nutzman et al., 2011), consideration of the effect of gravity darkening (e.g. Barnes et al., 2011), comparison of the measured and predicted stellar $v \sin I$ (Schlaufman, 2010), measurement of the chromospheric RM effect in the Ca II H & K lines (Czesla et al., 2012), and Doppler tomography. All of these alternative methods are complementary to the RM approach, allowing as they do the study of systems with vastly different properties, and with which that method struggles to cope.

5.1.2 Doppler tomography

Doppler Tomography is one of the more established alternatives to the RM effect, and was first applied to the case of a transiting planet by Collier Cameron et al. (2010a). Rather than use the radial velocity measurements, this method takes the cross-correlation functions (CCFs) produced during data reduction, and models the changes in their morphology that occur during a transit.

The alignment of the system is analysed through a comparison of the in-transit instrumental line profile with a model of the average out-of-transit stellar line profile. This latter model is created by the convolution of a limb-darkened stellar rotation profile, a Gaussian representing the local intrinsic line profile, and a term corresponding to the effect on the line profile of the 'shadow' created as the planet transits its host star. This 'bump' is time-variable, and moves through the stellar line profile as the planet moves from transit ingress to transit egress. The precise trajectory of the bump is dictated by b, and λ, which together determine

the precise value for the stellar radial velocity beneath the planetary 'shadow' at any moment during the transit. This leads to a more accurate model of the spectroscopic transit signature than is provided by RM analysis.

This method is able to break the degeneracy between the sky-projected alignment angle and stellar rotation velocity in systems with low impact parameter. It is best suited to analysing hot, rapidly rotating exoplanet host stars, but can be applied to any system provided that the spectra have sufficient SNR.

5.1.3 Revealing planets' histories

As discussed in Chapter 1, it is widely presumed that close-in gas giants do not form at the locations in which we observe them. The generally accepted scenario has hot Jupiters forming beyond the 'snow line' and migrating inwards to their observed separations (Sasselov & Lecar, 2000). It is the process by which this migration occurs that is disputed, with several competing hypotheses being available.

Loss of angular momentum through interactions with a protoplanetary disk provides one possible route for planetary migration (Goldreich & Tremaine, 1980; Lin et al., 1996), and was initially thought to be the dominant mechanism. It is generally assumed that the axis of such a disc is well aligned with the host star's spin axis owing to angular momentum conservation, so we would expect that disc migration would preferentially produce hot Jupiters with well-aligned orbits. Some misaligned planets would not be out of place under this mechanism's dominance, being the result of close planet-planet encounters following migration, but we would expect the majority of planets to exhibit spin-orbit alignment. It is worth pointing out, however, that this assumption of aligned protoplanetary disks is increasingly being challenged (e.g. Bate et al., 2010; Lai et al., 2011; Rogers et al., 2012) and investigated (Watson et al., 2011)

The Kozai-Lidov mechanism (Kozai, 1962; Lidov, 1962; Naoz et al., 2011, 2012) is the basis of a competing hypothesis for which evidence is mounting (see Chapter 6). The presence of a third, outer body in a planetary system can excite periodic oscillations in both the eccentricity and inclination of a planetary orbit; inward migration then follows, with tidal friction kicking in as the planet approaches its host, causing the orbit to shrink and circularise (Fabrycky & Tremaine, 2007). The oscillating inclination that results from Kozai-Lidov inter-

actions produces a continuum of inclinations once the orbits are stable, and thus we would expect the majority of hot Jupiters to exhibit misaligned orbits if the Kozai-Lidov mechanism operates.

Other proposed processes which could lead to the observed orbits of hot Jupiters are planet-planet scattering (Rasio & Ford, 1996; Weidenschilling & Marzari, 1996; Ford et al., 2001, 2003; Marzari & Weidenschilling, 2002), and tidal friction (Kiseleva & Eggleton, 1998; Kiseleva et al., 1998; Ferraz-Mello et al., 2008, 2009), but the true picture is probably some combination of two or more of these processes (Eggleton & Kiseleva-Eggleton, 2001; Fabrycky & Tremaine, 2007; Nagasawa et al., 2008). These mechanisms are naively expected to produce spin-orbit alignment distributions that are closer to isotropic. However the true picture has turned out to be more complex, and appears to lie somewhere between the two extremes of the isotropic and fully-aligned possibilities (see Chapter 6).

It is possible, to some extent, to distinguish between the competing hypotheses through measurement of spin-orbit alignment in hot Jupiter systems. Given the different angular distributions predicted, building up a significant number of spin-angle measurements is a useful means of determining which mechanism is acting. Unfortunately the true alignment angle, ψ, cannot be determined unless a spectroscopic measurement of $v \sin I$ is made, and the stellar rotation period is known. This yields an estimate of the inclination axis to the line-of-sight (Schlaufman, 2010). The situation is made more difficult by systematic uncertainties in $v \sin I$ measurements, and by the sine function, which flattens as it approaches 90° and therefore only yields useful measurements at low to intermediate inclinations. We are thus currently limited to measuring the angle as projected onto the plane of the sky. Yet even this provides an excellent diagnostic for competing theories of planetary system formation and exoplanet migration; as the number of systems for which the alignment is measured increases, so too does our understanding of these processes.

5.1.4 Expanding the sample

The question of how hot Jupiters appear where they are and with the spin-orbit angles that they have is far from settled. There is only so much that 'typical' transiting hot Jupiters can tell us, and it is becoming increasingly important to push the boundaries of the explored parameter space. It is the more unusual systems, lying at the extremes of the distributions in mass, effective temperature, and $v \sin I$, and that can only be accessed through methods

such as Doppler tomography, that will provide the best test of the hypothesis underlying the evolution of orbital alignment with time. It is also important to use newer analysis methods to examine systems in tandem with the consideration of the RM effect in order to get to grips with each method's intricacies, strengths, weaknesses, and inherent error characteristics.

In this chapter I will present measurements of the spin-orbit alignment angle for six hot Jupiters: WASP-16 b; WASP-25 b; WASP-31 b; WASP-32 b; WASP-38 b, and HAT-P-27/WASP-40 b (hereafter referred to as WASP-40). I will analyse each of the systems using the Rossiter-McLaughlin effect, and in some cases will also provide new analysis using Doppler tomography. I will characterise the alignment angle throughout as λ, following the convention established by Ohta et al. (2005) and widely followed in the literature, rather than the alternative convention of $\beta = -\lambda$ used by Triaud et al. (2010).

Table 5.1: *Parameters for the six WASP planetary systems for which I evaluate the spin-orbit alignment. Parameters for WASP-16 were taken from Lister et al. (2009). Parameters for WASP-25 were taken from Enoch et al. (2011b). Parameters for WASP-31 were taken from Anderson et al. (2011c). Parameters for WASP-32 and WASP-40 are from Maxted et al. (2010) and Anderson et al. (2011a) respectively. Parameters for WASP-38 are compiled from Barros et al. (2011a) and Simpson et al. (2011c). $v \sin I$ values have been updated through spectroscopic analysis of new HARPS data, and $v_{\rm mac}$ values were calculated using the Bruntt et al. (2010) calibration against $T_{\rm eff}$.*

Parameter	Unit	WASP-16	WASP-25	WASP-31	WASP-32	WASP-38	WASP-40
M_s	$M_\odot$	$1.022^{+0.074}_{-0.129}$	1.00 ± 0.03	1.161 ± 0.026	1.10 ± 0.03	1.203 ± 0.036	0.921 ± 0.034
R_s	$R_\odot$	$0.946^{+0.057}_{-0.052}$	0.92 ± 0.04	1.241 ± 0.039	1.11 ± 0.05	$1.331^{+0.030}_{-0.025}$	0.64 ± 0.031
Teff	K	5700 ± 150	5750 ± 100	6300 ± 100	6100 ± 100	6150 ± 80	5246 ± 153
$v \sin I$	km s^{-1}	2.3 ± 0.4	2.6 ± 0.4	8.1 ± 0.5	5.5 ± 0.4	8.3 ± 0.4	2.4 ± 0.5
$v_{\rm mac}$	km s^{-1}	2.3 ± 0.3	2.4 ± 0.3	4.2 ± 0.3	3.5 ± 0.3	3.7 ± 0.3	1.0 ± 0.3
M_p	MJup	$0.855^{+0.043}_{-0.076}$	0.58 ± 0.04	0.478 ± 0.030	3.60 ± 0.07	2.691 ± 0.058	0.617 ± 0.088
R_p	RJup	$1.008^{+0.083}_{-0.060}$	$1.22^{+0.06}_{-0.05}$	1.537 ± 0.060	1.18 ± 0.07	$1.094^{+0.029}_{-0.028}$	$1.038^{+0.068}_{-0.050}$
P	days	3.11860 ± 0.00001	3.764825 ± 0.000005	3.405909 ± 0.000005	2.718659 ± 0.000008	6.871814 ± 0.000045	3.0395589 ± 0.0000090
a	AU	$0.0421^{+0.0010}_{-0.0019}$	0.0473 ± 0.0004	0.04657 ± 0.00034	0.0394 ± 0.0003	$0.07522^{+0.00074}_{-0.00075}$	0.03995 ± 0.00050
e		0(adopted)	0(adopted)	0(adopted)	0.018 ± 0.0065	$0.0314^{+0.0046}_{-0.0041}$	0(adopted)
i	$^\circ$	$85.22^{+0.27}_{-0.43}$	88.0 ± 0.5	84.54 ± 0.27	85.3 ± 0.5	$88.83^{+0.51}_{-0.55}$	$85.01^{+0.20}_{-0.26}$

5.2 Analysis Methods

5.2.1 Rossiter-McLaughlin effect

My analysis mirrors that of Triaud et al. (2010), and uses the complete set of photometric and spectroscopic data for the objects that I am investigating in order to fully account for parameter correlations. I use an adapted version of the code described in Collier Cameron et al. (2007), fitting models of the photometric transit, the Keplerian RV and the RM effect to the system data. The fit of these models is refined using an MCMC technique to minimise the χ^2 statistic, and to explore the parameter space using the jump parameters T_0 (epoch of mid-transit), P (orbital period), W (transit width), b (impact parameter), γ velocity, $\dot{\gamma}$, K (RV semi-amplitude), $T_{\rm eff}$ (stellar effective temperature), $[Fe/H]$ (metallicity), $\sqrt{e}\cos\omega$, $\sqrt{e}\sin\omega$, $\sqrt{v\sin I}\cos\lambda$ and $\sqrt{v\sin I}\sin\lambda$.

The engine of the MCMC code developed by Collier Cameron et al. (2007) is the same as that described in Chapter 4; my adaptations are focused on the model used for the RM effect. Previous versions used that of Ohta et al. (2005), but for the work presented here I chose to replace this with a new implementation of the analytic formula of Hirano et al. (2011b). It uses a quadratic limb-darkening law and models the stellar line shape as the convolution of the intrinsic line shape, $S(v)$, and a broadening kernel, $M(v)$. The latter is calculated by disc-integrating the rotational and macroturbulence components of the Doppler shift across the entire stellar surface, neglecting differential rotation. A separate, analogous model is created for the line shape during a transit, this time calculating $M'(v)$ by integrating across only the region of the stellar surface that is blocked by the planet. Since the planet is small compared to the size of the star, the Doppler shift component of $M'(v)$ can be considered constant. This allows the instantaneous fractional flux decrease to be defined, along with the 'sub-planet velocity' (the average rotational RV of the region of the stellar surface occulted by the planet). The velocity anomaly during transit is then defined in terms of these two parameters.

To calculate the best-fitting model to the spectroscopic transit, the Hirano et al. method cross-correlates an in-transit spectrum with a template, and maximises the cross-correlation function. This method requires prior knowledge of several broadening coefficients, specifically the macroturbulence, $v_{\rm mac}$, for which my estimates are noted in Table 5.1, and the Lorentzian (γ_b) and Gaussian (β_b) spectral line dispersions. I assumed $\gamma_b = 0.9\,{\rm km\,s^{-1}}$ in line with

Hirano et al., and also assumed that the coefficient of differential rotation, $\alpha_{\rm rot} = 0$. WASP-16, WASP-25, and WASP-40 are all slow rotators, and whilst WASP-31, WASP-32, and WASP-38 should be considered as moderately fast rotators (according to the classification of Hirano et al. 2011b), without knowledge of the inclination of their stellar rotation axes it is difficult to place a value on $\alpha_{\rm rot}$ for these systems. β_b is calculated individually for each RV dataset, and depends on the instrument used to collect the data as it is a function of the spectral resolution.

The inclusion of the photometric data is an important aspect of this analysis. The transit width and depth, as well as the impact parameter, are determined from the photometric transit, and these parameters have a role to play in the characterisation of the form of the RM anomaly. The transit width helps to determine its duration, whilst the depth gives the planetary and stellar radii. The radii and impact parameter in turn help to determine $v \sin I$, upon which the amplitude of the anomaly depends (Queloz et al., 2000a). Although characterisation of the RM effect can be carried out using the spectroscopic data alone, by taking the photometric data into account in this way I can ensure consistency across the full set of system parameters, account for parameter correlations, and fully characterise the uncertainties in my results. For completeness, I also repeated my analysis using *only* RV data taken during nights that featured a transit event, but found little to distinguish them from my analysis of the full set of data.

The RV data are separated by instrument, and within those distinctions I also treat spectroscopic data taken on nights featuring planetary transits as separate datasets. My model for the orbital RV signature treats the sets of data as independent, producing individual offsets and radial velocity trends for each one. To account for stellar "jitter", each dataset is initially assigned a value of $1\,\mathrm{m\,s^{-1}}$, below the level of precision of the spectrographs used for this work, which is added in quadrature to the spectroscopic data. This is increased if necessary to ensure that the overall reduced $\chi^2 \approx 1$.

I apply four Bayesian priors in all possible combinations in an attempt to fully characterise the systems under consideration. I apply priors on orbital eccentricity (to allow for forcing of a circular orbit), spectroscopic $v \sin I$ (using the values from Table 5.1), long-term RV trend, and stellar radius (using the method of Enoch et al. (2010) in conjunction with the updated coefficients from Southworth 2011). To distinguish between the combinations of priors I con-

sider the minimal reduced spectroscopic χ^2, which I refer to as $\chi^2_{\rm red}$. If there is no combination of priors with a significantly lower value of $\chi^2_{\rm red}$ I choose the model with the fewest free parameters. The application of the stellar radius prior I consider on the basis of the statistical parameter S (the stellar radius penalty; Collier Cameron et al. 2007),

$$S = -2\ln P(M_s, R_s) = \frac{(R_s - R_0)^2}{\sigma_R^2}, \tag{5.1}$$

where M_s and R_s are the stellar mass and radius as calculated by the MCMC algorithm, R_0 is the stellar radius derived from the (J-H) colour, and σ_R is the 1σ error in R_0. S measures the discrepancy between the two stellar radius values, and if I find a large increase in S when the stellar radius prior is removed, I choose a solution in which it is applied as my preferred one.

5.2.2 Doppler tomography

My Doppler tomography method also uses the complete set of photometric and spectroscopic data for an exoplanet system, and is again based around a modified version of the MCMC code discussed by Collier Cameron et al. (2007). However it also uses a set of spectral CCFs corresponding to the set of spectroscopic transit data, and models these using Doppler tomography.

The modifications necessary for implementing this technique were first described by Collier Cameron et al. (2010a). A model of the average out-of-transit stellar line profile is created through convolution of a Gaussian representing the local line profile, $g(x)$, and a 1-dimensional rotational profile under the assumption of linear limb-darkening, $f(x)$. Both are normalised. A model of the observed line profile is computed through numerical integration of a convolution of $f(x)$ and $g(x-z)$, and is velocity shifted to account for the barycentric nature of the observations.

The presence of the planet is modelled by calculating the quantity and Doppler shift of light that is blocked at each stage of the transit. The position of the planet on the plane of the sky is defined by x_p and z_p in Figure 5.2, and when combined with an estimate of λ these define the perpendicular distance from the planet to the star's rotation axis in stellar radius units. This in turn defines the 'sub-planet velocity', and therefore the in-transit model that accounts for both the stellar line profile and the light blocked by the planet.

When fitting the model to the data, both are first orthogonalised by subtracting their

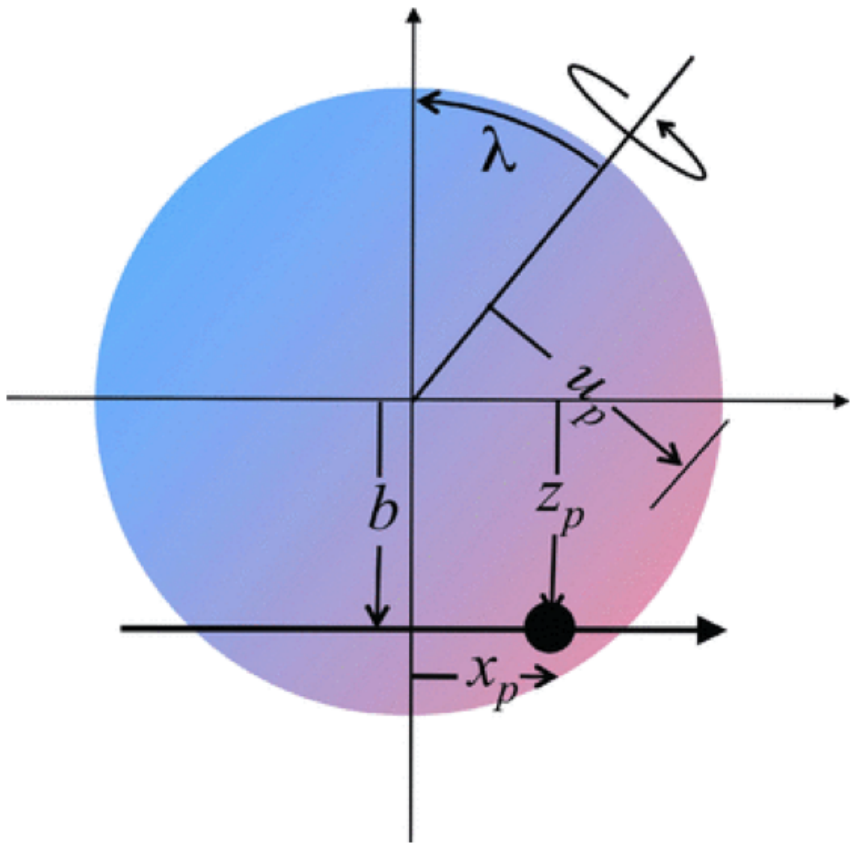

Figure 5.2: *An illustration of the different coordinates used when modelling spin-orbit alignment angle, λ, using Doppler tomography. b is the impact parameter in units of stellar radius. x_p and z_p define the instantaneous position of the planet on the plane of the sky, while u_p is the projected, perpendicular distance of the planet from the stellar rotation axis. (figure 1 of Collier Cameron et al. 2010a)*

respective optimal mean values. A χ^2 goodness-of-fit test provides a measure of the suitability of the model. An important point to note is that the spectroscopic data being used are often of higher resolution than the absolute resolving power of the instruments; I therefore bin both the data and the model by an appropriate, instrument dependent factor before calculating χ^2 to remove correlations between adjacent data.

The jump parameters considered by the MCMC algorithm are as discussed in Section 5.2.1, with the addition of v_{CCF}, the full-width half-maximum of the stellar CCF. This parameter is also included in the calculation of χ^2, but other details of the MCMC algorithm are as for my consideration of the RM effect. Rather than considering all sixteen combinations of my four Bayesian priors however, I apply only the combination that I have selected as most appropriate following my RM analysis.

5.3 WASP-16

WASP-16 b (Lister et al., 2009) is a close Jupiter analog orbiting a solar-type star (spectral type , $T_{\mathrm{eff}} = 5700 \pm 150\,\mathrm{K}$) with a period of 3.12 days. The planet is somewhat less massive than Jupiter but of comparable radius, whilst the host star is similar in mass, radius and metallicity to the Sun, but exhibits significant lithium depletion. Two half seasons and one full season of WASP-S (Pollacco et al., 2006) photometry was combined with observations from EulerCAM, mounted on the 1.2 m Leonard Euler telescope at La Silla (Lendl et al., 2012), to constrain the orbital parameters of the system. Follow-up spectroscopy was then obtained using the CORALIE high precision échelle spectrograph (Queloz et al., 2000a; Pepe et al., 2002), mounted on the Swiss 1.2 m Euler telescope, and used to confirm the existence of the planet. An additional RV datum was also acquired on 2010 July 14 to test the hypothesis of a long-term radial velocity trend.

For this work additional spectroscopy was needed. A transit was observed using the HARPS high precision échelle spectrograph (Mayor et al., 2003), mounted on the 3.6 m ESO telescope at La Silla, on the night of 2010 March 21; 32 data points were acquired over the duration of the night. This transit observation was affected by cloud cover, so an additional transit was observed on the night of 2011 May 12, producing an additional 28 RV measurements. Further measurements were also made on the days surrounding this transit (see Tables C.1, C.2 and C.3) to help characterise the broader RV curve more completely.

Analysis of the new HARPS spectra was carried out by Barry Smalley at Keele University. He assumed a macroturbulence of $v_{\rm mac} = 2.3 \pm 0.3\,{\rm km\,s^{-1}}$ using the calibration of Bruntt et al. (2010). They describe an analytical polynomial correlation between $T_{\rm eff}$ and $v_{\rm mac}$ (their equation (9)) by convolving synthetic line profiles with different $v \sin I$ and $v_{\rm mac}$ values, and fitting to high signal-to-noise spectra from several instruments, including HARPS. A value of $v \sin I = 2.3 \pm 0.4\,{\rm km\,s^{-1}}$ was obtained in this fashion, which was applied as the spectroscopic prior. Barry also calculated $v \sin I$ using a value of $v_{\rm mac} = 3.2$ derived using the calibration of Gray (2008), obtaining $v \sin I = 1.2 \pm 0.5$. However I chose to use the rotational velocity derived from the Bruntt et al. macroturbulence value, as their method allows a greater homogeneity of analysis between systems compared to Gray.

5.3.1 Rossiter-McLaughlin analysis

My original estimate of stellar "jitter" produced fits with $\chi^2_{\rm red} \approx 1.6$, leading me to re-estimate the "jitter" following Wright (2005). Line strengths for the calcium H and K emission lines had been calculated for each individual HARPS spectrum, and I used these to estimate values for the chromospheric activity metric S. I then calibrated these activity parameters against the Mount Wilson sample (see e.g. Baliunas et al. (1995)), and calculated absolute magnitudes of the stars involved using Gray (1994). Cross-referencing with the results of Wright produced three distinct values for the "jitter"; I eventually adopted the 20th percentile value of $3.6\,{\rm m\,s^{-1}}$ as a conservative estimate for the HARPS out-of-transit data, and the median estimate of $5.5\,{\rm m\,s^{-1}}$ for the pre-existing CORALIE data[1]. A complete set of results from my analysis can be found in Table 5.2.

Removing the stellar radius prior produced changes of between 0 and 1 percent in the stellar mass and radius, with corresponding changes in the stellar density of between 1 and 4 percent, for no discernible improvement in fit. Comparing impact parameter values, I found an average value of $\overline{b} = 0.83^{+0.04}_{-0.06}$ for the cases without the radius prior, and $\overline{b} = 0.83^{+0.03}_{-0.04}$ when the prior is active. The value of the stellar radius penalty, S, increased from an average of 0.20 to 0.66 when the prior is removed, a relatively small increase as suggested by the modest changes in stellar parameters. I therefore found little to distinguish between the cases with the prior applied, and those with the stellar radius freely varying, and chose not to apply this prior in my final solution.

[1]For an explanation of these estimates, see Wright (2005).

Adding a long-term, linear RV trend produced no improvement in $\chi^2_{\rm red}$, and with a magnitude of $|\dot{\gamma}| < 9\,{\rm m\,s^{-1}\,yr^{-1}}$ I disregarded the possibility that such a trend exists in the spectroscopic data. Adding a prior on the spectroscopic $v \sin I$ similarly gave almost no difference in the quality of the fit obtained, but did produce a change in the magnitude of the stellar rotation. For most combinations of priors without the $v \sin I$ prior my analysis returned $v \sin I \approx 1.4 \pm 0.3\,{\rm km\,s^{-1}}$, significantly slower than the spectroscopic value, whilst the value with the prior applied was $\approx 1.8 \pm 0.2$, which agrees with the spectroscopic value to within 1σ.

Allowing the eccentricity to float again led to no significant improvement in the fit, and all of the values of e returned by my various combinations of priors were consistent with $e = 0$ to within 2σ. I tested these small eccentricity values using equation (27) of Lucy & Sweeney (1971), which adopts a null hypothesis of a circular orbit and considers an orbit to be eccentric if this is rejected at the 5 percent significance level. This F-test indicated that none of the eccentricities were significant, and thus that a circular orbit is favoured.

I therefore adopt as my conclusive solution the case without the MS prior active, with no prior on $v \sin I$, no long-term trend in velocity, and a circular orbit, but I would like to stress that changing the priors had little impact on the parameter values returned by the MCMC algorithm. My adopted solution, the RV curve and RM effect for which can be seen in Figure 5.3, returns values of $\lambda = -0.9^{\circ}{}^{+6.8}_{-6.9}$ and $v \sin I = 1.5 \pm 0.3\,{\rm km\,s^{-1}}$; this is significantly slower than the spectroscopic value of $v \sin I$ that was obtained from spectral analysis. My solution also indicates a high impact parameter of 0.82 ± 0.02 that reduces the likelihood of a degeneracy developing between λ and $v \sin I$. Examination of Fig. 5.4 highlights this, with a triangular distribution that is centred close to $\lambda = 0^{\circ}$. The main section of this distribution lies within the limits $|\lambda| < 20^{\circ}$, providing further evidence for the well-aligned system that was strongly suggested by my best-fitting RM angle.

As previously noted, the amplitude of the RM anomaly for WASP-16 is quite small. The aligned nature of the system suggests that this can be put down to the star being an old, slowly rotating star, which would be consistent with the age estimate reported by Lister et al. (2009), which suggests an age > 5 Gyr based on a lack of detectable lithium. A second possible explanation could be that the host star is fact being viewed almost pole-on, which could still be consistent with an orbit that is aligned in the plane of the sky. This would lead to a low projected

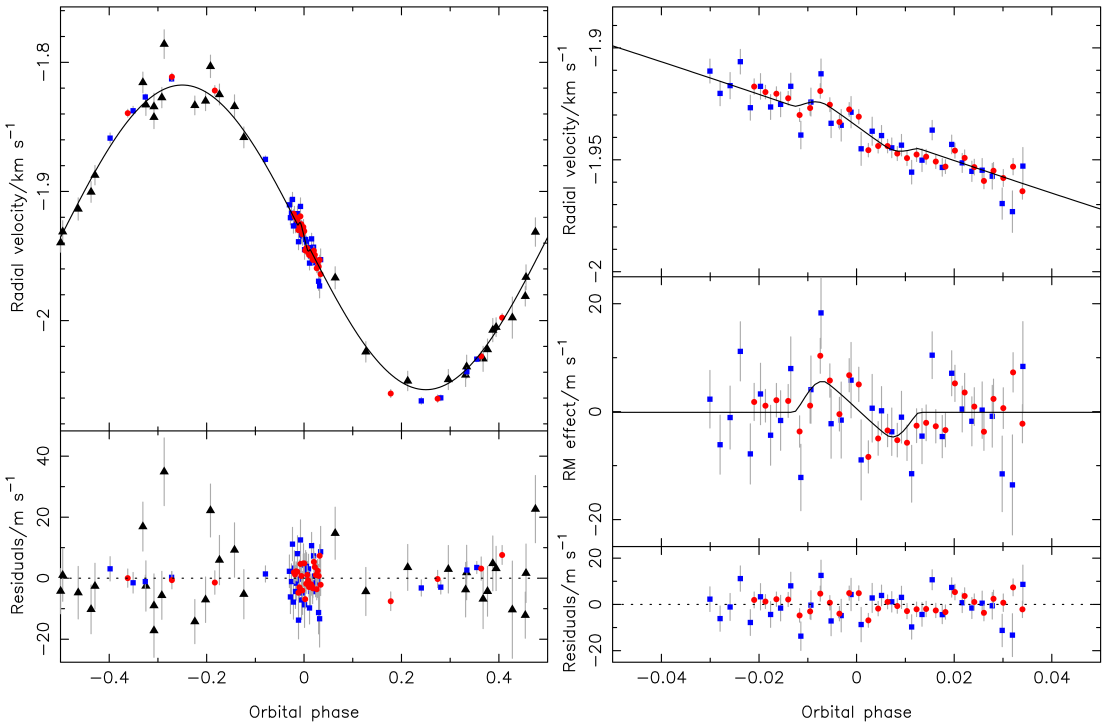

Figure 5.3: *Results from the fit to the data for WASP-16 using $e = 0$, no long-term radial velocity trend, no prior on the spectroscopic $v \sin I$, and without forcing the mass-radius relationship. Black, filled triangles represent data from CORALIE. Blue, filled squares represent data from the first HARPS run. Red, filled circles represent data from the second HARPS run. The best-fitting model is plotted as a solid black line.* ***Top left:*** *Complete radial velocity reflex motion curve.* ***Bottom left:*** *Residuals from the RV fit, exhibiting no correlation with phase.* ***Top right:*** *Close up of the transit region from the radial velocity curve showing the RM effect, along with the residuals.* ***Middle right:*** *Close up of the transit region, with the orbital contribution removed.* ***Bottom right:*** *Residuals for the radial velocity data within the RM window.*

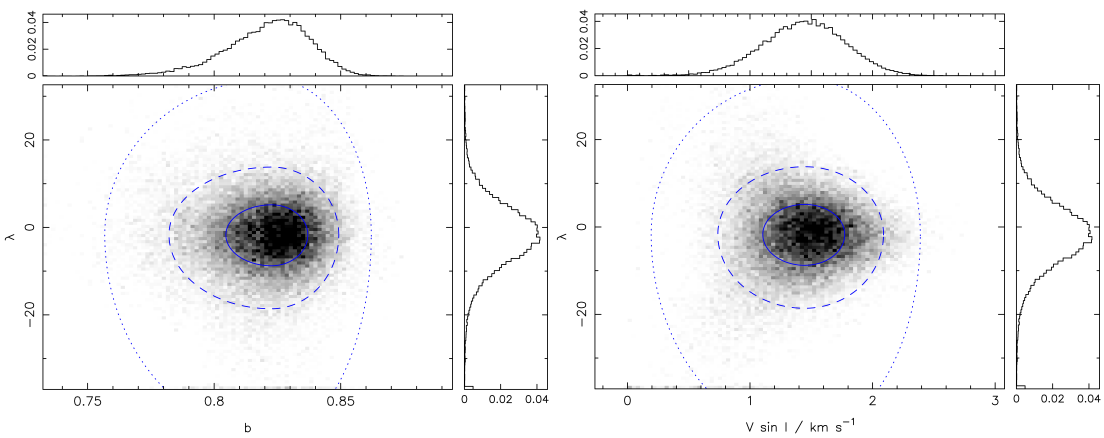

Figure 5.4: *Posterior probability distributions derived from the Markov chains, for the fit to WASP-16 described in Fig. 5.3. The error ellipses are produced using the 1σ (solid), 2σ (dashed), and 3σ (dotted) error bars. Marginalised, 1D distributions are displayed in the side panels.* ***Left:*** *b and λ.* ***Right:*** *$v \sin I$ and λ. This distribution has a triangular shape, and $\lambda = 0$ falls within the central body of the distribution. Both distributions have poorly constrained 99.73 percent confidence regions, and show a slight bias towards negative values of λ that is reflected in the results that I obtained (see Table 5.2.)*

Table 5.2: *A comparison of the χ^2 and $\chi^2_{\rm red}$ values from the Rossiter-McLaughlin analysis of WASP-16 for each combination of Bayesian priors. All values of χ^2 include the Bayesian penalties applicable for that combination of priors.*

$v \sin I$ prior	MS prior	$\dot{\gamma}/\mathrm{ms^{-1}yr^{-1}}$	eccentricity	$v \sin I/\mathrm{km\,s^{-1}}$	$\lambda/^\circ$	χ^2	$\chi^2_{\rm RV}$	$\chi^2_{\rm red}$
off	off	0	$0.012^{+0.011}_{-0.008}$	1.4 ± 0.3	$-1.6^{+7.0}_{-7.2}$	12924 ± 161	111 ± 15	1.0 ± 0.1
off	on	0	$0.015^{+0.011}_{-0.009}$	1.4 ± 0.3	$0.1^{+7.3}_{-6.3}$	12927 ± 161	111 ± 15	1.0 ± 0.1
off	off	$3.3^{+0.7}_{-1.5}$	$0.014^{+0.012}_{-0.009}$	1.4 ± 0.3	$0.0^{+6.9}_{-7.3}$	12923 ± 161	109 ± 15	1.0 ± 0.1
off	on	-0.1 ± 0.1	$0.013^{+0.011}_{-0.008}$	1.4 ± 0.3	$0.0^{+6.9}_{-6.3}$	12925 ± 161	115 ± 15	1.1 ± 0.1
off	off	0	0	1.5 ± 0.3	$-0.9^{+6.8}_{-6.9}$	12932 ± 161	115 ± 15	1.1 ± 0.1
off	on	0	0	$1.5^{+0.3}_{-0.4}$	-1.4 ± 6.9	12930 ± 161	116 ± 15	1.1 ± 0.1
off	off	$-0.05^{+0.05}_{-0.07}$	0	1.4 ± 0.3	$-1.5^{+6.7}_{-7.4}$	12932 ± 161	117 ± 15	1.1 ± 0.1
off	on	$-0.07^{+0.04}_{-0.05}$	0	1.5 ± 0.3	$-0.8^{+6.9}_{-6.6}$	12928 ± 161	116 ± 15	1.1 ± 0.1
2.3 ± 0.4	off	0	$0.015^{+0.011}_{-0.008}$	1.7 ± 0.2	$-0.9^{+5.9}_{-5.5}$	12923 ± 161	113 ± 15	1.1 ± 0.1
2.3 ± 0.4	on	0	$0.013^{+0.011}_{-0.008}$	$1.7^{+0.2}_{-0.3}$	$-1.5^{+6.3}_{-5.6}$	12929 ± 161	114 ± 15	1.1 ± 0.1
2.3 ± 0.4	off	$0.2^{+1.3}_{-0.5}$	$0.011^{+0.010}_{-0.007}$	1.8 ± 0.2	$-1.1^{+5.7}_{-5.6}$	12925 ± 161	113 ± 15	1.0 ± 0.1
2.3 ± 0.4	on	$5.8^{+3.0}_{-2.8}$	$0.011^{+0.011}_{-0.008}$	1.8 ± 0.2	$-0.7^{+5.6}_{-5.3}$	12925 ± 161	114 ± 15	1.1 ± 0.1
2.3 ± 0.4	off	0	0	1.8 ± 0.3	$-1.7^{+5.6}_{-5.7}$	12927 ± 161	117 ± 15	1.1 ± 0.1
2.3 ± 0.4	on	0	0	$1.8^{+0.3}_{-0.2}$	$-1.5^{+5.6}_{-5.3}$	12930 ± 161	118 ± 15	1.1 ± 0.1
2.3 ± 0.4	off	$-0.05^{+0.02}_{-0.04}$	0	1.8 ± 0.2	$-1.6^{+5.5}_{-5.3}$	12933 ± 161	117 ± 15	1.1 ± 0.1
2.3 ± 0.4	on	$-0.02^{+1.00}_{-1.24}$	0	1.8 ± 0.3	$-0.5^{+6.1}_{-5.2}$	12925 ± 161	116 ± 15	1.1 ± 0.1

rotation velocity, and a transit across the pole of the star would have a small RM amplitude, as observed here. The minimum stellar inclination is limited by the observed lithium depletion[2], but such a structure would imply a younger age for the star owing to the rapid true stellar rotation. Interestingly, isochronal analysis in Lister et al. (2009) implies an age of $2.3^{+5.8}_{-2.2}$ Gyr, consistent with the limit implied by the lithium depletion. However new isochronal fits, using my results and a range of stellar models, returned ages of $4.5^{+4.1}_{-4.3}$ Gyr (Padova models; Marigo et al. 2008), $3.4^{+3.4}_{-2.2}$ Gyr (YY models; Demarque et al. 2004), $5.7^{+4.6}_{-4.0}$ Gyr (Teramo models; Pietrinferni et al. 2004), $5.2^{+4.6}_{-3.5}$ Gyr (VRSS models; VandenBerg et al. 2006), and 5.9 ± 3.1 Gyr (DSEP models; Dotter et al. 2008). These ages further support the case for a slowly rotating host star, and are consistent with the star's observed lithium abundance.

Careful analysis of the HARPS spectra allowed Amaury Triaud to measure the chromospheric Ca II H & K emission. He found that $\log(R'_{HK}) = -5.10 \pm 0.15$, indicating a low level of chromospheric activity. This rules out the possibility that the star is misaligned along the line-of-sight, as much greater calcium emission would be expected from a young, rapidly rotating star. This agrees with the work of Schlaufman (2010), who finds no evidence for line-of-

[2]The abundance of lithium gives me a minimum age, as stated. If gyrochronology is assumed to be applicable, then this provides a maximum true stellar rotation velocity. This in turn allows me to use the detected $v \sin I$ to calculate the minimum possible stellar inclination.

sight misalignment in the WASP-16 system. In Chapter 2 I calculated ages of $1.6^{+0.9}_{-0.5}$, $7.47^{+4.0}_{-2.2}$, and $7.0^{+3.8}_{-2.1}$ Gyr using gyrochronology, under the assumption that the star has experienced the standard magnetic braking induced spin-down. These ages, together with the stellar model fits, tend to suggest that WASP-16 is coming towards the end of its main-sequence lifetime, which I estimate as $\tau_{\rm MS} = 6.6 \pm 0.4$ Gyr, or has indeed evolved away from the main-sequence.

A reanalysis of the WASP-1 and WASP-2 systems (Albrecht et al., 2011) highlighted the fact that in systems with low amplitude, low S/N RM anomalies, the angles reported tend towards 0° and 180° owing to the greater probability density in the distribution for λ. The same study cautions readers against drawing strong conclusions of alignment in such cases. My data for WASP-16 certainly show some of the characteristics discussed in the Albrecht et al. study, and it seems as though the system is indeed well-aligned, with λ close to 0.

An independent detection of the RM effect, also suggesting alignment, was announced at IAU Symposium 276 by Winn, and published in Albrecht et al. (2012b). They found $\lambda = 11^{\circ}{}^{+26}_{-19}$ and $v \sin I = 3.2 \pm 0.9\,\mathrm{km\,s^{-1}}$. However, they also found that their semi-amplitude, calculated from the transit-night data only, was significantly different to the value presented in Wright (2005). The reason for this remains unclear.

5.3.2 Doppler tomography

Tomographic analysis of the first HARPS dataset for WASP-16 can be found in Miller et al. (*submitted*).

5.4 WASP-25

WASP-25b (Enoch et al., 2011b) is a significantly bloated, sub-Jupiter mass planet orbiting a solar-type, somewhat metal-poor host star with an orbital period of 3.76 days. It's discovery was made using photometry from WASP-S and the LCOGT 2 m Faulkes Telescope South (FTS) at Siding Spring, Australia, coupled with spectroscopic follow-up using CORALIE.

HARPS was used to observe the transit taking place on the night of 2008 April 11. 44 observations were made that night, with additional data acquired on adjacent nights (see Appendix C, Table C.5).

The new HARPS spectra were again analysed by Barry Smalley. Assuming a macrotur-

Table 5.3: *A comparison of the χ^2 and $\chi^2_{\rm red}$ values from the Rossiter-McLaughlin analysis of WASP-25 for each combination of Bayesian priors. All values of χ^2 include the Bayesian penalties applicable for that combination of priors.*

$v\sin I$ prior	MS prior	$\dot{\gamma}/\mathrm{ms^{-1}yr^{-1}}$	eccentricity	$v\sin I/\mathrm{km\,s^{-1}}$	$\lambda/^\circ$	χ^2	$\chi^2_{\rm RV}$	$\chi^2_{\rm red}$
off	off	0	$0.016^{+0.017}_{-0.011}$	2.8 ± 0.3	$15.2^{+10.4}_{-9.6}$	14179 ± 168	83 ± 13	1.0 ± 0.2
off	on	0	$0.014^{+0.015}_{-0.010}$	2.8 ± 0.3	$14.0^{+8.9}_{-8.1}$	14180 ± 168	83 ± 13	1.0 ± 0.2
off	off	$105.1^{+27.6}_{-30.7}$	$0.017^{+0.014}_{-0.011}$	2.8 ± 0.3	$14.2^{+9.9}_{-9.1}$	14171 ± 168	74 ± 12	0.9 ± 0.2
off	on	$95.1^{+35.9}_{-31.7}$	$0.013^{+0.014}_{-0.009}$	2.8 ± 0.3	$13.9^{+9.0}_{-8.4}$	14172 ± 168	73 ± 12	0.9 ± 0.2
off	off	0	0	2.8 ± 0.3	$15.3^{+8.8}_{-8.7}$	14176 ± 168	83 ± 13	1.0 ± 0.2
off	on	0	0	2.8 ± 0.3	$13.0^{+9.0}_{-8.5}$	14178 ± 168	84 ± 13	1.0 ± 0.2
off	off	$99.1^{+33.4}_{-34.1}$	0	2.8 ± 0.3	$15.3^{+9.0}_{-9.9}$	14171 ± 168	75 ± 12	0.9 ± 0.2
off	on	$94.5^{+32.7}_{-30.8}$	0	2.9 ± 0.2	$13.8^{+8.7}_{-8.2}$	14173 ± 168	75 ± 12	0.9 ± 0.2
2.6 ± 0.4	off	0	$0.008^{+0.014}_{-0.006}$	$2.7^{+0.3}_{-0.4}$	$22.7^{+65.2}_{-13.5}$	12299 ± 157	83 ± 13	1.0 ± 0.2
2.6 ± 0.4	on	0	$0.013^{+0.014}_{-0.009}$	2.8 ± 0.2	$13.4^{+8.0}_{-7.9}$	14182 ± 168	83 ± 13	1.0 ± 0.2
2.6 ± 0.4	off	$96.0^{+31.1}_{-32.1}$	$0.015^{+0.014}_{-0.010}$	2.8 ± 0.2	$13.8^{+8.3}_{-9.0}$	14169 ± 168	74 ± 12	0.9 ± 0.2
2.6 ± 0.4	on	$99.8^{+32.5}_{-30.5}$	$0.013^{+0.014}_{-0.009}$	2.8 ± 0.2	$14.1^{+8.1}_{-8.5}$	14171 ± 168	75 ± 12	0.9 ± 0.2
2.6 ± 0.4	off	0	0	2.8 ± 0.2	$15.1^{+10.5}_{-9.8}$	14180 ± 168	83 ± 13	1.0 ± 0.2
2.6 ± 0.4	on	0	0	2.8 ± 0.2	$12.7^{+8.2}_{-8.0}$	13760 ± 166	83 ± 13	1.0 ± 0.2
2.6 ± 0.4	off	$96.6^{+32.5}_{-32.8}$	0	2.8 ± 0.2	$14.5^{+9.5}_{-8.7}$	14170 ± 168	74 ± 12	0.9 ± 0.2
2.6 ± 0.4	on	$90.7^{+44.2}_{-43.6}$	0	2.8 ± 0.2	$13.5^{+8.4}_{-8.4}$	14171 ± 168	75 ± 12	0.9 ± 0.2

bulence of $v_{\rm mac} = 2.4\pm0.3\,\mathrm{km\,s^{-1}}$ using the calibration of Bruntt et al. (2010), he found $v\sin I = 2.6\pm0.4\,\mathrm{km\,s^{-1}}$. The alternative macroturbulence calibration of Gray (2008) provided $v_{\rm mac} = 3.4\,\mathrm{km\,s^{-1}}$, leading to an estimate for the projected stellar rotation of $v\sin I = 1.5\pm0.5$. Once again I chose to to use the value derived using the Bruntt et al. macroturbulence value.

5.4.1 Rossiter-McLaughlin analysis

I found that my initial "jitter" estimates of $1\,\mathrm{m\,s^{-1}}$ for all of the RV data sets inadequately constrained my results, with $\chi^2_{\rm red}\approx1.3$. Evaluating the predicted "jitter" using Wright (2005) produced a 20th percentile estimate of $9\,\mathrm{m\,s^{-1}}$, which I applied to the CORALIE data taken from the discovery paper. One RV measurement was found to lie at 3σ from the best-fitting model, and to be consistent with the out of transit RV curve. This datum was omitted from my analysis, and will be discussed further at a later stage. A full set of results from my analysis is displayed in Table 5.3.

I found that allowing the eccentricity to float led to a negligible difference in $\chi^2_{\rm red}$, and that the eccentricity values being found were within 2σ of 0. I therefore concluded that the small eccentricity values being returned arose owing to the biases inherent in the MCMC method

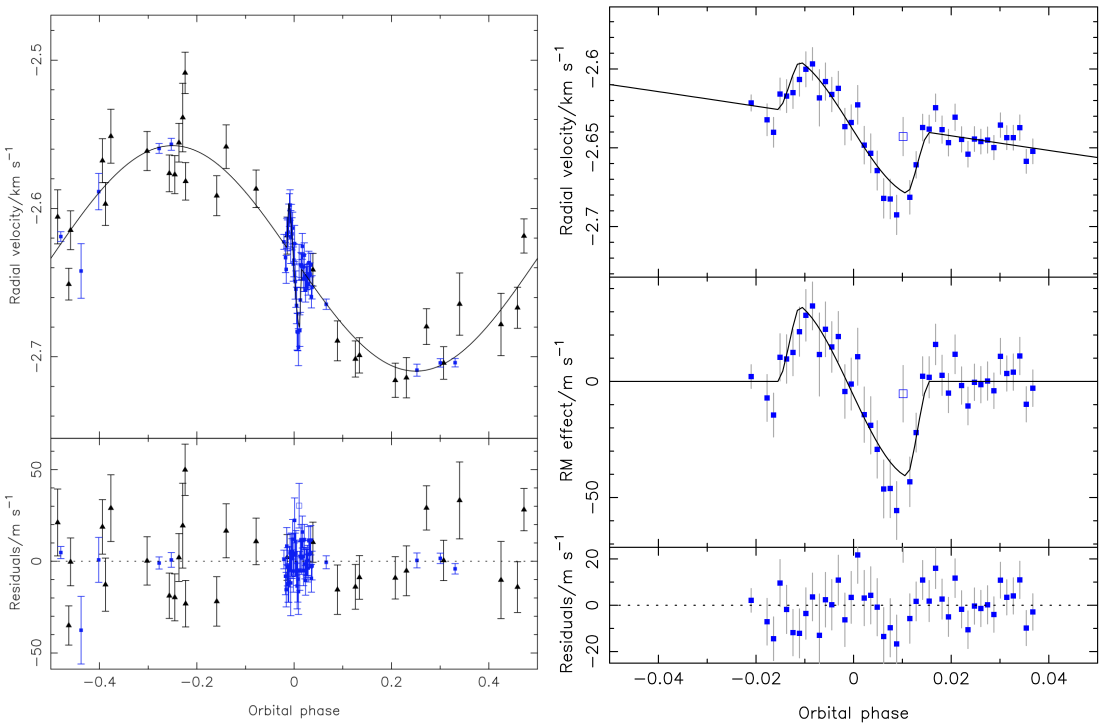

Figure 5.5: *Results from the fit to the data for WASP-25 of my optimal solution: a circular orbit, no long-term RV trend and no prior on the spectroscopic $v \sin I$. The main-sequence mass-radius relation was not enforced. The point denoted by the open square was found to lie 3σ from the best-fitting model, and was not included in the analysis. Legend as for Fig. 5.3.*

(Ford, 2006), and that the orbit of WASP-25 is circular. In this I agree with Enoch et al. (2011b). A circular orbit was confirmed using the F-test of Lucy & Sweeney (1971), which returned very high probabilities of the small eccentricity values having arisen by chance.

I found little difference between the quality of fit for the equivalent cases with the stellar radius prior active, and those without the same constraint. The relaxation of this prior leads to slightly larger values of λ, but also increases the discrepancy between the stellar mass and radius values. The stellar mass value varied by 1 to 3 percent between runs, and relaxing the radius prior reduced R_s by between 1 and 2 percent, dependent on the other priors being applied. The stellar density also showed changes of between 4 and 10 percent from $\overline{\rho}_{*,\mathrm{Rprior}} \approx 1.27\rho_\odot$ to $\overline{\rho}_{*,\mathrm{noprior}} \approx 1.36\rho_\odot$, averaged across all combinations of the other priors. Considering the impact parameter, I found that relaxing the stellar radius prior gave a value of $\overline{b} = 0.36^{+0.26}_{-0.27}$, whilst using the prior returned $\overline{b} = 0.41^{+0.15}_{-0.16}$, both averaged across all other combinations of priors. The radius penalty S increased from an average of 1.88 to 3.59 when the prior was removed. In light of these differences, I elected to apply the stellar radius prior in my final analysis.

Adding a long-term linear trend in RV improved the χ^2_{spec} of the solution, but not by a significant amount, and I found the value of the trend to be $\approx 100\,\mathrm{m\,s^{-1}\,yr^{-1}}$. To check whether a trend was truly present in the system, 2 additional RV measurements were obtained using HARPS on 2010 August 25 and 26. Analysing these in conjunction with previously obtained data shows no evidence for a long-term RV trend, and so I disregard this possibility for my final solution. Introducing a prior on the spectroscopic $v \sin I$ produced no improvement in the quality of fit to the data, irrespective of the other priors. I do not therefore apply such a prior in my final solution, and take this opportunity to obtain a separate measurement of the projected stellar rotation speed.

I selected the solution with $e = 0$, no long-term linear trend in RV and no prior on $v \sin I$, with the stellar radius prior active; the RV curve and RM effect can be seen in Figure reffig:5-3. This gives $\lambda = 13.0^{\circ}{}^{+9.0}_{-8.5}$, a detection of the RM effect at 1.5σ. I also obtained a value for the stellar rotation of $v \sin I = 2.8 \pm 0.3\,\mathrm{km\,s^{-1}}$, slightly greater than but in agreement with my updated spectroscopic value of $2.6 \pm 0.4\,\mathrm{km\,s^{-1}}$. The impact parameter for this solution is $0.42^{+0.04}_{-0.05}$. No correlation is apparent between $v \sin I$ and λ (see Figure 5.6), although there is evidence for a correlation between the impact parameter and λ. It is possible that this correlation is responsible for the poor fit of the model to some parts of the RM data.

The age of the system was analysed using the methods discussed in Chapter 2. The different analyses agree reasonably well; using stellar model fitting I found ages of < 3.10 Gyr (Padova models), $1.94^{+1.75}_{-1.79}$ Gyr (YY models), $6.09^{+2.77}_{-3.22}$ Gyr (Teramo models), $1.18^{+4.34}_{-0.51}$ Gyr (VRSS models), and $3.25^{+1.79}_{-1.53}$ Gyr (DSEP models), whilst gyrochronology returned ages of $1.90^{+0.39}_{-0.29}$ Gyr and $1.77^{+0.36}_{-0.27}$ Gyr. The system therefore appears to be of moderate age, although the age derived from the Teramo isochrones does allow for a older age that is close to the predicted main-sequence lifetime of $\tau_{\mathrm{ms}} \approx 8.2$ Gyr.

The mechanism responsible for the outlier that I omitted from my analysis is unknown, although I note that Simpson et al. (2011c) experienced a similar situation in their analysis of the WASP-38 system, positing seeing changes or telescope guiding faults as possible causes. I would like to suggest a third mechanism; the discrepant point might be caused by the planet traversing a stellar spot. In such a situation the spot would mask the presence of the planet, causing the RV measurement to diverge from the standard RM anomaly pattern. This scenario was suggested to explain a similar anomaly in the data for the WASP-3 system (Tripathi et al.,

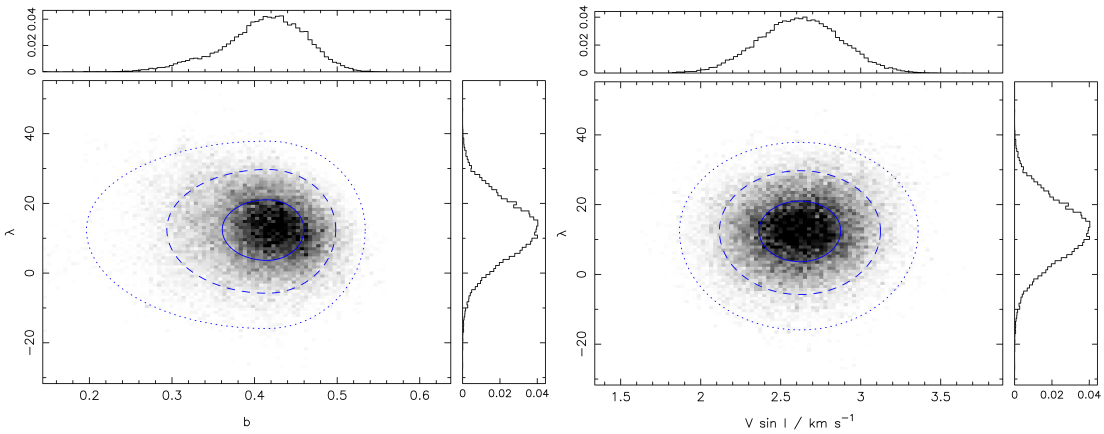

Figure 5.6: *Posterior probability distributions, derived from the Markov chain, for the fit to the data for WASP-25 described in Fig. 5.5. Legend as for Fig. 5.4.* ***Left:*** *b and λ. There are appears to be some small level of correlation between the two parameters.* ***Right:*** *$v \sin I$ and λ. $\lambda = 0$ falls outwith the 68.27 percent confidence contour, but within the 95.45 percent confidence contour, indicating a moderately significant detection of λ.*

2010), but I note that the divergence from the RM effect in that case showed a gradual rise and fall rather than the delta function change observed here, and was eventually attributed to the effect of moonlight. Unfortunately I lack simultaneous photometry from the night of the observed spectroscopic transit, which would show the presence of such a spot. It is also possible that some form of transient event, such as a white light stellar flare, is responsible for the drastic, sudden change in measured RV for this point. Such events were discussed in the context of LQ Hya (Montes et al., 1999), and were observed to produce chromospheric disturbance in the core of otherwise normal spectral lines. This dilution of the spectral lines could affect the continuum level during the flare event, and potentially lead to anomalous redshifting for a short period of time. Such an event would have to be of very short duration however, and coincide with the planet's transit chord. The combination of these two circumstances seems unlikely.

Should WASP-25 be considered to be aligned? Winn et al. (2010a) put forward a criterion of $\lambda \geq 10°$ to $> 3\sigma$ for misalignment; my result for WASP-25 clearly fails this test. Triaud et al. (2010) suggest an alternative criterion of $\lambda > 30°$ as the limit above which a system is sure to be misaligned given the average magnitude of the errors in λ that are found by analysis of the RM effect. WASP-25 also misses this target by some margin. But the data for the RM effect appear to be slightly asymmetric in Fig. 5.5, suggesting that the system is mildly misaligned (although I note that the best-fitting model does not reflect this).

This slight asymmetry in the RM anomaly might arise as a result of some form of systematic

effect. I have already mentioned the possibility of stellar spots in the context of the anomalous datum omitted from my analysis. Could they also provide a possible explanation for the asymmetry? Consider a star on which stellar spots are more numerous in one hemisphere than the other during the planetary transit, but on which they lie away from the transit chord. As the planet transits the more spotty hemisphere it will mask a comparatively larger fraction of the stellar flux than when it is transiting the less spotty hemisphere. The half of the anomaly corresponding to the spotted hemisphere would therefore have a greater amplitude than the half of the anomaly corresponding to the unspotted hemisphere, leading to an asymmetric RM effect. If the difference in the number and/or size of spots between the two hemispheres is small then the asymmetry would be only minor. This interesting systematic was discussed by Albrecht et al. (2011) for the case of WASP-2, and also seems to have played a role in the analysis of the RM effect of CoRoT-2 in Bouchy et al. (2008). In the case of WASP-25 the approaching, blue-shifted hemisphere would be required to have a slightly greater density of stellar spots than the receding, red-shifted hemisphere, which would also feed back into the possibility of a transient event being responsible for the anomalous datum.

I will return to the question of WASP-25's alignment in section 6.2.

5.4.2 Doppler tomography

Tomographic analysis of WASP-25 has yet to be carried out.

5.5 WASP-31

WASP-31 (Anderson et al., 2011c) is a bloated, 0.5 $M_{\rm Jup}$ planet orbiting an F-type star of sub-solar metallicity with a period of 3.5 days. The existence of the planetary transit was first picked up in photometry from WASP-S, and confirmed with high signal-to-noise photometric observations from the LCOGT 2 m Faulkes Telescope North (FTN) at Mt. Haleakala, Hawaii, and EulerCAM. Spectroscopy from CORALIE and HARPS was used to help pin down the nature of the system.

HARPS was also used to observe a full transit on the night of 2010 April 15, with 17 data points obtained. Additional observations were made on adjacent nights (see Appendix C, Tables C.6 and C.7). Barry Smalley again carried out spectral analysis of the new HARPS data, finding that the host star is a moderately rapid rotator, with $v \sin I = 8.1 \pm 0.5\,\mathrm{km\,s^{-1}}$. The

Table 5.4: *A comparison of the χ^2 and $\chi^2_{\rm red}$ values from the Rossiter-McLaughlin analysis of WASP-31 for each combination of Bayesian priors. All values of χ^2 include the Bayesian penalties applicable for that combination of priors.*

$v\sin I$ prior	MS prior	$\dot{\gamma}/\mathrm{ms^{-1}yr^{-1}}$	eccentricity	$v\sin I/\mathrm{km\,s^{-1}}$	$\lambda/^\circ$	χ^2	$\chi^2_{\rm RV}$	$\chi^2_{\rm red}$
off	off	0	$0.023^{+0.031}_{-0.017}$	$7.2^{+0.9}_{-0.7}$	2.2 ± 3.2	14703 ± 171	63 ± 11	0.9 ± 0.2
off	on	0	$0.039^{+0.031}_{-0.026}$	$7.5^{+1.0}_{-0.8}$	$2.2^{+3.1}_{-3.0}$	14699 ± 171	64 ± 11	0.9 ± 0.2
off	off	$12.1^{+6.5}_{-10.5}$	$0.038^{+0.030}_{-0.024}$	$7.4^{+0.9}_{-0.8}$	$2.5^{+3.1}_{-3.2}$	14702 ± 171	63 ± 11	0.9 ± 0.2
off	on	$4.9^{+7.8}_{-6.4}$	$0.047^{+0.037}_{-0.026}$	$7.6^{+0.9}_{-0.8}$	$2.7^{+2.7}_{-2.9}$	14701 ± 171	62 ± 11	0.9 ± 0.2
off	off	0	0	7.3 ± 0.7	$2.2^{+3.2}_{-3.1}$	14695 ± 171	64 ± 11	0.9 ± 0.2
off	on	0	0	7.4 ± 0.7	$2.2^{+3.4}_{-3.1}$	14709 ± 171	64 ± 11	0.9 ± 0.2
off	off	6.3 ± 7.9	0	$7.3^{+0.8}_{-0.7}$	2.2 ± 3.1	14701 ± 171	63 ± 11	0.9 ± 0.2
off	on	$0.1^{+7.7}_{-3.1}$	0	7.3 ± 0.7	$2.6^{+3.2}_{-3.1}$	14701 ± 171	64 ± 11	0.9 ± 0.2
8.1 ± 0.5	off	0	$0.027^{+0.032}_{-0.019}$	7.9 ± 0.4	2.3 ± 2.8	14694 ± 171	63 ± 11	0.9 ± 0.2
8.1 ± 0.5	on	0	$0.049^{+0.032}_{-0.025}$	8.0 ± 0.4	$2.5^{+3.1}_{-3.0}$	14700 ± 171	64 ± 11	0.9 ± 0.2
8.1 ± 0.5	off	$6.8^{+9.2}_{-8.9}$	$0.028^{+0.031}_{-0.020}$	7.9 ± 0.4	2.3 ± 2.9	14693 ± 171	64 ± 11	0.9 ± 0.2
8.1 ± 0.5	on	$6.1^{+8.5}_{-8.9}$	$0.055^{+0.034}_{-0.031}$	$7.9^{+0.5}_{-0.4}$	$2.6^{+2.8}_{-2.9}$	14707 ± 171	65 ± 11	0.9 ± 0.2
8.1 ± 0.5	off	0	0	7.8 ± 0.4	$1.9^{+3.0}_{-2.9}$	14698 ± 171	64 ± 11	0.9 ± 0.2
8.1 ± 0.5	on	0	0	7.8 ± 0.4	2.6 ± 3.0	14696 ± 171	65 ± 11	0.9 ± 0.2
8.1 ± 0.5	off	$6.4^{+8.5}_{-8.8}$	0	$7.9^{+0.5}_{-0.4}$	$2.3^{+2.7}_{-2.8}$	14680 ± 171	64 ± 11	0.9 ± 0.2
8.1 ± 0.5	on	$6.5^{+7.4}_{-10.0}$	0	7.8 ± 0.4	$2.5^{+3.3}_{-3.1}$	14683 ± 171	64 ± 11	0.9 ± 0.2

macroturbulence calibration of Bruntt et al. (2010) provided $v_{\rm mac} = 4.2\pm0.3\,\mathrm{km\,s^{-1}}$. Again, an alternative analysis used $v_{\rm mac} = 5.4$ from the calibration of Gray (1994), and returned a value of $v\sin I$ ($7.5\pm0.5\,\mathrm{km\,s^{-1}}$) that was used for comparison.

5.5.1 Rossiter-McLaughlin analysis

I found that there was no need to re-evaluate my initial "jitter" estimates, as $1\,\mathrm{m\,s^{-1}}$ for each set of RV data produced $\chi^2_{\rm red}$ consistent with 1 for all of my runs. Full results of my analysis can be found in Table 5.4.

I found no difference between the $\chi^2_{\rm red}$ values for any combination of priors. I found that relaxing the stellar radius had little effect on the fit to the spectroscopic data, but had a deleterious effect on the stellar parameters. Imposing the prior produced a decrease in stellar radius of between 2 and 6 percent and a corresponding increase in the stellar mass, as well as an increase in stellar density of between 10 and 22 percent from $\overline{\rho}_{*,\rm noprior} \approx 0.59\rho_\odot$ to $\overline{\rho}_{*,\rm Rprior} \approx 0.68\rho_\odot$, averaged across all other combinations of priors. Comparing the impact parameter and S statistic, I found $\overline{b} = 0.79^{+0.03}_{-0.05}$ and $\overline{S} = 15.2$ with no radius prior applied, and $\overline{b} = 0.77^{+0.03}_{-0.05}$ with $\overline{S} = 3.5$ when the stellar radius prior was enforced. Owing to the much more favourable S statistic, and the influence on the stellar parameters, I elected to use results

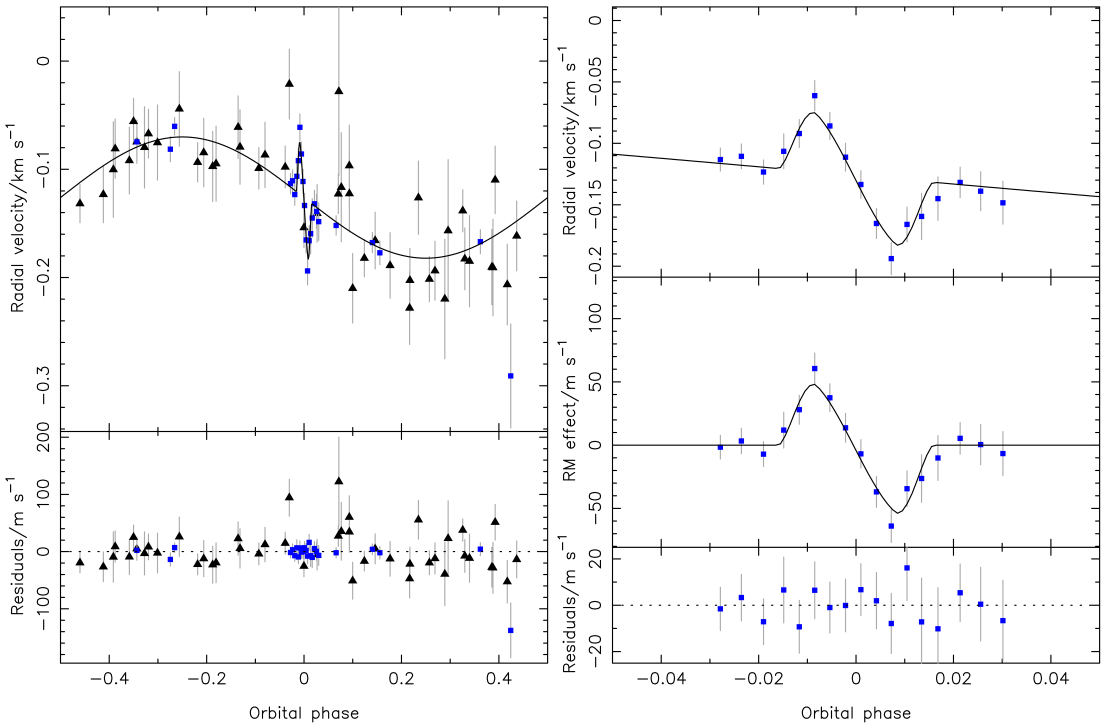

Figure 5.7: *Results from the fit to the data for my adopted solution for WASP-31, with a circular orbit, no prior on the spectroscopic $v \sin I$, no long-term radial velocity trend, and the mass-radius relationship applied. Legend as for Fig. 5.3.*

in which the stellar radius prior is applied. Adding a linear velocity trend gave no discernible difference in the quality of the fit to the spectroscopic data, and with a magnitude of $|\dot{\gamma}| < 20\,\mathrm{m\,s^{-1}\,yr^{-1}}$ I conclude that no such trend is present in the system. Adding a prior on the spectroscopic $v \sin I$ made little difference to the results despite the relatively rapid rotation, so I chose the simpler route and neglected such a prior. Finally, I chose a circular solution; the F-test of Lucy & Sweeney (1971) shows that the small eccentricity values returned when e is allowed to float are insignificant.

My optimal solution is therefore that obtained with no $v \sin I$ prior, no velocity trend, the MS prior active, and $e = 0$. This set of priors gives $\lambda = 2.2^{\circ}{}^{+3.4}_{-3.1}$, leading to the conclusion that the WASP-31 system is well-aligned. It is worth noting that this would be the conclusion whichever combination of priors I chose, as all of the values of λ that I obtained lie within 1σ of 0°. The impact parameter is $0.77^{+0.01}_{-0.02}$. The stellar rotation for this solution has a value of $v \sin I = 7.4 \pm 0.7\,\mathrm{km\,s^{-1}}$; as with my result for WASP-16 this is slower than the spectroscopic value, although in this case the values agree to within 1σ. Figure 5.7 displays the RV and RM curves for the optimal solution, whilst Figure 5.8 shows the posterior probability distributions. No correlations are apparent between b, $v \sin I$, and λ.

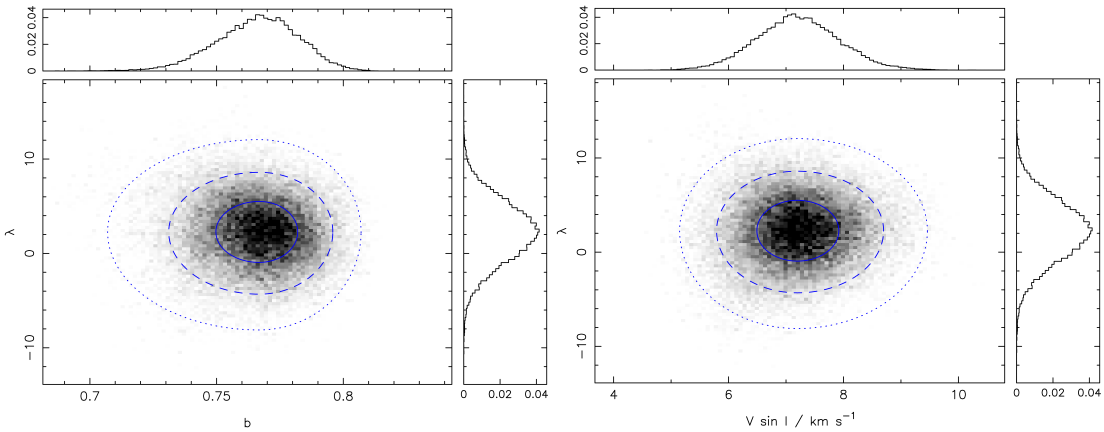

Figure 5.8: *Posterior probability distributions, derived from the Markov chain, for the fit to the data for WASP-31 described in Fig. 5.7. Legend as for Fig. 'reffig:5-2.* ***Left:*** *b and λ.* ***Right:*** *$v \sin I$ and λ. $\lambda = 0$ lies well within the main body of the distribution.*

WASP-31 is not included in the sample of Schlaufman (2010) owing to its time of publication. In order to check the possibility of misalignment along the line-of-sight, I follow the method of Schlaufman and calculate the rotation statistic, Θ. The age of WASP-31 A is somewhat uncertain however; its lithium abundance, gyrochronology and the presence of a close companion all suggest ages of ≈ 1 Gyr, whilst previous stellar model fits imply an older age of 4 ± 1 Gyr. My isochronal fits for the system (see Chapter 2) produced ages of 3.23 ± 1.40 Gyr (Padova models), 2.05 ± 1.17 Gyr (YY models), $3.60^{+2.26}_{-1.78}$ Gyr (Teramo models), $1.87^{+1.34}_{-1.02}$ Gyr (VRSS models), and $4.19^{+0.99}_{-2.76}$ Gyr (DSEP models). Using these estimates I calculate values of $\Theta = -3.7$, -1.0, -4.6, -1.3, and -2.9 respectively; WASP-31 is rotating more rapidly than expected given its age in all cases. The chance of significant misalignment along the line-of-sight therefore seems slim; the inclination of the WASP-31 b's orbit is $84.7 \pm 0.2°$, leaving little room for an increase in rotation velocity owing to line-of-sight misalignment.

Age estimates obtained using stellar activity measurements also suggest that the star is old, but interestingly gyrochronology analysis suggested an age of $0.83^{+0.17}_{-0.12}$ Gyr, which is much younger than any of the other age estimates that I calculated, although the lithium abundance age range does allow for such a young star. This gyrochronology age returns $\Theta = 2.34$, implying that the star is rotating more slowly than expected. Give all of this, perhaps the true age of the system lies somewhere close to 1 Gyr.

The systems has also been investigated by Albrecht et al. (2012b), who used priors on the ephemeris from Dragomir et al. (2011) (who had access to an additional lightcurve compared to the discovery paper) to obtain $v \sin I = 7.3 \pm 0.4\,\mathrm{km\,s^{-1}}$ and $\lambda = -6° \pm 3$, which is

inconsistent with my result. However when they used the data from Anderson et al. (2011c) for their ephemeris priors they obtained a value of the alignment angle of $\lambda = 2° \pm 3$, which *does* agree with the value that I have reported. This dependence of the result of the precise set of priors and timing information used is worrisome, and would seem to point towards the uncertainties on λ being greater than I have assessed them to be (I note that Albrecht et al. doubled the error bars on their result before including it in their analysis of the ensemble). My analysis does not use priors on the ephemeris, but in order to be rigourous I reassessed the system using my selected combination of priors, and the ephemeris data from Dragomir et al.. I found little to distinguish these results from those presented in Table 5.4; either the new initial ephemeris was insufficiently different to the one that I used to force a different solution, or the χ^2 surface has a very strong minimum at the solution that I found initially.

5.5.2 Doppler tomography

Analysis of WASP-31 using Doppler tomography can be found in Miller et al. (*submitted*).

5.6 WASP-32

WASP-32b is a dense hot Jupiter in a 2.72 day orbit around a Sun-like (spectral type G, $T_{\rm eff} = 6140^{+90}_{-100}$ K), lithium depleted star, and is one of only a small number of hot Jupiters with a mass greater than 3 Jupiter masses. Its discovery was presented by Maxted et al. (2010), who used photometry from WASP-S and the Faulkes Telescope North (FTN), in concert with spectroscopic observations from the CORALIE spectrograph, to determine the existence of the transiting planet.

The HARPS spectrograph was used to observe the transit of WASP-32 b on the night of 2011 September 26. Thirty observations were acquired over the duration of the night, and additional data were collected on the nights of 2011 September 24, 25 and 27 (see Appendix C, Table C.8). Simultaneous photometry of the same transit was obtained using EulerCam and the TRAPPIST telescope at La Silla (Jehin et al., 2011). Photometry of an additional transit was obtained using TRAPPIST, on 2011 November 24.

Barry Smalley and Amanda Doyle carried out a spectroscopic analysis of the new HARPS spectra to determine an updated estimate of $v \sin I$ for the host star. They assumed a macroturbulence of $v_{\rm mac} = 3.5 \pm 0.3\,{\rm km\,s^{-1}}$ using the calibration of Bruntt et al. (2010), and obtained

$v \sin I = 5.5 \pm 0.4\,\mathrm{km\,s^{-1}}$, in agreement with the value of $4.8 \pm 0.8\,\mathrm{km\,s^{-1}}$ found by Maxted et al. (2010) from their CORALIE spectra. I applied this new estimate of $v \sin I$ as my spectroscopic prior.

5.6.1 Rossiter-McLaughlin analysis

I initially applied a stellar "jitter" of $1.0\,\mathrm{m\,s^{-1}}$ to both the existing CORALIE RV data and the new HARPS data. The values of χ^2_{red} that were returned by my algorithm with this level of "jitter" applied all fall with 1σ of 1.0, indicating that the solution is well constrained. There was therefore no need to increase the level of stellar activity accounted for by my modelling.

Adding a long-term, linear RV trend produced no discernible effect on the quality of fit that I obtained, or on the value of χ^2_{red}. Relaxing the prior on the stellar radius led to only marginal changes in the values of S, M_s, R_s, ρ_s, and b. It also produced no change in the value of χ^2_{red}. I therefore conclude that any such trend is insignificant, and choose as my definitive solution a model which does not apply the prior. Similarly, I elect not to apply the prior on $v \sin I$ in my final solution. Whilst applying the prior produced an increase of $1.0\,\mathrm{km\,s^{-1}}$ in the value of $v \sin I$ returned by the MCMC algorithm, it had no impact on the value of χ^2_{red}.

The prior on orbital eccentricity required more careful analysis. Maxted et al. (2010) reported a marginal 2.8σ detection of eccentricity in the planet's orbit, and suggested that it could be confirmed through observations of the secondary eclipse. To my knowledge no such observations have been carried out, so the question of the system's eccentricity remains open. My models with floating eccentricity all find $e \leq 0.014$, slightly less than the value of $e = 0.018 \pm 0.0065$ found by Maxted et al. (2010), and none show any improvement in χ^2_{red} compared to the equivalent models with fixed, circular orbits. I tested the significance of the eccentricity values recovered by my algorithm using the F-test of Lucy & Sweeney (1971), which indicated that none of the eccentricities are significant, and thus that a circular orbit is favoured.

My adopted model thus uses the combination of a circular orbit and no long-term RV trend, with neither the $v \sin I$ or stellar radius priors applied. This model provides values of $\lambda = 8.6^{\circ}{}^{+6.4}_{-6.5}$, $v \sin I = 3.9 \pm 0.5\,\mathrm{km\,s^{-1}}$ (slightly slower than the value from spectroscopic analysis), $b = 0.66 \pm 0.02$ and $i = 85.1^{\circ} \pm 0.2$. The resulting RV curve is displayed in Fig. 5.9 alongside a close-up of the transit region, showing the RM anomaly. The amplitude of the

Table 5.5: *A comparison of the χ^2 and $\chi^2_{\rm red}$ values from the Rossiter-McLaughlin analysis of WASP-32 for each combination of Bayesian priors. All values of χ^2 include the Bayesian penalties applicable for that combination of priors.*

$v \sin I$ prior	MS prior	$\dot{\gamma}/\mathrm{ms^{-1}yr^{-1}}$	eccentricity	$v \sin I/\mathrm{km\,s^{-1}}$	$\lambda/^\circ$	χ^2	$\chi^2_{\rm RV}$	$\chi^2_{\rm red}$
off	off	0	$0.008^{+0.006}_{-0.005}$	3.9 ± 0.6	$8.3^{+7.2}_{-6.9}$	10474 ± 145	49 ± 10	1.0 ± 0.2
off	on	0	$0.008^{+0.005}_{-0.004}$	3.9 ± 0.5	$8.5^{+6.6}_{-6.4}$	10471 ± 145	49 ± 10	1.0 ± 0.2
off	off	-7.1 ± 2.3	0.006 ± 0.005	3.9 ± 0.6	$8.5^{+7.2}_{-6.4}$	10473 ± 145	48 ± 10	1.0 ± 0.2
off	on	$55.7^{+26.7}_{-35.3}$	$0.007^{+0.005}_{-0.004}$	3.9 ± 0.5	$8.5^{+6.8}_{-6.4}$	10468 ± 145	47 ± 10	0.9 ± 0.2
off	off	0	0	3.9 ± 0.5	$8.6^{+6.4}_{-6.5}$	10475 ± 145	52 ± 10	1.0 ± 0.2
off	on	0	0	3.9 ± 0.6	$8.5^{+7.4}_{-6.6}$	10472 ± 145	51 ± 10	1.0 ± 0.2
off	off	$13.0^{+8.9}_{-14.1}$	0	3.9 ± 0.5	$8.4^{+6.6}_{-6.4}$	10470 ± 145	51 ± 10	1.0 ± 0.2
off	on	$27.7^{+31.5}_{-41.4}$	0	$4.0^{+0.5}_{-0.6}$	$7.9^{+7.3}_{-6.8}$	10471 ± 145	50 ± 10	1.0 ± 0.2
5.5 ± 0.4	off	0	$0.008^{+0.006}_{-0.005}$	4.9 ± 0.3	7.6 ± 5.3	10476 ± 145	54 ± 10	1.1 ± 0.2
5.5 ± 0.4	on	0	$0.008^{+0.005}_{-0.004}$	4.9 ± 0.3	$7.7^{+5.9}_{-6.3}$	10471 ± 145	54 ± 10	1.1 ± 0.2
5.5 ± 0.4	off	$-15.2^{+12.5}_{-5.3}$	$0.008^{+0.005}_{-0.004}$	4.9 ± 0.3	$8.1^{+5.2}_{-5.4}$	10476 ± 145	55 ± 10	1.1 ± 0.2
5.5 ± 0.4	on	$30.5^{+16.4}_{-8.5}$	$0.008^{+0.006}_{-0.005}$	4.9 ± 0.3	$8.3^{+5.6}_{-5.0}$	10473 ± 145	52 ± 10	1.0 ± 0.2
5.5 ± 0.4	off	0	0	4.9 ± 0.3	$7.7^{+5.5}_{-5.4}$	10478 ± 145	57 ± 10	1.1 ± 0.2
5.5 ± 0.4	on	0	0	4.9 ± 0.3	$7.3^{+5.6}_{-5.4}$	10480 ± 145	56 ± 10	1.1 ± 0.2
5.5 ± 0.4	off	$23.7^{+7.8}_{-12.0}$	0	4.9 ± 0.3	$7.1^{+5.6}_{-5.1}$	10472 ± 145	55 ± 10	1.1 ± 0.2
5.5 ± 0.4	on	$7.9^{+6.1}_{-9.1}$	0	4.9 ± 0.3	$7.5^{+5.5}_{-5.4}$	10477 ± 145	56 ± 11	1.1 ± 0.2

anomaly is low owing to the moderate rotation speed of the host star, but the signal-to-noise is high and the anomaly is well constrained. I found that the semi-amplitudes returned for all three of the RV data sets (the CORALIE data from Maxted et al. (2010), the new HARPS out-of-transit data and the HARPS in-transit data) were in good agreement, and consistent with the results from the discovery paper. My barycentric velocities on the other hand whilst consistent with each other, are slightly slower than the value found by Maxted et al. (2010), even for their CORALIE spectroscopy.

5.6.2 Doppler tomography

The set of priors identified as comprising the best-fitting model for my RM analysis were applied to the Doppler tomography method, allowing me to assess only a single model. Fig. 5.10 displays the residual maps from my analysis, which returned values of $v \sin I = 3.9^{+0.4}_{-0.5}\,\mathrm{km\,s^{-1}}$ and $\lambda = 10.5^{\circ\,+6.4}_{-5.9}$.

There is little to choose between the results returned by my two analysis methods. In this case, since the constraints on the spin-orbit angle were well-defined by my original RM analysis, the tomographic method has been unable to provide much improvement. However it does confirm the results from my RM analysis, namely that the system is well aligned and

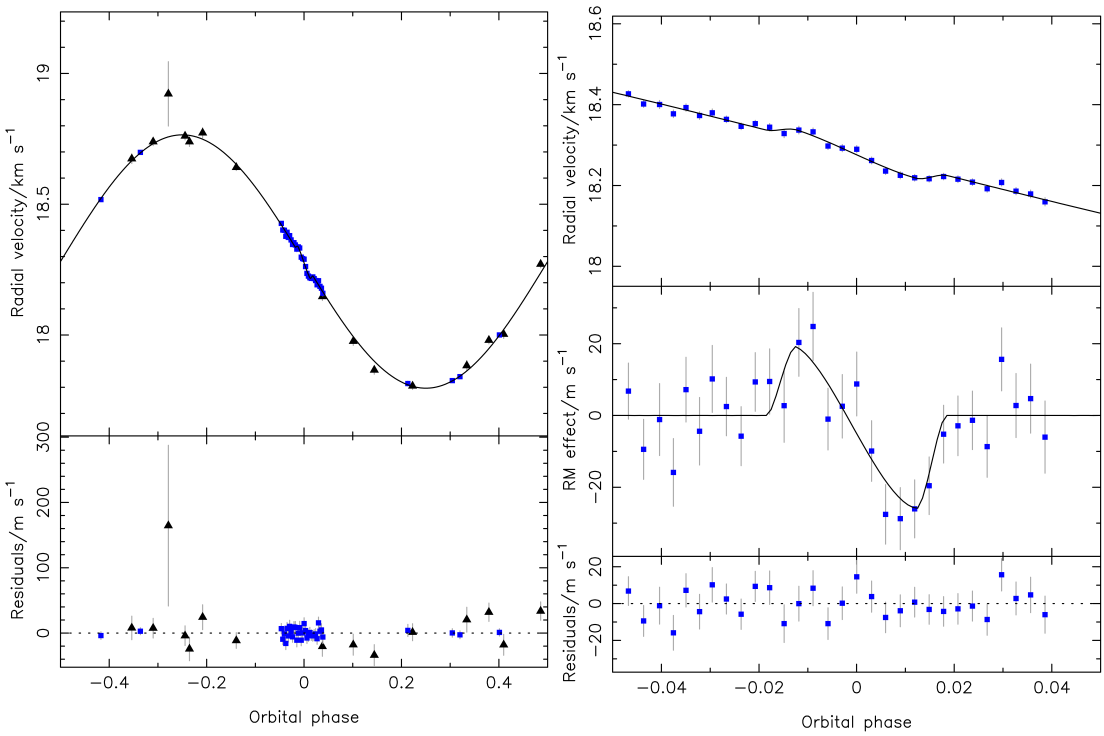

Figure 5.9: *Results from my adopted model for WASP-32: $e = 0$; no long-term radial velocity trend; no prior on the spectroscopic $v \sin I$, and no stellar radius prior. The best-fitting model is plotted as a solid black line.* ***Top left:*** *Complete radial velocity reflex motion curve. Legend as for Fig. 5.3.*

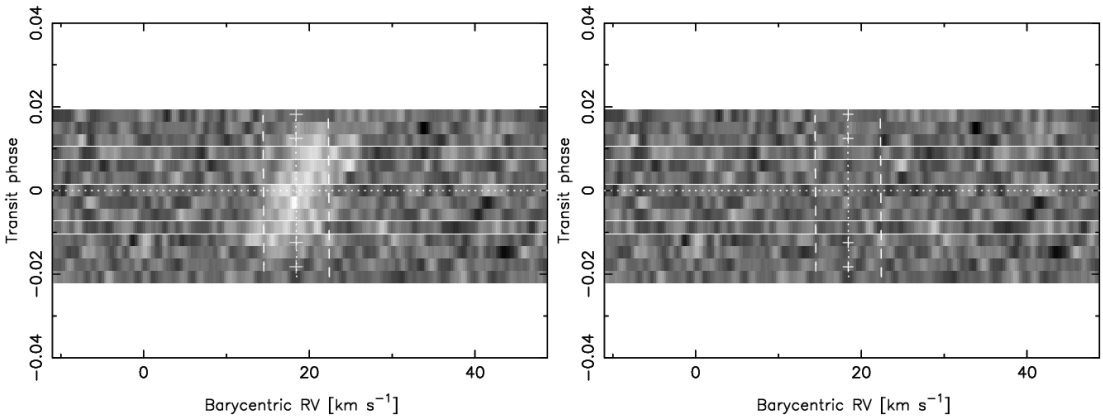

Figure 5.10: Left: *Residual map of WASP-32 time series CCFs with the model stellar spectrum subtracted. The signature of the planet moves from bottom-left to top-right, supporting the aligned, prograde orbit conclusion from my RM analysis.* ***Right:*** *The best-fitting model for the time-variable planet feature has been subtracted, leaving the overall residual map. The lack of any features in this figure indicate a lack of large-scale stellar activity.*
The horizontal dotted line marks the mid-transit phase. The vertical dotted line denotes the stellar radial velocity, whilst the vertical dashed lines indicate $\pm v \sin I$ *from this, effectively marking the position of the stellar limbs. The crosses mark the four contact points for the planetary transit.*

in a prograde orbit. This is easily seen in Fig. 5.10, which shows the time-series map of the residuals after the subtraction of the stellar line profile only; the effect of the planet therefore shows up as a bright 'streak' across the figure, centred on phase 0 and the barycentric radial velocity of the host star, and travelling between the $\pm v \sin I$ values. The trajectory of the planet signature unambiguously identifies the planetary orbit as prograde, moving as it does from bottom-left ($-v \sin I$ at the orbital phase corresponding to ingress) to top-right ($+v \sin I$ at the orbital phase corresponding to egress). Fig. 5.10 also displays the final residual map, after the removal of the planet signature. The lack of any notable, consistent deviation from the mean value of the map indicates a lack of significant stellar activity in the host star, as any such activity would produce signatures similar to that of the planet (e.g. non-radial pulsation in WASP-33, Collier Cameron et al. 2010b).

5.7 WASP-38

The WASP-38 system consists of a massive ($2.7\,M_{\rm Jup}$) hot Jupiter in a long (6.87 d), eccentric orbit around a bright (V=9.4), rapidly rotating star of spectral type F8 and $T_{\rm eff} = 6180^{+40}_{-60}$ K. Further information regarding its discovery can be found in Barros et al. (2011a). Photometry from the SuperWASP array, the RISE instrument mounted on the 2 m Liverpool Telescope (Steele et al., 2008; Gibson et al., 2008) and an 18 cm Takahashi astrograph at La Palma were

combined with spectroscopic measurements taken using the CORALIE and SOPHIE instruments to confirm the presence of the planet.

The Rossiter-McLaughlin effect of WASP-38 b has been analysed previously by Simpson et al. (2011c), who obtained spectroscopic observations of a transit event using the FIES spectrograph mounted on the Nordic Optical Telescope (NOT) at la Palma. Despite the low precision of their measurements, they were able to place useful constraints on the alignment angle using the shape of the RV anomaly during transit, ruling out high angles and confining the system to prograde orbits. They reported a final value of $\lambda = 15^{\circ}{}^{+33}_{-43}$, but were not able to provide a firm conclusion as to the alignment, or otherwise, of the system.

I obtained new spectroscopic observations using HARPS of the transit event on the night of 2011 June 15, and additional observations were made throughout 2011 to provide coverage of the entire radial velocity curve (see Table C.9). Photometric observations were made of a transit using TRAPPIST, on 2011 April 13, but unfortunately it was not possible to obtain simultaneous photometry of the spectroscopically observed event. As with the previous systems, Barry Smalley and Amanda Doyle analysed the new HARPS spectra to obtain a value for $v \sin I$ of $8.3 \pm 0.4\,\mathrm{km\,s^{-1}}$. A macroturbulence of $v_{\mathrm{mac}} = 3.7 \pm 0.3\,\mathrm{km\,s^{-1}}$ was assumed, again using the calibration of Bruntt et al. This $v \sin I$ is in excellent agreement with the values of $v \sin I = 8.6 \pm 0.4\,\mathrm{km\,s^{-1}}$ quoted by Barros et al. (2011a) and $v \sin I = 8.58 \pm 0.39\,\mathrm{km\,s^{-1}}$ found by Simpson et al. (2011c). The adopted v_{mac} is significantly lower than the $4.9 \pm 0.4\,\mathrm{km\,s^{-1}}$ that Barros et al. (2011a) used to fit their spectroscopy. Barros et al. used the calibration of Gray (2008), whereas the HARPS analysis used that of Bruntt et al. (2010). Reanalysing the new spectra using the Gray calibration returns a slightly lower value of $v \sin I = 7.9 \pm 0.4\,\mathrm{km\,s^{-1}}$, in agreement with the Barros et al. results. In spite of this, Barry Smalley feels that the Bruntt et al. calibration gives a better fit to the data, and it is therefore that result that I use for my spectroscopic prior.

5.7.1 Rossiter-McLaughlin analysis

My initial stellar "jitter" estimate of $1\,\mathrm{m\,s^{-1}}$ led to poorly constrained results, with the lowest χ^2_{red} value returned by any of the models being 1.7. I therefore recalculated the stellar "jitter" following Wright (2005), obtaining three distinct values. I found that in order to force $\chi^2_{\mathrm{red}} \approx 1$ I had to apply the conservative, 20th percentile estimate of $2.1\,\mathrm{m\,s^{-1}}$ to the new HARPS data, and the 80th percentile estimate of $6.6\,\mathrm{m\,s^{-1}}$ to the pre-existing FIES, CORALIE, and SOPHIE

data.

I found that applying the spectroscopic prior on $v \sin I$ made little difference to the quality of fit that I obtained, or to the values of $v \sin I$ and λ that I obtained when compared to the equivalent case without the application of the prior. Similarly, applying a long-term RV trend had no effect on the results, and the magnitude of any possible trend was found to be insignificant at $|\dot{\gamma}| < 22\,\mathrm{m\,s^{-1}\,yr^{-1}}$. The stellar radius prior however, despite producing only a small change in the values of χ^2_{red}, had a significant impact on the results that I obtained. Cases in which the prior was not applied saw average increases in the stellar mass and radius of 6 percent and 27 percent respectively over their equivalent cases in which the prior was applied, as well as an average decrease in the stellar density of 49 percent. Note that these changes do not necessarily match perfectly, as under my model the stellar density is calculated directly from the transit light curves, and is independent of the stellar mass and radius. Relaxing the prior also produced significant increases in $v \sin I$, and substantially raised the impact parameter from $\overline{b} = 0.15^{+0.33}_{-0.30}$ to $\overline{b} = 0.62^{+0.11}_{-0.13}$. Furthermore, I found that removing the prior increased the value of the stellar radius penalty, S, from $\overline{S} = 14.0$ to $\overline{S} = 105.3$.

Allowing the eccentricity to float led to a clear and significant difference in both χ^2_{red} and the total χ^2 for the combined photometric and spectroscopic model. The values returned by my algorithm lie at $\geq 7\sigma$ from $e = 0$, and were found to be significant by the F-test of Lucy & Sweeney (1971). This confirms the eccentricity detection of Barros et al. (2011a), and the values that I find are consistent with the value of $e = 0.0314^{+0.0046}_{-0.0041}$ reported by those authors.

My adopted model for this system therefore uses an eccentric orbit, does not include a long-term RV trend, does not apply a prior on $v \sin I$, and does utilise a prior on the stellar radius. This model returns values of $\lambda = 9.2^{\circ}{}^{+18.1}_{-15.5}$, $v \sin I = 7.7^{+0.5}_{-0.4}\,\mathrm{km\,s^{-1}}$ (slower than the spectroscopic result), $b = 0.09^{+0.13}_{-0.06}$ and $i = 89.6^{\circ}{}^{+0.3}_{-0.6}$, all of which indicate a well-aligned system. The radial velocity curves are displayed in Fig. 5.11. The difference in quality between the FIES data presented by Simpson et al. (2011c) and my new HARPS measurements is immediately apparent, particularly during the first half of the transit. The shape of the anomaly is well defined, and it has the large amplitude that is expected given the host star's rapid rotation. It also appears to be highly symmetric, lending credence to the conclusion that the system is likely well-aligned.

I find that the radial velocity semi-amplitudes and barycentric velocities vary somewhat

Table 5.6: *A comparison of the χ^2 and $\chi^2_{\rm red}$ values from the Rossiter-McLaughlin analysis of WASP-38 for each combination of Bayesian priors. All values of χ^2 include the Bayesian penalties applicable for that combination of priors.*

$v \sin I$ prior	MS prior	$\dot{\gamma}/\mathrm{ms^{-1}yr^{-1}}$	eccentricity	$v \sin I/\mathrm{km\,s^{-1}}$	$\lambda/^\circ$	χ^2	$\chi^2_{\rm RV}$	$\chi^2_{\rm red}$
off	off	0	0.029 ± 0.003	$8.2^{+0.4}_{-0.3}$	2.5 ± 2.3	22542 ± 212	147 ± 17	1.1 ± 0.1
off	on	0	$0.028^{+0.004}_{-0.003}$	7.3 ± 0.3	$1.3^{+13.3}_{-16.9}$	22581 ± 213	147 ± 17	1.1 ± 0.1
off	off	$2.0^{+3.2}_{-2.0}$	0.029 ± 0.003	8.2 ± 0.4	$2.5^{+2.5}_{-2.3}$	22542 ± 212	148 ± 17	1.1 ± 0.1
off	on	$0.4^{+0.3}_{-0.4}$	0.027 ± 0.003	7.3 ± 0.3	$5.3^{+8.9}_{-11.1}$	22563 ± 212	147 ± 17	1.1 ± 0.1
off	off	0	0	8.2 ± 0.4	$3.4^{+2.5}_{-2.4}$	22639 ± 213	251 ± 22	1.8 ± 0.2
off	on	0	0	7.3 ± 0.3	$8.7^{+9.1}_{-9.2}$	22685 ± 213	250 ± 22	1.8 ± 0.2
off	off	$-11.3^{+8.0}_{-10.0}$	0	$8.2^{+0.4}_{-0.3}$	3.6 ± 2.5	22644 ± 213	250 ± 22	1.8 ± 0.2
off	on	$-0.01^{+0.01}_{-0.01}$	0	7.4 ± 0.3	$16.2^{+8.7}_{-9.6}$	22667 ± 213	251 ± 22	1.8 ± 0.2
8.3 ± 0.4	off	0	0.028 ± 0.003	8.2 ± 0.3	$2.6^{+2.9}_{-2.6}$	22545 ± 212	148 ± 17	1.1 ± 0.2
8.3 ± 0.4	on	0	$0.028^{+0.004}_{-0.003}$	$7.6^{+0.3}_{-0.2}$	$5.3^{+11.7}_{-16.3}$	22590 ± 213	152 ± 17	1.1 ± 0.1
8.3 ± 0.4	off	-0.03 ± 0.01	$0.028^{+0.003}_{-0.004}$	8.2 ± 0.3	$2.2^{+2.3}_{-2.4}$	22546 ± 212	149 ± 17	1.1 ± 0.1
8.3 ± 0.4	on	$0.04^{+0.11}_{-0.15}$	$0.028^{+0.004}_{-0.003}$	7.7 ± 0.3	$15.9^{+21.6}_{-17.9}$	22577 ± 213	150 ± 17	1.1 ± 0.1
8.3 ± 0.4	off	0	0	$8.2^{+0.2}_{-0.3}$	$3.1^{+2.4}_{-2.5}$	22640 ± 213	252 ± 22	1.8 ± 0.2
8.3 ± 0.4	on	0	0	7.7 ± 0.3	$14.2^{+13.8}_{-10.8}$	22687 ± 213	253 ± 23	1.8 ± 0.2
8.3 ± 0.4	off	$0.1^{+0.7}_{-0.1}$	0	8.2 ± 0.3	$3.7^{+2.7}_{-2.3}$	22641 ± 213	252 ± 22	1.8 ± 0.2
8.3 ± 0.4	on	$-3.2^{+3.7}_{-7.6}$	0	$7.7^{+0.3}_{-0.2}$	$12.4^{+9.8}_{-9.4}$	22692 ± 213	251 ± 22	1.8 ± 0.2

between the 5 different spectroscopic data sets that I analysed (CORALIE data, SOPHIE data, FIES data, HARPS data out-of-transit, and HARPS data in-transit). In particular, the data obtained using FIES by Simpson et al. (2011c) has a much smaller semi-amplitude than any of the other data sets; $0.152 \pm 0.030\,\mathrm{km\,s^{-1}}$ compared to values between 0.246 ± 0.001 and $0.255 \pm 0.007\,\mathrm{km\,s^{-1}}$. Interestingly, Simpson et al. found a semi-amplitude of $0.2538 \pm 0.0035\,\mathrm{km\,s^{-1}}$ in their analysis, but I suspect that this was overwhelmingly derived from the SOPHIE and CORALIE data, which cover the entire orbital phase. The barycentric velocities agree well with the results of that previous study however.

5.7.2 Doppler tomography

I again used the set of priors adopted for my RM modelling as the basis for the Doppler tomography analysis, and Table 5.7 displays the results from this analysis, together with the results from Simpson et al. (2011c) and my own RM analysis. It is immediately apparent that I have been able to dramatically reduce the uncertainties on the projected spin-orbit alignment angle; I will return to the question of why this is in Section 5.9. The signature of the planet is clearly defined in Fig. 5.12, and in the final residual image there is no sign of any anomalies in the stellar line profiles, indicating that the host star is chromospherically quiet.

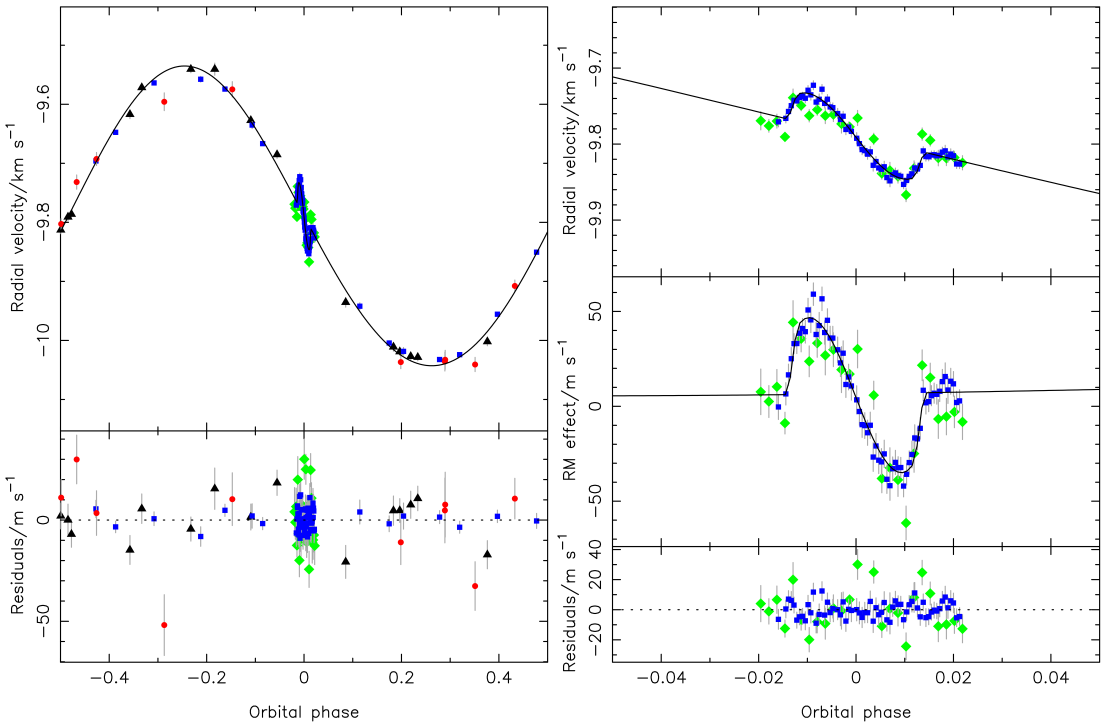

Figure 5.11: *Radial velocity curve produced by my optimal model for the WASP-38 system. The model uses an eccentric orbit and a prior on the stellar radius, but no long-term radial velocity trend is found and the prior on the spectroscopic $v \sin I$ is not applied. Data from SOPHIE are denoted by circles. Data from FIES are denoted by diamonds. Rest of legend as for Fig. 5.3.*

Table 5.7: *Results from my two analysis methods, compared against results from the previous Rossiter-McLaughlin analysis by Simpson et al. (2011c). I have significantly reduced the uncertainties on the projected spin-orbit alignment angle compared to their original work.*

Source	$v \sin I$/km s^{-1}	$\lambda/°$	b/R_s
Simpson et al. (2011c)	8.58 ± 0.39	15^{+33}_{-43}	$0.27^{+0.10}_{-0.14}$
This work: RM effect	$7.7^{+0.5}_{-0.4}$	$9.2^{+18.1}_{-15.5}$	$0.09^{+0.13}_{-0.06}$
This work: Tomography	$7.5^{+0.1}_{-0.2}$	$7.5^{+4.7}_{-6.1}$	$0.12^{+0.08}_{-0.07}$

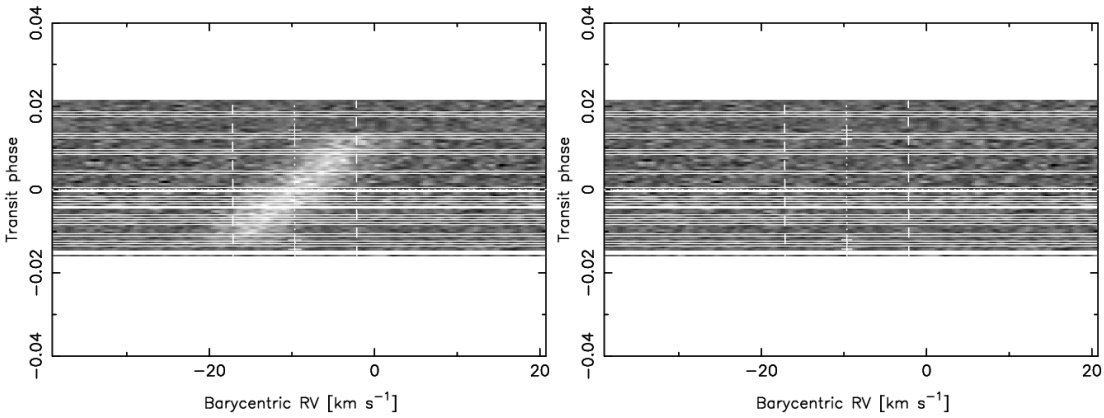

Figure 5.12: *Left: Residual map of WASP-38 time series CCFs with the model stellar spectrum subtracted. The bright signature of the planet is clearly visible, and it's trajectory from bottom left to top right clearly indicates a prograde orbit. Right: The best-fitting model for the time-variable planet feature has been subtracted, leaving the overall residual map. The lack of any remaining signatures suggests that the star is chromospherically quiet.*
Details as for Fig. 5.10.

5.8 HAT-P-27/WASP-40

HAT-P-27 (Béky et al., 2011) is a fairly typical hot Jupiter system, with a $0.6M_{\rm Jup}$ planet in a 3.04 d orbit around a late-G/early-K type star with $T_{\rm eff} = 5190^{+160}_{-170}$ K and super-solar metallicity. The system was characterised using photometry from HATnet and from KeplerCam on the 1.2m FLWO telescope, and spectroscopy from HIRES. It was also independently discovered by the WASP survey using the combined SuperWASP and WASP-S arrays, together with spectroscopy from SOPHIE, and designated WASP-40 (Anderson et al., 2011a).

New spectroscopic measurements were made using HARPS throughout the transit on the night of 2011 May 12, and additional observations carried out at a range of orbital phases throughout 2011 May. New photometric observations were also made using TRAPPIST on 2011 May 17, covering a full transit. I combined these new data with those from both Béky et al. (2011) and Anderson et al. (2011a) for my attempt to characterise the RM effect.

Barry Smalley and Amanda Doyle again used the new HARPS spectra to determine $v \sin I = 2.4 \pm 0.5\,{\rm km\,s^{-1}}$, and the calibration of Bruntt et al. (2010) to adopt $v_{\rm mac} = 1.0 \pm 0.3\,{\rm km\,s^{-1}}$. This estimate of $v \sin I$ agrees well with the $v \sin I = 2.5 \pm 0.9\,{\rm km\,s^{-1}}$ from Anderson et al. (2011a), but is substantially different to the value of $v \sin I = 0.4 \pm 0.4\,{\rm km\,s{-}1}$ obtained by Béky et al. (2011), who used $v_{\rm mac} = 3.29\,{\rm km\,s{-}1}$ based on the calibration of Valenti & Fischer (2005). Barry Smalley found that using such a high macroturbulence value led to a poor

fit for many of the spectral lines, even with $v \sin I = 0.0\,\mathrm{km\,s^{-1}}$, and therefore suggests that Béky et al. (2011) have overestimated the broadening in their SOPHIE spectra. The Valenti & Fischer (2005) calibration provides only an upper limit on the macroturbulence, which for cool stars such as WASP-40 can be significantly different from the true values.

5.8.1 Rossiter-McLaughlin analysis

I found that my original estimate of $1\,\mathrm{m\,s^{-1}}$ for the stellar "jitter" produced poorly constrained ($\chi^2_{\mathrm{red}} \approx 1.7$) models. I calculated possible values of $5.9\,\mathrm{m\,s^{-1}}$ (20th percentile), $7.5\,\mathrm{m\,s^{-1}}$ (median), and $9.8\,\mathrm{m\,s^{-1}}$ (80th percentile) using the method of Wright (2005), and apply the latter to the existing SOPHIE data. I also note that Béky et al. (2011) applied a "jitter" of $6.3\,\mathrm{m\,s^{-1}}$ to their HIRES data. To confirm that this was reasonable, I analysed the photometric data in conjunction with only the HIRES spectroscopic data, finding that my initial estimate of $1\,\mathrm{m\,s^{-1}}$ produced $\chi^2_{\mathrm{red}} = 10.0 \pm 1.5$, the 20th percentile value produced $\chi^2_{\mathrm{red}} = 1.1 \pm 0.5$, the median value produced $\chi^2_{\mathrm{red}} = 0.7 \pm 0.4$, and the 80th percentile value produced $\chi^2_{\mathrm{red}} = 0.4 \pm 0.3$, whilst applying their estimate produced $\chi^2_{\mathrm{red}} = 1.0 \pm 0.5$. I therefore follow Béky et al. and apply a "jitter" of $6.3\,\mathrm{m\,s^{-1}}$ to the HIRES data.

As with my RM analysis of WASP-32, I found that there was little to separate the different models for the WASP-40 system, as no significant differences were apparent in the values of χ^2_{red} that I obtained. The eccentricities returned for models with non-circular orbits were found to be insignificant by the statistical test of Lucy & Sweeney (1971), and the values were all found to be consistent with $e = 0$ to within 1.5σ. I also note that the addition of HARPS spectrographic measurements has reduced the value of any possible eccentricity in the system by a factor of 10 compared to the results in Anderson et al. (2011a). The addition of a long-term radial velocity trend to the model was found to provide no improvement in the quality of the fit obtained, and the low magnitude of any possible trend ($|\dot{\gamma}| < 43\,\mathrm{m\,s^{-1}\,yr^{-1}}$) leads me to conclude that no such trend is present in the system. Imposing a prior on the stellar radius produced only small changes in the mass ($|\delta M_s| \leq 2$ percent), radius ($\delta R_s \leq 3$ percent), and density ($\delta \rho_s \leq 7$ percent) of the host star. The impact parameter was similarly unaffected, with only the error bars increasing with the relaxation of the prior.

Adding a prior on $v \sin I$ using the spectroscopic measurement produced no change in the value of χ^2_{red}, but it significantly lowered the value of $v \sin I$ returned by the MCMC algorithm, and greatly reduced the uncertainties on the values of λ that were being produced. Examina-

Table 5.8: *A comparison of the χ^2 and $\chi^2_{\rm red}$ values from the Rossiter-McLaughlin analysis of WASP-40 for each combination of Bayesian priors. All values of χ^2 include the Bayesian penalties applicable for that combination of priors.*

$v\sin I$ prior	MS prior	$\dot{\gamma}/\mathrm{ms^{-1}yr^{-1}}$	eccentricity	$v\sin I/\mathrm{km\,s^{-1}}$	$\lambda/^\circ$	χ^2	$\chi^2_{\rm RV}$	$\chi^2_{\rm red}$
off	off	0	$0.013^{+0.018}_{-0.009}$	$0.6^{+0.7}_{-0.4}$	$24.4^{+75.2}_{-35.8}$	18306 ± 191	70 ± 12	1.3 ± 0.2
off	on	0	$0.017^{+0.023}_{-0.013}$	$0.6^{+0.7}_{-0.4}$	$24.0^{+64.9}_{-33.6}$	18312 ± 191	69 ± 12	1.3 ± 0.2
off	off	$29.3^{+13.2}_{-13.5}$	$0.014^{+0.017}_{-0.010}$	$0.6^{+0.7}_{-0.4}$	$24.2^{+74.0}_{-36.2}$	18299 ± 191	64 ± 11	1.2 ± 0.2
off	on	$0.3^{+0.2}_{-0.3}$	$0.016^{+0.019}_{-0.011}$	$0.7^{+0.7}_{-0.5}$	$22.4^{+59.6}_{-30.5}$	18193 ± 191	70 ± 12	1.3 ± 0.2
off	off	0	0	$0.6^{+0.7}_{-0.4}$	$24.2^{+76.0}_{-44.5}$	18159 ± 191	69 ± 12	1.3 ± 0.2
off	on	0	0	$0.6^{+0.7}_{-0.4}$	$21.9^{+73.2}_{-35.3}$	18310 ± 191	69 ± 12	1.3 ± 0.2
off	off	$-0.7^{+0.9}_{-0.7}$	0	$0.7^{+0.7}_{-0.5}$	$28.8^{+59.1}_{-43.9}$	18187 ± 191	70 ± 12	1.3 ± 0.2
off	on	$0.3^{+0.4}_{-0.4}$	0	$0.6^{+0.7}_{-0.4}$	$26.8^{+75.1}_{-39.5}$	18312 ± 191	69 ± 12	1.3 ± 0.2
2.4 ± 0.5	off	0	$0.015^{+0.021}_{-0.011}$	1.9 ± 0.4	$8.5^{+13.2}_{-10.4}$	18314 ± 191	71 ± 12	1.3 ± 0.2
2.4 ± 0.5	on	0	$0.013^{+0.018}_{-0.009}$	$1.8^{+0.4}_{-0.5}$	$10.6^{+19.4}_{-12.0}$	18305 ± 191	72 ± 12	1.4 ± 0.2
2.4 ± 0.5	off	$3.3^{+3.8}_{-9.1}$	$0.012^{+0.014}_{-0.009}$	1.9 ± 0.4	$9.1^{+16.0}_{-10.6}$	18311 ± 191	70 ± 12	1.3 ± 0.2
2.4 ± 0.5	on	$1.4^{+1.1}_{-1.0}$	$0.009^{+0.021}_{-0.006}$	1.8 ± 0.4	$10.9^{+13.5}_{-11.2}$	18314 ± 191	71 ± 12	1.3 ± 0.2
2.4 ± 0.5	off	0	0	1.9 ± 0.4	$8.8^{+13.5}_{-10.7}$	18311 ± 191	71 ± 12	1.3 ± 0.2
2.4 ± 0.5	on	0	0	1.9 ± 0.4	$8.7^{+12.6}_{-11.0}$	18312 ± 191	71 ± 12	1.3 ± 0.2
2.4 ± 0.5	off	$16.1^{+16.6}_{-20.6}$	0	1.8 ± 0.4	$9.7^{+13.4}_{-11.0}$	18301 ± 191	66 ± 12	1.3 ± 0.2
2.4 ± 0.5	on	$0.04^{+0.14}_{-0.10}$	0	1.9 ± 0.4	$8.1^{+12.2}_{-10.7}$	18304 ± 191	70 ± 12	1.3 ± 0.2

tion of the HARPS spectroscopy indicated that the amplitude of any RM effect was likely to be low, with the error bars on the data such that they obscured any possible anomaly in the RV curve. This indicated that the value of $v\sin I$ was likely to be small, and that the error bars on λ would likely be high. This information, combined with the lack of any difference in the quality of fit, led me to select a solution in which the prior on $v\sin I$ was not applied.

My adopted solution therefore uses the combination of a circular orbit and no long-term radial velocity trend, with neither the prior on $v\sin I$ nor the prior on the stellar mass applied. The radial velocity curve that results is shown in Fig. 5.13. Values of $\lambda = 24.2^{\circ}{}^{+76.0}_{-44.5}$, $v\sin I = 0.6^{+0.7}_{-0.4}\,\mathrm{km\,s^{-1}}$, $b = 0.87 \pm 0.01$ and $i = 85.0^{\circ} \pm 0.2$ were returned for this combination of conditions. I note that the value I obtain for the impact parameter is consistent with that found by Anderson et al. (2011a), who found a 40.5 percent likelihood that the system is grazing. I also note that this system serves as a good example of the systematic discussed by Albrecht et al. (2011). They showed that systems with low-amplitude, low signal-to-noise measurements of the Rossiter-McLaughlin effect were preferentially found to be either close to aligned ($\lambda = 0^{\circ}$) or anti-aligned ($\lambda = 180^{\circ}$), with the posterior-probability distributions of these systems showing a greater number of possible solutions around these angles. Fig. 5.14 shows the posterior probability distribution for λ against $v\sin I$ from my MCMC run. It is

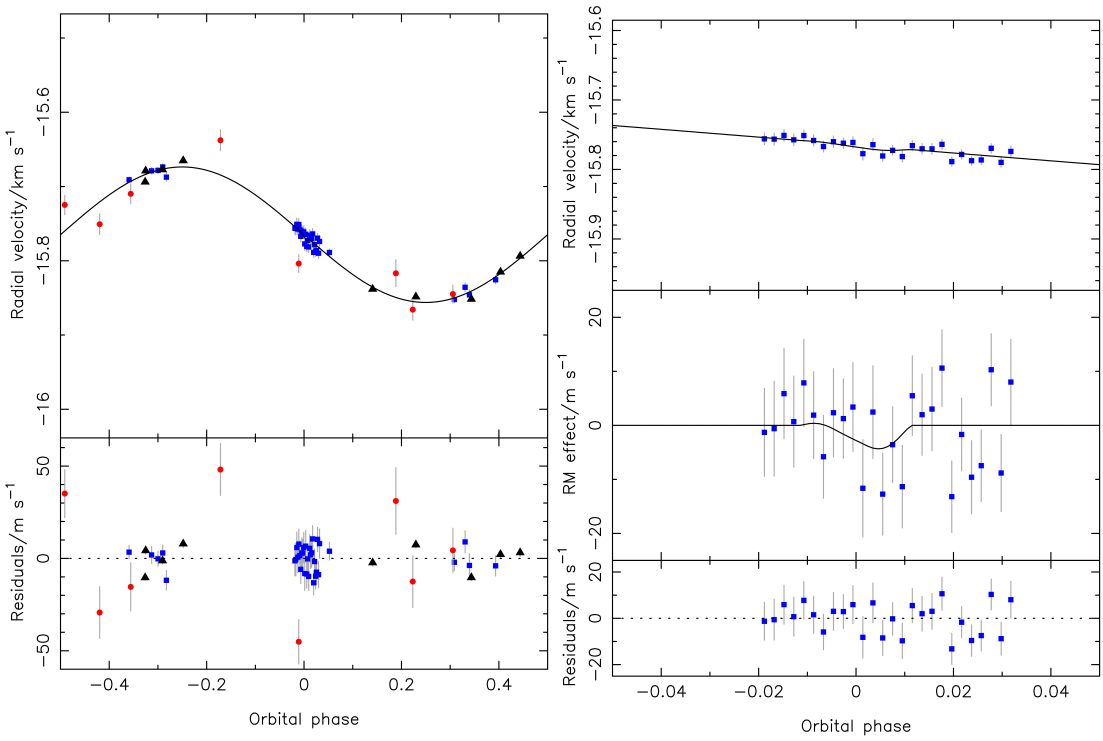

Figure 5.13: *Results from the fit to the radial velocity data for my adopted solution for WASP-40. A circular orbit was used, with no prior on the spectroscopic $v \sin I$, no long-term radial velocity trend, no prior on the stellar radius. Data from HIRES are denoted by triangles. Data from SOPHIE are denoted by circles. Data from HARPS are denoted by squares. Error bars are marked in grey; some are smaller than the size of the data points that they accompany. Format as for Fig. 5.3.*

immediately clear that there are a greater number of solutions, covering a greater range of values, for $v \sin I$ at angles close to 0°; the effect at 180° is less pronounced. I note that my solution lies relatively close to the former angle, as predicted by Albrecht et al. (2011), but I also note that my error bars are such that a wide range of alignment angles are included in the possible range of solutions that I find.

In light of this, I analysed the system using my preferred choice of priors and initial conditions, but with no Rossiter-McLaughlin fitting. I found that this produced results that showed no difference in terms of quality of fit from my adopted solution, with a value of $\chi^2_{\rm red,noRM} = 1.3 \pm 0.2$ that is in complete agreement with $\chi^2_{\rm red} = 1.3 \pm 0.2$ from the solution adopted above. I therefore consider these weak constraints on the alignment angle to be equivalent to a non-detection of the Rossiter-McLaughlin effect.

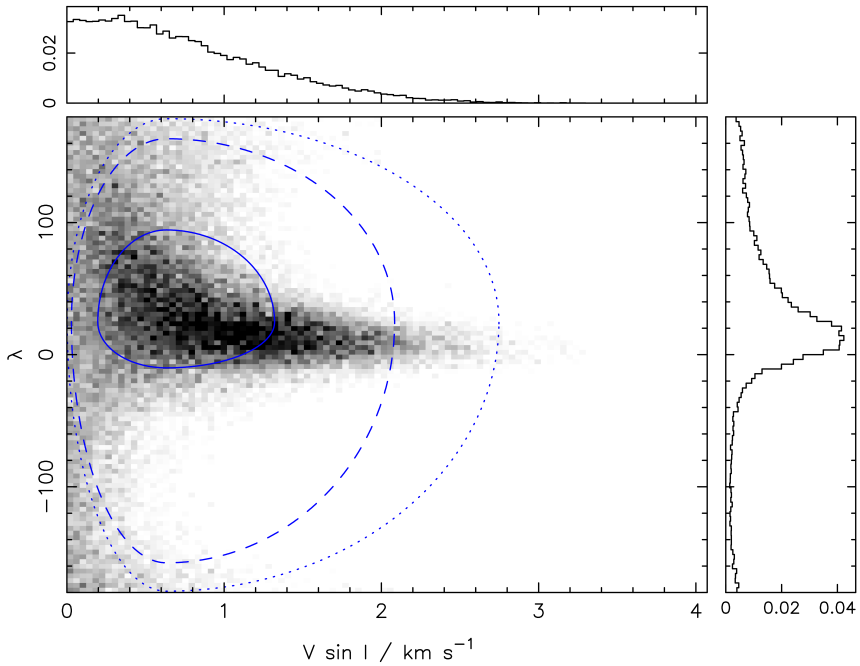

Figure 5.14: *Posterior probability distribution for $v \sin I$ and λ, derived from the Markov chain, for the fit to the data for WASP-40 described in Fig. 5.13. Legend as for Fig. 5.4. $\lambda = 0$ lies well within the main body of the distribution.*

5.8.2 Doppler tomography

I attempted to model the system using Doppler tomography, but the combination of the low signal-to-noise and slow rotation proved too difficult to analyse using this method. This nicely highlights a major limitation of the technique, namely systems with poor quality spectroscopic data. RM analysis is able to overcome the poor data quality to provide a result, although it may be inconclusive. However the tomography method is simply unable to process the data if the effect of the planetary transit on the stellar line profile is insignificant.

5.9 Why use Doppler Tomography?

As I discussed in Section 5.1, Doppler tomography is one of a number of methods for characterising spin-orbit alignment that are beginning to be used as alternatives to the traditional radial velocity based approach that I have used to analyse all six of the systems in this study. Although tomography has weaknesses, and cannot be applied to every planetary system (as witnessed with WASP-40), it has one great selling point over the radial velocity method. Tomography is able to lift the strong degeneracy that exists between $v \sin I$ and λ, and which is strongest in systems with low impact parameter.

The geometry of the path that the planetary orbit traces across the stellar disc affects the uncertainty in the spin-orbit alignment angle, particularly if that path is symmetric with respect to the approaching and receding hemispheres of the star. As the impact parameter increases, the range of alignment angles that can produce a symmetric RM curve decreases (Albrecht et al., 2011). The limiting cases illustrate this well. With $b = 0$, any value of λ will produce equal transit path lengths through the red- and blue-shifted halves of the stellar disc, whilst with $b = 1$, only $\lambda = 0°$ and $\lambda = 180°$ will have the same effect. Thus as b decreases, the uncertainty in the estimate of λ increases.

This is not the only parameter involved however. The stellar rotation, $v \sin I$, dictates the amplitude of the Rossiter-McLaughlin anomaly, but this is often ambiguous owing to the uncertainties present in the radial velocity measurements. It is often not clear, particularly for systems with low $v \sin I$, whether the anomaly is truly asymmetric, or whether it is an effect produced by the error bars (see WASP-25). This means that the same anomaly can often be fit in two different ways. Either $v \sin I$ is low and λ indicates misalignment, with the resulting asymmetry in the model used to fit the uncertainties, or λ is low and a rapid $v \sin I$ is used, with the greater amplitude providing the required fit. Often what results is a compromise solution, with large error bars on both parameters and some degree of degeneracy between them. This arises owing to the use of the Rossiter-McLaughlin effect to characterise both parameters simultaneously. The problem is exacerbated for systems with low signal-to-noise, for which the range of possible models that fit the data is greatly increased owing to the greater relative size of the uncertainties, and for systems with low impact parameter, for the reasons discussed above.

The Doppler tomography method does not suffer from this same problem, and is therefore able to provide better constraints on λ in these problematic cases. Directly modelling the separate components of the CCF provides several separate constraints on the parameters involved in the model, and the geometric calculation of the position of the planet's shadow on the stellar disc helps to remove ambiguity regarding λ. These two factors lift the degeneracy experienced with the traditional method.

WASP-38, as an example of a system with low impact parameter, provides a reasonable example of the advantages that the tomographic analysis method holds over the standard radial velocity method. Table 5.7 clearly shows that the error bars on λ have been decreased

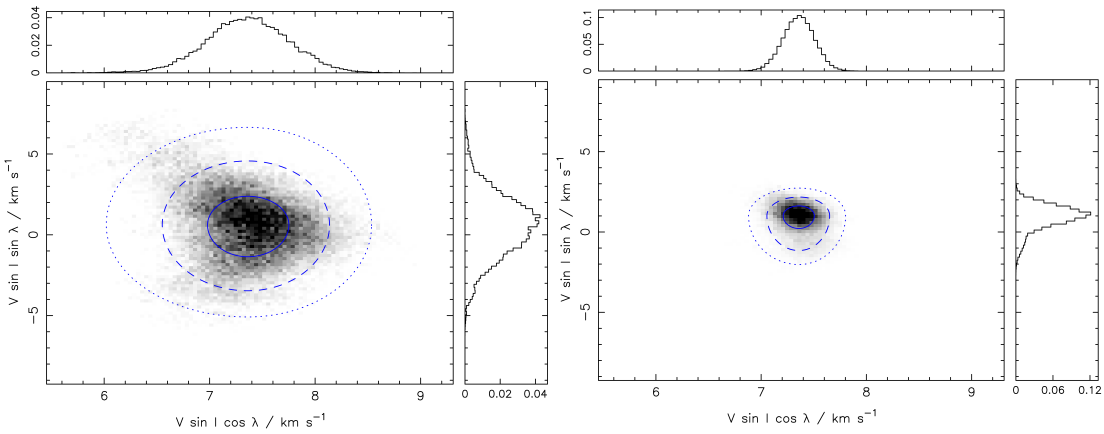

Figure 5.15: *Posterior probability distributions for $v \sin I$ and λ for both of the analysis methods discussed in this work. These distributions are for the analysis of the WASP-38 system discussed in Section 5.7. Legend as for Fig. 5.14.* ***Left:*** *Radial velocity measurement based Rossiter-McLaughlin analysis.* ***Right:*** *Doppler Tomography. The difference between the two methods is stark, with the tomographic analysis yielding a much reduced correlation between the parameters.*

by the use of Doppler tomography, and Fig. 5.15 shows the change in the relationship between the values of $v \sin I$ and λ for the two analysis methods. The two posterior probability density plots show completely different distributions, with that for the radial velocity method showing a clear correlation between the two parameters, with obvious degeneracies in the fitted values. The tomographic distribution, on the other hand, shows very little in the way of correlation, and although there is still some spread in the λ distribution the range of $v \sin I$ values has quite clearly been heavily restricted.

5.10 Conclusion

In this Chapter I have presented measurements of spin-orbit alignment in six planetary systems. I have also demonstrated the way in which Doppler Tomography can provide more stringent constraints on the uncertainty in λ compared to the Rossiter-McLaughlin effect, and shown that each method has cases where it is less than optimal. In the next Chapter I shall place these results in the context of full set of alignment angles, and analyse the effect that they have on the trends that are present within that sample.

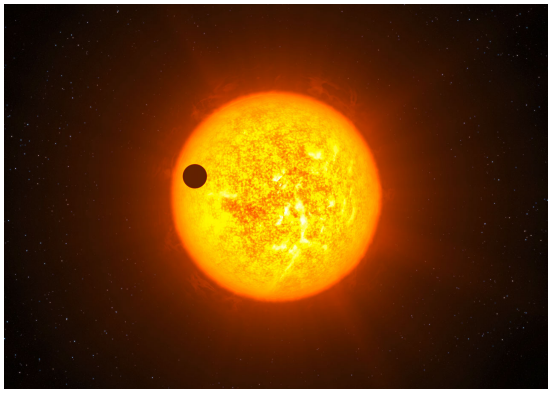

6

My alignment results in context

This chapter is based upon, and uses material from, Brown et al. (2012), MNRAS, 423, 1503-1520 and Brown et al. (2012), ApJ, 760, 139

The number of systems with measured or inferred spin-orbit alignment measurements is now such that it is possible to begin carrying out analysis of the ensemble of measurements. There have been many studies which attempt to identify trends within this sample, and each new additional result provides information that can be used to assess previously identified trends, or potentially discover new ones.

Fabrycky & Winn (2009) investigated 11 systems with known values of λ, deriving two theoretical distributions for ψ, the true alignment angle, using different assumptions about the form of the distribution. They suggested, based on an apparent dual population within their data set, that there might be two routes for planet migration, one producing mostly aligned planets and the other producing misaligned planets.

A possible trend in the data was noticed by (Johnson et al., 2009), who found that planets with high mass tend to be found in misaligned (but not retrograde), eccentric orbits. Subsequent observations have often supplied counter-examples to this trend (for example HAT-P-7: Winn et al. 2009; Narita et al. 2009b; WASP-18: Hellier et al. 2009; Triaud et al. 2010), but planets with $M_p \gtrsim 3\,M_{\rm Jup}$ do appear to have a different distribution of spin-orbit alignment angles (Hébrard et al., 2011a). This was tentatively interpreted as possible evidence for a combination of Kozai-Lidov cycles with tidal circularisation and realignment, but small number statistics were cited as a cautionary factor. Increasing the number of measurements has weakened the initial trend, with more systems in the 'massive planet' category being found to exhibit well-aligned systems. Nevertheless, the variance in the λ distribution remains, with high mass planets showing an apparent limit on their alignment angle of $|\lambda| < 50°$. More observations of high mass planets are still needed to determine the strength of this correlation however[1].

One of the more intriguing suggestions was put forward by Winn et al. (2010a), who speculated that the division into aligned and misaligned planets might be dependent on the effective temperature of the host star. Using a sample of 19 systems with known λ, they found that planets in misaligned orbits seem to preferentially orbit 'hot' stars ($T_{\rm eff} \gtrsim 6250\,$K), whilst aligned planetary orbits seem to be found mostly around 'cool' stars ($T_{\rm eff} \lesssim 6250\,$K). They suggested that this might be connected to the size of the convective envelope, with tidal realignment of orbits around 'hot' stars being suppressed owing to their small convective zone. Winn et al. further conjectured that the λ distribution at the time of their publication could be completely explained by a migration mechanism driven by a combination of Kozai-Lidov oscillations and planet-planet scattering, without the need to invoke disc migration. Moutou et al. (2011) found that there was no statistically significant difference between the 'hot' and 'cool' populations, at least for the limiting temperature chosen by Winn et al. (2010a), and subsequent measurements have been inconclusive.

Triaud et al. (2010) added 6 planets to the ensemble of known Rossiter-McLaughlin (RM) measurements. Calculating individual ψ distributions for each planet based on the assumption that stellar rotation axes are randomly oriented on the sky, they produced a total distribution for the ensemble of planets, finding that it matched the theoretical distribution of

[1]More recent work along similar lines has tended to concentrate on the ratio, q, of the planetary mass to the stellar mass rather than the planetary mass in isolation (Albrecht et al., 2012b), since this quantity appears in tidal evolution equations and plays a role in other mechanisms as well.

Fabrycky & Tremaine (2007) for Kozai-Lidov mechanism dominated migration, further implying that disc migration might be superfluous to requirements for explaining the presence of hot Jupiters.

A more recently discovered correlation is that of alignment angle with host star age. Triaud (2011) noticed that, for stars with $M_s \geq 1.2M_\odot$, all systems older than 2.5 Gyr are well-aligned. This implies that the distribution of λ changes with time, which in turn suggests that some misalignment mechanism must operate during the youth of hot Jupiter systems, followed by some method of realigning the system as it evolves. If age is the primary factor then having tidal interactions as the governing mechanism for this latter stage would fit with the observed age trend, as planets around older stars will have had longer to tidally realign. On the other hand it may also be that strongly misaligned planets are simply being destroyed much more quickly than their aligned cousins; indeed, such an effect has been theoretically demonstrated for retrograde planets, which are predicted to reach disruption distances several times faster than prograde planets (Barker & Ogilvie, 2009b; Winn et al., 2010a). This would lead to a decrease in the number of hot Jupiters with time, yet Triaud (2011) found no such trend. Either tidal realignment occurs faster than orbital decay, or some other mechanism is responsible for the observed evolution of the distribution of angles.

Albrecht et al. (2012b) re-examined all of these previously detected trends using an updated, homogeneous database of Rossiter-McLaughlin measurements that included both re-analyses and new measurements. They found that all of the existing trends are consistent with the idea that tidal interactions are responsible for the evolution of the spin-orbit alignment in hot Jupiter systems. They also considered the dependence of λ on the scaled orbital distance, finding that it too is consistent with a tide-driven evolutionary picture. Their estimates of characteristic tidal timescales showed that systems which were expected to align rapidly exhibit angles consistent with alignment, whilst those for which tidal realignment was predicted to be weaker display a nearly random distribution of angles. Albrecht et al. stopped short, however, of claiming any mechanism for the production of the initial distribution of λ which, from evidence collected so far, seems to be required to be isotropic (Fabrycky & Tremaine, 2007; Triaud et al., 2010).

I now consider the results that I presented in the previous Chapter, and which are summarised in Table 6.1, in the context of the complete set of systems with spin-orbit alignment

measurements, as listed in the Holt-Rossiter-McLaughlin database compiled by René Heller[2]. At the time of writing, 66 planets (64 systems) had such measurements published, including the 6 systems that I have analysed.

[2]As of 2013 January 10. http://www.aip.de/People/RHeller

Table 6.1: *A summary of my adopted results for WASP-16, WASP-25, WASP-31, WASP-32, WASP-38, and WASP-40. Those for WASP-32 and WASP-38 are derived from Doppler tomography, whilst those for the remaining systems are derived from the Rossiter-McLaughlin analysis.*

Parameter	Units	WASP-16	WASP-25	WASP-31	WASP-32	WASP-38	WASP-40
Fitted Parameters							
D		0.0109 ± 0.0003	0.0190 ± 0.0003	0.0153 ± 0.0003	0.0108 ± 0.0001	0.0069 ± 0.0001	0.0143 ± 0.0005
K	$\mathrm{m\,s^{-1}}$	0.118 ± 0.002	0.075 ± 0.004	0.056 ± 0.006	0.478 ± 0.011	0.252 ± 0.004	0.0912 ± 0.002
b	R_s	0.82 ± 0.02	$0.42^{+0.04}_{-0.05}$	$0.77^{+0.01}_{-0.02}$	0.66 ± 0.02	$0.12^{+0.08}_{-0.07}$	0.87 ± 0.01
W	days	0.0796 ± 0.0014	0.1152 ± 0.0008	0.1075 ± 0.0013	0.0990 ± 0.0007	0.1969 ± 0.0010	$0.070^{+0.001}_{-0.002}$
P	days	3.11859 ± 0.00001	3.76483 ± 0.00001	3.405900 ± 0.000004	2.718661 ± 0.000002	6.87188 ± 0.00001	$3.039577^{+0.000005}_{-0.000006}$
T_0	$BJD_{\mathrm{UTC}} - 2450000$	4618.7334 ± 0.0003	5278.7613 ± 0.0002	5219.9361 ± 0.0003	5681.1945 ± 0.0002	5322.1774 ± 0.0006	5407.9088 ± 0.0002
Derived parameters							
R_p/R_s		0.089 ± 0.006	$0.138^{+0.006}_{-0.007}$	0.124 ± 0.007	0.104 ± 0.005	0.083 ± 0.002	$0.120^{+0.009}_{-0.007}$
R_s/a		0.109 ± 0.004	0.091 ± 0.002	0.120 ± 0.003	0.129 ± 0.003	$0.0829^{+0.0008}_{-0.0007}$	$0.102^{+0.003}_{-0.004}$
R_s	$R_\odot$	0.98 ± 0.05	0.91 ± 0.03	1.20 ± 0.04	1.09 ± 0.03	1.35 ± 0.02	0.87 ± 0.04
M_s	$M_\odot$	$1.01^{0.05}_{-0.06}$	0.95 ± 0.04	1.14 ± 0.06	1.07 ± 0.05	1.23 ± 0.04	0.92 ± 0.06
ρ_s	$\rho_\odot$	$1.07^{+0.14}_{-0.12}$	$1.26^{+0.09}_{-0.08}$	0.66 ± 0.05	0.84 ± 0.05	0.50 ± 0.01	$1.38^{+0.16}_{-0.13}$
[Fe/H]		$0.004^{+0.108}_{-0.098}$	-0.11 ± 0.10	-0.16 ± 0.10	-0.13 ± 0.10	-0.02 ± 0.07	0.14 ± 0.11
$v \sin I$	$\mathrm{km\,s^{-1}}$	1.5 ± 0.3	2.8 ± 0.3	7.4 ± 0.7	$3.9^{+0.4}_{-0.5}$	$7.5^{+0.1}_{-0.2}$	$0.6^{+0.7}_{-0.4}$
R_p	$R_{\mathrm{Jup,eq}}$	1.00 ± 0.06	$1.22^{+0.04}_{-0.05}$	1.44 ± 0.06	1.10 ± 0.04	1.09 ± 0.02	$1.02^{+0.07}_{-0.06}$
M_p	M_{Jup}	0.86 ± 0.04	$0.56^{+0.03}_{-0.04}$	0.45 ± 0.05	$3.46^{+0.14}_{-0.12}$	2.71 ± 0.07	0.62 ± 0.03
a	AU	0.0419 ± 0.0008	0.0466 ± 0.0007	0.0463 ± 0.0008	0.0390 ± 0.0006	0.0758 ± 0.0008	0.0400 ± 0.0008
i	deg	84.9 ± 0.3	87.8 ± 0.3	84.7 ± 0.2	85.1 ± 0.2	$89.5^{+0.3}_{-0.4}$	85.0 ± 0.2
e		0(adopted)	0(adopted)	0(adopted)	0(adopted)	0.028 ± 0.003	0(adopted)
ω	deg	0	0	0	0	$-22.2^{+9.2}_{-8.1}$	0
λ	deg	$-0.9^{+6.8}_{-6.9}$	$13.0^{+9.0}_{-8.5}$	$2.2^{+3.4}_{-3.1}$	$10.5^{+6.4}_{-5.9}$	$7.5^{+4.7}_{-6.1}$	$24.2^{+76.0}_{-44.5}$
$\lvert\dot{\gamma}\rvert$	$\mathrm{m\,s\,yr^{-1}}$	0(adopted)	0(adopted)	0(adopted)	0(adopted)	0(adopted)	0(adopted)

6.1 Integration into the ensemble of results

The analyses of Winn et al. (2010a) and Albrecht et al. (2012b) provide a good starting point for integrating my new results into the existing ensemble of RM measurements. Fig. 6.1 reproduces fig. 2 from Winn et al. (2010a) (fig. 20 in Albrecht et al. 2012b), with the addition of all RM measurements made since its publication; I list the full sample of planets that I have used in Table 6.2. In order to provide a full picture of the current state of RM analysis, I elected to include most of the systems that Winn et al. (2010a) disregard during their analysis as having insufficiently precise measurements of λ[3]. Whilst it is true that making a definitive statement regarding alignment is more difficult for these systems owing to their large uncertainties, the criteria for granting misaligned status should take account of this. I am also interested in comparing my new measurements to the general form of the current ensemble. Omitting the systems listed above does not simplify this task. I do however exclude WASP-23 (Triaud et al., 2011), for which the result is still highly uncertain, and although WASP-2 has a measured value for λ, the most recent analysis of the system failed to detect a signal (Albrecht et al., 2011) and thus I also continue to exclude this system.

WASP-31 has an effective temperature of 6300 ± 100 K, which falls with 1σ of the border between the 'hot' and 'cool' categories of Winn et al. (2010a), albeit tending towards the 'hot' side. I cannot therefore draw any conclusions as to how it affects the trend proposed in that paper. WASP-40, at $T_{\rm eff} = 5190^{+160}_{-170}$, fits into the 'cool' category, but as previously noted it is effectively a non-detection and therefore it too provides no pertinent information as far as the trend with stellar effective temperature is concerned.

With an effective temperature of 5750 ± 100 K, WASP-25 falls into the 'cool' category ($T_{\rm eff} \leq 6250$ K) of Winn et al. (2010a), which they find to be preferentially aligned – their sample gives a probability of misalignment for 'cool' stars of 0.17. Updating this result using my expanded sample changes the probability to 0.22 using the criterion of Winn et al. (2010a), or to 0.13 using the criterion of $|\lambda| > 30°$ from Triaud et al. (2010). It is worth noting here that the apparently large differences in misalignment probability between the two criteria are an artefact of the sample size, which is still relatively small at 66 planets (32 'cool', 15 'hot', 13 'borderline'). Switching between the two criteria changes the number of misaligned systems by three for the 'cool' sub-sample, and has no effect on the number

[3]HAT-P-2, CoRoT-1, CoRoT-3, HD149026, Kepler-8, TrES-1 and TrES-2. See references within Winn et al. (2010a).

Table 6.2: *Relevant data for all of the planetary systems for which the Rossiter-McLaughlin effect had been characterised at the time of writing, excluding the systems that I have analysed and which are presented in Table 6.1.*

System	Reference	$i/°$	$v \sin I/\mathrm{km\,s^{-1}}$	Teff/K	$\lambda/°$
CoRoT-1	Pont et al. (2010); Torres et al. (2012)	85.1 ± 0.5	4.6 ± 0.9	6298 ± 66	-77.0 ± 11.0
CoRoT-2	Czesla et al. (2012); Torres et al. (2012)	$87.84^{+0.16}_{-0.17}$	$11.95^{+0.58}_{-0.55}$	5575 ± 66	$-1^{+6.6}_{-7.7}$
CoRoT-3	Deleuil et al. (2008); Triaud et al. (2009)	$86.10^{+0.73}_{-0.52}$	$35.8^{+8.2}_{-8.3}$	6740 ± 140	$-37.6^{+22.3}_{-10.0}$
CoRoT-11	Gandolfi et al. (2012)	83.41 ± 0.17	38.47 ± 0.07	6440 ± 120	0.1 ± 2.6
CoRoT-18	Hébrard et al. (2011b)	$86.5^{+1.4}_{-0.9}$	8.0 ± 1.0	5440 ± 100	10 ± 20
CoRoT-19	Guenther et al. (2012)	88.0 ± 0.7	6 ± 1	6090 ± 70	-52^{+27}_{-22}
Fomalhaut	Le Bouquin et al. (2009); Currie et al. (2012); Mamajek (2012)	65.9 ± 0.4	93	8540 ± 50	1.0 ± 3.3
HAT-P-1	Johnson et al. (2008)	86.28 ± 0.20	3.75 ± 0.58	5975 ± 45	3.7 ± 2.1
HAT-P-2	Loeillet et al. (2008); Albrecht et al. (2012b)	$90^{+0.85}_{-0.93}$	19.5 ± 1.4	6290 ± 60	9 ± 10
HAT-P-4	Winn et al. (2011b); Torres et al. (2012)	$88.76^{+0.89}_{-1.38}$	5.83 ± 0.35	5890 ± 67	-4.9 ± 11.9
HAT-P-6	Hébrard et al. (2011a); Albrecht et al. (2012b)	85.5 ± 0.4	7.8 ± 0.6	6570 ± 80	165 ± 6
HAT-P-7[1]	Pál et al. (2008); Albrecht et al. (2012b)	$80.8^{+2.8}_{-1.2}$	2.7 ± 0.5	6350 ± 80	155 ± 37
HAT-P-8	Moutou et al. (2011); Torres et al. (2012)	$87.5^{+1.9}_{-0.9}$	12.6 ± 1.0	6223 ± 67	$-17^{+9.2}_{-11.5}$
HAT-P-9	Moutou et al. (2011); Torres et al. (2012)	86.5 ± 0.2	13.4 ± 1.4	6253 ± 84	-16 ± 8
HAT-P-11[2]	Winn et al. (2010c); Sanchis-Ojeda & Winn (2011)	80^{+4}_{-3}	$1.00^{+0.95}_{-0.56}$	4780 ± 50	106^{+15}_{-12}
HAT-P-11[3]	Winn et al. (2010c); Sanchis-Ojeda & Winn (2011)	168^{+2}_{-5}	$1.00^{+0.95}_{-0.56}$	4780 ± 50	121^{+24}_{-21}
HAT-P-13 b	Winn et al. (2010b)	83.40 ± 0.68	1.66 ± 0.37	5640 ± 90	1.9 ± 8.6
HAT-P-14/WASP-27[1]	Winn et al. (2011b)	83.52 ± 0.22	8.18 ± 0.49	6600 ± 90	-170.9 ± 5.1
HAT-P-16	Buchhave et al. (2010); Moutou et al. (2011)	86.6 ± 0.7	3.9 ± 0.8	6158 ± 80	-10 ± 16
HAT-P-23	Bakos et al. (2011); Moutou et al. (2011)	85.1 ± 1.5	7.8 ± 1.6	5905 ± 80	15 ± 22
HAT-P-24	Kipping et al. (2010); Albrecht et al. (2012b)	88.6 ± 0.7	11.2 ± 0.9	6373 ± 80	20 ± 16
HAT-P-30/WASP-51	Johnson et al. (2011)	83.6 ± 0.4	3.07 ± 0.24	6304 ± 88	73.5 ± 9.0
HAT-P-32	Hartman et al. (2011); Albrecht et al. (2012b)	88.9 ± 0.4	20.6 ± 1.5	6207 ± 88	85 ± 1.5
HAT-P-34	Bakos et al. (2012); Albrecht et al. (2012b)	87.1 ± 1.2	24.3 ± 1.2	6442 ± 88	0 ± 14
HD149026	Carter et al. (2009); Albrecht et al. (2012b)	$84.5^{+0.60}_{-0.52}$	7.7 ± 0.8	6160 ± 50	12 ± 7
HD17156	Barbieri et al. (2009); Narita et al. (2009a)	87.21 ± 0.31	4.18 ± 0.31	6080 ± 80	10.0 ± 5.1
HD189733	Triaud et al. (2009)	$85.508^{+0.10}_{-0.05}$	3.32 ± 0.02	5040 ± 50	$-0.85^{+0.32}_{-0.28}$
HD209458	Winn et al. (2005); Albrecht et al. (2012b)	86.55 ± 0.03	4.4 ± 0.2	6070 ± 50	-5 ± 7
HD80606	Hébrard et al. (2010)	89.269 ± 0.018	1.7 ± 0.3	5570 ± 44	42 ± 8
Kepler-8	Jenkins et al. (2010); Albrecht et al. (2012b); Torres et al. (2012)	84.07 ± 0.33	8.9 ± 1.0	6251 ± 75	5 ± 7
Kepler-16[4]	Doyle et al. (2011); Winn et al. (2011a)	90 ± 9	0.920 ± 0.025	4337 ± 80	-1.6 ± 2.4
Kepler-17	Désert et al. (2011)	87.2 ± 0.15	4.7 ± 1.0	5630 ± 100	< 15.0
Kepler-30 b	Sanchis-Ojeda et al. (2012, 2013)	89.821 ± 0.167	1.94 ± 0.22	5498 ± 54	< 10
Kepler-30 c	Sanchis-Ojeda et al. (2012, 2013)	89.6773 ± 0.0302	1.94 ± 0.22	5498 ± 54	< 10
Kepler-30 d	Sanchis-Ojeda et al. (2012, 2013)	89.8406 ± 0.0202	1.94 ± 0.22	5498 ± 54	< 10
KOI-13[5]	Barnes et al. (2011)	85.0 ± 0.4	65 ± 10	8511 ± 400	23 ± 4
KOI-13[6]	Barnes et al. (2011)	85.0 ± 0.4	65 ± 10	8511 ± 400	156 ± 4
KOI-94 d	Hirano et al. (2012)	87.85 ± 0.55	$8.01^{+0.72}_{-0.73}$	6116 ± 30	-6^{+13}_{-11}
TrES-1	Charbonneau et al. (2005); Narita et al. (2007)	88.4 ± 0.3	1.3 ± 0.3	5230 ± 50	30 ± 21
TrES-2	Winn et al. (2008)	83.62 ± 0.14	1.0 ± 0.6	5850 ± 50	-9 ± 12
TrES-4	Narita et al. (2010b); Chan et al. (2011)	82.82 ± 0.37	8.5 ± 1.2	6200 ± 75	6.3 ± 4.7
WASP-1	Collier Cameron et al. (2007); Albrecht et al. (2011)	90 ± 2	$0.7^{+1.4}_{-0.5}$	6110 ± 45	-59^{+99}_{-26}
WASP-3	Miller et al. (2010); Torres et al. (2012)	$87.0^{+1.0}_{-1.1}$	13.9 ± 0.3	6375 ± 63	5^{+6}_{-3}
WASP-4	Sanchis-Ojeda et al. (2011)	$88.08^{+0.61}_{-0.43}$	2.14 ± 0.4	5500 ± 150	-1^{+14}_{-12}
WASP-5	Triaud et al. (2010)	86.1 ± 1.1	$3.24^{+0.35}_{-0.27}$	5700 ± 150	$12.1^{+8.0}_{-10.0}$
WASP-6	Gillon et al. (2009)	$88.47^{+0.65}_{-0.47}$	1.6 ± 0.3	5450 ± 100	-11^{+18}_{-14}
WASP-7	Southworth et al. (2011); Albrecht et al. (2012a)	$87.2^{+0.9}_{-1.2}$	14 ± 2	6400 ± 100	86 ± 6
WASP-8	Queloz et al. (2010)	$88.55^{+0.17}_{-0.18}$	2.0 ± 0.6	5600 ± 80	$-123.2^{+3.4}_{-4.4}$
WASP-12	Maciejewski et al. (2011a); Albrecht et al. (2012b); Torres et al. (2012)	$82.5^{+0.8}_{-0.7}$	$1.6^{+0.8}_{-0.4}$	6300 ± 150	59^{+15}_{-20}
WASP-14	Johnson et al. (2009); Blecic et al. (2011); Torres et al. (2012)	84.32 ± 0.62	2.80 ± 0.57	6462 ± 75	-33.1 ± 7.4
WASP-15	Triaud et al. (2010)	$85.96^{+0.29}_{-0.41}$	$4.27^{+0.26}_{-0.36}$	6300 ± 100	$-129.6^{+4.3}_{-5.2}$
WASP-17	Anderson et al. (2010); Triaud et al. (2010)	$86.63^{+0.39}_{-0.45}$	$9.92^{+0.40}_{-0.45}$	6509 ± 86	$-148.5^{+7.7}_{-6.7}$
WASP-18	Triaud et al. (2010); Albrecht et al. (2012b)	$80.6^{+1.1}_{-1.3}$	11.0 ± 0.5	6400 ± 100	13 ± 7
WASP-19	Hellier et al. (2011); Albrecht et al. (2012b)	79.4 ± 0.4	4.4 ± 0.9	5500 ± 100	15 ± 11
WASP-22	Anderson et al. (2011b)	88.26 ± 0.91	4.42 ± 0.34	5958^{+100}_{-95}	22 ± 16
WASP-24	Smith et al. (2012b)	83.3 ± 0.3	5.86 ± 0.63	6038 ± 95	-5.8 ± 4.1
WASP-26	Anderson et al. (2011b); Albrecht et al. (2012b)	82.91 ± 0.46	2.2 ± 0.7	5939 ± 100	-34^{+36}_{-26}
WASP-33	Collier Cameron et al. (2010b)	87.67 ± 1.81	86 ± 1	7430 ± 100	-107.7 ± 1.6
WASP-52	Hébrard et al. (2013)	85.35 ± 0.20	2.5 ± 1.0	5000 ± 100	24^{+17}_{-9}
WASP-71	Smith et al. (2013)	84.2 ± 1.8	9.91 ± 0.49	6050 ± 100	19.8 ± 9.9
XO-3	Southworth (2010); Hirano et al. (2011a)	83.89 ± 0.40	18.4 ± 0.2	6430 ± 50	37.4 ± 2.2
XO-4	Narita et al. (2010a)	88.8 ± 0.6	8.8 ± 0.5	6397 ± 70	$-46.7^{+8.1}_{-6.1}$

[1] Listed λ is $360 - \lambda_{\mathrm{reference}}$ [2] Edge-on case from reference. [3] Pole-on case from reference. [4] Binary system, with planet in circumbinary orbit. Data listed are for star A. [5] Prograde case adopted in reference. [6] Alternative, retrograde solution allowed for by geometrical analysis in reference.

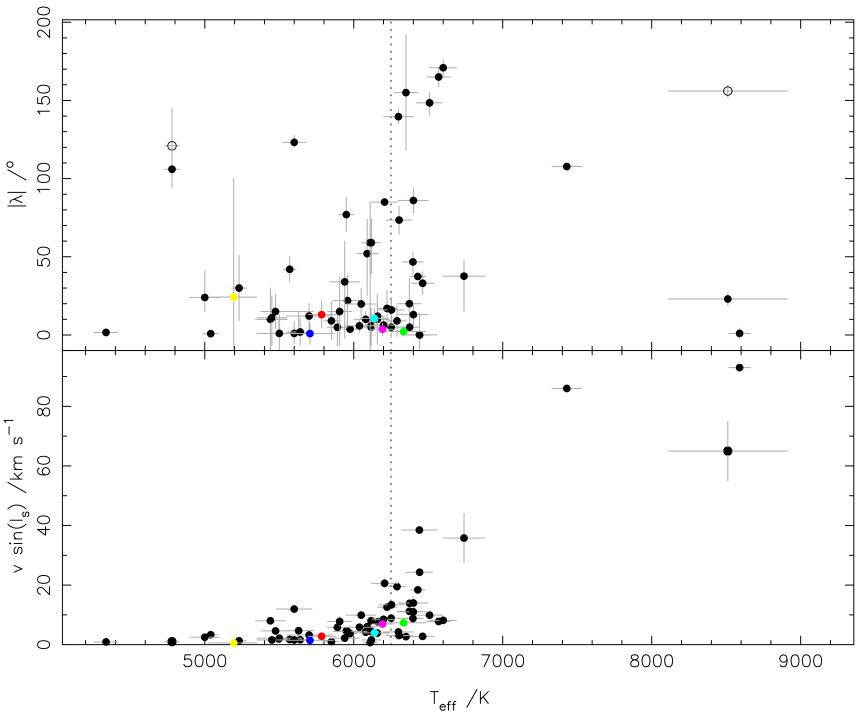

Figure 6.1: Top: *Projected stellar alignment, λ, as a function of stellar effective temperature, $T_{\rm eff}$, for all systems with confirmed measurements of spin-orbit alignment angle, λ.* ***Bottom:*** *Projected stellar rotation speed, $v \sin I$, as function of $T_{\rm eff}$. In both panels WASP-16 is marked in blue, WASP-25 in red, WASP-31 in green, WASP-32 in turquoise, WASP-38 in pink, and WASP-40 in yellow. The vertical dotted lines mark the distinction between 'cool' and 'hot' systems. Open circles represent the alternative solutions for HAT-P-11 (pole-on solution) and KOI-13 (retrograde solution).*

of misaligned systems in the 'hot' sub-sample. Under both criteria the apparent alignment of WASP-25 b's orbit is in accordance with the Winn et al. (2010a) hypothesis. WASP-16, $T_{\rm eff} = 5700 \pm 150$, WASP-32, $T_{\rm eff} = 6140^{+90}_{-100}$, and WASP-38, $T_{\rm eff} = 6180^{+40}_{-60}$ are also classified as 'cool' systems. All available information points towards these systems being aligned, and they therefore fit well with the hypothesis of Winn et al. (2010a).

An interesting point about Fig. 6.1 is the apparent lack of systems with mildly retrograde, close to polar orbits. There are currently only four systems with $80° \leq \lambda \leq 110°$, and only two more with $110° \leq \lambda \leq 140°$. There are none with $90° \leq \lambda \leq 100°$. I would like to speculate that truly polar orbits are perhaps unstable for some reason. Or perhaps it is simply my inability to determine the inclination of the stellar rotation axis that is at fault. It may be that some 'aligned' systems actually have close to polar orbits if this angle is accounted for (I will return to this idea later on). It may also be that observations simply have not been done yet for many systems in this region of the parameter space, and future publications may provide the data to fill this underpopulated area.

A drop in the number of systems at mid-range obliquity angles is clearly predicted by the

theoretical ψ angular distribution of Fabrycky & Tremaine (2007). It also clearly shows up in the angular distribution for the complete set of known obliquity angles, fig. 10 in Triaud et al. (2010). I reproduce this figure in Fig. 6.2, adding the probability distributions for the planets in Table 6.2 as well as those of the planetary systems from this study. ψ, the true alignment angle, is given by

$$\cos\psi = \cos I \cos i + \sin I \sin i \cos\lambda, \tag{6.1}$$

where I is the inclination of the stellar rotation axis to the line-of-sight, and i is the inclination of the orbital axis to the line-of-sight. To calculate the ψ distribution for each planet I carried out 10^6 Monte Carlo simulations, drawing values for I from a uniform $\cos I$ distribution to represent the random orientation of stellar rotation axes on the sky. I accounted for the error bars on i and λ by drawing values from Gaussian distributions with my optimal solutions as the mean values, scaled to the uncertainties in those values. The individual planets' distributions were then summed to produce the total distribution in Figure 6.2, which is similar to that of Triaud et al. (2010) and compares favourably to the theoretical histogram from Fabrycky & Tremaine (2007). The drop in probability at mid-range angles is in line with the underpopulated region of Fig. 6.1, and my additions bring the primary, low-angle peak closer in shape to the theoretical distribution. The overall shape of the secondary peak is less clear; it is still dominated by contributions from individual systems owing to the smaller number of planets with strongly misaligned orbits as compared to the number of aligned or weakly misaligned systems, but appears as though it may be broader and more shallow than the theoretical prediction.

Fig. 6.2 requires the assumption that I, the stellar inclination, is isotropic and that the angular distribution is unimodal. However the discussion of Winn et al. (2010a) implies that the distribution is in fact bimodal. A clearer demonstration of the agreement between theoretical predictions and current observations is therefore to look at the distribution of λ. This requires the transformation of the predicted ψ distribution of Fabrycky & Tremaine (2007) into λ. To do this, I again assumed an isotropic distribution for I, assumed transiting systems such that $i = 90°$, and used

$$\tan\lambda = \tan\psi \sin\alpha \tag{6.2}$$

where α is an azimuthal angle defined such that the zero-point is when the star's 'northern'

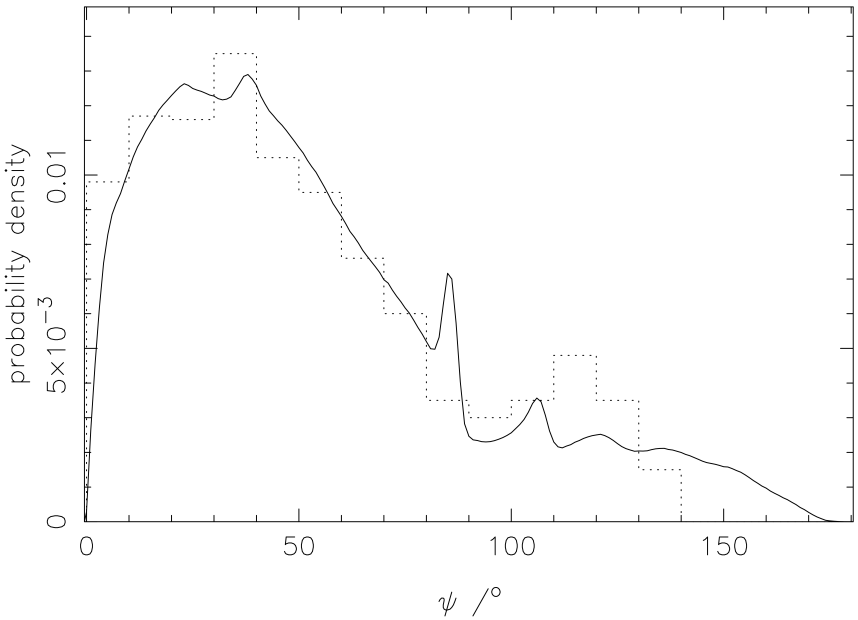

Figure 6.2: *The total distribution of the true obliquity angle, ψ, for the complete sample of systems for which λ has been measured. The dotted histogram represents the theoretical distribution of Fabrycky & Tremaine (2007). The overall forms are roughly comparable, although the shape of the total ψ distribution has changed substantially compared to fig. 10 of Triaud et al. (2010). The form of the primary peak agrees well with theoretical predictions, but the secondary, high angle peak predicted by the theoretical distribution is less clearly defined and appears to be shallower and broader than anticipated. The drop in probability density at mid-range angles, around $\psi \approx 90°$, is still visible.*

pole is directed at the observer. For each entry in the ψ distribution I selected a random value of ψ from the range of the bin in which that datum was located, and sampled a uniform distribution of $\sin\alpha$, to calculate the appropriate value of λ.

I reproduce the lower panel of fig. 9 from Triaud et al. (2010), taking into account all of the measurements of λ from Table 6.2. For HAT-P-7 and HAT-P-14, both of which have published with $\lambda > 180.0°$, I used $\lambda' = 360 - \lambda$. This cumulative λ distribution, Figure 6.3, avoids both of the assumptions inherent in Fig. 6.2. Agreement between the observational data and the theoretical predictions of Fabrycky & Tremaine (2007) has been improved compared to that exhibited in Triaud et al., particularly for mid- to high-range angles, but the observational data still show more low-obliquity systems than expected compared to the theoretical histogram.

Returning to the question of the scarcity, or otherwise, of polar orbits, I have investigated the likelihood of alignment along the line of sight for the systems in my sample. Following Schlaufman (2010), I conducted a comparison of the measured and predicted stellar $v \sin I$,

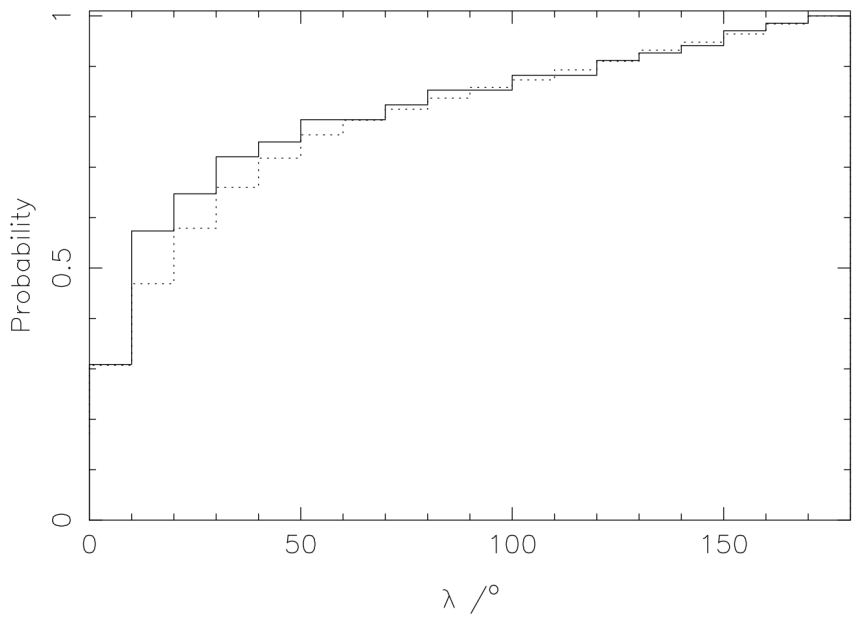

Figure 6.3: *Cumulative probability histogram for λ. The solid line denotes observational data, whilst the dotted line denotes the theoretical distribution of Fabrycky & Tremaine (2007), converted from ψ to λ. The agreement between the two distributions has improved with the addition of measurements made since the publication of Triaud et al. (2010), and the observational data now matches the theoretical prediction very well at high alignment angles. However there still seems to be an overabundance of systems with low obliquities.*

calculating the rotation statistic

$$\Theta = \frac{\overline{v \sin I_{\rm sim}} - v \sin I_{\rm obs}}{\sqrt{\sigma^2_{\rm obs} + \sigma^2_{\rm sim}}} \tag{6.3}$$

for all of the systems in Table 6.2. $\overline{v \sin I_{\rm sim}}$ is the mean simulated value of the projected stellar rotation (taken from a sample of 1000 simulated values), $\sigma_{\rm sim}$ is the width of the simulated distribution, $v \sin I_{\rm obs}$ is the observed stellar rotation, and $\sigma_{\rm obs}$ is the observed error. I attempted to be consistent in my choice of age estimate for the systems, using the values that I obtained from the Y^2 stellar models in Chapter 2 where possible. However for some of the systems I was forced to use estimates obtained using the Padova or Teramo stellar models instead.

Stars for which Θ is small show a good fit between the observed and simulated rotation speeds, indicating that they are oriented close to edge-on to our line-of-sight; more correctly it suggests that $i \approx I$, but since transiting planets must have $i \approx 90°$ it suggests that the stellar equator is close to our line-of-sight. Large positive (negative) values of Θ indicate that stars are rotating slower (faster) than expected given their age; if slower, then this can be interpreted as evidence that the stars are oriented somewhat pole-on. Plotting my Θ values

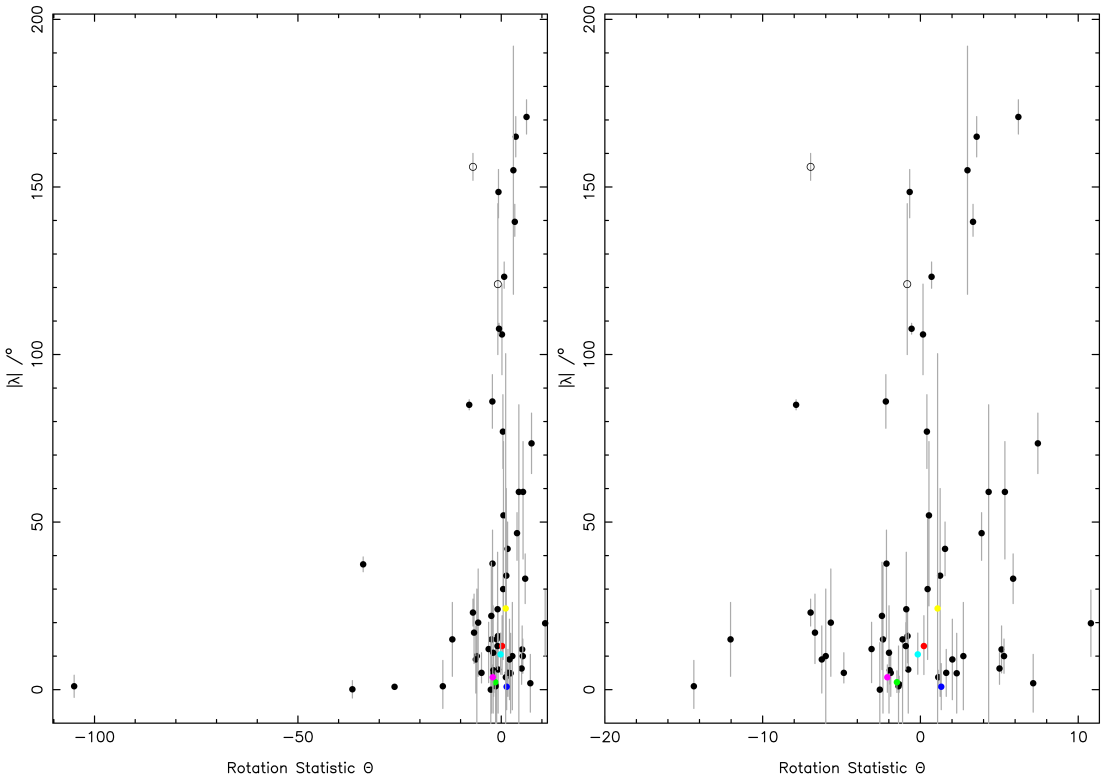

Figure 6.4: *Θ as a function of λ for the sample of planets with known alignment angles, as listed in Table 6.2 with the addition of the systems presented in herein. Legend as for Fig. 6.1.* ***Left:*** *All data.* ***Right:*** *A close-up of the main distribution, ignoring the systems with very large, negative values of Θ. Systems with apparently polar orbits according to their alignment angles show good agreement between orbital and stellar inclinations, suggesting that their planets' orbits are indeed of a polar nature*

as a function of $|\lambda|$ (see Fig. 6.4) reveals that there are several systems that appear to have a mismatch between i and I, and that these systems are spread fairly evenly across the range of λ values. Note though that the planets with apparently polar orbits ($80° \leq \lambda \leq 110°$) that were noted earlier seem to show good agreement between the two inclinations, seemingly confirming that their orbits are indeed polar in nature. Small number statistics could, of course, be playing a role here owing to the low number of systems in this alignment angle range, as noted previously. Interestingly, all six of the systems for which I presented new results in this Chapter show good agreement between i and I.

It is also interesting to note that there are many systems with large, negative values of Θ. These systems are rotating much more rapidly than predicted by their age using gyrochronology, suggesting that they have been spun up in some way. This could be interpreted as further evidence for the tidal spin-up effect discussed in Chapter 4. Plotting Θ as a function of orbital separation (Figure 6.5) reveals that these systems tend to be those with the closest planets.

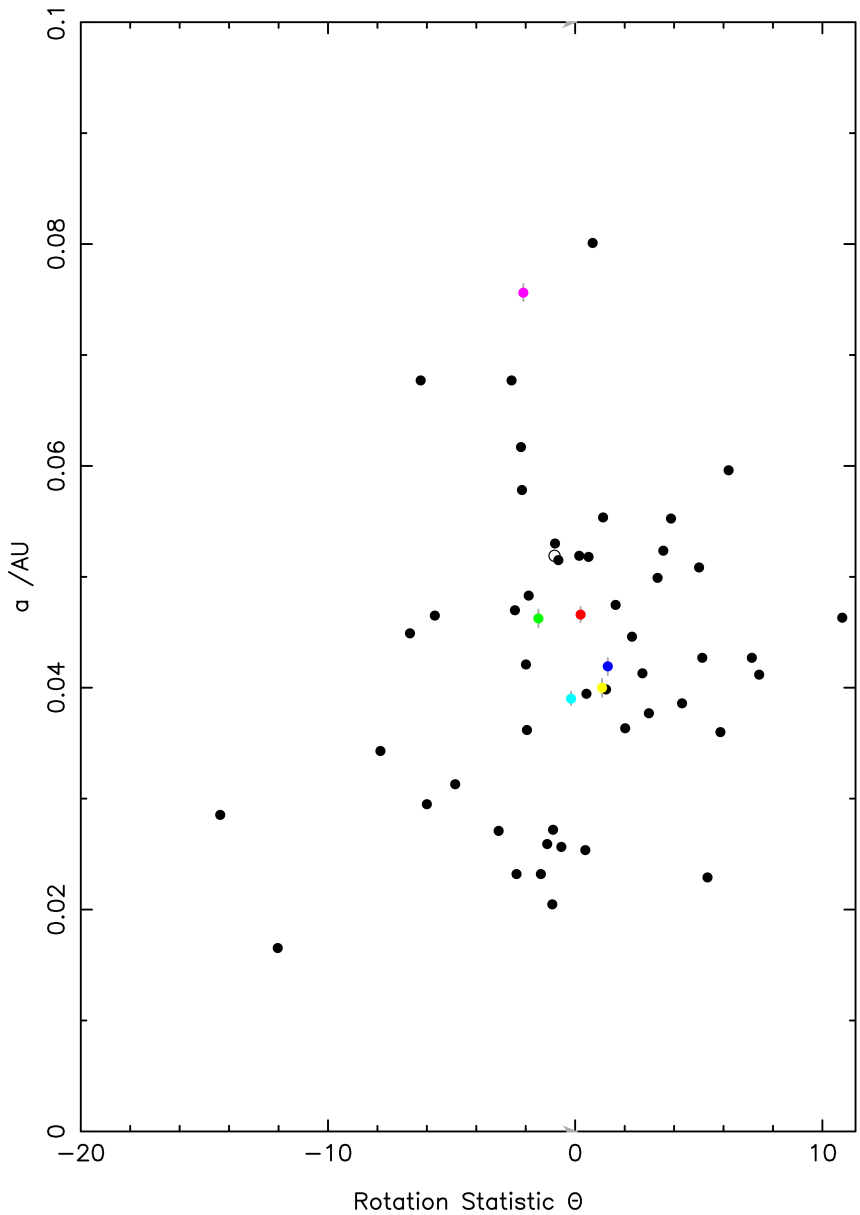

Figure 6.5: *Θ as a function of orbital separation, a, for the sample of planets with known alignment angles. The ranges of both Θ and a have been restricted for clarity, and focus on the main part of the distribution. Legend as for Fig. 6.1. Systems which appear to be rotating more quickly than expected, given their age, tend to be found at smaller orbital separations.*

6.1.1 Trends with mass

My new results have little effect on the known trend with planetary mass, as five of the six systems have $M_p < 3\,M_{\rm Jup}$. They therefore cannot provide counter-examples, as planets in this category are already thought to exhibit randomly distributed values of λ. The sixth system, WASP-32, has $M_p = 3.46^{+0.14}_{-0.12}\,{\rm M_{Jup}}$ and falls into the 'high mass planet' category. The system appears to be well-aligned, and fits well with previous measurements in the category which show low to moderate alignment angles, but are all at $|\lambda| < 50°$.

Considering the relationship between $|\lambda|$ and M_s throws up a couple of interesting discussion points. The first is that of the 60 systems for which the alignment angle has been measured, only three have $M_s \geq 1.5 M_\odot$ (only five have $M_s \geq 1.4 M_\odot$). This bias is not particularly surprising given that the peak in the stellar mass distribution for all known planetary systems lies around $1 M_\odot$, and that the number of systems drops off as stellar mass increases, but it is still a notable bias in the sample. The second point is that all three of the high-mass systems are well-aligned ($|\lambda| < 30°$; considering the prograde case for KOI-13). This suggests that planets around high-mass stars may be preferentially aligned, although more measurements will be needed of such systems, including confirmation of the prograde nature of KOI-13, before this can be confirmed[4].

As previously noted, it is perhaps more useful to consider the mass ratio rather than either of the individual component's masses, as it is this quantity which appears in tidal equations and other contexts. Figure 6.7 displays $|\lambda|$ as a function of mass ratio; unsurprisingly it shows a similar form to the upper panel of Figure 6.6, with very low mass ratio systems exhibiting an apparently random distribution of angles, whilst those systems with $M_{\rm rat} \gtrsim 0.0025$ show $\lambda < 50°$. The distinction between the two regions is perhaps a little more pronounced than when considering only the relationship with M_p, particularly if the alternative, retrograde case for KOI-13 is disregarded. If the hypothesis that alignment angle is tidally governed is correct then this distribution is to be expected, as a higher mass ratio indicates a stronger tidal interaction, and therefore more rapid circularisation and tidal realignment.

[4] I successfully applied for time using HARPS to observe a transit of KOI-13, in an effort to carry out Doppler tomography on the system. Unfortunately, no spectroscopic signature was observed.

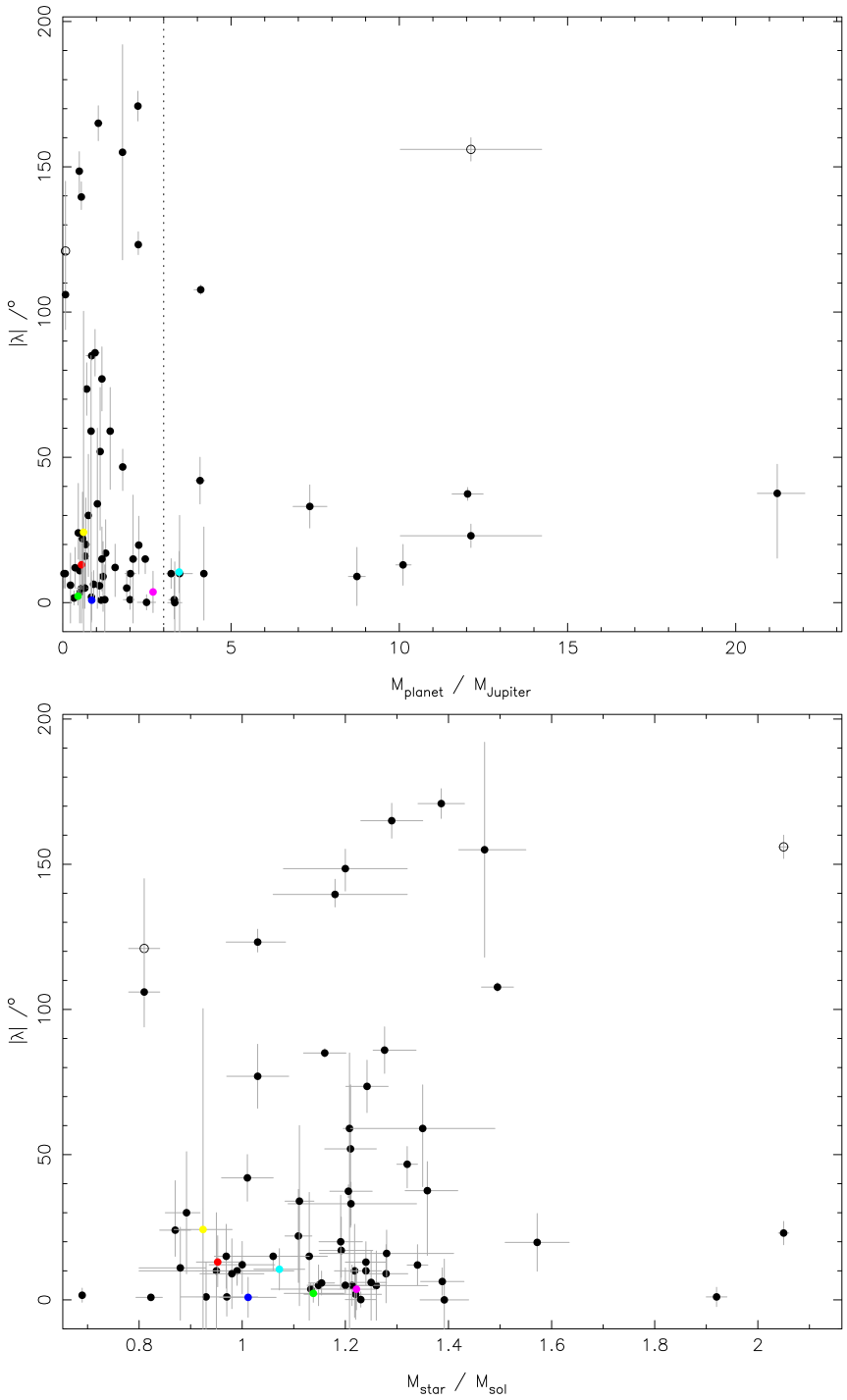

Figure 6.6: *λ as a function of planetary (**top**) and stellar (**bottom**) mass for the set of planets with known alignment angle, as listed in Table 6.2. Legend as for Fig. 6.1. The vertical dotted line in the left panel denotes $M_p = 3M_{\rm Jup}$, the planetary mass at which distribution of alignment angles appears to change form.*

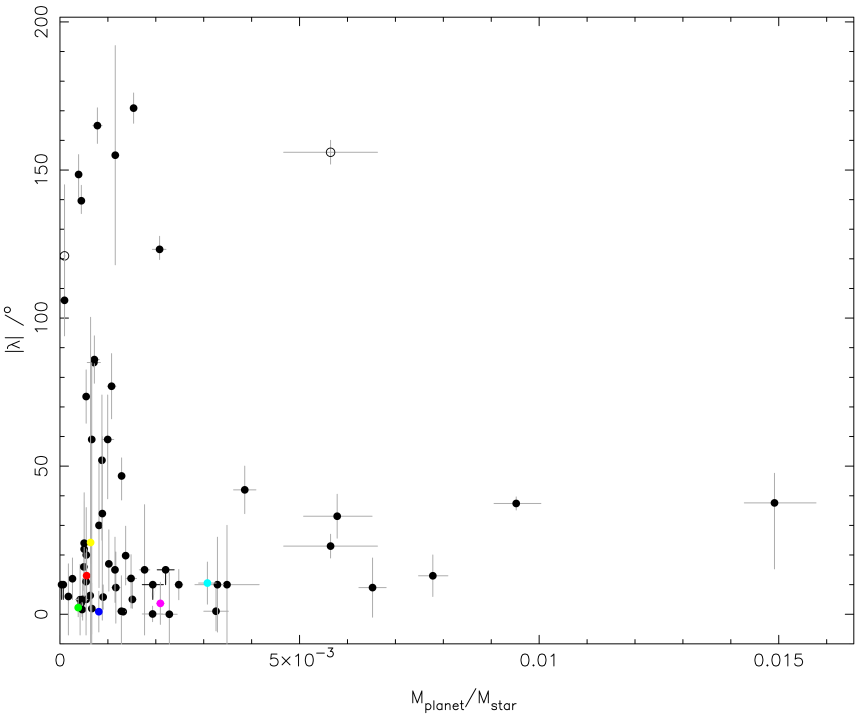

Figure 6.7: *Alignment angle, λ, as a function of mass ratio for all systems with known alignment angles. It is immediately apparent that systems with very low mass ratios exhibit a random distribution of alignment angles, whilst those with $M_{\rm rat} \gtrsim 0.0025$ seem to preferentially exhibit $\lambda < 50°$. Symbols as for Fig. 6.1.*

6.1.2 Stellar ages

Of the six systems studied in the preceding Chapter, five have host stars which are insufficiently massive to fulfil the selection criterion imposed by Triaud (2011) for his study of the trend of λ with stellar age. WASP-38 lies close to the cut-off mass; in some of my simulations it falls below the limit, but in my adopted solution it fulfils Triaud's criterion for inclusion. In Figure 6.8 I plot $|\lambda|$ as a function of stellar age, as calculated using the Yonsei-Yale isochrones, to see what effect this system has on the trend identified by Triaud.

In Chapter 2 I computed the ages for all six of the systems using a triangulation based stellar model fitting routine and several different sets of stellar models, in an attempt to better characterise the inherent uncertainties. For this work I took the effective temperature from the same spectroscopic analyses of HARPS spectra that provided the updated $v \sin I$ values in Table 5.1, and took the stellar density value as found by my preferred model under the tomographic method for WASP-32 and -38, and the RM model for the remaining systems. The ages that I obtained for the six systems are recapped in Table. 6.3.

Triaud (2011) pointed out that isochronal analysis is less precise for stars with $M_s < 1.2\,M_\odot$ owing to the increased length of their main-sequence lifetime, and their less pro-

Table 6.3: *Age estimates for the six systems for which I have measured the spin-orbit alignment angle, λ, as calculated in Chapter 2 through stellar model fitting. They are summarised here for reference and convenience.*

	Stellar model fitting age				
	Padova / Gyr	YY / Gyr	Teramo / Gyr	VRSS / Gyr	DSEP / Gyr
WASP-16	$4.50^{+4.12}_{-4.25}$	$3.37^{+3.36}_{-2.17}$	$5.73^{+4.61}_{-4.01}$	$5.22^{+4.58}_{-3.53}$	$5.86^{+3.11}_{-3.10}$
WASP-25	< 3.10	$1.94^{+1.75}_{-1.79}$	$6.09^{+2.77}_{-3.22}$	$1.18^{+4.34}_{-0.51}$	$3.25^{+1.79}_{-1.53}$
WASP-31	3.23 ± 1.40	2.05 ± 1.17	$3.60^{+2.26}_{-1.78}$	$1.87^{+1.34}_{-1.02}$	$4.19^{+0.99}_{-2.76}$
WASP-32	$2.36^{+1.72}_{-0.85}$	$2.22^{+0.62}_{-0.73}$	$4.50^{+1.88}_{-1.69}$	$1.41^{+1.36}_{-1.10}$	$3.98^{+0.68}_{-1.19}$
WASP-38	$3.41^{+0.48}_{-0.43}$	$3.29^{+0.42}_{-0.53}$	$3.59^{+0.77}_{-0.70}$	$3.20^{+0.73}_{-0.59}$	$4.81^{+0.52}_{-0.63}$
WASP-40	> 1.20	$6.36^{+5.86}_{-3.11}$	> 4.96	> 5.73	$9.19^{+4.94}_{-3.88}$

nounced radius increase (and therefore density decrease), when compared to more massive stars. I found a mass of $1.07 \pm 0.05\,M_\odot$ for WASP-32 using my tomographic analysis method, in agreement with the value from Maxted et al. (2010); the wide age range that I found is therefore expected given the preceding comments. The WASP-38 system on the other hand shows much better agreement between its different age estimates. With a mass of $1.23 \pm 0.04\,M_\odot$ from tomographic analysis, the system lies closer to the arbitrary cut-off of Triaud (2011), so one might expect that the age would be better constrained. Nevertheless, all five age estimates for WASP-38 agree with the postulated trend for alignment angle to decrease with time. WASP-16 ($M_s = 1.02^{+0.04}_{-0.03}\,M_\odot$), WASP-25 ($M_s = 1.02 \pm 0.02\,M_\odot$), and WASP-31 ($M_s = 1.16 \pm 0.04\,M_\odot$) all fall below the cut-off mass selected by Triaud, but also fit with this hypothesis.

WASP-40 is poorly constrained, and I was unable to place upper limits on the age using the available isochrones for three out of the five model sets that I tried. It is hard to conclude anything from this, but the different models do agree that the system is older than any of the other systems. Anderson et al. (2011a) found an age for the system of 6 ± 5 Gyr using the Padova stellar models formulation of Marigo et al. (2008) and Bertelli et al. (2008), which is consistent with my values. They found a lower age ($1.2^{+1.3}_{-0.8}$ Gyr) using gyrochronology, in their case based on an estimate of the rotation period derived from $v \sin I$, but this does not match my own gyrochronology estimates (see Table A.2) which are nonsensical, as all imply that the system is older than the accepted age of the Universe). From this information I tentatively predict, following the trend noticed by Triaud (2011), that the system will prove to be aligned if the uncertainty on λ is able to be reduced.

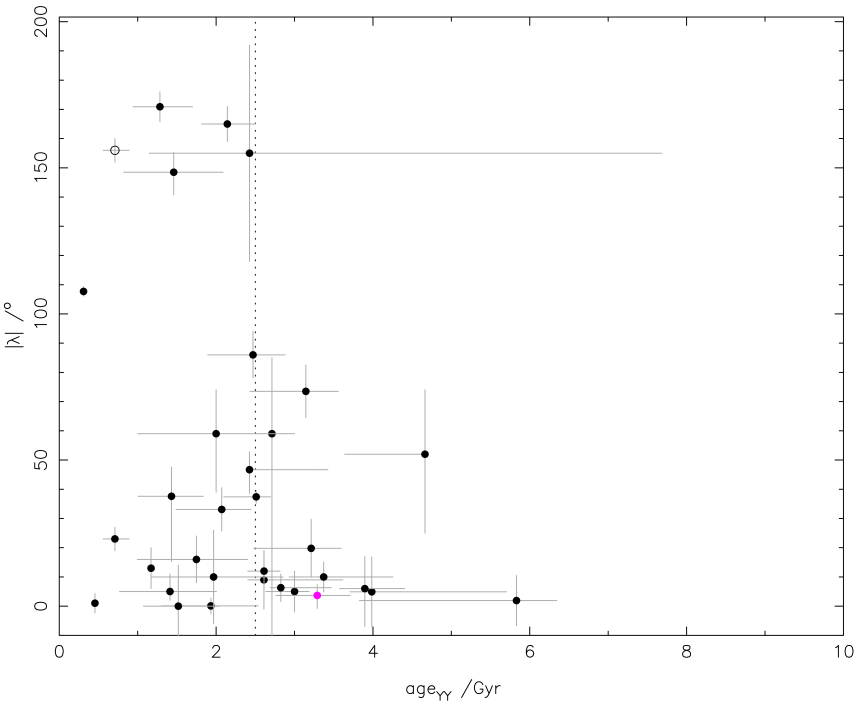

Figure 6.8: *Alignment angle λ, for systems with $M_s < 1.2\,M_\odot$, as a function of stellar age found using stellar model fitting and the Yonsei-Yale isochrones. Of the systems that I have studied, only WASP-38 fulfils the selection criteria; however it provides no useful information regarding the previously identified trend. Symbols as for Fig. 6.1.*

6.1.3 Tidal timescales

In Chapter 2 I discussed the effect of tidal interactions on the stellar age estimates produced by gyrochronology. To do this I calculated tidal timescales using equations from Albrecht et al. (2012b), which I will again reproduce here:

$$\frac{1}{\tau_{\rm CE}} = \frac{1}{10 \cdot 10^9 {\rm yr}} q^2 \left(\frac{a/R_s}{40}\right)^{-6} \tag{6.4}$$

and

$$\frac{1}{\tau_{\rm RA}} = \frac{1}{0.25 \cdot 5 \cdot 10^9 {\rm yr}} q^2 \left(1+q\right)^{5/6} \left(\frac{a/R_s}{6}\right)^{-17/2}. \tag{6.5}$$

The two equations account for the fact that the effective temperature range being considered encompasses planets with substantially different convective envelope masses. As I have already commented, the critical temperature dividing 'hot' planets from 'cool' planets roughly aligns with the point at which the convective envelope disappears completely; an equation applicable to purely radiative planets is therefore required.

The stellar effective temperatures of five of my six systems are, as mentioned previously,

below that critical temperature. These systems therefore fall under the convective envelope version of the tidal timescale equation. Using parameters from Table 6.1, I calculate the tidal timescales for all six systems using 6.4. I find $\tau_{\rm CE} = 2.2 \times 10^3$ Gyr for WASP-16, $\tau_{\rm CE} = 1.4 \times 10^4$ Gyr for WASP-25, $\tau_{\rm CE} = 5.5 \times 10^1$ Gyr for WASP-32, $\tau_{\rm CE} = 1.8 \times 10^3$ Gyr for WASP-38, and $\tau_{\rm CE} = 5.4 \times 10^3$ Gyr for WASP-40. For WASP-31, which has an effective temperature such that it sits on the borderline between the 'hot' and 'cool' sub-populations, I calculated tidal timescales using both formulations. I obtained $\tau_{\rm CE} = 5.5 \times 10^3$ Gyr, and $\tau_{\rm RA} = 7.3 \times 10^{-18}$ yr, implying that the convective envelope timescale should be considered, and that it is consistent with the rest of my sample.

These values fit into the scheme that Albrecht et al. (2012b) developed, whereby systems in which the tidal timescale is short preferentially show low values of λ, whereas those with longer timescales appear to present an almost random distribution of λ. The timescales for the six systems that I have studied are relatively short compared to the extremes of the distribution found by Albrecht et al., particularly where WASP-32 is concerned, and the projected alignment angles that I have measured are all small.

6.2 A new misalignment test

There seems to be little consensus as to the best way of classifying systems as aligned or misaligned. For most of the systems with measurements of λ this is not a serious problem; either $|\lambda| > 90°$, or the error bars are such that the obliquity is consistent with zero. But as the number of RM measurements continues to grow, there will be an increasing number of systems in a similar situation to WASP-25, which exhibits a mildly asymmetrical RM anomaly but does not fulfil any of the current misalignment criteria.

There are two main criteria currently in use by the community. Winn et al. (2010a) use $|\lambda| > 10°$ at $\geq 3\sigma$ significance to define a misaligned system. Triaud et al. (2010) take $|\lambda| > 30°$ as their threshold, on the basis that errors in the obliquity angle are of the order of 10°, and therefore this gives 3σ significance as well. I have developed a new test for misalignment that takes a completely different approach.

To develop this new test I considered a sample of WASP planets for which the RM effect has been characterised using RV data. I use the most recent published parameters for each system, regardless of the analysis method that was used; for WASP-3, for example, I use the

Table 6.4: *Relevant data for my new misalignment criterion, for a sample of 17 WASP planets with existing Rossiter-McLaughlin measurements. λ and $v \sin I$ values are those obtained from my new MCMC analyses. BIC values were calculated from the spectroscopic χ^2 values, using the number of in-transit RV measurements only. My new misalignment criterion defines systems with a BIC ratio $B \geq 1.01$ as misaligned, those with $B \leq 0.99$ as aligned, and those with $0.99 < B < 1.01$ as of indeterminate status.*

System	reference	$\lambda/^\circ$	$v \sin I/\mathrm{km\,s^{-1}}$	BIC	$\mathrm{BIC_{align}}$	ΔBIC	B
WASP-1	Albrecht et al. (2011)	$-68.2^{+94.5}_{-17.9}$	$3.2^{+8.6}_{-2.1}$	197.31 ± 20.40	197.35 ± 20.27	0.04	1.000
WASP-3	Tripathi et al. (2010)	$5.7^{+18.3}_{-19.1}$	$11.3^{+0.5}_{-0.4}$	271.12 ± 23.90	272.45 ± 23.80	1.33	1.005
WASP-4	Triaud et al. (2010)	$-19.0^{+47.3}_{-40.9}$	$2.2^{1.2}_{-0.3}$	89.81 ± 14.72	87.20 ± 14.30	-2.61	0.971
WASP-5	Triaud et al. (2010)	$25.8^{+8.2}_{-7.2}$	3.4 ± 0.3	184.73 ± 19.78	195.99 ± 20.20	11.26	1.061
WASP-6	Gillon et al. (2009)	$-9.9^{+15.7}_{-14.7}$	1.5 ± 0.2	126.28 ± 17.08	123.48 ± 16.71	-2.80	0.978
WASP-7	Albrecht et al. (2012b)	$108.7^{+4.8}_{-6.1}$	$36.8^{+4.2}_{-3.6}$	148.19 ± 17.96	307.61 ± 25.24	159.42	2.076
WASP-8	Queloz et al. (2010)	$-98.0^{+3.4}_{-5.3}$	$4.5^{+2.3}_{-1.3}$	368.86 ± 28.21	1067.12 ± 46.72	698.26	2.893
WASP-12	Albrecht et al. (2012b)	$59.1^{+4.3}_{-4.5}$	1.3 ± 0.1	2056.3 ± 64.4	2150.3 ± 65.7	94.0	1.046
WASP-14	Joshi et al. (2009)	$-28.5^{+5.5}_{-5.4}$	2.7 ± 0.3	159.73 ± 19.13	179.77 ± 19.92	20.04	1.125
WASP-15	Triaud et al. (2010)	$-137.7^{+6.6}_{-5.7}$	4.06 ± 0.3	146.07 ± 17.95	333.63 ± 26.23	187.56	2.284
WASP-17	Triaud et al. (2010)	$-146.5^{+5.3}_{-4.7}$	9.3 ± 0.5	226.51 ± 22.36	609.24 ± 35.43	382.73	2.690
WASP-18	Triaud et al. (2010)	$11.0^{+5.3}_{-5.2}$	12.4 ± 0.4	114.99 ± 16.36	113.14 ± 16.01	-1.84	0.984
WASP-19	Hellier et al. (2011)	$1.7^{+6.1}_{-5.9}$	3.1 ± 0.3	75.40 ± 13.06	72.41 ± 12.62	-2.99	0.960
WASP-22	Anderson et al. (2011b)	$-1.3^{+15.5}_{-15.0}$	4.0 ± 0.5	62.16 ± 12.35	59.58 ± 11.83	-2.58	0.958
WASP-24	Simpson et al. (2011c)	$-7.6^{+5.2}_{-5.9}$	$5.0^{+0.5}_{-0.4}$	105.09 ± 15.48	102.01 ± 15.03	-3.08	0.971
WASP-26	Albrecht et al. (2012b)	$-10.5^{+4.1}_{-4.7}$	2.8 ± 0.3	224.95 ± 21.92	229.97 ± 22.06	5.02	1.022
HAT-P-14/WASP-27	Winn et al. (2011b)	$-166.3^{+6.8}-3.1$	$5.8^{+0.4}_{-0.7}$	396.49 ± 28.84	555.12 ± 33.79	158.63	1.400
HAT-P-30/WASP-51	Johnson et al. (2011)	$70.9^{+6.3}_{-5.3}$	$3.2^{+0.2}_{-0.1}$	320.09 ± 25.84	1478.31 ± 54.55	1008.89	4.650
WASP-52	Hébrard et al. (2013)	$-28.6^{+16.5}_{-45.1}$	$1.5^{+1.2}_{-0.7}$	139.57 ± 17.15	141.75 ± 17.17	2.18	1.016
WASP-16	Brown et al. (2012a)	$0.9^{+6.9}_{-6.8}$	$1.5^{+0.3}_{-0.3}$	128.0 ± 16.9	126.2 ± 16.5	-1.80	0.986
WASP-25	Brown et al. (2012a)	$13.0^{+9.0}_{-8.5}$	2.8 ± 0.3	96.25 ± 14.86	101.9 ± 15.7	5.65	1.059
WASP-31	Brown et al. (2012a)	$2.2^{+3.4}_{-3.1}$	7.4 ± 0.7	72.8 ± 12.9	70.9 ± 12.5	-1.90	0.974
WASP-32	Brown et al. (2012b)	$10.5^{+6.4}_{-5.9}$	$3.9^{+0.4}_{-0.5}$	62.6 ± 11.2	57.3 ± 10.7	-5.30	0.915
WASP-38	Brown et al. (2012b)	$7.5^{+4.7}_{-6.1}$	$7.5^{+0.1}_{-0.2}$	140.3 ± 16.8	133.1 ± 16.3	-7.20	0.949
WASP-40/HAT-P-27	Brown et al. (2012b)	$24.2^{+76.0}_{-44.5}$	$0.6^{+0.7}_{-0.4}$	79.6 ± 12.6	77.1 ± 12.4	-2.50	0.969

study by Miller et al. (2010) even though it is tomographic in nature, rather than the older RM analysis of Tripathi et al. (2010). The rationale behind this is that I am simply using these parameters as the starting point for a re-analysis using my own routines, and thus the method by which they were obtained is irrelevant. The full sample that I used is listed in Table 6.4.

My test is based on the Bayesian Information Criterion (BIC) (Liddle, 2007),

$$\mathrm{BIC} = \chi^2_{\mathrm{RV}} + k \ln(n), \tag{6.6}$$

where k is the number of parameters and n is the number of data. Changing the value of λ only affects the form of the model RV curve in-transit; I therefore just consider those RV points that lie within a region of the RV curve around phase 0 defined by the fractional transit

width (the transit window) when computing the second term of the BIC. The number of parameters changes according to the choice of priors applied to the MCMC run; adding a long-term RV trend, fitting the RM effect, and allowing the eccentricity to float all add one or more additional parameters to the model.

I carry out two MCMC analyses for each of the systems in my sample, using all available radial velocity data. Both runs use the same combination of priors, selected based on the analysis in the paper from which I drew the pre-existing parameters. The first analysis allows both $\sqrt{v \sin I} \cos \lambda$ and $\sqrt{v \sin I} \sin \lambda$ to float, whilst the second forces an aligned orbit by fixing $\sqrt{v \sin I} \sin \lambda = 0$. I calculate the BIC for both runs, before calculating

$$B = \mathrm{BIC}_{\mathrm{align}}/\mathrm{BIC}. \tag{6.7}$$

For the six systems presented herein I use my adopted solutions, and carry out an additional run to provide the aligned case. In the case of WASP-32 and WASP-38 I used the RM run with my adopted set of priors as the test case, rather than the tomographic solution.

I find several distinct groups of systems within my results, which lead me to define three categories of alignment into which systems with RM measurements can be classified. Ten systems, including WASP-16, -31, -32, -38, and -40, were found to have $B \leq 0.990$, implying that the model with $\lambda = 0$ provides a better fit that the free-floating λ model. Of these systems, all would be classified as aligned according to either of the existing misalignment criteria. A further four systems are clustered between $B = 1.00$ and $B = 1.03$, forming a distinct group in Figure 6.9. Forcing an aligned orbit would seem to make little difference to the quality of the fit between data and model in these cases. Of these systems three would be classed as aligned according to Winn et al. (2010a) and Triaud et al. (2010), but the fourth (WASP-1) would actually be classed as misaligned according to Triaud et al. (2010). Three of the four have at least one 1σ error bar that has a magnitude greater than that of their assigned alignment angle. The remaining systems in Figure 6.9 clearly lie distinct from those discussed so far; many are clearly classifiable as misaligned, with $|\lambda| > 100°$ and $B > 2$.

In light of these results, I define three categories of alignment. Systems for which $B \leq 0.99$ I classify as aligned. Those with $B \geq 1.03$ I classify as misaligned. Systems falling between these categories, with $0.99 < B < 1.03$ I classify as of indeterminate alignment. Albrecht et al. (2012b) note that the BIC test is affected by the relative numbers of RV measurements

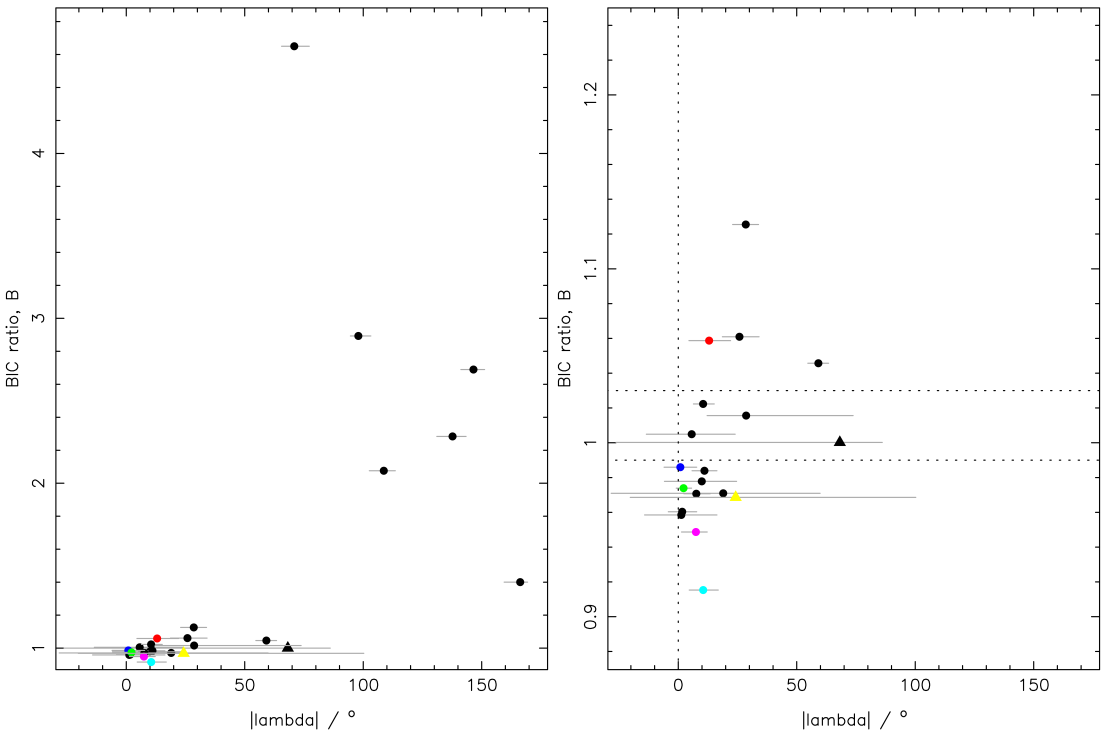

Figure 6.9: *B as a function of λ for the sample of planets in Table 6.4, as well as the systems presented in this study. This shows the separation of the systems into several groupings, which lead me to define four categories of alignment; this changes the existing classification of some systems. Colours as for Fig. 6.1. Solid triangles denote systems which fall into the 'no detection' category. The horizontal dotted lines mark $B = 1.03$ and $B = 0.99$, the divisions between my categories. The vertical dotted line denotes $|\lambda| = 0°$.* ***Left:*** *All data.* ***Right:*** *A close-up of the heavily populated region in the lower left of the plot, around $B = 1.00$ and $|\lambda| = 0°$.*

in transit compared to out of transit, and that it assumes that no correlated noise is present. I acknowledge that these are indeed shortcomings of my test, and that they might affect the boundaries between the three categories, but I would point out that the test is still quantitative, as opposed to the qualitative nature of the previous tests in Triaud et al. (2010) and Winn et al. (2010a).

I would also define a fourth category, that of 'no detection', as containing those systems with $v \sin I$ consistent with 0 to within 2σ. My analysis routines are set-up in such a way that $v \sin I = 0$ within 1σ is a highly unlikely scenario; indeed, a lower error bar on $v \sin I$ of greater magnitude than the value itself is nonsensical, as negative rotation is a physical impossibility when considering only the magnitude of the rotation. WASP-40 falls into this category, as I feel is appropriate given the poor signal-to-noise of the data that I obtained, and the indistinct Rossiter-McLaughlin effect that I find. So too does WASP-1, which is consistent with the analysis of Albrecht et al. (2011). The results for TrES-2 (Winn et al., 2008) and HAT-P-11 (Winn et al., 2010c), listed in Table 6.2, would also fall under 'no detection'.

Some of the systems in Table 6.4 warrant a little more examination. My new MCMC runs for WASP-4 produced very large error bars on λ, but the system still ends up in the aligned category thanks to the high quality of the data that is available for the system. Triaud et al. (2010) noted a substantial correlation between λ and $v \sin I$ for WASP-4, arising due to the low impact parameter, which may be producing the large lower error. WASP-25 is classified as 'misaligned' under my new criteria, as was suspected given the asymmetry in the shape of its Rossiter-McLaughlin anomaly. Not only does it fall in this category, but the detection would seem to be quite firm according to Figure 6.9. This is at odds with its classification as quite firmly 'aligned' under both existing criteria. A similar situation is observed for WASP-5, although it exhibits a greater $|\lambda|$ value which, with similar 1σ errors, more plausibly suggests a misaligned system. WASP-14 is classed as aligned under Triaud et al. (2010) and misaligned under Winn et al. (2010a); my test supports the latter classification.

Of the undetermined systems, WASP-26 stands out as inconsistent with the rest of its classification group. The error bars on my new value of λ for WASP-26 are less than half the magnitude of the value itself; the other three systems all have one error bar with a magnitude greater than the angle that I found. However, the in-transit spectroscopic measurements for the system that were obtained by Anderson et al. (2011b) and Albrecht et al. (2012b) show

significant scatter, and the Rossiter-McLaughlin anomaly is quite poorly defined. Anderson et al. in fact presented their data as a non-detection, and Albrecht et al. found $\lambda = -34^{\circ}{}^{+36}_{-26}$. A status of 'undetermined' thus seems a better fit for the WASP-26 system than might originally be thought.

6.3 Conclusion

In this Chapter I placed my spin-orbit alignment results in the context provided by the complete set of measurements that existed in the literature at the time of writing. I also investigated whether they provided any new information regarding previously known trends in the data. Finally, I created and discussed a new method for categorising the alignment, or otherwise, of an exoplanet's orbit. My new method was developed using a sample of WASP planets with known alignment angles, and applied to my own results.

When considering the trends in the alignment angle in this manner, my new results provide little assistance in assessing the importance of tidal interactions for the evolution of spin-orbit alignment. Based on previous studies it would seem that tidal forces might have a role to play. But if this is to be confirmed then it is important that work investigating how such forces affect planetary systems (such as my own as presented in this thesis) is carried out.

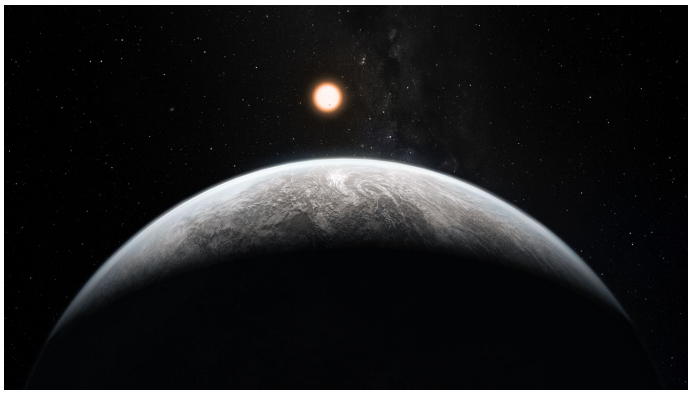

7

Conclusions and outlook

Whilst my doctoral work seems, at first glance, to cover disparate topics from across the spectrum of exoplanetary research, there is in fact an overarching theme to this thesis: tidal interactions between hot Jupiters and their host stars. As I have shown, these can have a large influence on both the physical and dynamical properties of planetary systems, and their influence can be felt in many different areas.

In my work I have investigated and characterised several different phenomena which result from tidal interactions. By investigating the ages of exoplanet host stars and comparing the results obtained by different methods, I showed in Chapter 2 that the presence of strong tidal forces might be influencing the ages that we estimate through gyrochronology by modifying their rotation. By modelling the past and future evolution of close-in hot Jupiters, I showed in Chapter 4 that this effect can be substantial, and that when the planet spirals-in to its Roche limit the rotation of the star can be spun-up to levels similar to that experienced at the age of young open clusters. Finally, by characterising the projected spin-orbit alignment

angle of several hot Jupiters in Chapter 5, and by examining their place in the full ensemble of known measurements in Chapter 6, I provided further evidence that tidal interactions might be playing a role in the re-alignment of hot Jupiter orbits.

7.1 Moving towards the future

The work that I have presented in this thesis is only a small part of what is possible. There are many directions in which this work could be extended, some of which I have already made a start on. Aspects of the suggestions I am about to make will form part of the work that I intend to carry out in the near future.

7.1.1 Extending my ages analysis

As I mentioned in my conclusions to Chapter 2, the sample sizes that I used for parts of my analysis were limited. Definitively identifying the influence of tidal interactions on the discrepancy between stellar model fitting and gyrochronology ages will require an enlarged sample. This would enable me to say something about the global effect of tides on the rotation rates of host stars. Whilst the system-specific modelling that I presented in Chapter 4 shows that the effect can be pronounced, the picture regarding the wider ensemble of planetary systems is less clear, as my results in Chapter 2 show. Merely expanding the sample should not be the sole focus though, as some of the uncertainty in my conclusions arise from the large errors that are involved. More precise measurements of $T_{\rm eff}$ and ρ_s for stars that fall inside my parameter space would allow more precise age assessment, which would in turn allow firmer conclusions to be drawn.

Upcoming space missions such as Gaia (Eyer et al., 2013) and CHEOPS (Characterising ExOPlanet Satellite; Broeg et al. 2013) have enormous potential in this regard. CHEOPS aims to measure transit lightcurves at very high signal-to-noise, allowing accurate stellar densities to be computed directly from the transit profiles. GaiaÕs objectives are more directly relevant, and include measurements of stellar effective temperatures, stellar radial and rotational velocities, and stellar surface gravities.

A comparison sample would provide useful information as well. Analysing the ages of a sample of isolated stars in the same manner would help to determine whether the discrepancy between stellar model fitting and gyrochronology is indeed the result of tidal interactions.

Another obvious extension to the work presented in Chapter 2 would be to investigate additional age determination methods, such as asteroseismology. Data from both the Kepler and CoRoT missions have under-utilised potential with regards to this technique, which is unrelated to either isochrone fitting or gyrochronology and would therefore provide an independent source of comparison.

7.1.2 How much influence do tides really have on spin-orbit alignment?

In Chapter 6 I showed that my analyses of the spin orbit alignment in five new systems, and my reanalysis of one system using new data and techniques, were consistent with the idea that tidal interactions are responsible for the realignment of systems that are misaligned by primordial, dynamical interactions. But is this really the case? Although the evidence suggests that tidal realignment occurs, there are strong arguments against the phenomenon.

Increasing the number of stars with measured spin-orbit alignment would help to answer this question. Further measurements of λ would help to characterise the shape of the boundary between 'hot' and 'cool' planets', allowing a stronger conclusion to be drawn regarding the presence of the convective zone and misalignment. With more measurements of λ I would also be able to increase the sample size for my age estimate comparison. Comparing the tidal strength, the nuclear burning timescale, and the estimated ages for such systems could potentially be revealing if stronger tides are found to truly affect the difference in age estimates for aligned systems.

7.1.3 Varied outcomes for tidal interaction modelling?

In Chapter 4 I modelled the tide-driven evolution of two hot Jupiter systems. Much as with my work on ages in Chapter 2, an obvious route for expansion of this work is to increase the sample size. The addition of further planets, with a range of known parameters, would allow me to develop a model of the broader picture. At what point in the initial parameter space do tidal interactions become sufficiently strong to cause the spin-up that I have found in the WASP-18 and WASP-19 systems? What about alternative outcomes, such as the outspiral of a planetary orbit, which occurs when the stellar rotation period is shorter than the planet's orbital period? Or the onset of synchronicity, which appears to be an extremely rare occurrence? What are the details of the interaction with retrograde orbits? Where does the agreement between the gyrochronology age and the evolutionary age break down in Q' space?

Again, increasing the sample isn't the whole solution though. There are a number of improvements that can be made to the model that I have used. Accounting for the variety of possible stellar structures would improve my model, as would accounting for the evolution of additional stellar parameters, and it would be interesting to see how different sets of stellar evolution models affected the results.

7.2 Closing thoughts

There have been many studies investigating different aspects of the tides that act on exoplanets and their stars, of which the works that I have presented in this thesis are a small fraction. Whilst our understanding of the basic principles is sound, the detail and nuance of the effect of tides on the evolution of planetary systems is still under investigation. Each new result seems to uncover some hitherto unknown aspect of their influence, some unforeseen piece of the puzzle. But it is vital that we fully comprehend tidal interactions if we are to understand the birth, life, and death of planetary systems.

A

Age results

This Appendix presents the results of the age calculations outlined in Chapter 2. I used both stellar model fitting and gyrochronology to estimate the age for a sample of 137 exoplanet and brown dwarf host stars. The stellar models used are the Padova (Girardi et al., 2010; Marigo et al., 2008), Yonsei-Yale (YY) (Demarque et al., 2004), Dartmouth Stellar Evolution (DSEP) (Dotter et al., 2008), Teramo (Pietrinferni et al., 2004), and Victoria-Regina (VRSS) (VandenBerg et al., 2006) sets. The gyrochronology formulations are those characterised by equations (2.10) (Barnes, 2007; Meibom et al., 2009; James et al., 2010), (2.11) (Collier Cameron et al., 2009), and (2.12) (Delorme et al., 2011b).

Table A.1: *Age estimates for the host stars of 137 exoplanets and brown dwarfs, derived from stellar model fitting. Five different sets of stellar models are used to provide some insight into the systematic uncertainties involved in this method.* † *indicates those systems for which my model fits were used in associated publications (Note that many of these have been updated from the original results presented in those publications).*

System	Paper containing data used for analysis	Padova Age /Gyr	Y^2 Age /Gyr	Teramo Age /Gyr	VRSS Age /Gyr	DSEP Age /Gyr
WASP-1†	Wheatley et al. (2010)	$2.7^{+0.27}_{-0.21}$	$2.71^{+0.21}_{-0.17}$	$3.13^{+0.78}_{-0.38}$	$2.82^{+0.36}_{-0.18}$	$3.22^{+0.25}_{-0.22}$
WASP-2†	Wheatley et al. (2010)	$10.83^{+1.76}_{-1.76}$	$9.73^{+2.61}_{-2.45}$	> 8.88	> 11.58	$10.53^{+2.65}_{-1.98}$
WASP-3	Miller et al. (2010)	$1.33^{+0.86}_{-0.63}$	$1.41^{+0.59}_{-0.64}$	$0.90^{+0.76}_{-0.67}$	< 1.46	$2.66^{+0.93}_{-0.85}$
WASP-4†	Triaud et al. (2010)	$6.73^{+2.93}_{-4.30}$	$5.13^{+1.98}_{-1.76}$	$8.23^{+2.76}_{-3.35}$	$7.53^{+4.26}_{-2.76}$	$7.43^{+2.00}_{-2.27}$
WASP-5†	Triaud et al. (2010)	$6.17^{+2.86}_{-2.13}$	$5.04^{+2.65}_{-1.62}$	$9.31^{+3.86}_{-1.95}$	$6.57^{+3.84}_{-1.69}$	$7.47^{+2.38}_{-1.78}$
WASP-6	Gillon et al. (2009)	> 7.94	$8.45^{+3.25}_{-3.29}$	> 11.95	$10.87^{+5.63}_{-4.10}$	$10.40^{+2.92}_{-2.98}$
WASP-7	Southworth et al. (2011)	$2.03^{+0.69}_{-0.57}$	$2.47^{+0.41}_{-0.58}$	$2.30^{+0.45}_{-0.61}$	$2.04^{+0.56}_{-0.56}$	$2.96^{+0.61}_{-0.41}$
WASP-8	Queloz et al. (2010)	–	< 3.58	< 7.10	< 6.43	$3.19^{+2.66}_{-2.40}$
WASP-10	Maciejewski et al. (2011b)	–	< 10.94	> 16.0	–	–
HAT-P-10/WASP-11	Bakos et al. (2009)	< 11.87	$4.32^{+3.46}_{-2.63}$	> 5.3	$12.39^{+4.79}_{-5.89}$	> 3.97
WASP-12	Maciejewski et al. (2013)	$3.32^{+0.54}_{-0.44}$	$3.49^{+1.32}_{-0.26}$	$4.66^{+5.73}_{-0.98}$	$4.20^{+0.15}_{-1.38}$	$5.00^{+2.73}_{-0.62}$
WASP-13	Barros et al. (2012)	$3.98^{+1.40}_{-0.32}$	$4.78^{+0.73}_{-0.96}$	$6.23^{+0.79}_{-0.70}$	$5.90^{+0.71}_{-0.80}$	$6.10^{+0.87}_{-0.33}$
WASP-14	Joshi et al. (2009)	$2.46^{+0.75}_{-0.61}$	$2.07^{+0.37}_{-0.58}$	$2.80^{+1.00}_{-0.62}$	$1.51^{+0.51}_{-0.81}$	$2.49^{+1.29}_{-0.39}$
WASP-15†	Triaud et al. (2010)	$4.29^{+1.02}_{-0.62}$	$3.61^{+0.52}_{-0.52}$	$5.14^{+1.36}_{-1.31}$	$3.49^{+1.25}_{-0.49}$	$5.00^{+0.85}_{-1.03}$
WASP-16†	Brown et al. (2012a)	$4.50^{+4.12}_{-4.25}$	$3.37^{+3.36}_{-2.17}$	$5.73^{+4.61}_{-4.01}$	$5.22^{+4.58}_{-3.53}$	$5.86^{+3.11}_{-3.10}$
WASP-17†	Miller et al. (*submitted*)	$1.16^{+0.53}_{-0.73}$	$1.46^{+0.63}_{-0.64}$	$1.77^{+0.61}_{-0.68}$	$1.03^{+0.63}_{-0.65}$	$1.86^{+0.64}_{-0.64}$
WASP-18†	Miller et al. (*submitted*)	$3.24^{+3.06}_{-3.06}$	< 1.17	$0.66^{+1.02}_{-0.60}$	–	$0.78^{+1.02}_{-0.58}$
WASP-19†	Anderson et al. (2013)	> 8.25	$8.91^{+2.21}_{-0.92}$	> 10.51	> 9.73	$11.37^{+2.79}_{-2.31}$
WASP-20	Cameron et al. (*in prep*)	–	–	–	–	< 1.49
WASP-21	Barros et al. (2011b)	–	$12.37^{+2.77}_{-1.90}$	$15.69^{+0.31}_{-3.46}$	$13.02^{+3.55}_{-2.06}$	$13.06^{+1.94}_{-1.97}$
WASP-22	Anderson et al. (2011b)	$4.58^{+1.73}_{-1.13}$	$4.25^{+1.17}_{-1.01}$	$6.27^{+2.03}_{-1.63}$	$5.23^{+1.96}_{-1.19}$	$5.81^{+1.28}_{-0.98}$
WASP-23†	Miller et al. (*submitted*)	> 12.59	$14.04^{+5.96}_{-4.75}$	–	–	–
WASP-24	Smith et al. (2012b)	$3.87^{+1.20}_{-0.79}$	$3.64^{+0.98}_{-0.54}$	$5.75^{+1.43}_{-1.75}$	$4.09^{+1.22}_{-1.12}$	$4.75^{+1.35}_{-0.85}$
WASP-25†	Brown et al. (2012a)	< 3.10	$1.94^{+1.75}_{-1.79}$	$6.09^{+2.77}_{-3.22}$	$1.18^{+4.34}_{-0.51}$	$3.25^{+1.79}_{-1.53}$
WASP-26	Anderson et al. (2011b)	$6.58^{+1.81}_{-1.74}$	$5.73^{+1.50}_{-1.41}$	$7.22^{+1.78}_{-1.58}$	$6.29^{+1.69}_{-1.24}$	$7.25^{+1.60}_{-1.08}$
HAT-P-14/WASP-27†	Simpson et al. (2011a)	$1.02^{+0.33}_{-0.24}$	$1.28^{+0.42}_{-0.34}$	$1.45^{+0.33}_{-0.70}$	$0.73^{+0.49}_{-0.21}$	$1.84^{+0.34}_{-0.31}$
WASP-28	West et al. (*in prep.*)	$4.28^{+3.33}_{-2.14}$	$3.12^{+2.82}_{-1.76}$	$3.76^{+3.72}_{-2.49}$	$2.90^{+2.91}_{-2.68}$	$4.47^{+1.96}_{-2.01}$
WASP-29†	Hellier et al. (2010)	–	> 11.55	–	–	> 9.90

Continued on next page

Table A.1 – *Continued from previous page*

System	Paper containing data used for analysis	Padova Age /Gyr	Y^2 Age /Gyr	Teramo Age /Gyr	VRSS Age /Gyr	DSEP Age /Gyr
WASP-30	Triaud et al. (2013b)	$2.69^{+0.37}_{-0.17}$	$2.70^{+0.36}_{-0.24}$	$3.52^{+0.32}_{-0.60}$	$2.50^{+0.24}_{-0.49}$	$3.64^{+0.48}_{-0.43}$
WASP-31†	Brown et al. (2012a)	$3.23^{+1.40}_{-1.40}$	$2.05^{+1.17}_{-1.17}$	$3.60^{+2.26}_{-1.78}$	$1.87^{+1.34}_{-1.02}$	$4.19^{+0.99}_{-2.76}$
WASP-32†	Brown et al. (2012b)	$2.36^{+1.72}_{-0.85}$	$2.22^{+0.62}_{-0.73}$	$4.50^{+1.88}_{-1.69}$	$1.41^{+1.36}_{-1.10}$	$3.98^{+0.68}_{-1.19}$
WASP-33†	Smith et al. (2011)	< 0.89	< 0.31	$0.31^{+0.19}_{-0.22}$	> 0.10	–
WASP-34	Smalley et al. (2011)	–	–	–	–	< 12.53
WASP-35†	Enoch et al. (2011a)	$5.41^{+1.72}_{-2.66}$	$4.02^{+1.66}_{-1.56}$	$7.56^{+2.07}_{-1.99}$	$4.71^{+1.82}_{-2.18}$	$5.55^{+1.16}_{-1.20}$
WASP-36	Smith et al. (2012a)	$2.15^{+2.53}_{-1.96}$	$1.86^{+1.96}_{-1.24}$	$2.65^{+2.68}_{-2.16}$	< 4.01	$3.30^{+1.85}_{-1.86}$
WASP-37†	Simpson et al. (2011b)	> 8.32	$10.43^{+3.66}_{-3.30}$	> 8.51	$10.69^{+5.49}_{-3.78}$	$10.31^{+4.01}_{-2.55}$
WASP-38†	Brown et al. (2012b)	$3.41^{+0.48}_{-0.43}$	$3.29^{+0.42}_{-0.53}$	$3.59^{+0.77}_{-0.70}$	$3.20^{+0.73}_{-0.59}$	$4.81^{+0.52}_{-0.63}$
WASP-39†	Faedi et al. (2011)	> 6.88	$8.51^{+3.91}_{-3.42}$	> 14.05	$12.1^{+2.5}_{-5.0}$	> 7.35
HAT-P-27/WASP-40†	Brown et al. (2012b)	> 1.20	$6.36^{+5.86}_{-3.11}$	> 4.96	> 5.73	$9.19^{+4.94}_{-3.88}$
WASP-41	Maxted et al. (2011)	> 3.01	$6.97^{+4.57}_{-3.34}$	> 3.88	$11.10^{+2.63}_{-6.48}$	$9.07^{+4.85}_{-3.47}$
WASP-42	Lendl et al. (2012)	–	$11.95^{+5.48}_{-4.34}$	–	> 15.17	$12.20^{+2.80}_{-2.80}$
WASP-43	Gillon et al. (2012)	–	> 16.98	–	> 2.39	> 6.52
WASP-44	Mancini et al. (2013a)	–	–	$2.36^{+0.71}_{-0.71}$	< 2.65	< 2.93
WASP-45	Anderson et al. (2012)	–	–	$0.43^{+4.65}_{-0.01}$	< 4.80	< 3.76
WASP-46	Anderson et al. (2012)	–	$10.84^{+3.81}_{-4.03}$	$15.52^{+0.48}_{-5.30}$	$11.50^{+6.50}_{-4.54}$	$11.44^{+3.56}_{-3.28}$
WASP-47	Hellier et al. (2012)	> 10.50	$11.28^{+2.94}_{-2.35}$	–	> 12.62	> 11.49
WASP-48†	Enoch et al. (2011a)	$7.05^{+1.79}_{-2.72}$	$5.96^{+1.63}_{-0.91}$	$8.12^{+1.76}_{-1.56}$	$6.46^{+1.54}_{-1.26}$	$7.45^{+1.45}_{-1.33}$
WASP-49	Lendl et al. (2012)	$7.89^{+4.70}_{-3.70}$	$6.23^{+2.83}_{-2.33}$	$9.52^{+4.41}_{-3.55}$	$7.69^{+4.56}_{-3.29}$	$7.60^{+2.59}_{-2.54}$
WASP-50	Tregloan-Reed & Southworth (2013)	$1.06^{+0.80}_{-0.84}$	$1.86^{+4.41}_{-1.20}$	$2.21^{+2.79}_{-2.03}$	$1.13^{+1.15}_{-0.90}$	$1.28^{+1.85}_{-0.98}$
HA-P-30/WASP-51†	Enoch et al. (2011a)	$3.96^{+0.50}_{-0.96}$	$3.14^{+0.41}_{-0.72}$	$3.10^{+0.73}_{-0.81}$	$3.17^{+1.12}_{-0.66}$	$4.80^{+0.62}_{-1.10}$
WASP-52†	Hébrard et al. (*in prep.*)	> 2.31	$4.10^{+3.22}_{-3.15}$	$10.98^{+3.13}_{-6.52}$	$7.20^{+6.32}_{-5.40}$	< 6.62
WASP-53	Cameron (*priv. comm.*)	< 2.30	< 6.95	> 0.056	> 0.306	< 4.61
WASP-54†	Faedi et al. (2013)	$5.24^{+1.19}_{-1.17}$	$5.56^{+0.89}_{-0.51}$	$6.10^{+1.38}_{-0.84}$	$5.79^{+1.14}_{-0.75}$	$6.55^{+1.20}_{-0.77}$
WASP-55	Hellier et al. (2012)	$6.68^{+2.97}_{-2.11}$	$5.33^{+2.17}_{-2.35}$	$8.12^{+2.93}_{-2.82}$	$4.62^{+3.48}_{-1.87}$	$6.51^{+2.28}_{-1.68}$
WASP-56†	Faedi et al. (2013)	$6.84^{+4.33}_{-2.71}$	$5.84^{+3.45}_{-2.04}$	$8.70^{+4.29}_{-3.00}$	$9.51^{+3.69}_{-3.88}$	$8.22^{+3.42}_{-2.33}$
WASP-57†	Faedi et al. (2013)	< 5.29	$2.61^{+1.95}_{-1.81}$	$4.16^{+3.57}_{-2.25}$	$2.57^{+2.58}_{-0.97}$	$4.00^{+1.78}_{-1.78}$
WASP-58†	Hébrard et al. (*in prep.*)	> 12.59	$4.22^{+4.31}_{-4.13}$	> 11.58	$16.09^{+1.91}_{-4.49}$	> 11.24
WASP-59†	Hébrard et al. (*in prep.*)	–	< 13.40	–	$0.94^{+5.70}_{-0.71}$	–
WASP-60†	Hébrard et al. (*in prep.*)	$4.61^{+3.49}_{-2.57}$	$5.40^{+1.43}_{-2.26}$	$6.33^{+3.00}_{-2.23}$	$5.79^{+2.90}_{-2.74}$	> 3.68
WASP-61	Hellier et al. (2012)	$3.16^{+1.18}_{-0.55}$	$2.83^{+0.69}_{-0.44}$	$2.53^{+0.99}_{-0.82}$	$2.66^{+0.92}_{-0.73}$	$4.00^{+1.31}_{-1.08}$

Continued on next page

Table A.1 – *Continued from previous page*

System	Paper containing data used for analysis	Padova Age /Gyr	Y^2 Age /Gyr	Teramo Age /Gyr	VRSS Age /Gyr	DSEP Age /Gyr
WASP-62	Hellier et al. (2012)	$1.50^{+0.72}_{-0.79}$	$1.85^{+0.55}_{-0.57}$	$2.84^{+1.09}_{-1.10}$	$1.72^{+0.72}_{-0.82}$	$2.84^{+0.98}_{-1.10}$
WASP-63	Hellier et al. (2012)	$8.01^{+1.32}_{-1.21}$	$7.82^{+1.09}_{-1.13}$	$8.89^{+1.35}_{-1.37}$	$8.03^{+1.15}_{-1.21}$	$9.00^{+1.18}_{-1.27}$
WASP-64	Gillon et al. (2013)	> 7.89	$8.94^{+3.15}_{-2.55}$	$11.42^{+4.58}_{-4.15}$	$11.42^{+4.90}_{-3.19}$	$10.96^{+2.72}_{-2.93}$
WASP-65†	Gómez Maqueo Chew et al. (*in prep.*)	> 8.26	$8.92^{+1.87}_{-1.97}$	$11.42^{+4.01}_{-2.75}$	$11.31^{+3.14}_{-2.49}$	$10.80^{+2.36}_{-2.03}$
WASP-66	Hellier et al. (2012)	$5.18^{+0.90}_{-0.83}$	$5.02^{+0.78}_{-1.33}$	$5.06^{+1.10}_{-0.92}$	$4.74^{+1.03}_{-1.30}$	$5.82^{+1.02}_{-0.94}$
WASP-67	Hellier et al. (2012)	> 10.60	$10.36^{+4.63}_{-2.69}$	> 12.61	> 12.18	> 9.79
WASP-68	Cameron (*priv. comm.*)	$4.86^{+2.27}_{-1.29}$	$5.04^{+1.69}_{-1.25}$	–	$6.00^{+1.31}_{-1.85}$	$6.78^{+1.39}_{-1.07}$
WASP-69	Cameron (*priv. comm.*)	–	–	–	–	–
WASP-70	Cameron (*priv. comm.*)	$9.54^{+1.56}_{-1.44}$	$8.37^{+1.24}_{-1.21}$	$10.80^{+1.64}_{-1.39}$	$10.00^{+2.00}_{-1.78}$	$10.19^{+1.43}_{-1.35}$
WASP-71	Smith et al. (2013)	$3.27^{+0.33}_{-0.74}$	$3.21^{+0.38}_{-0.74}$	$3.16^{+0.55}_{-0.46}$	$3.04^{+0.50}_{-0.26}$	$3.67^{+0.76}_{-0.30}$
WASP-72	Gillon et al. (2013)	$3.63^{+1.39}_{-0.87}$	$3.40^{+1.09}_{-0.54}$	$3.81^{+0.39}_{-1.40}$	$3.22^{+1.12}_{-0.62}$	$4.73^{+0.79}_{-0.81}$
WASP-73	Cameron (*priv. comm.*)	$4.02^{+0.86}_{-1.34}$	$4.43^{+0.63}_{-0.92}$	–	$4.10^{+0.71}_{-0.89}$	$4.74^{+0.95}_{-1.06}$
WASP-74	Cameron (*priv. comm.*)	$8.30^{+2.54}_{-2.04}$	$7.53^{+2.23}_{-2.55}$	$10.44^{+2.84}_{-2.37}$	$8.45^{+2.84}_{-2.12}$	$9.00^{+2.77}_{-2.00}$
WASP-75†	Gómez Maqueo Chew et al. (*in prep.*)	$3.01^{+1.33}_{-1.08}$	$3.12^{+0.78}_{-0.95}$	$4.32^{+1.63}_{-1.49}$	$3.45^{+1.66}_{-0.84}$	$4.37^{+0.97}_{-0.82}$
WASP-76	Cameron (*priv. comm.*)	$2.19^{+0.04}_{-0.06}$	$2.11^{+0.06}_{-0.07}$	~ 2.00	$1.96^{+0.04}_{-0.06}$	$2.60^{+0.06}_{-0.001}$
WASP-77	Cameron (*priv. comm.*)	$6.29^{+5.13}_{-3.10}$	$5.34^{+2.19}_{-2.08}$	> 7.81	$9.48^{+5.41}_{-4.08}$	$7.82^{+2.75}_{-2.43}$
WASP-78	Smalley et al. (2012)	$3.39^{+0.23}_{-0.75}$	$3.97^{+0.38}_{-0.51}$	$3.90^{+0.41}_{-0.63}$	$3.85^{+0.40}_{-0.78}$	$4.38^{+0.40}_{-0.61}$
WASP-79	Smalley et al. (2012)	$1.86^{+0.18}_{-0.20}$	$1.96^{+0.87}_{-0.20}$	$1.64^{+0.45}_{-0.17}$	$1.88^{+0.22}_{-0.19}$	$2.36^{+0.28}_{-0.30}$
WASP-80	Triaud et al. (2013a)	–	–	–	–	< 0.411
WASP-81	Cameron (*priv. comm.*)	> 0.70	> 1.97	–	> 1.52	< 5.07
WASP-82	Cameron (*priv. comm.*)	$2.31^{+1.18}_{-0.32}$	$2.54^{+0.65}_{-0.36}$	$3.33^{+0.61}_{-1.45}$	$2.31^{+1.38}_{-0.28}$	$2.95^{+1.08}_{-0.39}$
WASP-83	Cameron (*priv. comm.*)	> 6.54	$9.63^{+4.71}_{-4.23}$	–	$16.47^{+1.53}_{-6.18}$	> 7.77
WASP-84	Cameron (*priv. comm.*)	–	–	–	–	–
WASP-85	Cameron (*priv. comm.*)	$4.04^{+6.68}_{-3.77}$	$3.90^{+3.76}_{-2.21}$	–	–	$5.72^{+4.80}_{-2.38}$
WASP-86	Cameron (*priv. comm.*)	$2.12^{+1.05}_{-0.50}$	$2.33^{+1.42}_{-1.61}$	–	> 1.80	$3.00^{+5.01}_{-0.85}$
WASP-87	Cameron (*priv. comm.*)	$2.02^{+0.36}_{-0.24}$	$2.26^{+0.42}_{-0.34}$	$2.46^{+0.56}_{-0.56}$	$2.00^{+0.31}_{-0.40}$	$2.72^{+0.57}_{-0.32}$
WASP-88	Cameron (*priv. comm.*)	$1.10^{+0.15}_{-0.11}$	$1.19^{+0.17}_{-0.11}$	$0.83^{+0.13}_{-0.08}$	$1.20^{+0.17}_{-0.10}$	$0.50^{+0.23}_{-0.17}$
WASP-89	Cameron (*priv. comm.*)	> 7.45	$7.99^{+3.79}_{-2.19}$	> 14.60	> 10.02	$10.86^{+4.14}_{-2.83}$
WASP-90	Cameron (*priv. comm.*)	> 1.82	< 2.85	–	–	> 1.12
WASP-91	Cameron (*priv. comm.*)	–	> 15.75	–	–	> 15.00
WASP-92	Cameron (*priv. comm.*)	< 5.81	< 3.20	< 0.75	< 15.54	< 4.18
WASP-93	Cameron (*priv. comm.*)	$1.61^{+0.41}_{-0.43}$	$1.72^{+0.47}_{-0.40}$	$1.83^{+0.42}_{-0.33}$	$1.45^{+0.49}_{-0.44}$	$2.34^{+0.43}_{-0.50}$

Continued on next page

Table A.1 – *Continued from previous page*

System	Paper containing data used for analysis	Padova Age /Gyr	Y^2 Age /Gyr	Teramo Age /Gyr	VRSS Age /Gyr	DSEP Age /Gyr
WASP-94	Cameron (*priv. comm.*)	$2.72^{+0.56}_{-0.63}$	$2.90^{+0.61}_{-0.66}$	–	–	$3.53^{+1.35}_{-0.70}$
WASP-95	Cameron (*priv. comm.*)	$8.28^{+3.06}_{-2.50}$	$7.02^{+2.78}_{-2.50}$	$11.50^{+3.87}_{-3.18}$	$9.00^{+3.39}_{-2.92}$	$9.19^{+2.90}_{-2.39}$
WASP-96	Cameron (*priv. comm.*)	> 9.43	$10.74^{+4.30}_{-3.46}$	–	> 11.37	> 9.62
WASP-97	Cameron (*priv. comm.*)	$5.15^{+3.24}_{-3.40}$	$4.77^{+2.02}_{-1.58}$	–	$5.82^{+3.71}_{-3.20}$	$6.35^{+2.72}_{-2.46}$
WASP-98	Cameron (*priv. comm.*)	–	–	–	–	–
QATAR-1†	Alsubai et al. (2011)	–	$12.67^{+7.29}_{-5.07}$	> 16.0	–	> 8.83
CoRot-1	Pont et al. (2010)	$0.63^{+0.59}_{-0.59}$	$0.96^{+0.72}_{-0.83}$	$1.05^{+0.69}_{-0.38}$	< 1.73	$1.64^{+0.80}_{-0.75}$
CoRot-2		$2.41^{+4.30}_{-0.95}$	$3.01^{+2.26}_{-1.50}$	$4.29^{+3.21}_{-2.59}$	$4.35^{+3.08}_{-2.42}$	$5.01^{+1.61}_{-0.91}$
CoRot-3	Triaud et al. (2009)	$1.37^{+0.39}_{-0.40}$	$1.43^{+0.41}_{-0.43}$	$1.28^{+0.31}_{-0.47}$	$1.20^{+0.41}_{-0.40}$	$1.90^{+0.41}_{-0.36}$
CoRot-11	Gandolfi et al. (2012)	$1.73^{+0.84}_{-0.70}$	$1.93^{+0.60}_{-0.63}$	$1.61^{+0.69}_{-0.74}$	$1.56^{+0.70}_{-0.68}$	$2.41^{+1.27}_{-0.46}$
CoRot-18	Hébrard et al. (2011b)	–	$11.80^{+5.71}_{-9.80}$	> 1.84	> 8.49	> 7.08
CoRot-19	Guenther et al. (2012)	$3.69^{+1.01}_{-0.33}$	$4.66^{+0.04}_{-1.02}$	$5.06^{+0.63}_{-0.95}$	$3.46^{+1.93}_{-0.06}$	$5.85^{+0.49}_{-0.70}$
Fomalhaut	Mamajek (2012)	$0.42^{+0.03}_{-0.02}$	$0.45^{+0.03}_{-0.02}$	$0.34^{+0.03}_{-0.02}$	$0.46^{+0.03}_{-0.03}$	–
HAT-P-1	Johnson et al. (2008)	< 2.98	$2.15^{+1.07}_{-1.18}$	$1.79^{+1.88}_{-1.39}$	$2.03^{+1.52}_{-0.68}$	$2.72^{+0.98}_{-1.32}$
HAT-P-2	Southworth (2010)	$2.38^{+0.14}_{-0.52}$	$2.61^{+1.01}_{-0.20}$	$2.13^{+8.09}_{-0.17}$	$2.40^{+2.44}_{-0.20}$	> 2.84
HAT-P-4	Winn et al. (2011b)	$4.36^{+0.67}_{-0.85}$	$3.98^{+1.72}_{-0.28}$	$6.14^{+0.90}_{-0.64}$	$4.74^{+1.72}_{-1.00}$	$5.20^{+1.78}_{-0.68}$
HAT-P-6	Noyes et al. (2008)	$2.47^{+0.34}_{-0.48}$	$2.14^{+0.36}_{-0.33}$	$2.75^{+0.59}_{-0.45}$	$1.78^{+0.34}_{-0.38}$	$2.50^{+0.36}_{-0.32}$
HAT-P-7	Pál et al. (2008)	< 2.38	$2.43^{+5.26}_{-1.28}$	$1.89^{+0.93}_{-0.67}$	$2.20^{+0.28}_{-0.20}$	< 3.00
HAT-P-8	Mancini et al. (2013a)	$3.64^{+0.53}_{-0.43}$	$3.70^{+0.39}_{-0.49}$	$3.26^{+0.35}_{-0.46}$	$3.64^{+0.33}_{-0.85}$	$5.00^{+0.43}_{-1.16}$
HAT-P-9	Shporer et al. (2009)	$1.30^{+1.02}_{-0.95}$	$1.75^{+0.65}_{-0.75}$	$1.45^{+1.03}_{-0.79}$	$1.74^{+0.78}_{-0.99}$	$2.15^{+0.71}_{-0.60}$
HAT-P-11	Bakos et al. (2010)	–	$5.03^{+3.98}_{-3.37}$	–	> 3.90	–
HAT-P-13	Winn et al. (2010b)	$8.40^{+1.48}_{-1.70}$	$5.83^{+0.51}_{-2.00}$	$8.98^{+1.50}_{-1.37}$	$7.64^{+1.44}_{-1.26}$	$6.50^{+1.97}_{-1.13}$
HAT-P-16	Buchhave et al. (2010)	$1.39^{+1.06}_{-0.96}$	$1.97^{+0.89}_{-0.79}$	$1.80^{+0.83}_{-1.21}$	$1.76^{+1.13}_{-1.03}$	$2.50^{+0.82}_{-0.78}$
HAT-P-23	Bakos et al. (2011)	$3.94^{+1.74}_{-1.59}$	$3.96^{+0.61}_{-1.41}$	$4.57^{+2.06}_{-1.31}$	$4.65^{+1.77}_{-1.76}$	$4.88^{+0.86}_{-1.37}$
HAT-P-24	Kipping et al. (2010)	$4.35^{+0.55}_{-0.99}$	$3.03^{+0.51}_{-0.66}$	$4.03^{+1.02}_{-0.84}$	$2.41^{+0.99}_{-0.54}$	$4.35^{+0.81}_{-0.71}$
HAT-P-32		$1.12^{+1.10}_{-0.89}$	$1.45^{+0.89}_{-0.55}$	$0.96^{+1.36}_{-0.69}$	$0.94^{+0.96}_{-0.51}$	$3.08^{+0.73}_{-1.09}$
HAT-P-34	Bakos et al. (2012)	$1.41^{+0.55}_{-0.63}$	$1.52^{+0.52}_{-0.44}$	$1.56^{+0.34}_{-0.62}$	$1.38^{+0.47}_{-0.58}$	$2.04^{+0.40}_{-0.55}$
HD149026	Carter et al. (2009)	$2.54^{+0.24}_{-0.23}$	$2.61^{+0.20}_{-0.21}$	$2.76^{+0.34}_{-0.26}$	$2.63^{+0.22}_{-0.29}$	$3.02^{+0.29}_{-0.21}$
HD17156	Barbieri et al. (2009)	$3.23^{+0.75}_{-0.47}$	$3.37^{+0.88}_{-0.44}$	$3.38^{+1.16}_{-0.63}$	$3.75^{+0.44}_{-0.97}$	$4.00^{+0.29}_{-0.37}$
HD189733	Triaud et al. (2009)	$7.96^{+2.43}_{-2.84}$	$7.20^{+1.45}_{-2.36}$	$8.06^{+2.69}_{-2.86}$	$9.33^{+2.47}_{-3.46}$	$6.57^{+1.10}_{-1.97}$
HD209458	Southworth (2010)	$1.83^{+0.55}_{-0.44}$	$2.27^{+0.45}_{-0.56}$	$2.65^{+0.92}_{-0.51}$	$1.92^{+0.59}_{-0.42}$	$3.87^{+0.76}_{-0.07}$
HD80606	Hébrard et al. (2010)	$4.56^{+1.73}_{-1.82}$	$3.68^{+1.55}_{-1.25}$	$7.83^{+2.21}_{-2.18}$	$7.34^{+2.46}_{-1.89}$	$5.73^{+1.64}_{-1.21}$

Continued on next page

Table A.1 – *Continued from previous page*

System	Paper containing data used for analysis	Padova Age /Gyr	Y^2 Age /Gyr	Teramo Age /Gyr	VRSS Age /Gyr	DSEP Age /Gyr
Kepler-8	Jenkins et al. (2010)	$2.76^{+0.40}_{-0.25}$	$3.00^{+0.19}_{-0.37}$	$3.07^{+0.47}_{-0.42}$	$2.85^{+1.23}_{-0.29}$	$3.93^{+0.75}_{-0.50}$
Kepler-16	Doyle et al. (2011)	–	–	> 16.0	–	$5.56^{+2.82}_{-0.40}$
Kepler-17	Désert et al. (2011)	$3.18^{+2.77}_{-2.96}$	$2.21^{+2.00}_{-1.17}$	$4.06^{+4.14}_{-2.18}$	$5.07^{+2.24}_{-2.38}$	$4.08^{+2.27}_{-1.65}$
Kepler-30 b	Sanchis-Ojeda et al. (2012)	–	–	< 3.14	< 3.39	$1.76^{+1.40}_{-1.37}$
KOI-13		$0.04^{+0.03}_{-0.03}$	$0.71^{+0.18}_{-0.15}$	$0.71^{+0.18}_{-0.15}$	$0.71^{+0.18}_{-0.15}$	–
KOI-94 d	Hirano et al. (2012)	$3.66^{+0.74}_{-0.42}$	$3.90^{+0.51}_{-0.32}$	$4.93^{+0.20}_{-1.22}$	$4.56^{+0.02}_{-0.98}$	$5.52^{+0.43}_{-0.36}$
TrES-01	Southworth (2010)	$3.54^{+3.30}_{-2.77}$	$3.63^{+2.39}_{-1.49}$	$7.16^{+3.45}_{-2.69}$	$7.31^{+4.26}_{-3.33}$	$4.91^{+2.41}_{-1.69}$
TrES-02	Sozzetti et al. (2007)	< 4.35	$3.15^{+1.40}_{-1.29}$	$4.10^{+1.87}_{-2.10}$	$3.25^{+1.91}_{-2.13}$	$4.45^{+1.46}_{-1.25}$
TrES-04	Chan et al. (2011)	$3.02^{+0.55}_{-0.63}$	$2.83^{+0.64}_{-0.13}$	$2.78^{+0.53}_{-0.66}$	$2.68^{+0.65}_{-0.21}$	$3.75^{+0.49}_{-0.76}$
XO-3	Southworth (2010)	$2.52^{+0.17}_{-0.30}$	$2.51^{+0.18}_{-0.41}$	$2.13^{+0.26}_{-0.21}$	$2.05^{+0.26}_{-0.44}$	$2.96^{+0.42}_{-0.19}$
XO-4	Southworth (2010)	$2.61^{+0.31}_{-0.29}$	> 2.42	$2.25^{+1.80}_{-0.21}$	> 2.13	> 2.81

Table A.2: *Ages for the exoplanet and brown dwarf host stars from Table A.1, as calculated using gyrochronology. Three different formulations of the $P_{\rm rot}$-colour-age relation have been used to provide different estimates of the ages of the systems. age$_1$ values were calculated using the period-colour-age relation of Barnes (2007), with updated coefficients. age$_2$ estimates were derived using Collier Cameron et al. (2009), and age$_3$ estimates following Delorme et al. (2011b). (B-V) colours are derived from NOMAD data, and (J-K) colours from 2MASS data. $P_{\rm rot}$ values were calculated using $v \sin I$, i, and R_s values; measured $P_{\rm rot}$ values were used for systems marked *. Some systems return ages greater than the currently accepted age of the Universe; these are clearly incorrect, and are omitted from my analysis.*

System	Reference	$v \sin I$ /km s^{-1}	i	R_s /$R_\odot$	$P_{\rm rot}$ /days	(B-V)	(J-K)	age$_1$ /Gyr	age$_2$ /Gyr	age$_3$ /Gyr
WASP-1	Stempels et al. (2007); Wheatley et al. (2010)	5.79 ± 0.35	89.2 ± 0.8	1.462 ± 0.019	$12.8^{+0.8}_{-0.7}$	0.721	0.31	$0.81^{+0.10}_{-0.09}$	$1.61^{+0.20}_{-0.16}$	$1.57^{+0.19}_{-0.16}$
WASP-2	Triaud et al. (2010); Wheatley et al. (2010)	$0.99^{+0.27}_{-0.32}$	84.92 ± 0.11	0.823 ± 0.011	$41.8^{+19.4}_{-8.9}$	0.966	0.534	$3.66^{+3.81}_{-1.33}$	$8.16^{+7.97}_{-2.85}$	$7.39^{+7.22}_{-2.58}$
WASP-3	Miller et al. (2010)	$13.9^{+0.3}_{-0.3}$	$87.0^{+1.0}_{-1.1}$	$1.21^{+0.04}_{-0.03}$	$4.41^{+0.16}_{-0.15}$	0.400	0.242	–	$0.29^{+0.02}_{-0.02}$	$0.29^{+0.02}_{-0.02}$
WASP-4*	Triaud et al. (2010)	$2.14^{+0.38}_{-0.35}$	$89.5^{+0.5}_{-0.2}$	$0.903^{+0.054}_{-0.053}$	$22.2^{+3.3}_{-3.3}$	1.016	0.433	$1.01^{+0.29}_{-0.06}$	$3.24^{+0.89}_{-0.18}$	$3.01^{+0.83}_{-0.17}$
WASP-5	Triaud et al. (2010)	$3.24^{+0.35}_{-0.27}$	$86.1^{+0.7}_{-1.5}$	$1.060^{+0.076}_{-0.028}$	$16.7^{+1.7}_{-1.7}$	0.490	0.351	$20.27^{+4.12}_{-3.72}$	$2.35^{+0.45}_{-0.41}$	$2.25^{+0.44}_{-0.40}$
WASP-6	Triaud et al. (2010)	$4.27^{+0.26}_{-0.36}$	$85.96^{+0.29}_{-0.41}$	$1.440^{+0.064}_{-0.057}$	$27.2^{+3.6}_{-3.9}$	0.970	0.444	$1.62^{+0.43}_{-0.40}$	$4.54^{+1.13}_{-1.09}$	$4.21^{+1.05}_{-1.01}$
WASP-7	Albrecht et al. (2012a)	14^{+2}_{-2}	$87.2^{+0.9}_{-1.2}$	$1.432^{+0.092}_{-0.092}$	$5.16^{+0.92}_{-0.70}$	0.436	0.252	–	$0.37^{+0.13}_{-0.09}$	$0.37^{+0.13}_{-0.09}$
WASP-8	Queloz et al. (2010)	$1.59^{+0.08}_{-0.09}$	$88.55^{+0.15}_{-0.17}$	$0.945^{+0.051}_{-0.036}$	$30.3^{+2.3}_{-2.0}$	0.695	0.415	$4.56^{+0.68}_{-0.54}$	$5.87^{+0.83}_{-0.66}$	$5.49^{+0.78}_{-0.62}$
WASP-10*	Maciejewski et al. (2011b)	$4.1^{+1.0}_{-1.0}$	$89.5^{+0.4}_{-0.9}$	$0.67^{+0.03}_{-0.02}$	$11.91^{+0.05}_{-0.05}$	0.570	0.620	$1.86^{+0.01}_{-0.01}$	$0.74^{+0.006}_{-0.005}$	$0.66^{+0.005}_{-0.005}$
WASP-11	Bakos et al. (2009); Torres et al. (2012)	$1.9^{+0.9}_{-0.9}$	$88.6^{+0.5}_{-0.4}$	$0.79^{+0.02}_{-0.02}$	$20.8^{+18.2}_{-6.6}$	0.991	0.594	$0.94^{+2.12}_{-0.48}$	$2.10^{+4.36}_{-1.04}$	$1.88^{+3.90}_{-0.93}$
WASP-12	Maciejewski et al. (2011a); Torres et al. (2012)	$3.4^{+0.9}_{-0.9}$	$82.5^{+0.8}_{-0.7}$	$1.63^{+0.08}_{-0.08}$	$24.0^{+8.8}_{-5.1}$	0.531	0.289	$11.69^{+9.29}_{-4.18}$	$5.26^{+3.93}_{-1.81}$	$5.16^{+3.85}_{-1.78}$
WASP-13	Barros et al. (2012)	< 4.9	$85.19^{+0.26}_{-0.26}$	$1.559^{+0.041}_{-0.041}$	$16.1^{+0.5}_{-0.4}$	0.754	0.323	$1.09^{+0.06}_{-0.06}$	$2.35^{+0.12}_{-0.11}$	$2.27^{+0.12}_{-0.11}$
WASP-14	Joshi et al. (2009)	$2.80^{+0.57}_{-0.57}$	$84.32^{+0.62}_{-0.62}$	$1.306^{+0.066}_{-0.073}$	$23.5^{+6.1}_{-4.1}$	0.410	0.248	–	$5.65^{+2.87}_{-1.65}$	$5.66^{+2.87}_{-1.66}$
WASP-15	Triaud et al. (2010)	$4.27^{+0.26}_{-0.36}$	$85.96^{+0.29}_{-0.41}$	$1.440^{+0.064}_{-0.057}$	$17.1^{+1.7}_{-1.3}$	0.335	0.263	–	$3.07^{+0.56}_{-0.39}$	$3.05^{+0.56}_{-0.39}$
WASP-16	Brown et al. (2012a)	$1.474^{+0.301}_{-0.316}$	$84.86^{+0.32}_{-0.32}$	$0.983^{+0.047}_{-0.049}$	$33.8^{+9.2}_{-6.0}$	1.222	0.395	$1.60^{+0.91}_{-0.49}$	$7.47^{+4.00}_{-2.21}$	$7.04^{+3.77}_{-2.08}$
WASP-17	Miller et al. (*submitted*)	$8.368^{+0.156}_{-0.186}$	$88.67^{+0.88}_{-0.59}$	$1.410^{+0.036}_{-0.037}$	$8.53^{+0.29}_{-0.27}$	0.223	0.285	–	$0.84^{+0.05}_{-0.05}$	$0.82^{+0.05}_{-0.05}$
WASP-18	Hellier et al. (2009)	$10.77^{+0.04}_{-0.04}$	$86.0^{+2.5}_{-2.5}$	$1.216^{+0.067}_{-0.054}$	$5.69^{+0.32}_{-0.25}$	0.422	0.278	–	$0.41^{+0.04}_{-0.03}$	$0.41^{+0.04}_{-0.03}$
WASP-19*	Anderson et al. (2013); Hebb et al. (2010)	$4.63^{+0.27}_{-0.27}$	$79.42^{+0.39}_{-0.39}$	$0.993^{+0.018}_{-0.018}$	10.5 ± 0.2	0.330	0.430	–	$0.86^{+0.03}_{-0.03}$	$0.80^{+0.03}_{-0.03}$

Continued on next page

Table A.2 – *Continued from previous page*

System	Reference	$v \sin I$ /km s^{-1}	i	R_s /$R_\odot$	$P_{\rm rot}$ /days	(B-V)	(J-K)	age$_1$ /Gyr	age$_2$ /Gyr	age$_3$ /Gyr
WASP-20	Cameron et al. (*submitted*)	$5.81^{+1.14}_{-0.83}$	$89.35^{+0.54}_{-0.54}$	$0.951^{+0.29}_{-0.29}$	$8.07^{+3.10}_{-2.62}$	0.489	0.311	$5.50^{+4.61}_{-2.86}$	$0.71^{+0.56}_{-0.36}$	$0.69^{+0.54}_{-0.35}$
WASP-21	Bouchy et al. (2010)	$1.5^{+0.6}_{-0.6}$	$88.75^{+0.84}_{-0.70}$	$1.06^{+0.04}_{-0.04}$	$35.9^{+23.4}_{-10.4}$	0.625	0.368	$9.25^{+14.43}_{-4.37}$	$8.85^{+12.86}_{-4.04}$	$8.41^{+12.22}_{-3.84}$
WASP-22	Anderson et al. (2011b)	$4.42^{+0.34}_{-0.34}$	$88.26^{+0.91}_{-0.91}$	$1.219^{+0.052}_{-0.033}$	$14.0^{+1.3}_{-1.1}$	0.352	0.316	–	$1.87^{+0.32}_{-0.25}$	$1.82^{+0.31}_{-0.24}$
WASP-23	Triaud et al. (2011)	$2.03^{+0.37}_{-0.35}$	$88.39^{+0.79}_{-0.45}$	$0.765^{+0.033}_{-0.049}$	$18.8^{+4.1}_{-3.1}$	0.400	0.510	–	$2.06^{+0.87}_{-0.56}$	$1.88^{+0.79}_{-0.51}$
WASP-24	Smith et al. (2012b)	$5.86^{+0.63}_{-0.63}$	$83.30^{+0.30}_{-0.30}$	$1.354^{+0.032}_{-0.032}$	$11.6^{+1.4}_{-1.1}$	0.745	0.309	$0.61^{+0.15}_{-0.11}$	$1.36^{+0.31}_{-0.23}$	$1.32^{+0.30}_{-0.22}$
WASP-25	Brown et al. (2012a)	$2.83^{+0.26}_{-0.27}$	$87.83^{+0.31}_{-0.27}$	$0.910^{+0.028}_{-0.029}$	$16.2^{+1.8}_{-1.5}$	0.360	0.422	–	$1.90^{+0.39}_{-0.29}$	$1.77^{+0.36}_{-0.27}$
WASP-26	Anderson et al. (2011b)	$2.2^{+0.7}_{-0.7}$	$82.91^{+0.46}_{-0.46}$	$1.303^{+0.059}_{-0.059}$	$29.8^{+13.8}_{-7.1}$	0.297	0.331	–	$6.92^{+6.72}_{-2.67}$	$6.67^{+6.48}_{-2.57}$
HAT-P-14/WASP-27	Simpson et al. (2011a)	$8.18^{+0.49}_{-0.49}$	$83.52^{+0.22}_{-0.22}$	$1.468^{+0.042}_{-0.042}$	$9.01^{+0.63}_{-0.55}$	0.388	0.243	–	$1.03^{+0.13}_{-0.11}$	$1.04^{+0.13}_{-0.11}$
WASP-28	West et al. (*submitted*), Smalley et al. (*priv. comm.*)	$4.1^{+0.6}_{-0.6}$	$89.1^{+0.6}_{-0.6}$	$1.05^{+0.06}_{-0.06}$	$12.9^{+2.4}_{-1.8}$	0.470	0.346	–	$1.51^{+0.54}_{-0.36}$	$1.44^{+0.51}_{-0.34}$
WASP-29	Hellier et al. (2010)	$1.5^{+0.6}_{-0.6}$	$88.8^{+0.7}_{-0.7}$	$0.808^{+0.044}_{-0.044}$	$26.9^{+17.7}_{-7.6}$	0.793	0.570	$2.51^{+3.94}_{-1.16}$	$3.48^{+5.08}_{-1.56}$	$3.12^{+4.56}_{-1.40}$
WASP-30	Triaud et al. (2013b)	$12.1^{+0.4}_{-0.5}$	$89.43^{+0.51}_{-0.93}$	$1.389^{+0.033}_{-0.025}$	$5.82^{+0.28}_{-0.23}$	0.222	0.309	–	$0.40^{+0.03}_{-0.03}$	$0.39^{+0.03}_{-0.03}$
WASP-31	Brown et al. (2012a)	$7.35^{+0.69}_{-0.69}$	$84.71^{+0.24}_{-0.22}$	$1.199^{+0.045}_{-0.045}$	$8.21^{+0.92}_{-0.76}$	0.318	0.262	–	$0.83^{+0.17}_{-0.13}$	$0.82^{+0.17}_{-0.13}$
WASP-32	Brown et al. (2012b)	$3.94^{+0.42}_{-0.48}$	$85.08^{+0.24}_{-0.22}$	$1.087^{+0.031}_{-0.032}$	$13.9^{+2.0}_{-1.4}$	0.769	0.342	$0.79^{+0.23}_{-0.15}$	$1.74^{+0.47}_{-0.31}$	$1.67^{+0.45}_{-0.29}$
WASP-33	Smith et al. (2011)	$86.05^{+0.19}_{-0.19}$	$86.97^{+0.23}_{-0.23}$	$1.464^{+0.023}_{-0.023}$	$0.86^{+0.01}_{-0.01}$	0.251	0.113	–	$0.02^{+0.001}_{-0.001}$	$0.03^{+0.001}_{-0.001}$
WASP-34	Smalley et al. (2011)	$1.4^{+0.6}_{-0.6}$	$85.2^{+0.2}_{-0.2}$	$0.93^{+0.12}_{-0.12}$	$33.2^{+24.2}_{-10.5}$	0.737	0.380	$4.53^{+8.07}_{-2.30}$	$7.49^{+12.40}_{-3.68}$	$7.08^{+11.73}_{-3.48}$
WASP-35	Enoch et al. (2011a)	$3.9^{+0.4}_{-0.4}$	$87.96^{+0.62}_{-0.49}$	$1.09^{+0.14}_{-0.14}$	$14.1^{+2.4}_{-2.2}$	0.570	0.362	$2.56^{+0.89}_{-0.68}$	$1.70^{+0.56}_{-0.44}$	$1.62^{+0.53}_{-0.41}$
WASP-36	Smith et al. (2012a)	$3.3^{+1.2}_{-1.2}$	$83.61^{+0.21}_{-0.21}$	$0.951^{+0.018}_{-0.018}$	$14.4^{+8.1}_{-3.8}$	0.340	0.315	–	$1.97^{+2.41}_{-0.82}$	$1.91^{+2.34}_{-0.80}$
WASP-37	Simpson et al. (2011b)	$2.4^{+1.6}_{-1.6}$	$88.82^{+0.77}_{-0.86}$	$1.003^{+0.053}_{-0.053}$	$20.0^{+25.3}_{-7.6}$	0.280	0.406	–	$2.85^{+9.42}_{-1.64}$	$2.67^{+8.83}_{-1.54}$
WASP-38	Brown et al. (2012b)	$7.49^{+0.15}_{-0.16}$	$89.46^{+0.32}_{-0.37}$	$1.351^{+0.022}_{-0.018}$	$9.13^{+0.24}_{-0.22}$	0.434	0.289	–	$0.93^{+0.04}_{-0.04}$	$0.92^{+0.04}_{-0.04}$
WASP-39	Faedi et al. (2011)	$1.4^{+0.6}_{-0.6}$	$87.83^{+0.25}_{-0.22}$	$0.895^{+0.023}_{-0.023}$	$32.3^{+24.0}_{-9.5}$	0.640	0.461	$6.89^{+12.59}_{-3.31}$	$5.96^{+10.12}_{-2.77}$	$5.50^{+9.33}_{-2.55}$
HAT-P-27/WASP-40	Brown et al. (2012b)	$0.586^{+0.694}_{-0.414}$	$84.95^{+0.24}_{-0.24}$	$0.875^{+0.039}_{-0.040}$	$66.9^{+94.4}_{-33.7}$	0.912	0.517	$9.94^{+41.65}_{-7.26}$	$19.53^{+74.50}_{-13.95}$	$17.76^{+67.75}_{-12.69}$
WASP-41	Maxted et al. (2011)	$1.6^{+1.1}_{-1.1}$	$87.7^{+0.08}_{-0.08}$	$0.90^{+0.05}_{-0.05}$	$27.1^{+33.5}_{-10.6}$	0.694	0.419	$3.71^{+13.06}_{-2.24}$	$4.76^{+15.32}_{-2.79}$	$4.45^{+14.31}_{-2.61}$
WASP-42	Lendl et al. (2012)	$2.7^{+0.4}_{-0.4}$	$88.25^{+0.27}_{-0.23}$	$0.863^{+0.041}_{-0.034}$	$16.2^{+3.0}_{-2.2}$	0.520	0.509	$6.92^{+2.55}_{-1.63}$	$1.58^{+0.55}_{-0.36}$	$1.44^{+0.50}_{-0.33}$

Continued on next page

Table A.2 – *Continued from previous page*

System	Reference	$v \sin I$ /km s^{-1}	i	R_s /$R_\odot$	P_{rot} /days	(B-V)	(J-K)	age$_1$ /Gyr	age$_2$ /Gyr	age$_3$ /Gyr
WASP-43*	Gillon et al. (2012)	$4.0^{+0.4}_{-0.4}$	$82.33^{+0.20}_{-0.20}$	$0.667^{+0.010}_{-0.011}$	$15.6^{+0.4}_{-0.4}$	1.06	0.728	$0.48^{+0.02}_{-0.02}$	$1.00^{+0.05}_{-0.05}$	$0.87^{+0.04}_{-0.04}$
WASP-44	Anderson et al. (2012); Mancini et al. (2013a)	$3.2^{+0.9}_{-0.9}$	$86.02^{+1.11}_{-0.86}$	$0.865^{+0.025}_{-0.025}$	$13.6^{+5.4}_{-3.0}$	0.810	0.361	$0.66^{+0.57}_{-0.25}$	$1.59^{+1.29}_{-0.57}$	$1.51^{+1.23}_{-0.54}$
WASP-45	Anderson et al. (2012)	$2.3^{+0.7}_{-0.7}$	$84.47^{+0.54}_{-0.79}$	$0.945^{+0.087}_{-0.071}$	$20.8^{+9.0}_{-5.0}$	1.565	0.459	$0.44^{+0.42}_{-0.18}$	$2.73^{+2.46}_{-1.07}$	$2.52^{+2.27}_{-0.98}$
WASP-46*	Anderson et al. (2012)	$1.9^{+1.2}_{-1.2}$	$82.63^{+0.38}_{-0.38}$	$0.917^{+0.028}_{-0.028}$	$16.1^{+1.0}_{-1.0}$	0.710	0.352	$1.31^{+0.16}_{-0.15}$	$2.20^{+0.25}_{-0.24}$	$2.10^{+0.24}_{-0.23}$
WASP-47	Hellier et al. (2012)	$3.0^{+0.6}_{-0.6}$	$89.2^{+0.5}_{-0.7}$	$1.15^{+0.03}_{-0.02}$	$19.4^{+4.7}_{-3.3}$	0.750	0.421	$1.58^{+0.80}_{-0.46}$	$2.61^{+1.25}_{-0.73}$	$2.44^{+1.17}_{-0.68}$
WASP-48	Enoch et al. (2011a)	$12.2^{+0.7}_{-0.7}$	$80.09^{+0.88}_{-0.79}$	$1.09^{+0.14}_{-0.14}$	$4.45^{+0.62}_{-0.62}$	0.623	0.255	$0.19^{+0.05}_{-0.05}$	$0.28^{+0.07}_{-0.07}$	$0.28^{+0.07}_{-0.07}$
WASP-49	Lendl et al. (2012)	$0.9^{+0.3}_{-0.3}$	$84.89^{+0.19}_{-0.19}$	$0.976^{+0.034}_{-0.034}$	$54.8^{+27.0}_{-13.6}$	0.535	0.397	$51.09^{+57.13}_{-21.20}$	$17.61^{+18.43}_{-7.05}$	$16.56^{+17.34}_{-6.63}$
WASP-50*	Gillon et al. (2011); Tregloan-Reed & Southworth (2013)	$2.6^{+0.5}_{-0.5}$	$84.74^{+0.24}_{-0.24}$	$0.855^{+0.018}_{-0.018}$	$16.3^{+0.5}_{-0.5}$	0.972	0.432	$0.62^{+0.04}_{-0.03}$	$1.87^{+0.10}_{-0.10}$	$1.74^{+0.10}_{-0.09}$
HAT-P-30/WASP-51	Enoch et al. (2011a)	$3.6^{+0.4}_{-0.4}$	$82.48^{+0.16}_{-0.15}$	$1.28^{+0.17}_{-0.17}$	$17.8^{+3.3}_{-2.9}$	0.561	0.291	$4.38^{+1.62}_{-1.25}$	$3.08^{+1.07}_{-0.84}$	$3.01^{+1.05}_{-0.83}$
WASP-52*	Hébrard et al. (*in prep.*)	$3.6^{+0.9}_{-0.9}$	$85.35^{+0.20}_{-0.20}$	$0.792^{+0.015}_{-0.015}$	16.4 ± 0.04	0.912	0.502	$0.72^{+0.003}_{-0.003}$	$1.63^{+0.007}_{-0.007}$	$1.49^{+0.006}_{-0.007}$
WASP-53	Cameron (*priv. comm.*)	$2.7^{+0.3}_{-0.3}$	$87.62^{+0.26}_{-0.25}$	$0.755^{+0.027}_{-0.027}$	$14.1^{+1.8}_{-1.5}$	0.966	0.569	$0.48^{+0.12}_{-0.09}$	$1.10^{+0.27}_{-0.20}$	$0.99^{+0.24}_{-0.18}$
WASP-54	Faedi et al. (2013)	$4.0^{+0.8}_{-0.8}$	$84.97^{+0.63}_{-0.59}$	$1.828^{+0.091}_{-0.081}$	$23.0^{+6.0}_{-3.9}$	0.559	0.330	$7.24^{+3.92}_{-2.13}$	$4.39^{+2.25}_{-1.24}$	$4.24^{+2.16}_{-1.20}$
WASP-55	Hellier et al. (2012)	$3.1^{+1.0}_{-1.0}$	$89.2^{+0.6}_{-0.6}$	$1.06^{+0.03}_{-0.02}$	$17.3^{+8.1}_{-4.2}$	0.910	0.379	$0.79^{+0.84}_{-0.32}$	$2.33^{+2.32}_{-0.92}$	$2.21^{+2.20}_{-0.87}$
WASP-56	Faedi et al. (2013)	$1.5^{+0.9}_{-0.9}$	$88.1^{+0.3}_{-0.4}$	$1.049^{+0.081}_{-0.064}$	$34.8^{+38.6}_{-13.0}$	1.251	0.342	$1.62^{+4.92}_{-0.95}$	$8.92^{+24.84}_{-5.05}$	$8.56^{+23.83}_{-4.85}$
WASP-57	Faedi et al. (2013)	$3.7^{+1.3}_{-1.3}$	$88.0^{+0.1}_{-0.2}$	$0.836^{+0.07}_{-0.16}$	$11.0^{+6.2}_{-3.2}$	0.740	0.381	$0.57^{+0.74}_{-0.27}$	$1.04^{+1.27}_{-0.47}$	$0.98^{+1.20}_{-0.45}$
WASP-58	Hébrard et al. (*in prep.*)	$2.8^{+0.9}_{-0.9}$	$86.97^{+1.55}_{-1.55}$	$1.25^{+0.17}_{-0.17}$	$22.5^{+11.5}_{-6.0}$	0.623	0.341	$3.90^{+4.57}_{-1.72}$	$4.08^{+4.48}_{-1.74}$	$3.92^{+4.30}_{-1.67}$
WASP-59	Hébrard et al. (*in prep.*)	$2.3^{+1.2}_{-1.2}$	$89.27^{+0.52}_{-0.52}$	$0.613^{+0.044}_{-0.044}$	$13.2^{+12.2}_{-4.5}$	0.990	0.717	$0.40^{+0.97}_{-0.22}$	$0.76^{+1.68}_{-0.40}$	$0.66^{+1.47}_{-0.35}$
WASP-60	Hébrard et al. (*in prep.*)	$3.4^{+0.8}_{-0.8}$	$87.86^{+1.61}_{-1.61}$	$1.14^{+0.13}_{-0.13}$	$16.9^{+5.8}_{-3.6}$	1.470	0.379	$0.33^{+0.24}_{-0.12}$	$2.26^{+1.55}_{-0.79}$	$2.14^{+1.47}_{-0.75}$
WASP-61	Hellier et al. (2012)	$10.3^{+0.5}_{-0.5}$	$89.35^{+0.45}_{-0.66}$	$1.36^{+0.03}_{-0.03}$	$6.68^{+0.36}_{-0.34}$	0.311	0.211	–	$0.66^{+0.07}_{-0.06}$	$0.68^{+0.07}_{-0.06}$
WASP-62	Hellier et al. (2012)	$8.7^{+0.4}_{-0.4}$	$88.3^{+0.9}_{-0.6}$	$1.28^{+0.05}_{-0.05}$	$7.44^{+0.46}_{-0.44}$	0.432	0.328	$8.19^{+0.97}_{-0.88}$	$0.59^{+0.07}_{-0.06}$	$0.57^{+0.06}_{-0.06}$
WASP-63	Hellier et al. (2012)	$2.8^{+0.5}_{-0.5}$	$87.8^{+1.3}_{-1.3}$	$1.88^{+0.10}_{-0.06}$	$34.2^{+7.7}_{-5.4}$	0.546	0.425	$17.96^{+8.33}_{-4.94}$	$7.15^{+3.13}_{-1.89}$	$6.67^{+2.92}_{-1.76}$
WASP-64	Gillon et al. (2013)	$3.4^{+0.8}_{-0.8}$	$86.57^{+0.80}_{-0.60}$	$1.058^{+0.025}_{-0.025}$	$15.7^{+4.8}_{-3.0}$	0.400	0.412	–	$1.83^{+1.12}_{-0.58}$	$1.71^{+1.05}_{-0.54}$
WASP-65	Gómez Maqueo Chew et al. (*in prep.*)	$3.6^{+0.5}_{-0.5}$	$87.45^{+0.15}_{-0.13}$	$1.070^{+0.010}_{-0.010}$	$15.0^{+2.4}_{-1.9}$	−0.052	0.323	–	$2.09^{+0.63}_{-0.44}$	$2.02^{+0.61}_{-0.42}$

Continued on next page

Table A.2 – *Continued from previous page*

System	Reference	$v \sin I$ /km s^{-1}	i	R_s /$R_\odot$	$P_{\rm rot}$ /days	(B-V)	(J-K)	age$_1$ /Gyr	age$_2$ /Gyr	age$_3$ /Gyr
WASP-66	Hellier et al. (2012)	$13.4^{+0.9}_{-0.9}$	$85.9^{+0.9}_{-0.9}$	$1.75^{+0.09}_{-0.09}$	$6.59^{+0.6-}_{-0.53}$	0.357	0.267	–	$0.55^{+0.09}_{-0.08}$	$0.55^{+0.09}_{-0.08}$
WASP-67	Hellier et al. (2012)	$2.1^{+0.4}_{-0.4}$	$85.8^{+0.3}_{-0.4}$	$0.87^{+0.04}_{-0.04}$	$20.9^{+4.97}_{-3.5}$	0.327	0.479	–	$2.63^{+1.22}_{-0.74}$	$2.42^{+1.12}_{-0.68}$
WASP-68	Cameron (*priv. comm.*)	$2.3^{+0.8}_{-0.8}$	$89.13^{+0.56}_{-0.99}$	$1.595^{+0.055}_{-0.044}$	$35.2^{+18.3}_{-9.2}$	0.630	0.393	$8.63^{+10.22}_{-3.74}$	$8.07^{+8.94}_{-3.38}$	$7.60^{+8.42}_{-3.18}$
WASP-69	Cameron (*priv. comm.*)	$2.2^{+0.4}_{-0.4}$	$87.65^{+0.186}_{-0.199}$	$0.665^{+0.027}_{-0.026}$	$15.3^{+3.5}_{-2.4}$	1.05	0.573	$0.47^{+0.22}_{-0.13}$	$1.26^{+0.55}_{-0.33}$	$1.13^{+0.50}_{-0.30}$
WASP-70A	Cameron (*priv. comm.*)	$1.8^{+0.4}_{-0.4}$	$86.86^{+0.710}_{-0.707}$	$1.261^{+0.069}_{-0.067}$	$35.2^{+10.4}_{-6.6}$	0.940	0.416	$2.81^{+1.74}_{-0.90}$	$7.67^{+4.49}_{-2.37}$	$7.17^{+4.20}_{-2.21}$
WASP-70B	Cameron (*priv. comm.*)	$3.9^{+0.8}_{-0.8}$	$86.86^{+0.710}_{-0.707}$	$1.261^{+0.069}_{-0.067}$	$16.4^{+4.4}_{-2.9}$	0.940	0.416	$0.67^{+0.37}_{-0.20}$	$1.95^{+1.03}_{-0.57}$	$1.82^{+0.96}_{-0.53}$
WASP-71	Smith et al. (2013)	$9.91^{+0.49}_{-0.49}$	$84.2^{1.8}_{-1.8}$	$2.32^{+0.14}_{-0.14}$	$11.8^{+1.0}_{-0.9}$	0.761	0.316	$0.60^{+0.09}_{-0.08}$	$1.38^{+0.21}_{-0.18}$	$1.33^{+0.20}_{-0.17}$
WASP-72	Gillon et al. (2013)	$6.0^{+0.7}_{-0.7}$	$86.8^{+2.0}_{-3.1}$	$1.71^{+0.16}_{-0.09}$	$14.6^{+2.3}_{-1.8}$	0.608	0.347	$1.94^{+0.60}_{-0.43}$	$1.86^{+0.55}_{-0.39}$	$1.79^{+0.53}_{-0.38}$
WASP-73	Cameron (*priv. comm.*)	$6.1^{+0.6}_{-0.6}$	$86.30^{+2.287}_{-2.446}$	$2.121^{+0.234}_{-0.132}$	$17.8^{+2.6}_{-2.1}$	0.478	0.324	$70.73^{+20.84}_{-14.70}$	$2.80^{+0.78}_{-0.56}$	$2.71^{+0.76}_{-0.54}$
WASP-74	Cameron (*priv. comm.*)	$4.7^{+0.4}_{-0.4}$	$80.52^{+0.485}_{-0.634}$	$1.440^{+0.060}_{-0.051}$	$15.3^{+1.5}_{-1.3}$	0.603	0.327	$2.21^{+0.43}_{-0.34}$	$2.14^{+0.40}_{-0.31}$	$2.06^{+0.38}_{-0.30}$
WASP-75	Gómez Maqueo Chew et al. (*in prep.*)	$4.3^{+0.8}_{-0.8}$	$82.15^{+0.21}_{-0.23}$	$1.256^{+0.029}_{-0.029}$	$14.6^{+3.4}_{-2.3}$	0.672	0.300	$1.31^{+0.62}_{-0.36}$	$2.11^{+0.94}_{-0.56}$	$2.06^{+0.92}_{-0.55}$
WASP-76	Cameron (*priv. comm.*)	$3.3^{+0.6}_{-0.6}$	$88.28^{+1.169}_{-1.455}$	$1.586^{+0.178}_{-0.157}$	$24.4^{+6.1}_{-4.4}$	0.575	0.298	$6.75^{+3.51}_{-2.10}$	$5.27^{+2.58}_{-1.58}$	$5.15^{+2.53}_{-1.54}$
WASP-77A	Cameron (*priv. comm.*)	$4.0^{+0.2}_{-0.2}$	$89.23^{+0.518}_{-0.670}$	$0.946^{+0.011}_{-0.010}$	$12.0^{+0.6}_{-0.6}$	0.747	0.361	$0.64^{+0.07}_{-0.06}$	$1.26^{+0.12}_{-0.11}$	$1.20^{+0.12}_{-0.10}$
WASP-77B	Cameron (*priv. comm.*)	$2.8^{+0.5}_{-0.5}$	$89.23^{+0.518}_{-0.670}$	$0.946^{+0.011}_{-0.010}$	$17.1^{+3.7}_{-2.6}$	0.747	0.361	$1.26^{+0.56}_{-0.34}$	$2.40^{+1.00}_{-0.62}$	$2.29^{+0.95}_{-0.59}$
WASP-78	Smalley et al. (2012)	$7.2^{+0.8}_{-0.8}$	$83.2^{+2.3}_{-1.6}$	$2.20^{+0.12}_{-0.12}$	$15.3^{+2.1}_{-1.7}$	0.655	0.278	$1.57^{+0.43}_{-0.32}$	$2.43^{+0.64}_{-0.47}$	$2.40^{+0.63}_{-0.46}$
WASP-79	Smalley et al. (2012)	$19.1^{+0.7}_{-0.7}$	$83.3^{+0.5}_{-0.5}$	$1.91^{+0.09}_{-0.09}$	$5.03^{+0.31}_{-0.30}$	0.371	0.243	–	$0.36^{+0.04}_{-0.04}$	$0.37^{+0.04}_{-0.04}$
WASP-80	Triaud et al. (2013a)	$3.46^{+0.34}_{-0.35}$	$89.92^{+0.07}_{-0.12}$	$0.571^{+0.016}_{-0.016}$	$8.34^{+0.98}_{-0.77}$	0.929	0.867	$0.19^{+0.04}_{-0.03}$	$0.34^{+0.07}_{-0.05}$	$0.30^{+0.07}_{-0.05}$
WASP-81	Cameron (*priv. comm.*)	2.0 (assumed)	$88.62^{+0.812}_{-1.007}$	$1.296^{+0.226}_{-0.264}$	$32.8^{+5.7}_{-6.8}$	0.650	0.371	$6.69^{+2.33}_{-2.35}$	$7.49^{+2.48}_{-2.53}$	$7.11^{+2.35}_{-2.41}$
WASP-82	Cameron (*priv. comm.*)	$5.1^{+0.4}_{-0.4}$	$87.40^{+1.583}_{-1.957}$	$1.938^{+0.116}_{-0.077}$	$19.3^{+1.9}_{-1.6}$	0.377	0.287	–	$3.58^{+0.66}_{-0.53}$	$3.51^{+0.65}_{-0.52}$
WASP-83	Cameron (*priv. comm.*)	$1.1^{+0.9}_{-0.9}$	$89.10^{+0.573}_{-0.749}$	$0.978^{+0.069}_{-0.073}$	$39.9^{+59.4}_{-16.2}$	−0.097	0.411	–	$9.68^{+39.64}_{-5.87}$	$9.07^{+37.13}_{-5.50}$
WASP-84	Cameron (*priv. comm.*)	$4.1^{+0.3}_{-0.3}$	$88.32^{+0.239}_{-0.264}$	$0.754^{+0.058}_{-0.051}$	$9.34^{+1.01}_{-0.92}$	0.785	0.491	$0.35^{+0.08}_{-0.06}$	$0.61^{+0.12}_{-0.10}$	$0.56^{+0.11}_{-0.09}$
WASP-85	Cameron (*priv. comm.*)	2.0 (assumed)	$88.38^{+1.047}_{-1.267}$	$0.941^{+0.053}_{-0.031}$	$23.8^{+1.34}_{-0.77}$	0.673	0.542	$3.22^{+0.35}_{-0.19}$	$2.93^{+0.30}_{-0.17}$	$2.65^{+0.27}_{-0.15}$
WASP-86	Cameron (*priv. comm.*)	2.0 (assumed)	$86.44^{+2.388}_{-4.313}$	$2.244^{+0.546}_{-0.272}$	$56.6^{+13.7}_{-6.9}$	0.572	0.269	$33.65^{+16.85}_{-7.29}$	$25.60^{+12.11}_{-5.32}$	$25.34^{+11.99}_{-5.27}$

Continued on next page

Table A.2 – *Continued from previous page*

System	Reference	$v \sin I$ /km s^{-1}	i	R_s /$R_\odot$	P_{rot} /days	(B-V)	(J-K)	age$_1$ /Gyr	age$_2$ /Gyr	age$_3$ /Gyr
WASP-87	Cameron (*priv. comm.*)	$9.6^{+0.7}_{-0.7}$	$81.59^{+1.334}_{-1.147}$	$1.635^{+0.090}_{-0.103}$	$8.49^{+0.84}_{-0.77}$	0.599	0.280	$0.75^{+0.15}_{-0.12}$	$0.84^{+0.15}_{-0.13}$	$0.83^{+0.15}_{-0.13}$
WASP-88	Cameron (*priv. comm.*)	$8.4^{+0.8}_{-0.8}$	$73.50^{+1.975}_{-1.503}$	$4.438^{+0.242}_{-0.369}$	$25.3^{+3.25}_{-2.77}$	0.595	0.246	$6.03^{+1.53}_{-1.18}$	$6.49^{+1.56}_{-1.21}$	$6.50^{+1.57}_{-1.21}$
WASP-89	Cameron (*priv. comm.*)	$2.5^{+0.9}_{-0.9}$	$89.16^{+0.523}_{-0.630}$	$0.885^{+0.025}_{-0.020}$	$17.8^{+10.0}_{-4.7}$	0.480	0.542	$52.81^{+68.75}_{-22.95}$	$1.75^{+2.13}_{-0.73}$	$1.58^{+1.92}_{-0.66}$
WASP-90	Cameron (*priv. comm.*)	$6.0^{+0.5}_{-0.5}$	$83.45^{+1.492}_{-1.461}$	$1.714^{+0.229}_{-0.247}$	$14.3^{+2.4}_{-2.3}$	0.210	0.302	–	$2.02^{+0.64}_{-0.54}$	$1.97^{+0.62}_{-0.52}$
WASP-91	Cameron (*priv. comm.*)	$2.4^{+0.4}_{-0.4}$	$86.54^{+0.344}_{-0.435}$	$0.886^{+0.039}_{-0.031}$	$18.7^{+3.8}_{-2.8}$	0.719	0.563	$1.67^{+0.69}_{-0.43}$	$1.84^{+0.72}_{-0.46}$	$1.66^{+0.65}_{-0.41}$
WASP-92	Cameron (*priv. comm.*)	2.0 (assumed)	$85.20^{+3.326}_{-4.215}$	$1.345^{+0.288}_{-0.187}$	$33.7^{+7.3}_{-4.7}$	0.250	0.315	–	$8.99^{+3.76}_{-2.12}$	$8.72^{+3.65}_{-2.06}$
WASP-93	Cameron (*priv. comm.*)	2.0 (assumed)	$80.90^{+0.570}_{-0.938}$	$1.557^{+0.105}_{-0.077}$	$38.8^{+2.6}_{-1.9}$	0.568	0.291	$17.36^{+2.25}_{-1.58}$	$12.33^{+1.52}_{-1.07}$	$12.08^{+1.49}_{-1.05}$
WASP-94	Cameron (*priv. comm.*)	$3.9^{+0.5}_{-0.5}$	$85.24^{+1.034}_{-1.043}$	$1.536^{+0.162}_{-0.130}$	$19.9^{+3.5}_{-2.9}$	0.655	0.285	$2.56^{+0.92}_{-0.64}$	$3.81^{+1.29}_{-0.92}$	$3.74^{+1.27}_{-0.90}$
WASP-95	Cameron (*priv. comm.*)	2.0 (assumed)	$84.96^{+0.792}_{-0.881}$	$1.248^{+0.068}_{-0.056}$	$31.5^{+1.7}_{-1.4}$	0.651	0.372	$6.14^{+0.64}_{-0.51}$	$6.93^{+0.69}_{-0.55}$	$6.57^{+0.65}_{-0.52}$
WASP-96	Cameron (*priv. comm.*)	$1.5^{+1.3}_{-1.3}$	$85.36^{+0.528}_{-0.864}$	$1.037^{+0.094}_{-0.063}$	$31.2^{+45.6}_{-13.4}$	1.340	0.353	$1.18^{+5.19}_{-0.77}$	$7.13^{+28.54}_{-4.51}$	$6.81^{+27.27}_{-4.31}$
WASP-97	Cameron (*priv. comm.*)	2.0 (assumed)	$86.08^{+1.412}_{-1.059}$	$1.097^{+0.066}_{-0.064}$	$27.7^{+1.7}_{-1.6}$	0.707	0.377	$3.64^{+0.43}_{-0.39}$	$5.44^{+0.61}_{-0.56}$	$5.16^{+0.58}_{-0.53}$
WASP-98	Cameron (*priv. comm.*)	0.5 (assumed)	$86.36^{+0.329}_{-0.492}$	$0.774^{+0.049}_{-0.038}$	$78.2^{+4.9}_{-3.9}$	0.580	0.407	$56.87^{+6.83}_{-5.19}$	$32.47^{+3.71}_{-2.84}$	$30.45^{+3.48}_{-2.66}$
QATAR-1	Alsubai et al. (2011)	$2.1^{+0.8}_{-0.8}$	$83.47^{+0.40}_{-0.36}$	$0.823^{+0.025}_{-0.025}$	$19.6^{+4.9}_{-3.9}$	1.060	0.590	$0.74^{+1.03}_{-0.33}$	$1.90^{+2.47}_{-0.83}$	$1.70^{+2.21}_{-0.74}$
CoRot-1	Barge et al. (2008); Torres et al. (2012)	$4.6^{+0.9}_{-0.9}$	$85.1^{+0.5}_{-0.5}$	$1.14^{+0.03}_{-0.03}$	$12.5^{+3.1}_{-2.1}$	B not known	0.313	–	$1.54^{+0.74}_{-0.42}$	$1.49^{+0.72}_{-0.41}$
CoRot-2*	Alonso et al. (2008)	$11.95^{+0.58}_{-0.55}$	$87.84^{+0.16}_{-0.17}$	$0.902^{+0.018}_{-0.018}$	$4.5^{+0.14}_{-0.14}$	0.854	0.473	$0.07^{+0.004}_{-0.004}$	$0.17^{+0.01}_{-0.01}$	$0.16^{+0.01}_{-0.01}$
CoRot-3	Triaud et al. (2009)	$35.8^{+8.2}_{-8.3}$	$86.10^{+0.73}_{-0.52}$	$1.56^{+0.09}_{-0.09}$	$2.20^{+0.67}_{-0.43}$	0.907	0.320	$0.02^{+0.01}_{-0.01}$	$0.07^{+0.04}_{-0.02}$	$0.07^{+0.04}_{-0.02}$
CoRot-11	Gandolfi et al. (2012)	$38.47^{+0.07}_{-0.07}$	$83.41^{+0.17}_{-0.17}$	$1.33^{+0.04}_{-0.04}$	$1.74^{+0.05}_{-0.05}$	0.930	0.341	$0.01^{+0.001}_{-0.001}$	$0.04^{+0.002}_{-0.002}$	$0.04^{+0.002}_{-0.002}$
CoRot-18*	Hébrard et al. (2011b)	$8.0^{+1.0}_{-1.0}$	$86.5^{+1.4}_{-0.9}$	$1.00^{+0.13}_{-0.13}$	$5.4^{+0.4}_{-0.4}$	0.800	0.431	$0.12^{+0.02}_{-0.02}$	$0.26^{+0.04}_{-0.03}$	$0.24^{+0.03}_{-0.03}$
CoRot-19	Guenther et al. (2012)	6^{+1}_{-1}	$88.0^{+0.7}_{-0.7}$	$1.65^{+0.04}_{-0.04}$	$13.9^{+2.8}_{-2.0}$	0.863	0.487	$0.59^{+0.24}_{-0.15}$	$1.25^{+0.49}_{-0.30}$	$1.15^{+0.45}_{-0.28}$
Fomalhaut	Mamajek (2012)	93^{+1}_{-1}	$65.9^{+0.4}_{-0.4}$	$1.842^{+0.019}_{-0.019}$	$0.91^{+0.01}_{-0.01}$	0.09	unknown	–	–	–
HAT-P-1	Johnson et al. (2008)	$3.75^{+0.58}_{-0.58}$	$86.28^{+0.20}_{-0.20}$	$1.115^{+0.050}_{-0.050}$	$15.0^{+2.8}_{-2.1}$	0.60	0.298	$2.17^{+0.83}_{-0.52}$	$2.21^{+0.80}_{-0.51}$	$2.16^{+0.79}_{-0.50}$
HAT-P-2	Loeillet et al. (2008); Pál et al. (2010)	$19.5^{+1.4}_{-1.4}$	$90.0^{+0.85}_{-0.93}$	$1.64^{+0.08}_{-0.08}$	$4.25^{+0.40}_{-0.34}$	0.46	0.193	–	$0.31^{+0.05}_{-0.04}$	$0.32^{+0.06}_{-0.043}$
HAT-P-4	Winn et al. (2011b)	$5.83^{+0.35}_{-0.35}$	$88.76^{+0.89}_{-1.38}$	$1.617^{+0.057}_{-0.050}$	$14.0^{+1.0}_{-0.9}$	0.71	unknown	$1.01^{+0.14}_{-0.12}$	–	–

Continued on next page

Table A.2 – *Continued from previous page*

System	Reference	$v \sin I$ /km s^{-1}	i	R_s /$R_\odot$	$P_{\rm rot}$ /days	(B-V)	(J-K)	age$_1$ /Gyr	age$_2$ /Gyr	age$_3$ /Gyr
HAT-P-6	Noyes et al. (2008); Albrecht et al. (2012b)	$7.8^{+0.6}_{-0.6}$	$85.51^{+0.35}_{-0.35}$	$1.46^{+0.06}_{-0.06}$	$9.44^{+0.90}_{-0.77}$	0.41	0.245	–	$1.12^{+0.20}_{-0.16}$	$1.12^{+0.20}_{-0.16}$
HAT-P-7	Pál et al. (2008); Albrecht et al. (2012b)	$2.7^{+0.5}_{-0.5}$	$80.8^{+2.8}_{-1.2}$	$1.84^{+0.23}_{-0.11}$	$34.9^{+8.9}_{-6.2}$	0.49	0.221	$80.13^{+42.50}_{-24.68}$	$12.33^{+6.18}_{-3.65}$	$12.52^{+6.27}_{-3.71}$
HAT-P-8	Torres et al. (2012); Mancini et al. (2013b)	$12.6^{+1.0}_{-1.0}$	$87.5^{+1.9}_{-0.9}$	$1.475^{+0.032}_{-0.032}$	$5.91^{+0.53}_{-0.45}$	0.41	0.261	–	$0.46^{+0.08}_{-0.06}$	$0.46^{+0.08}_{-0.06}$
HAT-P-9	Shporer et al. (2009); Torres et al. (2012)	$13.4^{+1.4}_{-1.4}$	$86.5^{+0.2}_{-0.2}$	$1.32^{+0.07}_{-0.07}$	$4.96^{+0.62}_{-0.52}$	0.01	0.259	–	$0.34^{+0.08}_{-0.06}$	$0.34^{+0.08}_{-0.06}$
HAT-P-13		$8.18^{+0.49}_{-0.49}$	$83.52^{+0.22}_{-0.22}$	$1.468^{+0.054}_{-0.054}$	$9.02^{+0.67}_{-0.60}$	0.42	0.243	$9.01^{+5.57}_{-2.93}$	$14.98^{+8.73}_{-4.69}$	$14.32^{+8.34}_{-4.48}$
HAT-P-16	Buchhave et al. (2010); Moutou et al. (2011)	$3.9^{+0.8}_{-0.8}$	$86.6^{+0.7}_{-0.7}$	$1.237^{+0.054}_{-0.054}$	$16.0^{+4.2}_{-2.8}$	0.47	0.297	–	$2.49^{+1.29}_{-0.72}$	$2.44^{+1.27}_{-0.70}$
HAT-P-23	Bakos et al. (2011); Moutou et al. (2011)	$7.8^{+1.6}_{-1.6}$	$85.1^{+1.5}_{-1.5}$	$1.203^{+0.035}_{-0.035}$	$7.77^{+2.11}_{-1.35}$	1.11	0.312	$0.12^{+0.07}_{-0.04}$	$0.66^{+0.35}_{-0.19}$	$0.64^{+0.34}_{-0.19}$
HAT-P-24	Kipping et al. (2010); Albrecht et al. (2012b)	$11.2^{+0.9}_{-0.9}$	$88.6^{+0.7}_{-0.7}$	$1.317^{+0.068}_{-0.068}$	$5.95^{+0.60}_{-0.53}$	0.45	0.254	–	$0.48^{+0.09}_{-0.07}$	$0.48^{+0.09}_{-0.07}$
HAT-P-32	Hartman et al. (2011); Albrecht et al. (2012b)	$20.6^{+1.5}_{-1.5}$	$88.9^{+0.4}_{-0.4}$	$1.219^{+0.016}_{-0.016}$	$3.00^{+0.24}_{-0.21}$	0.35	0.261	–	$0.14^{+0.02}_{-0.02}$	$0.14^{+0.02}_{-0.02}$
HAT-P-34	Bakos et al. (2012); Albrecht et al. (2012b)	$24.3^{+1.2}_{-1.2}$	$87.1^{+1.2}_{-1.2}$	$1.535^{+0.102}_{-0.102}$	$3.19^{+0.28}_{-0.26}$	0.41	0.213	–	$0.18^{+0.03}_{-0.03}$	$0.18^{+0.03}_{-0.03}$
HD149026	Carter et al. (2009); Albrecht et al. (2012b)	$7.7^{+0.8}_{-0.8}$	$84.5^{+0.60}_{-0.52}$	$1.534^{+0.049}_{-0.047}$	$10.0^{+1.2}_{-1.0}$	0.61	unknown	$0.95^{+0.22}_{-0.17}$	–	–
HD17156	Barbieri et al. (2009); Narita et al. (2009a)	$4.18^{+0.31}_{-0.31}$	$87.21^{+0.31}_{-0.31}$	$1.44^{+0.08}_{-0.08}$	$17.4^{+1.7}_{-1.5}$	0.62	unknown	$2.47^{+0.47}_{-0.38}$	–	–
HD189733	Collier Cameron et al. (2010a)	$3.10^{+0.03}_{-0.03}$	$85.51^{+0.10}_{-0.05}$	$0.766^{+0.007}_{-0.013}$	$12.4^{+0.2}_{-0.2}$	B unknown	J unknown	–	–	–
HD209458	Southworth (2010)	$4.4^{+0.2}_{-0.2}$	$86.55^{+0.03}_{-0.03}$	$1.162^{+0.012}_{-0.012}$	$13.3^{+0.7}_{-0.6}$	0.58	0.283	$2.08^{+0.20}_{-0.18}$	$1.87^{+0.17}_{-0.15}$	$1.84^{+0.16}_{-0.15}$
HD80606	Hébrard et al. (2010)	$1.7^{+0.3}_{-0.3}$	$89.27^{+0.018}_{-0.018}$	$1.007^{+0.024}_{-0.024}$	$29.8^{+6.6}_{-4.5}$	0.78	unknown	$3.20^{+1.44}_{-0.84}$	–	–
Kepler-8	Jenkins et al. (2010); Albrecht et al. (2012b)	$8.9^{+1.0}_{-1.0}$	$84.07^{+0.33}_{-0.33}$	$1.486^{+0.062}_{-0.062}$	$8.38^{+1.13}_{-0.89}$	V unknown	0.283	–	$0.81^{+0.21}_{-0.15}$	$0.80^{+0.20}_{-0.14}$
Kepler-16*	Doyle et al. (2011); Winn et al. (2011a)	$0.920^{+0.025}_{-0.025}$	90^{+9}_{-9}	$0.649^{+0.001}_{-0.001}$	$35.1^{+1.0}_{-1.0}$	V unknown	0.819	–	$3.69^{+0.19}_{-0.19}$	$3.18^{+0.16}_{-0.16}$
Kepler-17	Désert et al. (2011)	$4.7^{+1.0}_{-1.0}$	$87.2^{+0.15}_{-0.15}$	$1.02^{+0.03}_{-0.03}$	$11.9^{+1.1}_{-1.1}$	V unknown	0.407	–	$1.12^{+0.20}_{-0.18}$	$1.05^{+0.19}_{-0.16}$
Kepler-30 b	Fabrycky et al. (2012)	$1.94^{+0.22}_{-0.22}$	$89.82^{+0.17}_{-0.17}$	$0.95^{+0.12}_{-0.12}$	$16.0^{+0.4}_{-0.4}$	V unknown	0.42	–	$1.86^{+0.08}_{-0.08}$	$1.73^{+0.08}_{-0.08}$
KOI-13	Barnes et al. (2011)	65^{+10}_{-10}	$85.9^{+0.4}_{-0.4}$	$1.756^{+0.014}_{-0.014}$	$1.36^{+0.25}_{-0.18}$	0.21	0.041	–	$0.07^{+0.02}_{-0.02}$	$0.08^{+0.03}_{-0.02}$
KOI-94 d	Hirano et al. (2012)	$8.01^{+0.72}_{-0.73}$	$87.85^{+0.55}_{-0.55}$	$1.61^{+0.11}_{-0.12}$	$10.1^{+1.3}_{-1.1}$	unknown	0.292	–	$1.12^{+0.26}_{-0.20}$	$1.09^{+0.25}_{-0.20}$
TrES-01	Narita et al. (2007)	$1.3^{+0.3}_{-0.3}$	$88.4^{+0.3}_{-0.3}$	$0.818^{+0.02}_{-0.02}$	$40.2^{+22.9}_{-14.6}$	unknown	unknown	–	–	–
TrES-02	Sozzetti et al. (2007); Winn et al. (2008)	$1.0^{+0.6}_{-0.6}$	$83.62^{+0.14}_{-0.14}$	$1.00^{+0.036}_{-0.036}$	$48.7^{+51.4}_{-17.6}$	unknown	unknown	–	–	–

Continued on next page

Table A.2 – *Continued from previous page*

System	Reference	$v \sin I$ /km s^{-1}	i	R_s /$R_\odot$	$P_{\rm rot}$ /days	(B-V)	(J-K)	age$_1$ /Gyr	age$_2$ /Gyr	age$_3$ /Gyr
TrES-04	Chan et al. (2011)	$8.5^{+1.2}_{-1.2}$	$82.81^{+0.37}_{-0.37}$	$1.798^{+0.052}_{-0.052}$	$10.6^{+1.8}_{-1.3}$	unknown	unknown	–	–	–
XO-3	Hirano et al. (2011a)	$18.4^{+0.2}_{-0.2}$	$83.89^{+0.40}_{-0.40}$	$1.409^{+0.054}_{-0.054}$	$3.85^{+0.15}_{-0.15}$	0.42	0.222	–	$0.24^{+0.02}_{-0.02}$	$0.24^{+0.02}_{-0.02}$
XO-4	Narita et al. (2010a)	$8.8^{+0.5}_{-0.5}$	$88.8^{+0.6}_{-0.6}$	$1.530^{+0.362}_{-0.069}$	$9.08^{+1.87}_{-0.87}$	0.34	0.261	–	$1.00^{+0.39}_{-0.16}$	$0.99^{+0.39}_{-0.16}$

B

Comparing age estimation methods

This Appendix presents a graphical comparison of the ages obtained through different age estimation methods, using the results presented in Appendix A. In Chapter 2 I presented the results of the comparison between the Yonsei-Yale (YY) stellar models (Demarque et al., 2004) and the gyrochronology formulation of Collier Cameron et al. (2009), and commented on the differences between the results obtained using these methods.

Here I present similar comparisons between the ages obtained using the Padova (Girardi et al., 2010; Marigo et al., 2008), Yonsei-Yale (YY), Dartmouth Stellar Evolution (DSEP) (Dotter et al., 2008), Teramo (Pietrinferni et al., 2004), and Victoria-Regina (VRSS) (VandenBerg et al., 2006) stellar models, and the gyrochronology formulations characterised by equations (2.10) (Barnes, 2007; Meibom et al., 2009; James et al., 2010), (2.11) (Collier Cameron et al., 2009), and (2.12) (Delorme et al., 2011b). As in Chapter 2, all comparisons between different methods use only those systems with valid results for both methods, and systems with calculated ages greater than the current best estimate of the age of the Universe were disregarded.

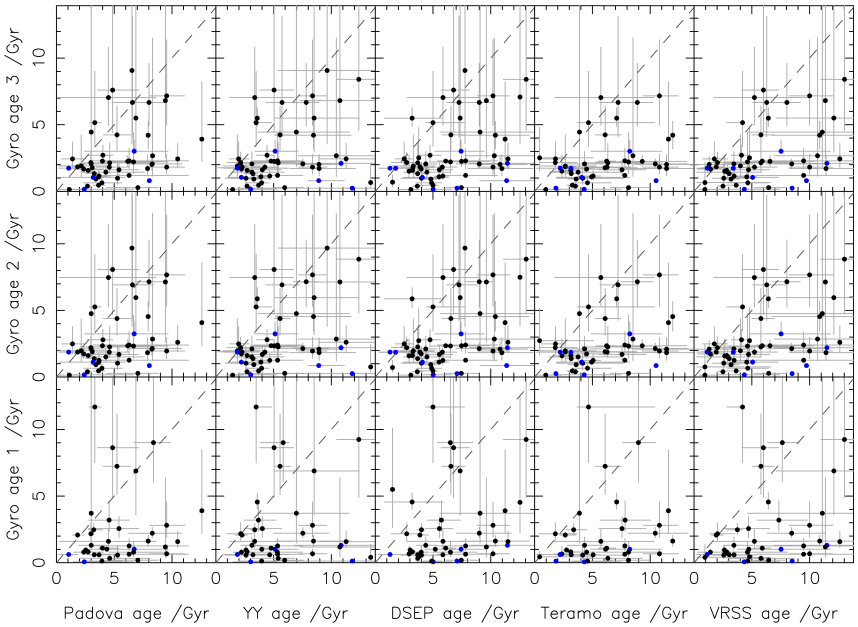

Figure B.1: *Scatter plots comparing the age estimates produced by fitting different stellar models to the ages calculated using different gyrochronology formulations. Dashed lines denote $y = x$, and the maximum age on both axes is set to the age of the Universe. Direct measurements of the stellar rotation period were available for systems marked in blue. For systems marked in black, $P_{\rm rot}$ was inferred from $v \sin I$ and R_s. For all combinations there is a clear preponderance of data on the stellar model fitting side of the $y = x$ line. This indicates that all of the gyrochronology methods seem to return older ages than all of the stellar models.*

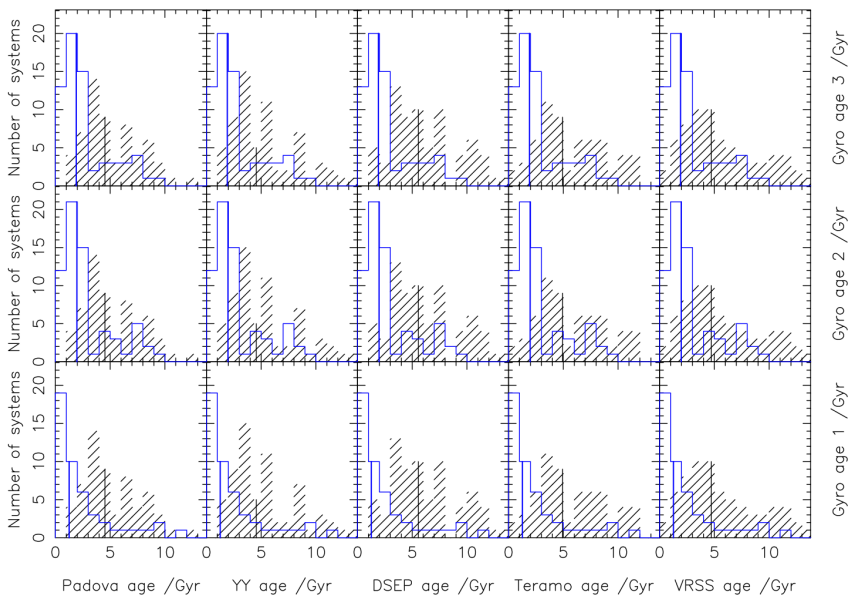

Figure B.2: *Age distributions for the results that I obtained from stellar model fitting and gyrochronology. Blue, open distributions are calculated using gyrochronology results, and black, hashed histograms are calculated using stellar model fitting results. Thick, vertical lines denote the median of the distributions. In all cases the peak of the gyrochronology distribution lies at a younger age than the peak of the stellar model fitting distribution. Similarly, the median gyrochronology age is younger than the median stellar model fitting age in all cases.*

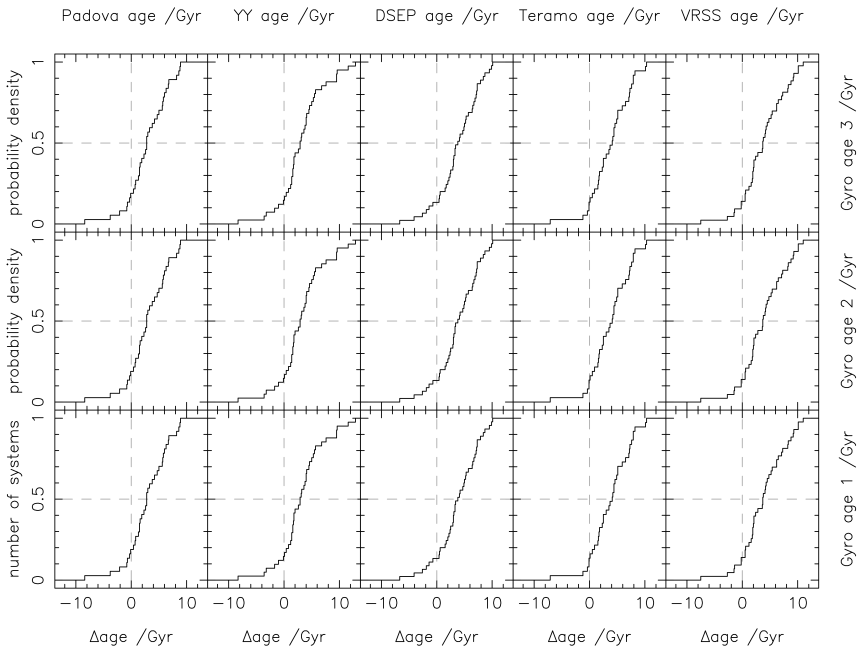

Figure B.3: *Cumulative probability distributions for the difference between the age estimates obtained by stellar model fitting and by gyrochronology. The dotted lines denote* $\Delta\text{age} = 0$ *and* $\text{probability} = 0.5$. *The x -axis range is* $\pm$ *the age of the Universe. In all panels there is a clear offset towards positive* Δage, *confirming that stellar model fitting is returning ages which are older than those from gyrochronology.*

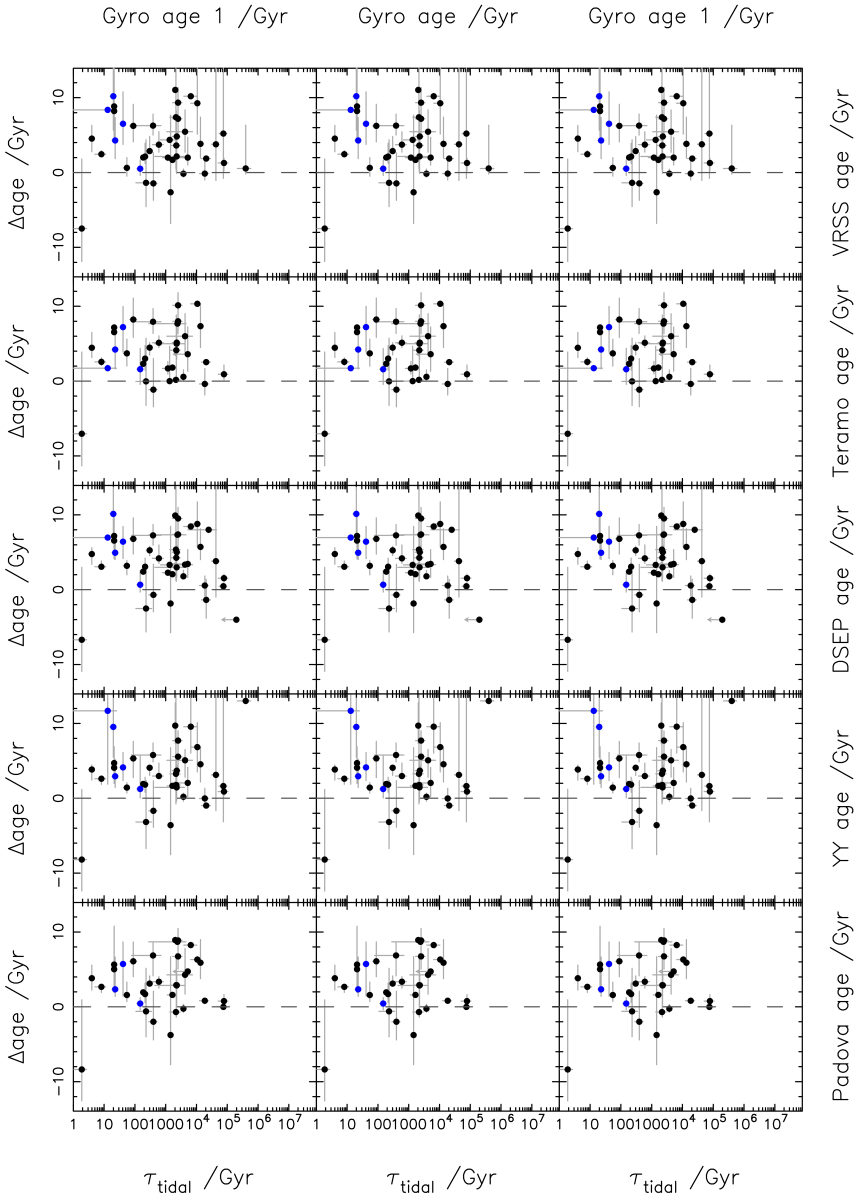

Figure B.4: *Δage as a function of $\tau_{\rm tidal}$, the tidal realignment timescale, for all combinations of stellar model choice and gyrochronology formulation. The shorter the timescale, the stronger the tidal interactions within the system, and the greater the angular momentum exchange. Some of the combinations of stellar model and gyrochronology formulation show slight evidence for a trend of increasing Δage with decreasing $\tau_{\rm tidal}$, but over all panels the effect is minimal. Legend as for Figure B.1.*

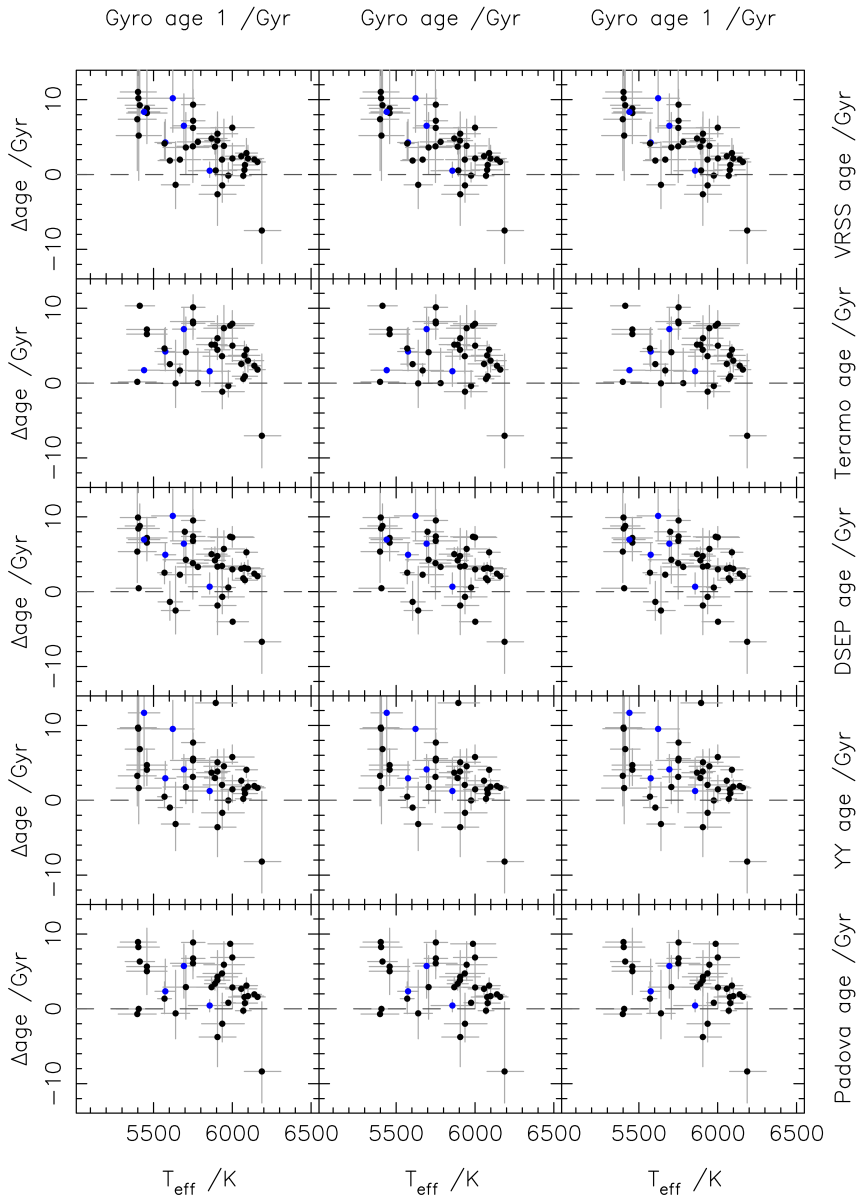

Figure B.5: *Δage as a function of stellar effective temperature $T_{\rm eff}$, for all combinations of stellar model choice and gyrochronology formulation. For four of the five stellar models there is a clear trend for Δage to increase with decreasing $T_{\rm eff}$ (towards later spectral types). The exception is the Padova model set, which shows a shallower decline in Δage. Legend as for Figure B.1.*

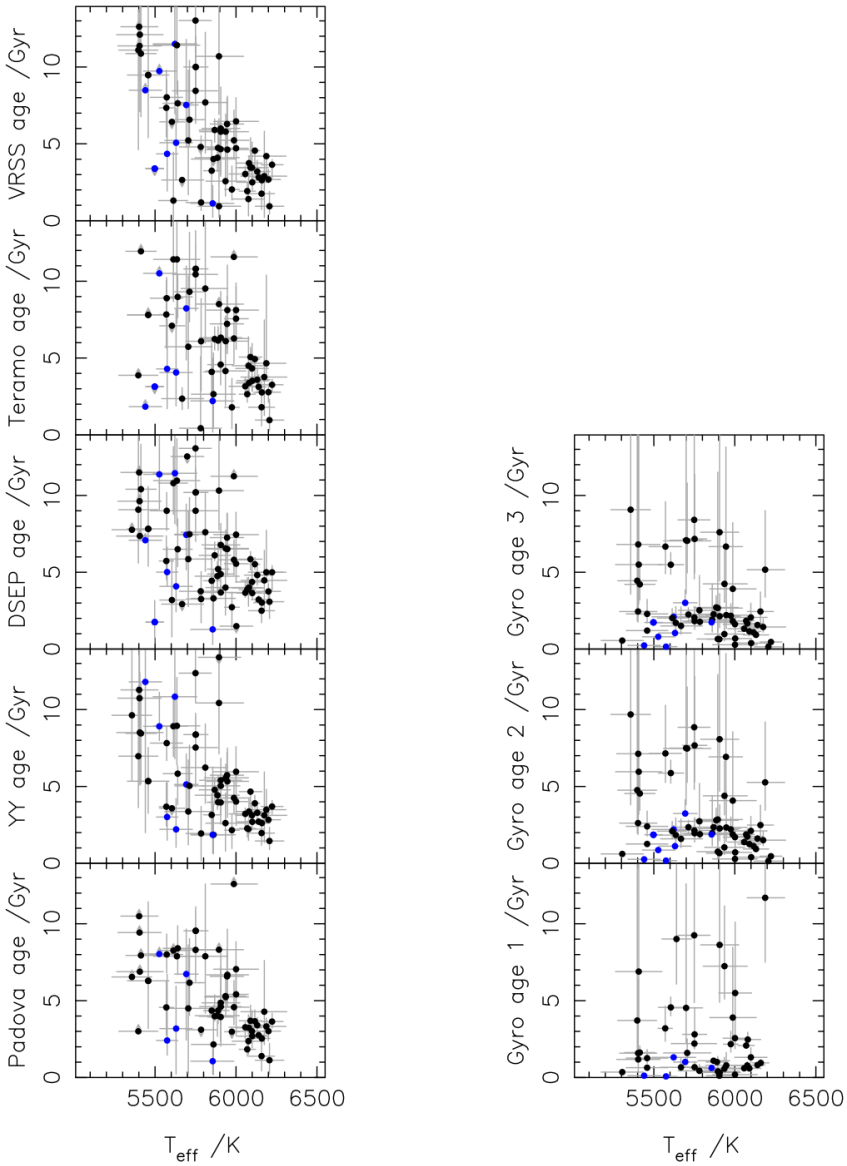

Figure B.6: *Age as a function of stellar effective temperature for all stellar model choices and all gyrochronology formulations.* ***Left column:*** *Ages calculated through stellar model fitting.* ***Right column:*** *Ages calculated through gyrochronology. All stellar model data show the same trend for decreasing* Δage *with increasing* $T_{\rm eff}$*, but the ages from the gyrochronology methods show no such trend. Legend as for Figure 2.6.*

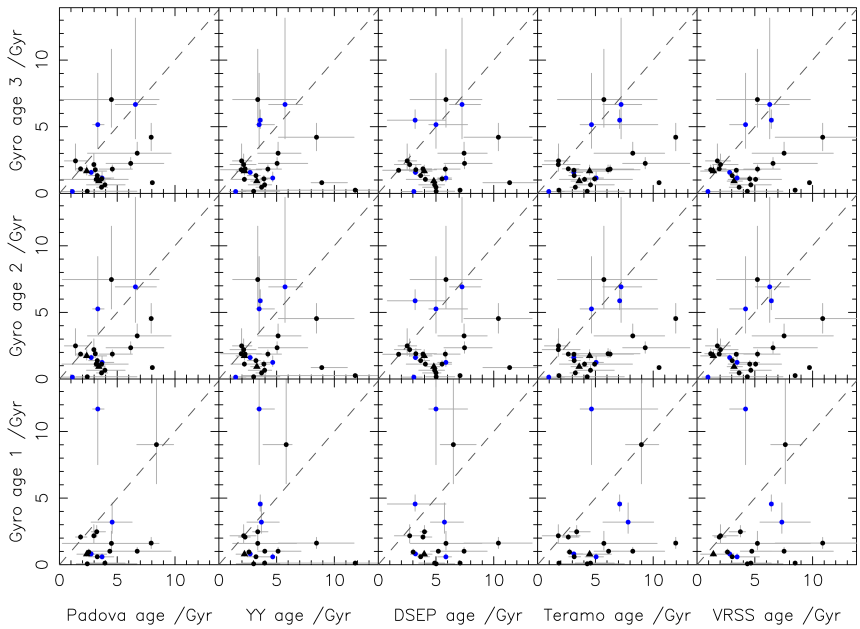

Figure B.7: *As Figure B.1, but for the sub-sample of systems with measured spin-orbit alignment angle. Black data denote systems which are judged to be 'aligned' according to the criterion of Winn et al. (2010a), whilst blue data mark 'misaligned' systems. Filled triangles mark systems for which λ was measured through Doppler tomography.*

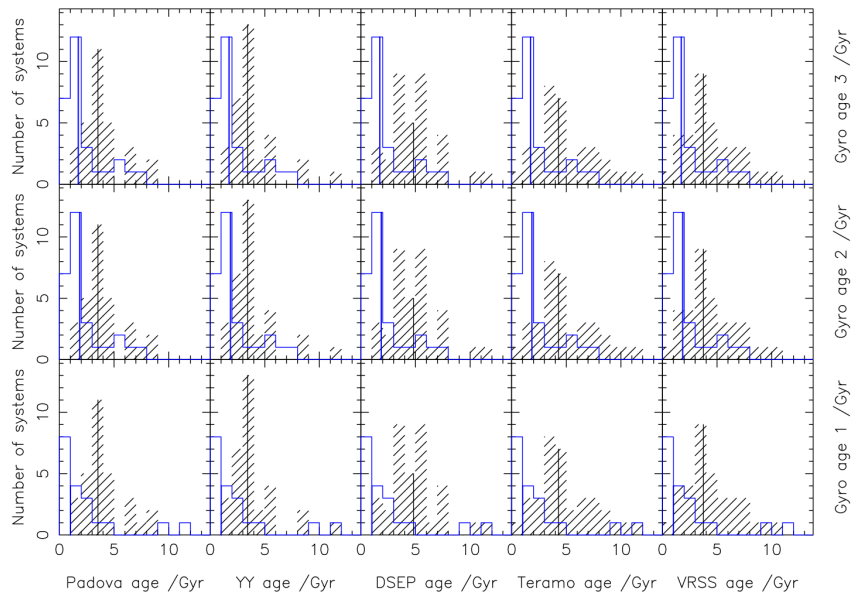

Figure B.8: *As Figure B.2, for the sub-sample of systems with measured spin-orbit alignment angles. Legend as for Figure B.2.*

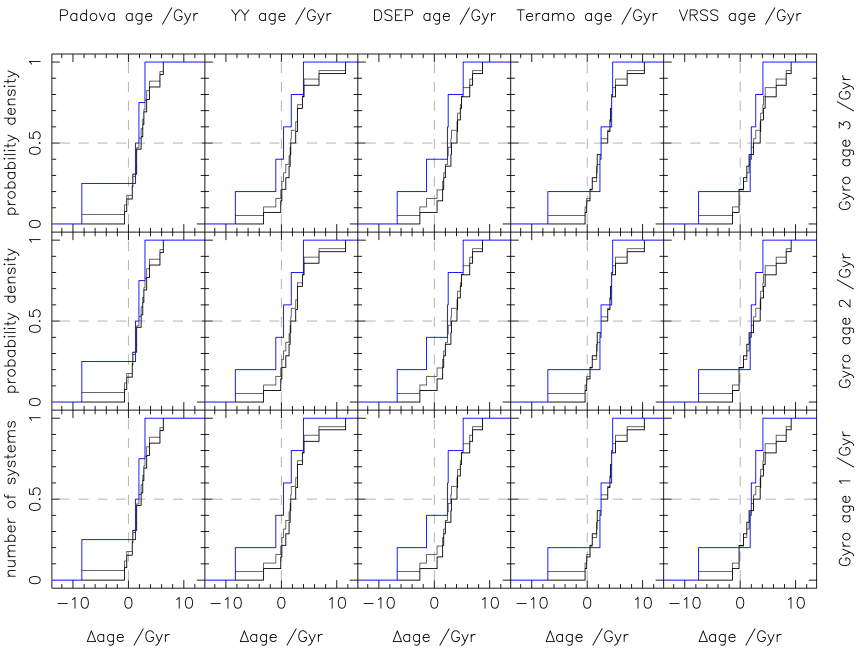

Figure B.9: *As for Figure B.3, for the sub-sample of systems with measured spin-orbit alignment. The grey distribution was calculated for all of the systems in this sub-sample. The black distribution and blue distribution were calculated for 'aligned' and 'misaligned' systems only. There is a clear offset towards positive* Δage *for all of the full distributions and all of the 'aligned' distributions. Most of the 'misaligned' distributions also show an offset, with the exception of those for the YY stellar models which pass through* $\Delta\text{age} = 0$.

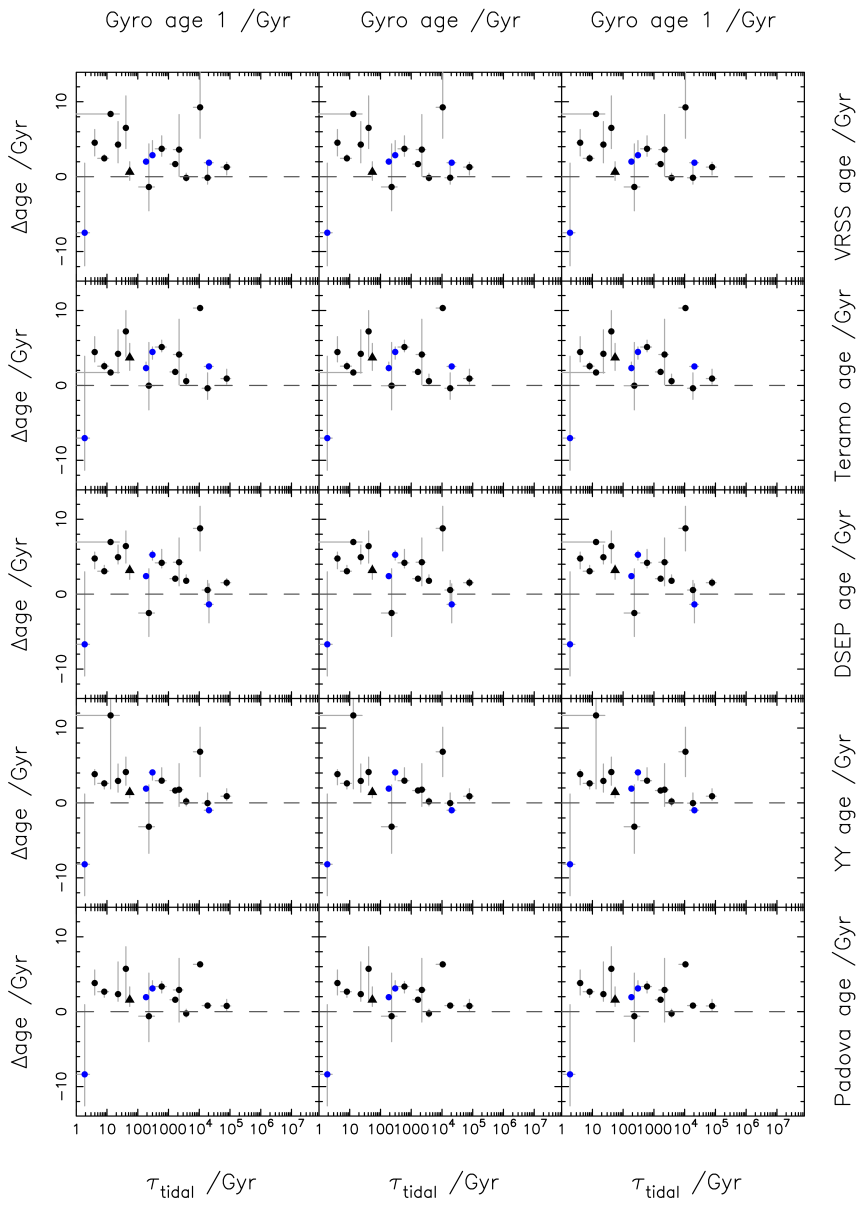

Figure B.10: *As for Figure B.4, for the sub-sample of systems with measured spin-orbit alignment. Legend as for Figure B.7. For some combinations of stellar model choice and gyrochronology formulation the 'misaligned' systems show an increase in* Δage *as* $\tau_{\rm tidal}$ *decreases. The 'aligned' systems show no trend.*

C

Journal of observations

This appendix presents the spectroscopic measurements which were obtained specifically for the analyses of the spin-orbit alignment of the WASP-16, -25, -31, -32, -38, and -40 which were presented in Chapter 5. The observations are separated according to system and instrument used.

Table C.1: *Radial velocity data for WASP-16 obtained using the CORALIE high precision échelle spectrograph.*

HJD(-2450000)	RV/km s^{-1}	σ_{RV}/km s^{-1}
4535.864842	−1.99772	0.01591
4537.849158	−1.96688	0.00853
4538.858364	−2.00734	0.00899
4558.780835	−1.83336	0.00723
4560.709473	−2.00513	0.00725

Continued on next page

Table C.1 – *Continued from previous page*

HJD(-2450000)	RV/km s^{-1}	σ_{RV}/km s^{-1}
4561.688137	−1.82730	0.00785
4589.705102	−1.84255	0.00875
4591.706755	−2.03571	0.00892
4652.495906	−1.82493	0.00808
4656.551645	−2.02421	0.00787
4657.577293	−1.96640	0.00957
4663.539741	−2.02961	0.00969
4664.616769	−1.78590	0.01108
4682.521501	−1.98118	0.00754
4881.869213	−2.02245	0.00813
4882.801025	−1.83289	0.00823
4884.737094	−2.04565	0.00778
4891.805707	−1.90043	0.00798
4892.723980	−1.83413	0.00891
4941.728231	−1.88737	0.00748
4943.730102	−2.04677	0.00753
4944.739293	−1.91359	0.00860
4945.799895	−1.85815	0.00807
4947.745317	−1.93960	0.00741
4948.673112	−1.82992	0.00743
4972.707323	−1.93123	0.00854
4975.733486	−1.93144	0.01100
4982.647535	−1.83433	0.01036
4984.642389	−2.04210	0.00892
4985.694776	−1.81561	0.00802
5391.544362	−1.80313	0.00867

Table C.2: *Radial velocity data for WASP-16, for the first transit obtained using the HARPS high precision échelle spectrograph on the night of 2010 March 21.*

HJD(-2450000)	RV/km s^{-1}	σ_{RV}/km s^{-1}
5275.661171	−1.80610	0.00337
5275.907691	−1.78144	0.00188
5276.661941	−1.88264	0.00533
5276.668446	−1.89263	0.00546
5276.674824	−1.88914	0.00583
5276.681375	−1.87845	0.00547
5276.687753	−1.89900	0.00557
5276.694258	−1.88947	0.00569
5276.700693	−1.89868	0.00555
5276.707094	−1.89750	0.00552
5276.713599	−1.88945	0.00586
5276.720046	−1.91121	0.00614
5276.726493	−1.89650	0.00623
5276.732929	−1.88385	0.00657
5276.739376	−1.90596	0.00640
5276.745812	−1.90686	0.00704
5276.752143	−1.90101	0.00698
5276.758579	−1.91736	0.00742
5276.765605	−1.90950	0.00627
5276.771589	−1.91143	0.00447
5276.778140	−1.91692	0.00439
5276.784344	−1.91573	0.00479
5276.790838	−1.92779	0.00526
5276.797459	−1.92243	0.00510
5276.803964	−1.90902	0.00433

Continued on next page

Table C.2 – *Continued from previous page*

HJD(-2450000)	RV/km s^{-1}	σ_{RV}/km s^{-1}
5276.810411	−1.92567	0.00391
5276.816441	−1.91540	0.00416
5276.823178	−1.92366	0.00424
5276.829336	−1.92742	0.00454
5276.835887	−1.92693	0.00522
5276.842334	−1.92962	0.00572
5276.848723	−1.94183	0.00699
5276.855228	−1.94543	0.00926
5276.861907	−1.92508	0.00830
5277.630948	−2.02847	0.00222
5277.861599	−1.99854	0.00196
5278.632376	−1.82733	0.00398
5278.857922	−1.79546	0.00208
5279.627285	−1.84379	0.00264
5279.913540	−1.91554	0.00242
5280.624797	−2.03079	0.00266
5280.916481	−2.00824	0.00283

Table C.3: *Radial velocity data for WASP-16, for the second transit obtained using the HARPS high precision échelle spectrograph on the night of 2011 May 12.*

HJD(-2450000)	RV/km s^{-1}	σ_{RV}/km s^{-1}
5685.845943	−2.02724	0.00305
5687.838150	−1.79259	0.00383
5692.662149	−1.99841	0.00380
5692.796210	−1.96847	0.00309
5693.517817	−1.81013	0.00298

Continued on next page

Table C.3 – *Continued from previous page*

HJD(-2450000)	RV/km s^{-1}	σ_{RV}/km s^{-1}
5693.800775	−1.78196	0.00285
5694.581176	−1.88349	0.00344
5694.588340	−1.88597	0.00302
5694.595389	−1.88670	0.00310
5694.602900	−1.88871	0.00305
5694.610180	−1.89619	0.00290
5694.616904	−1.89308	0.00323
5694.623386	−1.88547	0.00323
5694.629531	−1.89159	0.00309
5694.635631	−1.89935	0.00312
5694.641904	−1.89371	0.00307
5694.648003	−1.89694	0.00318
5694.654149	−1.91191	0.00298
5694.660364	−1.91005	0.00311
5694.666406	−1.91009	0.00300
5694.672609	−1.91343	0.00311
5694.678824	−1.91547	0.00327
5694.684924	−1.91384	0.00313
5694.691070	−1.91484	0.00330
5694.697227	−1.91701	0.00308
5694.703373	−1.91926	0.00308
5694.709460	−1.91211	0.00335
5694.715664	−1.91534	0.00353
5694.721821	−1.91948	0.00349
5694.727979	−1.92566	0.00346
5694.734078	−1.92109	0.00367
5694.740351	−1.92435	0.00377

Continued on next page

Table C.3 – *Continued from previous page*

HJD(-2450000)	RV/km s^{-1}	σ_{RV}/km s^{-1}
5694.746612	−1.91926	0.00364
5694.752596	−1.93024	0.00354
5695.501446	−2.03120	0.00281

Table C.4: *Radial velocity data for WASP-25 obtained using the CORALIE high precision échelle spectrograph.*

HJD(-2450000)	RV/km s^{-1}	σ_{RV}/km s^{-1}
4829.822664	−2.57717	0.01282
4896.769798	−2.65105	0.01069
4940.709168	−2.71589	0.01154
4941.704336	−2.61855	0.01153
4942.725717	−2.57632	0.01238
4943.637434	−2.61828	0.01246
4944.715466	−2.67966	0.01207
4945.726530	−2.61467	0.01305
4946.616622	−2.58169	0.01266
4947.601618	−2.64133	0.01096
4947.791245	−2.68927	0.01347
4948.613002	−2.70418	0.01098
4949.803142	−2.55132	0.01819
4950.622083	−2.59141	0.01348
4951.695324	−2.70149	0.01218
4971.645302	−2.67821	0.02101
4972.672436	−2.56129	0.01319
4973.515713	−2.58676	0.01269
4974.678659	−2.71413	0.01359

Continued on next page

Table C.4 – *Continued from previous page*

HJD(-2450000)	RV/km s^{-1}	σ_{RV}/km s^{-1}
4975.537940	−2.66695	0.01384
4976.683662	−2.55567	0.01304
4982.619435	−2.66448	0.02096
4983.621314	−2.56777	0.01486
4983.644577	−2.59698	0.01450
4984.578450	−2.55837	0.01474
4985.609967	−2.69905	0.01189
4995.555496	−2.50858	0.01396
5009.628712	−2.60564	0.01823
5010.596729	−2.53871	0.02313

Table C.5: *Radial velocity data for WASP-25 obtained using the HARPS high precision échelle spectrograph. The point denoted by * was omitted from the analysis (see text for details).*

HJD(-2450000)	RV/km s^{-1}	σ_{RV}/km s^{-1}
5296.540546	−2.54661	0.00329
5296.635060	−2.54381	0.00398
5297.506446	−2.61464	0.00509
5297.518749	−2.62531	0.01007
5297.523714	−2.63325	0.00942
5297.528714	−2.60898	0.01012
5297.533807	−2.61031	0.01041
5297.538714	−2.60809	0.00999
5297.543714	−2.59973	0.01056
5297.548668	−2.59327	0.01108
5297.553761	−2.58984	0.01028
5297.559131	−2.61140	0.01786

Continued on next page

Table C.5 – *Continued from previous page*

HJD(-2450000)	RV/km s^{-1}	σ_{RV}/km s^{-1}
5297.563761	−2.60108	0.01177
5297.568668	−2.60927	0.01087
5297.573715	−2.60539	0.01075
5297.578761	−2.62964	0.01153
5297.583668	−2.62703	0.01118
5297.588669	−2.61584	0.01225
5297.593715	−2.64141	0.01190
5297.598669	−2.64658	0.01232
5297.603715	−2.65755	0.01234
5297.608715	−2.67520	0.01246
5297.613761	−2.67558	0.01254
5297.618715	−2.68567	0.01244
5297.623669*	−2.63635	0.01215
5297.628854	−2.67450	0.01065
5297.633761	−2.65389	0.00837
5297.638715	−2.63022	0.00840
5297.643773	−2.63126	0.00885
5297.648727	−2.61768	0.00871
5297.653727	−2.63157	0.00862
5297.658681	−2.63982	0.00841
5297.663773	−2.62371	0.00834
5297.668773	−2.63776	0.00800
5297.673727	−2.64716	0.00811
5297.678727	−2.63753	0.00780
5297.683681	−2.63915	0.00781
5297.688820	−2.63818	0.00823
5297.693727	−2.64295	0.00763

Continued on next page

Table C.5 – *Continued from previous page*

HJD(-2450000)	RV/km s^{-1}	σ_{RV}/km s^{-1}
5297.698774	−2.62870	0.00772
5297.703635	−2.63667	0.00757
5297.708727	−2.63667	0.00781
5297.713727	−2.63031	0.00803
5297.718681	−2.65168	0.00756
5297.723774	−2.64533	0.00785
5297.833578	−2.65676	0.00352
5298.535157	−2.69608	0.00406
5298.716015	−2.69119	0.00285
5298.830796	−2.69107	0.00287
5299.544943	−2.60603	0.00327
5299.701761	−2.62922	0.01842
5299.838220	−2.57573	0.01224

Table C.6: *Radial velocity data for WASP-31 obtained using the CORALIE high precision échelle spectrograph.*

HJD(-2450000)	RV/km s^{-1}	σ_{RV}/km s^{-1}
4835.809755	−0.20260	0.02945
4837.773728	−0.08457	0.03163
4840.765776	−0.07974	0.03752
4880.767231	−0.20651	0.03722
4939.627676	−0.07528	0.03471
4941.567460	−0.19372	0.02721
4942.654757	−0.12324	0.02598
4943.610624	−0.07939	0.03435
4944.555415	−0.16578	0.02620

Continued on next page

Table C.6 – *Continued from previous page*

HJD(-2450000)	RV/km s^{-1}	σ_{RV}/km s^{-1}
4945.544750	−0.16158	0.03220
4946.591778	−0.04422	0.03441
4947.555094	−0.14075	0.02656
4948.588069	−0.18274	0.02861
4950.597039	−0.08667	0.03009
4951.608264	−0.22821	0.03366
4971.548671	−0.02806	0.07763
4973.489951	−0.09189	0.03084
4974.608541	−0.02130	0.03225
4975.511060	−0.12628	0.03381
4983.595539	−0.10028	0.04415
4984.467744	−0.06112	0.02895
4985.530406	−0.18886	0.03032
4994.508045	−0.09735	0.03237
4994.531307	−0.09484	0.03469
4995.463376	−0.12246	0.03547
4995.486741	−0.20999	0.03214
4996.459605	−0.19034	0.03472
4996.482971	−0.10984	0.03117
4999.536757	−0.21980	0.05522
4999.560099	−0.15670	0.06560
5006.521354	−0.18493	0.04217
5012.492297	−0.09667	0.03739
5013.497045	−0.19082	0.04459
5029.465780	−0.11660	0.05041
5168.846768	−0.15389	0.01852
5203.782854	−0.20152	0.02084

Continued on next page

Table C.6 – *Continued from previous page*

HJD(-2450000)	RV/km s^{-1}	σ_{RV}/km s^{-1}
5290.715577	−0.09351	0.01809
5291.699859	−0.12273	0.01821
5293.696819	−0.07455	0.01987
5294.733907	−0.09785	0.01925
5296.704921	−0.13168	0.01772
5298.693406	−0.18210	0.01718
5300.589643	−0.06706	0.02250
5326.628560	−0.13831	0.01945
5327.604475	−0.08093	0.02737
5328.608442	−0.09912	0.01913
5334.544675	−0.05571	0.02129

Table C.7: *Radial velocity data for WASP-31 obtained using the HARPS high precision échelle spectrograph.*

HJD(-2450000)	RV/km s^{-1}	σ_{RV}/km s^{-1}
5298.496133	−0.15638	0.00896
5298.749145	−0.17218	0.00931
5299.504441	−0.17141	0.01114
5299.716991	−0.29541	0.04800
5300.509357	−0.07910	0.01138
5300.742948	−0.08587	0.01161
5301.582822	−0.11516	0.00934
5301.597544	−0.11250	0.01003
5301.612960	−0.12527	0.00984
5301.627126	−0.10841	0.01418
5301.638028	−0.09394	0.01141

Continued on next page

Table C.7 – *Continued from previous page*

HJD(-2450000)	RV/km s^{-1}	σ_{RV}/km s^{-1}
5301.648803	−0.06309	0.01227
5301.659393	−0.08776	0.01100
5301.670307	−0.11321	0.01136
5301.681082	−0.13542	0.01119
5301.691973	−0.16717	0.01218
5301.702354	−0.19579	0.01297
5301.713349	−0.16796	0.01407
5301.723522	−0.16142	0.01884
5301.734934	−0.14695	0.01771
5301.750477	−0.13378	0.01244
5301.764794	−0.14088	0.01586
5301.780360	−0.15031	0.01738
5305.613529	−0.18166	0.01096
5307.584640	−0.06475	0.00809

Table C.8: *Radial velocity data for WASP-32 obtained using the HARPS high precision échelle spectrograph.*

HJD(-2450000)	RV/km s^{-1}	σ_{RV}/km s^{-1}
5828.581434	17.82469	0.00919
5828.829629	17.83582	0.00647
5829.586912	18.52797	0.00579
5829.807179	18.70852	0.00529
5830.593731	18.43669	0.00780
5830.602145	18.41150	0.00836
5830.611046	18.41026	0.01001
5830.618766	18.38721	0.00942

Continued on next page

Table C.8 – *Continued from previous page*

HJD(-2450000)	RV/km s^{-1}	σ_{RV}/km s^{-1}
5830.625803	18.40267	0.00901
5830.633338	18.38290	0.00940
5830.640444	18.38975	0.00933
5830.648303	18.37346	0.00814
5830.656497	18.35622	0.00822
5830.664356	18.36270	0.00816
5830.672365	18.35400	0.00908
5830.680433	18.33837	0.01021
5830.688639	18.34691	0.00943
5830.696567	18.34257	0.00950
5830.704912	18.30751	0.00858
5830.712840	18.30229	0.00884
5830.720907	18.29955	0.00890
5830.729183	18.27168	0.00844
5830.736960	18.24540	0.00829
5830.745178	18.23510	0.00865
5830.753176	18.22897	0.00807
5830.761231	18.22650	0.00802
5830.769298	18.23197	0.00804
5830.777296	18.22548	0.00830
5830.785363	18.21815	0.00815
5830.793546	18.20186	0.00854
5830.801613	18.21736	0.00877
5830.809623	18.19578	0.00891
5830.817771	18.18887	0.00960
5830.825780	18.16949	0.01005
5831.590826	17.85109	0.00602

Continued on next page

Table C.8 – *Continued from previous page*

HJD(-2450000)	RV/km s^{-1}	σ_{RV}/km s^{-1}
5831.811104	18.01057	0.00551

Table C.9: *Radial velocity data for WASP-38 obtained using the HARPS high precision échelle spectrograph.*

HJD(-2450000)	RV/km s^{-1}	σ_{RV}/km s^{-1}
5656.783091	−9.51508	0.00337
5657.783221	−9.52550	0.00299
5660.811940	−9.98361	0.00319
5662.834946	−9.64728	0.00423
5680.716630	−9.95563	0.00389
5681.710237	−9.97538	0.00295
5683.728896	−9.59883	0.00285
5714.660893	−9.89326	0.00588
5716.602469	−9.90687	0.00307
5727.508875	−9.72505	0.00658
5727.519373	−9.72057	0.00586
5727.523134	−9.71142	0.00564
5727.527081	−9.70382	0.00585
5727.530912	−9.69675	0.00523
5727.534824	−9.69758	0.00528
5727.538562	−9.69301	0.00529
5727.542879	−9.69153	0.00527
5727.546791	−9.69410	0.00599
5727.550656	−9.68355	0.00613
5727.554603	−9.68966	0.00672
5727.558272	−9.67696	0.00592

Continued on next page

Table C.9 – *Continued from previous page*

HJD(-2450000)	RV/km s^{-1}	σ_{RV}/km s^{-1}
5727.562045	−9.69909	0.00646
5727.566397	−9.69542	0.00694
5727.570343	−9.68220	0.00618
5727.574140	−9.70082	0.00615
5727.578017	−9.69531	0.00609
5727.581882	−9.70552	0.00618
5727.585586	−9.70640	0.00618
5727.592484	−9.71415	0.00667
5727.596430	−9.72199	0.00718
5727.600203	−9.71776	0.00651
5727.604046	−9.73514	0.00681
5727.607923	−9.73209	0.00676
5727.611800	−9.73769	0.00745
5727.619335	−9.74676	0.00739
5727.623177	−9.75379	0.00724
5727.627020	−9.76161	0.00671
5727.630746	−9.76295	0.00678
5727.634589	−9.76762	0.00661
5727.638466	−9.76457	0.00690
5727.642667	−9.78228	0.00754
5727.646510	−9.77732	0.00655
5727.650422	−9.78573	0.00707
5727.654183	−9.78749	0.00695
5727.658164	−9.78420	0.00719
5727.661868	−9.79843	0.00745
5727.666231	−9.80281	0.00769
5727.670143	−9.79479	0.00621

Continued on next page

Table C.9 – *Continued from previous page*

HJD(-2450000)	RV/km s^{-1}	σ_{RV}/km s^{-1}
5727.673905	−9.79231	0.00634
5727.677747	−9.79598	0.00576
5727.681543	−9.79677	0.00532
5727.685386	−9.80741	0.00569
5727.689656	−9.80222	0.00564
5727.693430	−9.79689	0.00612
5727.697226	−9.79349	0.00704
5727.701242	−9.78573	0.00693
5727.705049	−9.78707	0.00585
5727.708915	−9.78243	0.00568
5727.713197	−9.76337	0.00552
5727.716936	−9.77080	0.00593
5727.720871	−9.77108	0.00529
5727.724713	−9.76885	0.00528
5727.728544	−9.76841	0.00528
5727.732306	−9.76986	0.00514
5727.736484	−9.76921	0.00541
5727.740141	−9.76496	0.00641
5727.744192	−9.76324	0.00720
5727.747999	−9.77120	0.00705
5727.751981	−9.76748	0.00679
5727.755823	−9.76974	0.00648
5727.760256	−9.78057	0.00585
5727.764376	−9.78068	0.00588
5749.637217	−9.96974	0.00642
5753.648280	−9.50884	0.00481
5802.476558	−9.58648	0.00600

Continued on next page

Table C.9 – *Continued from previous page*

HJD(-2450000)	RV/km s^{-1}	σ_{RV}/km s^{-1}
5806.489798	−9.80177	0.00370
5809.496470	−9.61798	0.00300

Table C.10: *Radial velocity data for WASP-40 obtained using the HARPS high precision échelle spectrograph.*

HJD(-2450000)	RV/km s^{-1}	σ_{RV}/km s^{-1}
5686.691040	−15.68740	0.00531
5691.594153	−15.83574	0.00593
5691.621178	−15.84591	0.00639
5691.784798	−15.82559	0.00548
5692.677700	−15.67883	0.00455
5692.747097	−15.67360	0.00411
5693.571851	−15.75439	0.00814
5693.577950	−15.75479	0.00878
5693.584107	−15.74939	0.00838
5693.590207	−15.75567	0.00843
5693.596480	−15.74962	0.00807
5693.602579	−15.75667	0.00803
5693.608737	−15.76548	0.00767
5693.614952	−15.75844	0.00817
5693.621167	−15.76064	0.00735
5693.627093	−15.75956	0.00822
5693.633296	−15.77570	0.00901
5693.639569	−15.76272	0.00858
5693.645669	−15.77900	0.00757
5693.651884	−15.77096	0.00700

Continued on next page

Table C.10 – *Continued from previous page*

HJD(-2450000)	RV/km s^{-1}	σ_{RV}/km s^{-1}
5693.657925	−15.77981	0.00764
5693.664152	−15.76408	0.00737
5693.670263	−15.76868	0.00751
5693.676467	−15.76874	0.00774
5693.682682	−15.76226	0.00709
5693.688781	−15.78715	0.00662
5693.694927	−15.77673	0.00671
5693.701142	−15.78574	0.00677
5693.707184	−15.78466	0.00663
5693.713387	−15.76800	0.00666
5693.719603	−15.78821	0.00713
5693.725633	−15.77244	0.00792
5693.787541	−15.78723	0.00474
5694.567017	−15.85210	0.00448
5695.576799	−15.69093	0.00362
5695.757478	−15.67832	0.00406

Online resources

[1] - http://www.exoplanet.eu

[2] - http://www.aip.de/People/RHeller

Chapter heading images

The images that I have used for my chapter headings are all artist impressions of exoplanets. No infringement of copyright is intended through their use.

Chapter 1 - A retrograde hot Jupiter. Credit: Lynette Cook

Chapter 2 - HD 189733 b. Credit: C. Carreau/Esa

Chapter 3 - HD 189733 b. Credit: ESA, NASA, M. Kornmesser (ESA/Hubble) and STScI

Chapter 4 - HAT-P-7 b. Credit: NASA, ESA and G. Bacon (STScI)

Chapter 5 - HD 189733 b. Credit: ESA, NASA, G. Tinetti (University College London, UK & ESA) and M. Kornmesser (ESA/Hubble)

Chapter 6 - Corot-9 b. Credit: ESO/L. Calçada

Chapter 7 - HD 85512 b. Credit: ESO/M. Kornmesser

Bibliography

Adibekyan, V. Z., Sousa, S. G., Santos, N. C., Delgado Mena, E., González Hernández, J. I., Israelian, G., Mayor, M., & Khachatryan, G. 2012, A&A, 545, A32, 1207.2388

Agüeros, M. A. et al. 2011, ApJ, 740, 110, 1107.4039

Aguilar, M. et al. 2013, Physical Review Letters, 110, 141102

Albrecht, S., Reffert, S., Snellen, I., Quirrenbach, A., & Mitchell, D. S. 2007, A&A, 474, 565, 0708.2918

Albrecht, S., Reffert, S., Snellen, I. A. G., & Winn, J. N. 2009, Nature, 461, 373, 0909.2861

Albrecht, S., Winn, J. N., Butler, R. P., Crane, J. D., Shectman, S. A., Thompson, I. B., Hirano, T., & Wittenmyer, R. A. 2012a, ApJ, 744, 189, 1111.5016

Albrecht, S. et al. 2011, ApJ, 738, 50, 1106.2548

——. 2012b, ApJ, 757, 18, 1206.6105

Alexander, M. E. 1973, Ap&SS, 23, 459

Alonso, R. et al. 2008, A&A, 482, L21, 0803.3207

Alsubai, K. A. et al. 2011, MNRAS, 417, 709, 1012.3027

Alves, S., Do Nascimento, Jr., J. D., & de Medeiros, J. R. 2010, MNRAS, 408, 1770, 1007.0145

Anderson, D. R. et al. 2011a, PASP, 123, 555, 1101.4643

——. 2012, MNRAS, 422, 1988, 1105.3179

——. 2011b, A&A, 534, A16, 1106.6092

——. 2011c, A&A, 531, A60, 1011.5882

——. 2008, MNRAS, 387, L4, 0801.1685

——. 2010, ApJ, 709, 159, 0908.1553

——. 2013, MNRAS, 430, 3422, 1112.5145

Asplund, M., Grevesse, N., & Sauval, A. J. 2006, Communications in Asteroseismology, 147, 76

Bakos, G. Á. et al. 2011, ApJ, 742, 116, 1008.3388

——. 2012, AJ, 144, 19, 1201.0659

Bakos, G. Á., Lázár, J., Papp, I., Sári, P., & Green, E. M. 2002, PASP, 114, 974, arXiv:astro-ph/0206001

Bakos, G. Á. et al. 2009, ApJ, 696, 1950, 0809.4295

——. 2010, ApJ, 710, 1724, 0901.0282

Baliunas, S. L. et al. 1995, ApJ, 438, 269

Baraffe, I., Chabrier, G., & Barman, T. 2010, Reports on Progress in Physics, 73, 016901, 1001.3577

Barbieri, M. et al. 2009, A&A, 503, 601, 0812.0785

Barclay, T. et al. 2013, Nature, 494, 452

Barge, P. et al. 2008, A&A, 482, L17, 0803.3202

Barker, A. J., & Ogilvie, G. I. 2009a, in IAU Symposium, Vol. 259, IAU Symposium, ed. K. G. Strassmeier, A. G. Kosovichev, & J. E. Beckman, 295–302, 0902.4554

Barker, A. J., & Ogilvie, G. I. 2009b, MNRAS, 395, 2268, 0902.4563

Barnes, J. W., Linscott, E., & Shporer, A. 2011, ApJS, 197, 10, 1110.3514

Barnes, S. A. 2001, ApJ, 561, 1095, arXiv:astro-ph/0107350

——. 2003, ApJ, 586, 464, arXiv:astro-ph/0303631

——. 2007, ApJ, 669, 1167, 0704.3068

Barnes, S. A., & Kim, Y.-C. 2010, ApJ, 721, 675, 1104.2350

Barros, S. C. C. et al. 2011a, A&A, 525, A54, 1010.0849

Barros, S. C. C., Pollacco, D. L., Gibson, N. P., Howarth, I. D., Keenan, F. P., Simpson, E. K., Skillen, I., & Steele, I. A. 2011b, MNRAS, 416, 2593, 1106.2118

Barros, S. C. C., Pollacco, D. L., Gibson, N. P., Keenan, F. P., Skillen, I., & Steele, I. A. 2012, MNRAS, 419, 1248, 1108.3996

Barstow, J. K., Aigrain, S., Irwin, P. G. J., Bowles, N., Fletcher, L. N., & Lee, J.-M. 2013, MNRAS, 430, 1188

Basu, S., & Antia, H. M. 2013, Journal of Physics Conference Series, 440, 012017

Batalha, N. M. et al. 2010, ApJ, 713, L109, 1001.0349

Bate, M. R., Lodato, G., & Pringle, J. E. 2010, MNRAS, 401, 1505, 0909.4255

Beck, J. G., & Giles, P. 2005, ApJ, 621, L153

Béky, B. et al. 2011, ApJ, 734, 109, 1101.3511

Bentley, S. J. 2010, PhD thesis, Keele University

Bernal, J. 1988, National Institute of Standards and Technology Technical Note, 1252

——. 1991, National Institute of Standards and Technology Internal Report, 4716

Bertelli, G., Girardi, L., Marigo, P., & Nasi, E. 2008, A&A, 484, 815, 0803.1460

Blecic, J. et al. 2011, ArXiv e-prints, 1111.2363

Bodaghee, A., Santos, N. C., Israelian, G., & Mayor, M. 2003, A&A, 404, 715, arXiv:astro-ph/0304360

Bordé, P., Rouan, D., & Léger, A. 2003, A&A, 405, 1137, arXiv:astro-ph/0305159

Borucki, W. et al. 2008, in IAU Symposium, Vol. 249, IAU Symposium, ed. Y.-S. Sun, S. Ferraz-Mello, & J.-L. Zhou, 17–24

Bouchy, F. et al. 2010, A&A, 519, A98, 1006.2605

Bouchy, F., Pont, F., Melo, C., Santos, N. C., Mayor, M., Queloz, D., & Udry, S. 2005, A&A, 431, 1105, arXiv:astro-ph/0410346

Bouchy, F. et al. 2008, A&A, 482, L25, 0803.3209

Broeg, C. et al. 2013, in European Physical Journal Web of Conferences, Vol. 47, European Physical Journal Web of Conferences, 3005, 1305.2270

Brown, D. J. A. et al. 2012a, MNRAS, 423, 1503, 1203.4971

——. 2012b, ApJ, 760, 139

Brown, T. M., Libbrecht, K. G., & Charbonneau, D. 2002, PASP, 114, 826, arXiv:astro-ph/0205246

Bruntt, H. et al. 2010, MNRAS, 405, 1907, 1002.4268

Buchhave, L. A. et al. 2010, ApJ, 720, 1118, 1005.2009

Butler, R. P. et al. 2006, ApJ, 646, 505, arXiv:astro-ph/0607493

Carone, L., & Pätzold, M. 2007, Planet. Space Sci., 55, 643

Carroll, B. W., & Ostlie, D. A. 2006, An introduction to modern astrophysics and cosmology

Carter, J. A., Winn, J. N., Gilliland, R., & Holman, M. J. 2009, ApJ, 696, 241, 0902.1542

CDMS Collaboration et al. 2013, ArXiv e-prints, 1304.4279

Chabrier, G. 2009, Plasma Physics and Controlled Fusion, 51, 124014, 0912.2968

Chan, T., Ingemyr, M., Winn, J. N., Holman, M. J., Sanchis-Ojeda, R., Esquerdo, G., & Everett, M. 2011, AJ, 141, 179, 1103.3078

Charbonneau, D. et al. 2005, ApJ, 626, 523, arXiv:astro-ph/0503457

Charbonneau, D., Brown, T. M., Noyes, R. W., & Gilliland, R. L. 2002, ApJ, 568, 377, arXiv:astro-ph/0111544

Chauvin, G., Lagrange, A.-M., Dumas, C., Zuckerman, B., Mouillet, D., Song, I., Beuzit, J.-L., & Lowrance, P. 2004, A&A, 425, L29, arXiv:astro-ph/0409323

Christian, D. J. et al. 2009, MNRAS, 392, 1585, 0806.1482

Churchwell, E. et al. 2009, PASP, 121, 213

Claret, A. 2000, A&A, 363, 1081

——. 2003, A&A, 401, 657

——. 2004a, A&A, 428, 1001

——. 2004b, A&A, 424, 919

——. 2005, A&A, 440, 647

——. 2006, A&A, 453, 769

——. 2007, A&A, 467, 1389

Collier Cameron, A., Bruce, V. A., Miller, G. R. M., Triaud, A. H. M. J., & Queloz, D. 2010a, MNRAS, 403, 151, 0911.5361

Collier Cameron, A. et al. 2009, MNRAS, 400, 451, 0908.0189

——. 2010b, MNRAS, 407, 507, 1004.4551

Collier Cameron, A., & Jianke, L. 1994, MNRAS, 269, 1099

Collier Cameron, A. et al. 2006, MNRAS, 373, 799, arXiv:astro-ph/0609418

——. 2007, MNRAS, 380, 1230, 0707.0417

Company, R., Portilla, M., & Gimenez, A. 1988, ApJ, 335, 962

Counselman, III, C. C. 1973, ApJ, 180, 307

Covey, K. R., Agüeros, M. A., Lemonias, J. J., Law, N. M., Kraus, A. L., & Palomar Transient Factory Collaboration. 2011, in Astronomical Society of the Pacific Conference Series, Vol. 448, 16th Cambridge Workshop on Cool Stars, Stellar Systems, and the Sun, ed. C. Johns-Krull, M. K. Browning, & A. A. West, 269, 1012.0061

Currie, T. et al. 2012, ArXiv e-prints, 1210.6620

Czesla, S., Schröter, S., Wolter, U., von Essen, C., Huber, K. F., Schmitt, J. H. M. M., Reichart, D. E., & Moore, J. P. 2012, A&A, 539, A150

Darwin, G. H. 1880, Astronomische Nachrichten, 96, 217

Delaunay, B. 1934, Otdelenie Matematicheskikh i Estestvennykh Nauk, 7, 793

Deleuil, M. et al. 2008, A&A, 491, 889, 0810.0919

Delorme, P., Cameron, A. C., Hebb, L., Rostron, J., Lister, T. A., Norton, A. J., Pollacco, D., & West, R. G. 2011a, in Astronomical Society of the Pacific Conference Series, Vol. 448, 16th Cambridge Workshop on Cool Stars, Stellar Systems, and the Sun, ed. C. Johns-Krull, M. K. Browning, & A. A. West, 841

Delorme, P., Collier Cameron, A., Hebb, L., Rostron, J., Lister, T. A., Norton, A. J., Pollacco, D., & West, R. G. 2011b, MNRAS, 413, 2218, 1101.1222

Demarque, P., Woo, J.-H., Kim, Y.-C., & Yi, S. K. 2004, ApJS, 155, 667

Désert, J.-M. et al. 2011, ApJS, 197, 14, 1107.5750

Dittmann, J. A., Close, L. M., Green, E. M., & Fenwick, M. 2009, ApJ, 701, 756, 0906.4320

Dobbs-Dixon, I., Lin, D. N. C., & Mardling, R. A. 2004, ApJ, 610, 464, arXiv:astro-ph/0408191

Dominik, M. et al. 2008, Astronomische Nachrichten, 329, 248, 0801.2162

Donahue, R. A. 1993, PhD thesis, New Mexico State University, University Park.

Dotter, A., Chaboyer, B., Jevremović, D., Kostov, V., Baron, E., & Ferguson, J. W. 2008, ApJS, 178, 89, 0804.4473

Doyle, L. R. et al. 2011, Science, 333, 1602, 1109.3432

Dragomir, D. et al. 2011, AJ, 142, 115, 1108.2308

Edvardsson, B., Andersen, J., Gustafsson, B., Lambert, D. L., Nissen, P. E., & Tomkin, J. 1993, A&A, 275, 101

Eggleton, P. P. 1983, ApJ, 268, 368

Eggleton, P. P., Kiseleva, L. G., & Hut, P. 1998, ApJ, 499, 853, arXiv:astro-ph/9801246

Eggleton, P. P., & Kiseleva-Eggleton, L. 2001, ApJ, 562, 1012, arXiv:astro-ph/0104126

Ehrenreich, D. et al. 2008, A&A, 483, 933, 0803.1831

Enoch, B. et al. 2011a, AJ, 142, 86, 1104.2827

——. 2011b, MNRAS, 410, 1631, 1009.5917

Enoch, B., Collier Cameron, A., Parley, N. R., & Hebb, L. 2010, A&A, 516, A33, 1004.1991

Eyer, L., Holl, B., Pourbaix, D., Mowlavi, N., Siopis, C., Barblan, F., Evans, D. W., & North, P. 2013, Central European Astrophysical Bulletin, 37, 115, 1303.0303

Fabrycky, D., & Tremaine, S. 2007, ApJ, 669, 1298, 0705.4285

Fabrycky, D. C. et al. 2012, ApJ, 750, 114, 1201.5415

Fabrycky, D. C., & Winn, J. N. 2009, ApJ, 696, 1230, 0902.0737

Faedi, F. et al. 2011, A&A, 531, A40, 1102.1375

——. 2013, A&A, 551, A73, 1210.2329

Fassett, C. I., & Head, J. W. 2008, Icarus, 198, 37

Ferraz-Mello, S., Rodríguez, A., & Hussmann, H. 2008, Celestial Mechanics and Dynamical Astronomy, 101, 171, 0712.1156

——. 2009, Celestial Mechanics and Dynamical Astronomy, 104, 319

Foley, R. J. et al. 2013, ApJ, 767, 57, 1212.2209

Ford, E. B. 2006, ApJ, 642, 505, arXiv:astro-ph/0512634

Ford, E. B., Havlickova, M., & Rasio, F. A. 2001, Icarus, 150, 303, arXiv:astro-ph/0010178

Ford, E. B., & Rasio, F. A. 2006, ApJ, 638, L45, arXiv:astro-ph/0512632

Ford, E. B., Rasio, F. A., & Yu, K. 2003, in Astronomical Society of the Pacific Conference Series, Vol. 294, Scientific Frontiers in Research on Extrasolar Planets, ed. D. Deming & S. Seager, 181–188, arXiv:astro-ph/0210275

Fossati, L., Ayres, T. R., Haswell, C. A., Bohlender, D., Kochukhov, O., & Flöer, L. 2013, ApJ, 766, L20, 1303.3375

Fressin, F. et al. 2012, Nature, 482, 195, 1112.4550

Gandolfi, D. et al. 2012, A&A, 543, L5, 1206.4037

Gaudi, B. S., & Winn, J. N. 2007, ApJ, 655, 550, arXiv:astro-ph/0608071

Ge, J. et al. 2008, in Bulletin of the American Astronomical Society, Vol. 40, AAS/Division for Planetary Sciences Meeting Abstracts #40, 386

Gibson, N. P. et al. 2008, A&A, 492, 603, 0810.3526

Gibson, N. P., Pont, F., & Aigrain, S. 2011, MNRAS, 411, 2199, 1010.1753

Gillessen, S. et al. 2012, Nature, 481, 51, 1112.3264

Gilli, G., Israelian, G., Ecuvillon, A., Santos, N. C., & Mayor, M. 2006, A&A, 449, 723, arXiv:astro-ph/0512219

Gillon, M. et al. 2013, A&A, 552, A82, 1210.4257

——. 2009, A&A, 501, 785, 0901.4705

——. 2011, A&A, 533, A88, 1108.2641

——. 2012, A&A, 542, A4, 1201.2789

Girardi, L. et al. 2010, ApJ, 724, 1030, 1009.4618

Goldreich, P., & Soter, S. 1966, Icarus, 5, 375

Goldreich, P., & Tremaine, S. 1980, ApJ, 241, 425

Goodman, J., & Lackner, C. 2009, ApJ, 696, 2054, 0812.1028

Gray, D. F. 1994, PASP, 106, 1248

——. 2008, The Observation and Analysis of Stellar Photospheres

Greenberg, R. 2009, ApJ, 698, L42

Gu, P.-G., Lin, D. N. C., & Bodenheimer, P. H. 2003, ApJ, 588, 509, arXiv:astro-ph/0303362

Guenther, E. W. et al. 2012, A&A, 537, A136, 1112.1035

Hansen, B. M. S. 2010, ApJ, 723, 285, 1009.3027

——. 2012, ApJ, 757, 6, 1204.3903

Hartman, J. D., Bakos, G. Á., Kovács, G., & Noyes, R. W. 2010, MNRAS, 408, 475

Hartman, J. D. et al. 2011, ApJ, 742, 59, 1106.1212

——. 2009, ApJ, 691, 342, 0803.1488

Hastings, W. K. 1970, Biometrika, 57, pp. 97

Hebb, L. et al. 2010, ApJ, 708, 224, 1001.0403

Hébrard, G. et al. 2013, A&A, 549, A134, 1211.0810

——. 2010, A&A, 516, A95, 1004.0790

——. 2011a, A&A, 527, L11, 1101.5009

——. 2011b, A&A, 533, A130, 1107.2032

Heller, R., Jackson, B., Barnes, R., Greenberg, R., & Homeier, D. 2010, A&A, 514, A22, 1002.1246

Hellier, C. et al. 2012, MNRAS, 426, 739, 1204.5095

——. 2009, Nature, 460, 1098

——. 2010, ApJ, 723, L60, 1009.5318

Hellier, C., Anderson, D. R., Collier-Cameron, A., Miller, G. R. M., Queloz, D., Smalley, B., Southworth, J., & Triaud, A. H. M. J. 2011, ApJ, 730, L31, 1101.3293

Hirano, T. et al. 2012, ApJ, 759, L36, 1209.4362

Hirano, T., Narita, N., Sato, B., Winn, J. N., Aoki, W., Tamura, M., Taruya, A., & Suto, Y. 2011a, PASJ, 63, L57, 1108.4493

Hirano, T., Suto, Y., Winn, J. N., Taruya, A., Narita, N., Albrecht, S., & Sato, B. 2011b, ApJ, 742, 69, 1108.4430

Holt, J. R. 1893, A&A, 12, 646

Hube, D. P., & Couch, J. S. 1982, Ap&SS, 81, 357

Hut, P. 1980, A&A, 92, 167

——. 1981, A&A, 99, 126

Ibgui, L., & Burrows, A. 2009, ApJ, 700, 1921, 0902.3998

Iorio, L. 2011, Ap&SS, 331, 485, 1006.2707

Jackson, B., Barnes, R., & Greenberg, R. 2008a, MNRAS, 391, 237, 0808.2770

——. 2009, ApJ, 698, 1357, 0904.1170

Jackson, B., Greenberg, R., & Barnes, R. 2008b, ApJ, 678, 1396, 0802.1543

——. 2008c, ApJ, 681, 1631, 0803.0026

James, D. J. et al. 2010, A&A, 515, A100, 1004.0047

Jehin, E. et al. 2011, The Messenger, 145, 2

Jenkins, J. M. et al. 2010, ApJ, 724, 1108, 1001.0416

Johnson, J. A., Winn, J. N., Albrecht, S., Howard, A. W., Marcy, G. W., & Gazak, J. Z. 2009, PASP, 121, 1104, 0907.5204

Johnson, J. A. et al. 2011, ApJ, 735, 24, 1103.3825

——. 2008, ApJ, 686, 649, 0806.1734

Jordán, A., & Bakos, G. Á. 2008, ApJ, 685, 543, 0806.0630

Joshi, Y. C. et al. 2009, MNRAS, 392, 1532, 0806.1478

Kains, N. et al. 2013, A&A, 552, A70, 1303.1184

Kaltenegger, L., Sasselov, D., & Rugheimer, S. 2013, ArXiv e-prints, 1304.5058

Kipping, D. M. et al. 2010, ApJ, 725, 2017, 1008.3389

Kiseleva, L. G., & Eggleton, P. P. 1998, in Astronomical Society of the Pacific Conference Series, Vol. 154, Cool Stars, Stellar Systems, and the Sun, ed. R. A. Donahue & J. A. Bookbinder, 2118

Kiseleva, L. G., Eggleton, P. P., & Mikkola, S. 1998, MNRAS, 300, 292

Knutson, H. A., Charbonneau, D., Allen, L. E., Burrows, A., & Megeath, S. T. 2008, ApJ, 673, 526, 0709.3984

Konacki, M., Torres, G., Sasselov, D. D., & Jha, S. 2005, ApJ, 624, 372, arXiv:astro-ph/0412400

Kopal, Z. 1959, Close binary systems

Kozai, Y. 1962, AJ, 67, 591

Kraft, R. P. 1967, ApJ, 150, 551

Lachaume, R., Dominik, C., Lanz, T., & Habing, H. J. 1999, A&A, 348, 897

Lai, D., Foucart, F., & Lin, D. N. C. 2011, MNRAS, 412, 2790, 1008.3148

Lanza, A. F. 2010, A&A, 512, A77, 0912.4585

Lanza, A. F., Damiani, C., & Gandolfi, D. 2011, A&A, 529, A50, 1012.5791

Latham, D. W., Stefanik, R. P., Mazeh, T., Mayor, M., & Burki, G. 1989, Nature, 339, 38

Le Bouquin, J.-B., Absil, O., Benisty, M., Massi, F., Mérand, A., & Stefl, S. 2009, A&A, 498, L41, 0904.1688

Leconte, J., Chabrier, G., Baraffe, I., & Levrard, B. 2010, A&A, 516, A64, 1004.0463

Léger, A. et al. 2004, Icarus, 169, 499, arXiv:astro-ph/0308324

Lendl, M. et al. 2012, A&A, 544, A72, 1205.2757

Levrard, B., Winisdoerffer, C., & Chabrier, G. 2009, ApJ, 692, L9, 0901.2048

Liddle, A. R. 2007, MNRAS, 377, L74, arXiv:astro-ph/0701113

Lidov, M. L. 1962, Planet. Space Sci., 9, 719

Lin, D. N. C., Bodenheimer, P., & Richardson, D. C. 1996, Nature, 380, 606

Lin, M. C., & Manocha, D., eds. 1996, Applied Computational Geometry: Towards Geometric Engineering, ed. M. C. Lin & D. Manocha, Vol. 1148 (Berlin: Springer)

Lister, T. A. et al. 2009, ApJ, 703, 752, 0908.0297

Lodders, K. 2010, in Principles and Perspectives in Cosmochemistry, ed. A. Goswami & B. E. Reddy, 379, 1010.2746

Loeillet, B. et al. 2008, A&A, 481, 529, 0707.0679

Lucy, L. B., & Sweeney, M. A. 1971, AJ, 76, 544

Maciejewski, G. et al. 2013, A&A, 551, A108, 1301.5976

Maciejewski, G., Errmann, R., Raetz, S., Seeliger, M., Spaleniak, I., & Neuhäuser, R. 2011a, A&A, 528, A65, 1102.2421

Maciejewski, G., Raetz, S., Nettelmann, N., Seeliger, M., Adam, C., Nowak, G., & Neuhäuser, R. 2011b, A&A, 535, A7, 1109.4749

Mamajek, E. E. 2012, ApJ, 754, L20, 1206.6353

Mamajek, E. E., & Hillenbrand, L. A. 2008, ApJ, 687, 1264, 0807.1686

Mancini, L. et al. 2013a, MNRAS, 430, 2932, 1301.3005

——. 2013b, A&A, 551, A11, 1212.3701

Mardling, R. A., & Lin, D. N. C. 2002, ApJ, 573, 829

Marigo, P., Girardi, L., Bressan, A., Groenewegen, M. A. T., Silva, L., & Granato, G. L. 2008, A&A, 482, 883, 0711.4922

Marzari, F., & Weidenschilling, S. J. 2002, Icarus, 156, 570

Matsumura, S., Peale, S. J., & Rasio, F. A. 2010, ApJ, 725, 1995, 1007.4785

Matsumura, S., Takeda, G., & Rasio, F. A. 2008, ApJ, 686, L29, 0808.3724

Maxted, P. F. L. et al. 2010, PASP, 122, 1465, 1010.1742

——. 2011, PASP, 123, 547, 1012.2977

Mayor, M. et al. 2003, The Messenger, 114, 20

Mayor, M., & Queloz, D. 1995, Nature, 378, 355

Mazeh, T. et al. 2013, ArXiv e-prints, 1301.5499

McLaughlin, D. B. 1924, ApJ, 60, 22

Meibom, S. et al. 2011, ApJ, 733, L9, 1104.2912

Meibom, S., & Mathieu, R. D. 2005, ApJ, 620, 970, arXiv:astro-ph/0412147

Meibom, S., Mathieu, R. D., & Stassun, K. G. 2009, ApJ, 695, 679, 0805.1040

Melo, C., Santos, N. C., Pont, F., Guillot, T., Israelian, G., Mayor, M., Queloz, D., & Udry, S. 2006, A&A, 460, 251, arXiv:astro-ph/0609259

Metropolis, N., Rosenbluth, A. W., Rosenbluth, M. N., Teller, A. H., & Teller, E. 1953, J. Chem. Phys., 21, 1087

Miller, G. R. M. et al. 2010, A&A, 523, A52, 1010.3474

Miller, N., Fortney, J. J., & Jackson, B. 2009, ApJ, 702, 1413, 0907.1268

Miralda-Escudé, J. 2002, ApJ, 564, 1019, arXiv:astro-ph/0104034

Montes, D., Saar, S. H., Collier Cameron, A., & Unruh, Y. C. 1999, MNRAS, 305, 45, arXiv:astro-ph/9811452

Moutou, C. et al. 2011, A&A, 533, A113, 1105.3849

Murray, C. D., & Dermott, S. F. 1999, Solar system dynamics

Nagasawa, M., Ida, S., & Bessho, T. 2008, ApJ, 678, 498, 0801.1368

Naoz, S., Farr, W. M., Lithwick, Y., Rasio, F. A., & Teyssandier, J. 2011, Nature, 473, 187, 1011.2501

Naoz, S., Farr, W. M., & Rasio, F. A. 2012, ApJ, 754, L36, 1206.3529

Narita, N. et al. 2007, PASJ, 59, 763, arXiv:astro-ph/0702707

Narita, N., Hirano, T., Sanchis-Ojeda, R., Winn, J. N., Holman, M. J., Sato, B., Aoki, W., & Tamura, M. 2010a, PASJ, 62, L61, 1008.3803

Narita, N. et al. 2009a, PASJ, 61, 991, 0905.4727

Narita, N., Sato, B., Hirano, T., & Tamura, M. 2009b, PASJ, 61, L35, 0908.1673

Narita, N., Sato, B., Hirano, T., Winn, J. N., Aoki, W., & Tamura, M. 2010b, PASJ, 62, 653, 1003.2268

Neves, V., Santos, N. C., Sousa, S. G., Correia, A. C. M., & Israelian, G. 2009, A&A, 497, 563, 0902.3374

Noyes, R. W. et al. 2008, ApJ, 673, L79, 0710.2894

Noyes, R. W., Hartmann, L. W., Baliunas, S. L., Duncan, D. K., & Vaughan, A. H. 1984a, ApJ, 279, 763

Noyes, R. W., Weiss, N. O., & Vaughan, A. H. 1984b, ApJ, 287, 769

Nutzman, P. A., Fabrycky, D. C., & Fortney, J. J. 2011, ApJ, 740, L10, 1107.2106

Ogilvie, G. I., & Lin, D. N. C. 2004, ApJ, 610, 477, arXiv:astro-ph/0310218

——. 2007, ApJ, 661, 1180, arXiv:astro-ph/0702492

Ohta, Y., Taruya, A., & Suto, Y. 2005, ApJ, 622, 1118, arXiv:astro-ph/0410499

Pál, A., & Bakos, G. Á. 2006, PASP, 118, 1474, arXiv:astro-ph/0609658

Pál, A. et al. 2010, MNRAS, 401, 2665, 0908.1705

——. 2008, ApJ, 680, 1450, 0803.0746

Parker, E. N. 1958, ApJ, 128, 664

Pätzold, M., Carone, L., & Rauer, H. 2004, A&A, 427, 1075, arXiv:astro-ph/0408328

Pätzold, M., & Rauer, H. 2002, ApJ, 568, L117

Pepe, F., Mayor, M., Galland, F., Naef, D., Queloz, D., Santos, N. C., Udry, S., & Burnet, M. 2002, A&A, 388, 632, arXiv:astro-ph/0202457

Perryman, M. A. C. 2000, Reports on Progress in Physics, 63, 1209, arXiv:astro-ph/0005602

Pieters, C. M. et al. 2009, Science, 326, 568

Pietrinferni, A., Cassisi, S., Salaris, M., & Castelli, F. 2004, ApJ, 612, 168, arXiv:astro-ph/0405193

Pinsonneault, M. H., DePoy, D. L., & Coffee, M. 2001, ApJ, 556, L59, arXiv:astro-ph/0105257

Planck Collaboration et al. 2013, ArXiv e-prints, 1303.5062

Pollacco, D. L. et al. 2006, PASP, 118, 1407, arXiv:astro-ph/0608454

Pont, F. 2009, MNRAS, 396, 1789, 0812.1463

Pont, F. et al. 2010, MNRAS, 402, L1, 0908.3032

Pont, F., & Eyer, L. 2004, MNRAS, 351, 487, arXiv:astro-ph/0401418

Press, W. H., Teukolsky, S. A., Vetterling, W. T., & Flannery, B. P. 1992, Numerical recipes in C: The art of scientific computing

——. 2007, Numerical recipes: The art of scientific computing

Queloz, D. et al. 2010, A&A, 517, L1, 1006.5089

Queloz, D., Eggenberger, A., Mayor, M., Perrier, C., Beuzit, J. L., Naef, D., Sivan, J. P., & Udry, S. 2000a, A&A, 359, L13, arXiv:astro-ph/0006213

Queloz, D., Mayor, M., Naef, D., Santos, N., Udry, S., Burnet, M., & Confino, B. 2000b, in From Extrasolar Planets to Cosmology: The VLT Opening Symposium, ed. J. Bergeron & A. Renzini, 548

Radick, R. R., Thompson, D. T., Lockwood, G. W., Duncan, D. K., & Baggett, W. E. 1987, ApJ, 321, 459

Ragozzine, D., & Wolf, A. S. 2009, ApJ, 698, 1778, 0807.2856

Rasio, F. A., & Ford, E. B. 1996, Science, 274, 954

Reiners, A. et al. 2009, in American Institute of Physics Conference Series, Vol. 1094, American Institute of Physics Conference Series, ed. E. Stempels, 250–257, 0809.4546

Rennó, N. O. et al. 2009, Journal of Geophysical Research: Planets, 114, n/a

Rice, W. K. M., Armitage, P. J., & Hogg, D. F. 2008, MNRAS, 384, 1242, 0712.0823

Rogers, T. M., Lin, D. N. C., & Lau, H. H. B. 2012, ApJ, 758, L6, 1209.2435

Rossiter, R. A. 1924, ApJ, 60, 15

Russell, H. N. 1927, Astronomy

Saffe, C., Gómez, M., & Chavero, C. 2005, A&A, 443, 609, arXiv:astro-ph/0510092

Sanchis-Ojeda, R. et al. 2012, Nature, 487, 449, 1207.5804

Sanchis-Ojeda, R., & Winn, J. N. 2011, ApJ, 743, 61, 1107.2920

Sanchis-Ojeda, R., Winn, J. N., & Fabrycky, D. C. 2013, Astronomische Nachrichten, 334, 180, 1211.2002

Sanchis-Ojeda, R., Winn, J. N., Holman, M. J., Carter, J. A., Osip, D. J., & Fuentes, C. I. 2011, ApJ, 733, 127, 1103.4859

Sasselov, D. D. 2003, ApJ, 596, 1327, arXiv:astro-ph/0303403

Sasselov, D. D., & Lecar, M. 2000, ApJ, 528, 995, arXiv:astro-ph/9911390

Schatzman, E. 1962, Annales d'Astrophysique, 25, 18

Schlaufman, K. C. 2010, ApJ, 719, 602, 1006.2851

Schlesinger, F. 1910, Publications of the Allegheny Observatory of the University of Pittsburgh, 1, 123

——. 1916, Publications of the Allegheny Observatory of the University of Pittsburgh, 3, 23

Scholz, A., & Eislöffel, J. 2007, MNRAS, 381, 1638, 0708.2274

Scholz, A., Irwin, J., Bouvier, J., Sipőcz, B. M., Hodgkin, S., & Eislöffel, J. 2011, MNRAS, 413, 2595, 1101.1967

Seager, S., & Mallén-Ornelas, G. 2003, ApJ, 585, 1038, arXiv:astro-ph/0206228

Sestito, P., & Randich, S. 2005, A&A, 442, 615, arXiv:astro-ph/0507537

Shkolnik, E., Bohlender, D. A., Walker, G. A. H., & Collier Cameron, A. 2008, ApJ, 676, 628, 0712.0004

Shkolnik, E., Walker, G. A. H., & Bohlender, D. A. 2003, ApJ, 597, 1092

Shkolnik, E., Walker, G. A. H., Bohlender, D. A., Gu, P.-G., & Kürster, M. 2005, ApJ, 622, 1075, arXiv:astro-ph/0411655

Shporer, A. et al. 2009, ApJ, 690, 1393, 0806.4008

Silva-Valio, A. 2008, ApJ, 683, L179, 0808.2156

Simpson, E. K. et al. 2011a, AJ, 141, 161, 1009.3470

——. 2011b, AJ, 141, 8, 1008.3096

——. 2011c, MNRAS, 414, 3023, 1011.5664

Skrutskie, M. F. et al. 2006, AJ, 131, 1163

Skumanich, A. 1972, ApJ, 171, 565

Smalley, B. et al. 2012, A&A, 547, A61, 1206.1177

——. 2011, A&A, 526, A130, 1012.2278

Smith, A. M. S. et al. 2013, A&A, 552, A120, 1211.3045

——. 2012a, AJ, 143, 81, 1110.5313

——. 2012b, A&A, 545, A93, 1203.6017

Smith, A. M. S., Anderson, D. R., Skillen, I., Collier Cameron, A., & Smalley, B. 2011, MNRAS, 416, 2096, 1101.2432

Smith, B. A., & Terrile, R. J. 1984, Science, 226, 1421

Socrates, A., & Katz, B. 2012, ArXiv e-prints, 1209.5723

Soderblom, D. R. 1985, Icarus, 61, 343

——. 1998, Ap&SS, 261, 59

——. 2010, ARA&A, 48, 581, 1003.6074

Soderblom, D. R., Duncan, D. K., & Johnson, D. R. H. 1991, ApJ, 375, 722

Southworth, J. 2009, MNRAS, 394, 272, 0811.3277

——. 2010, MNRAS, 408, 1689, 1006.4443

——. 2011, MNRAS, 417, 2166, 1107.1235

Southworth, J. et al. 2011, A&A, 527, A8, 1012.5181

Sozzetti, A., Torres, G., Charbonneau, D., Latham, D. W., Holman, M. J., Winn, J. N., Laird, J. B., & O'Donovan, F. T. 2007, ApJ, 664, 1190, 0704.2938

Steele, I. A., Bates, S. D., Gibson, N., Keenan, F., Meaburn, J., Mottram, C. J., Pollacco, D., & Todd, I. 2008, in Society of Photo-Optical Instrumentation Engineers (SPIE) Conference Series, Vol. 7014, Society of Photo-Optical Instrumentation Engineers (SPIE) Conference Series, 0809.3351

Stempels, H. C., Collier Cameron, A., Hebb, L., Smalley, B., & Frandsen, S. 2007, MNRAS, 379, 773, 0705.1677

Stepien, K. 1988, ApJ, 335, 907

Sterne, T. E. 1939a, MNRAS, 99, 451

——. 1939b, MNRAS, 99, 662

Sudarsky, D., Burrows, A., & Pinto, P. 2000, ApJ, 538, 885, arXiv:astro-ph/9910504

Sukhbold, T., & Howell, S. B. 2009, PASP, 121, 1188, 0812.2013

Swain, M. R., Vasisht, G., Tinetti, G., Bouwman, J., Chen, P., Yung, Y., Deming, D., & Deroo, P. 2009, ApJ, 690, L114

Tegmark, M. et al. 2004, Phys. Rev. D, 69, 103501, arXiv:astro-ph/0310723

Tingley, B., & Sackett, P. D. 2005, ApJ, 627, 1011, arXiv:astro-ph/0503575

Torres, G., Fischer, D. A., Sozzetti, A., Buchhave, L. A., Winn, J. N., Holman, M. J., & Carter, J. A. 2012, ApJ, 757, 161, 1208.1268

Torres, G. et al. 2011, ApJ, 727, 24, 1008.4393

Tregloan-Reed, J., & Southworth, J. 2013, MNRAS, 431, 966, 1212.0686

Triaud, A. H. M. J. 2011, A&A, 534, L6, 1109.5813

Triaud, A. H. M. J. et al. 2013a, A&A, 551, A80, 1303.0254

——. 2010, A&A, 524, A25, 1008.2353

——. 2013b, A&A, 549, A18, 1208.4940

——. 2009, A&A, 506, 377, 0907.2956

——. 2011, A&A, 531, A24, 1103.2603

Tripathi, A. et al. 2010, ApJ, 715, 421, 1004.0692

Valenti, J. A., & Fischer, D. A. 2005, ApJS, 159, 141

VandenBerg, D. A., Bergbusch, P. A., & Dowler, P. D. 2006, ApJS, 162, 375, arXiv:astro-ph/0510784

Vaughan, A. H., Preston, G. W., Baliunas, S. L., Hartmann, L. W., Noyes, R. W., Middelkoop, F., & Mihalas, D. 1981, ApJ, 250, 276

Vican, L. 2012, AJ, 143, 135, 1203.1966

Vidal-Madjar, A., Lecavelier des Etangs, A., Désert, J.-M., Ballester, G. E., Ferlet, R., Hébrard, G., & Mayor, M. 2003, Nature, 422, 143

Vidotto, A. A., Jardine, M., & Helling, C. 2010, ApJ, 722, L168, 1009.5947

Vogt, H. 1926, Astronomische Nachrichten, 226, 301

Watson, C. A., Littlefair, S. P., Diamond, C., Collier Cameron, A., Fitzsimmons, A., Simpson, E., Moulds, V., & Pollacco, D. 2011, MNRAS, 413, L71, 1009.4132

Weber, E. J., & Davis, Jr., L. 1967, ApJ, 148, 217

Weidenschilling, S. J., & Marzari, F. 1996, Nature, 384, 619

Weidner, C., & Horne, K. 2010, A&A, 521, A76, 1007.4500

Weitz, C. M., & Parker, T. J. 2000, in Lunar and Planetary Institute Science Conference Abstracts, Vol. 31, Lunar and Planetary Institute Science Conference Abstracts, 1693

Welsh, W. F., Orosz, J. A., Seager, S., Fortney, J. J., Jenkins, J., Rowe, J. F., Koch, D., & Borucki, W. J. 2010, ApJ, 713, L145, 1001.0413

Wheatley, P. J. et al. 2010, ArXiv e-prints, 1004.0836

——. 2013, ArXiv e-prints, 1302.6592

Wilson, O. C. 1963, ApJ, 138, 832

Winn, J. N. et al. 2011a, ApJ, 741, L1, 1109.3198

Winn, J. N., Fabrycky, D., Albrecht, S., & Johnson, J. A. 2010a, ApJ, 718, L145, 1006.4161

Winn, J. N. et al. 2011b, AJ, 141, 63, 1010.1318

Winn, J. N., Johnson, J. A., Albrecht, S., Howard, A. W., Marcy, G. W., Crossfield, I. J., & Holman, M. J. 2009, ApJ, 703, L99, 0908.1672

Winn, J. N. et al. 2010b, ApJ, 718, 575, 1003.4512

——. 2010c, ApJ, 723, L223, 1009.5671

——. 2008, ApJ, 682, 1283, 0804.2259

——. 2005, ApJ, 631, 1215, arXiv:astro-ph/0504555

Wolff, S. C., Boesgaard, A. M., & Simon, T. 1986, ApJ, 310, 360

Wolszczan, A., & Frail, D. A. 1992, Nature, 355, 145

Wright, J. T. 2005, PASP, 117, 657, arXiv:astro-ph/0505214

Yoder, C. F., & Peale, S. J. 1981, Icarus, 47, 1

Zacharias, N., Monet, D. G., Levine, S. E., Urban, S. E., Gaume, R., & Wycoff, G. L. 2004, in Bulletin of the American Astronomical Society, Vol. 36, American Astronomical Society Meeting Abstracts, 1418

Zahn, J.-P. 1977, A&A, 57, 383

——. 1989, A&A, 220, 112